Silicon Pixel Sensors in the Inner Tracking System of the CMS Experiment

Dissertation
zur Erlangung des Doktorgrades
an der Fakultät für Mathematik, Informatik und Naturwissenschaften
Fachbereich Physik
der Universität Hamburg

vorgelegt von

Finn Feindt

Hamburg

2021

Gutachter/innen der Dissertation:	Prof. Dr. Erika Garutti
	Dr. Daniel Pitzl
Zusammensetzung der Prüfungskommission:	Prof. Dr. Erika Garutti
	Prof. Dr. Ingrid-Maria Gregor
	Prof. Dr. Daniela Pfannkuche
	Dr. Daniel Pitzl
	Prof. Dr. Peter Schleper
Vorsitzende/r der Prüfungskommission:	Prof. Dr. Daniela Pfannkuche
Datum der Disputation:	30.09.2021
Vorsitzender Fach-Promotionsausschusses PHYSIK:	Prof. Dr. Wolfgang Hansen
Leiter des Fachbereichs PHYSIK:	Prof. Dr. Günter H. W. Sigl
Dekan der Fakultät MIN:	Prof. Dr. Heinrich Graener

Abstract

Silicon sensors for the Compact Muon Solenoid (CMS) pixel detector are optimized to operate in a challenging environment. This work addresses two topics, related to silicon pixel sensors in CMS.

Through 2017 and 2018 (Phase-1) the Large Hadron Collider (LHC) provided a peak instantaneous luminosity of about $2 \times 10^{34}\,\mathrm{cm^{-2}\,s^{-1}}$, colliding bunches of protons at a nominal frequency of $40\,\mathrm{MHz}$. A $1\,\mathrm{MeV}$ neutron equivalent fluence $\phi_{eq} = 7.9 \times 10^{14}\,\mathrm{cm^{-2}}$ accumulated in the innermost barrel layer of the pixel detector. Full-depletion voltage and leakage current of the pixel sensors were measured through Phase-1 and compared to model predictions. In this work, the model for these predictions is revised, and systematic effects in the measurements are evaluated.

The bigger part of this work is about silicon sensors for the Phase-2 Upgrade of the CMS pixel detector. As part of this upgrade, the current pixel detector will be replaced by the mid-2020s, when the High-Luminosity LHC (HL-LHC) starts operation. The HL-LHC will deliver a peak instantaneous luminosity up to $7.5 \times 10^{34}\,\mathrm{cm^{-2}\,s^{-1}}$, and a fluence $\phi_{eq} = 2.3 \times 10^{16}\,\mathrm{cm^{-2}}$ is expected in the innermost barrel layer of the pixel detector after $3000\,\mathrm{fb^{-1}}$ of integrated luminosity. To cope with the expected track densities, the new pixel sensors will have pixel sizes of either $25 \times 100\,\mathrm{\mu m^2}$ or $50 \times 50\,\mathrm{\mu m^2}$. The final sensor design is subject to an intensive R&D program for planar and 3D sensors manufactured at various vendors. In this work, planar $\mathrm{n^+p}$ sensors with a thickness of $150\,\mathrm{\mu m}$ manufactured by Hamamatsu Photonics K.K are investigated. The investigated sensors are bump-bonded to the ROC4SENS readout chip and tested in an electron beam with energies of about $5\,\mathrm{GeV}$ at Deutsches Elektronen-SYnchrotron (DESY). Observables like cluster size, signal, noise, hit efficiency and spatial resolution are reconstructed and investigated as a function of the bias voltage and beam incidence angle. Sensor modules are tested before and after irradiation with protons to $\phi_{eq} = 5.4 \times 10^{15}\,\mathrm{cm^{-2}}$, and reactor neutrons to $\phi_{eq} = 14.4 \times 10^{15}\,\mathrm{cm^{-2}}$. For beam incidence parallel to the sensor normal, bias voltages of $400\,\mathrm{V}$ to $500\,\mathrm{V}$ suffice to reach hit efficiencies of $99\,\%$ after irradiation, meeting the requirements for the second layer of the upgraded detector. The hit resolution for sensors with $50 \times 50\,\mathrm{\mu m^2}$ pixels is found to be $4.0\,\mathrm{\mu m}$ before and $5.7\,\mathrm{\mu m}$ after proton irradiation to $\phi_{eq} = 2.3 \times 10^{15}\,\mathrm{cm^{-2}}$ at the optimal track angle.

Kurzfassung

Siliziumsensoren für den Compact Muon Solenoid (CMS) Pixeldetektor sind für eine herausfordernde Umgebung optimiert. Diese Arbeit widmet sich zwei Aspekten von Silizium-Pixelsensoren bei CMS.

In den Jahren 2017 und 2018 (Phase-1) lieferte der Large Hadron Collider (LHC) eine instantane Luminosität von bis zu ca. $2 \times 10^{34}\,\mathrm{cm^{-2}\,s^{-1}}$. Dabei kollidieren Pakete von Protonen bei einer nominellen Frequenz von $40\,\mathrm{MHz}$. Auf diese Weise wurde in der innersten zylindrischen Lage eine $1\,\mathrm{MeV}$ Neutronen äquivalente Fluenz $\phi_{eq} = 7.9 \times 10^{14}\,\mathrm{cm^{-2}}$ angesammelt. Die Verarmungsspannungen und Leckströme in der innersten zylindrischen Lage wurden während Phase-1 gemessen und mit Modellvorhersagen verglichen. In dieser Arbeit wurden das Vorhersagemodell überarbeitet und systematische Effekte evaluiert.

Der größte Teil dieser Arbeit widmet sich Siliziumsensoren für das Phase-2 Upgrade des CMS Pixeldetektors. Der neue Detektor soll den jetzige ersetzt haben, wenn der High-Luminosity LHC (HL-LHC) Mitte der 2020er Jahre in Betrieb geht. Der HL-LHC wird eine instantane Luminosität von bis zu ca. $7.5 \times 10^{34}\,\mathrm{cm^{-2}\,s^{-1}}$ erreichen. In der innersten zylindrischen Lage des Pixeldetektors wird nach $3000\,\mathrm{fb^{-1}}$ integrierter Luminosität eine Fluenz $\phi_{eq} = 2.3 \times 10^{16}\,\mathrm{cm^{-2}}$ erwartet. Um die erwartete Dichte von Teilchenspuren zu bewältigen, werden die neuen Pixelsensoren Pixel mit einer Größe von $25 \times 100\,\mathrm{\mu m^2}$ oder $50 \times 50\,\mathrm{\mu m^2}$ haben. Das endgültige Sensordesign ist Gegenstand eines intensiven Forschungs- und Entwicklungsprogramms für planare und 3D-Sensoren mit verschiedenen Herstellern. In dieser Arbeit werden $150\,\mathrm{\mu m}$ dicke planare $\mathrm{n^+p}$ Sensoren untersucht, die von Hamamatsu Photonics K.K hergestellt wurden. Diese Sensoren sind mit dem ROC4SENS Auslesechip verbunden und werden in einem Elektronenstrahl mit einer Energie von ungefähr $5\,\mathrm{GeV}$ am Deutsches Elektronen-SYnchrotron (DESY) getestet. Observablen wie die Clustergröße, die Signalstärke, das Rauschen, die Nachweiseffizienz und das räumliche Auflösungsvermögen werden rekonstruiert und als Funktion der Betriebsspannung und des Winkels zwischen Sensor und Strahl untersucht. Sensormodule werden vor und nach Bestrahlung mit Protonen bis $\phi_{eq} = 5.4 \times 10^{15}\,\mathrm{cm^{-2}}$ und Reaktorneutronen bis $\phi_{eq} = 14.4 \times 10^{15}\,\mathrm{cm^{-2}}$ getestet. Trifft der Strahl den Sensor parallel zu seiner Normalen, sind Betriebsspannung zwischen $400\,\mathrm{V}$ und $500\,\mathrm{V}$ nötig, um nach Bestrahlung eine Nachweiseffizienz von $99\,\%$ zu erreichen. Damit sind die Anforderungen für die zweite zylindrische Lage des neuen Detektors erfüllt. Für den optimalen Winkel zwischen Strahl und Sensor, ist das räumliche Auflösungsvermögen von Sensoren mit $50 \times 50\,\mathrm{\mu m^2}$ Pixeln $4.0\,\mathrm{\mu m}$ vor und $5.7\,\mathrm{\mu m}$ nach Protonenbestrahlung mit $\phi_{eq} = 2.3 \times 10^{15}\,\mathrm{cm^{-2}}$.

Contents

1. Introduction

In [1] J.R.R Tolkien writes 'And he that breaks a thing to find out what it is has left the path of wisdom.' (p. 337). I have to disagree with the said quote. In science things might need to be broken to investigate their properties, may it be the dissection of plants or reverse engineering. But the value gained — knowledge — must exceed the value of what is broken. To maximize the benefits of the investigations, one has to carefully observe and document. High energy physics experiments follow similar approaches. For example, protons are destroyed in deep inelastic proton-electron scattering to study their structure, like it was done at Hadron Elektron Ring Anlage (HERA) [2]. Such experiments require many repetitions and the observation and reconstruction of the scattering products. This is beyond human capabilities and highly specialized detectors are built to detect the collision products, measure their properties, and store the results of the measurements for later analysis.

The Standard Model of particle physics (SM) includes a large part of mankind's present knowledge about particle physics and is described e.g. in [3]. It is formulated in terms of a quantum field theory, includes all directly observed particles, and describes three of the four fundamental forces. The particles are fermions carrying a spin of $1/2$ and bosons carrying a spin of 0 or 1. The fermions are the fundamental constituents of matter while the spin 1 bosons mediate the three forces. The particles obtain their masses through interaction with the spin 0 Higgs boson. The SM is an impressively powerful theory and correctly predicts the production cross sections for many final states observed in the Compact Muon Solenoid (CMS) detector [4]. Still, there are open questions. One is related to the fact that the SM does not include the fourth force, gravity, which is so far not described in terms of a quantum field theory. Others are discussed, e.g. in [3]. The velocity distributions of stars in the galaxies suggest the existence of mass in addition to the mass we observe, which is referred to as dark matter and can so far not be associated with SM particles. Also, there is an asymmetry between matter and antimatter in the universe, which is not explained within the SM — at least not to the extent we observe. Including recent results on the magnetic moment of antimuons, measurements and SM predictions disagree by 4.2 standard deviations [5]. New theoretical models like Supersymmetry [6] and Grand Unified Theories [7] provide solutions to some of these shortcomings and predict new particles. Some of them should be observable at the TeV scale, accessible at the Large Hadron Collider (LHC). Collider experiments like the CMS experiment strive to find these new particles or further tensions between measurements and SM predictions.

1. Introduction

Such experiments are unique enterprises and very challenging in terms of their instrumentation. This work is about silicon pixel sensors in the inner tracking system of the CMS detector. These pixel sensors are the active elements closest to the interaction point and are used to reconstruct tracks of charged particles. Therefore, they are a critical component of the detection system. Another consequence of the proximity to the interaction point is the exposure to a high flux of particles, causing severe radiation damage to the silicon detector.

Silicon detectors are an established technology with applications in particle physics and other fields. For tracking applications in high energy physics, segmented silicon sensors like strip and pixel sensors are used. Hybrid pixel detectors [8] require dedicated readout chips to process the signals, which are directly connected to the pixel cells of the sensor. Monolithic active pixel sensors, see e.g. [9], combine the sensor and the readout chip in a single device. Charge-coupled devices [10] are sensors for optical photons and are used in digital cameras to record images or videos. Other types of silicon detectors sensitive to optical photons are avalanche-photodiodes employing an internal gain mechanism to increase the sensitivity to single photons. Silicon photomultipliers [11] are arrays of avalanche-photodiodes and are frequently used in combination with scintillators in calorimeters or detectors for medical applications like positron emission tomography.

This work begins with an introduction to the physics of silicon pixel sensors in chapter 2 and a description of the CMS detector with focus on the silicon pixel sensors investigated in this work in chapter 3. The operation of a pixel detector in a running experiment is a challenging task and requires regular monitoring of the detector's performance and tuning of operational parameters. This is especially true in the presence of radiation damage causing changes in detector properties. In chapter 4 monitoring and modeling of two properties of the pixel sensor, its leakage current, and its full depletion voltage through the years 2017 and 2018, are discussed. The focus is on systematic effects complicating modeling of these properties, which is essential to choose cooling settings, especially in maintenance periods. The main focus of this work is on the characterization of pixel sensors foreseen for the upgrade of the detector in the mid-2020s and their resilience to non-ionizing energy loss. The characterization is based on test-beam measurements. The corresponding test-beam setup is described in chapter 5 and the analysis of the data is described in chapter 6. The final design and technological choices for the new pixel sensors are not yet fixed and several options are considered. The results of the test-beam characterization are presented in chapter 7 and compared for different prototypes, providing valuable information to choose the final design and technologies. Test-beam measurements are expensive and time-consuming, and it is not feasible to investigate all conditions which will be realized in the final experiment. In chapter 8 the test-beam measurements are used to validate a simulation framework for non-irradiated sensors. This is used to predict the performance of these sensors in the presence of a magnetic field. It can be used to make predictions for a larger set of conditions in the future.

2. Physics of Silicon Pixel Sensors

Silicon pixel sensors are a key element of many tracking detectors, used to detect charged particles and to determine their trajectories, referred to as tracks. In addition to that, the arrival time of charged particles and the energy deposited in the sensor material are measured.

In high energy physics experiments these informations are used in many ways to derive more fundamental properties of the collision products, thoroughly discussed e.g. in [12]. To name some of those: The curvature of the trajectories in the magnetic field of a detector allows to derive the momentum of the charged particle. Particles with sufficiently short live times may decay within the volume of the tracking detector and generate secondary vertices with a certain distance to the primary vertex, the impact parameter. Lifetimes are a basic property of fundamental particles and hadrons, thus impact parameters are an important ingredient to particle identification — on a probabilistic level. In addition, also the relation between particle momentum and its energy loss (deposited energy) may be used for particle identification. In presence of multiple primary collisions, referred to as pileup, the trajectory [13] and timing information [14] can be used to assign a track to one of these primary collisions, a primary vertex. The trajectories are used to link measurements in other sub-detectors, such as calorimeters and muon chambers in the context of particle flow reconstruction [13]. Finally, the tracking system can provide information to the trigger system [15].

Next to silicon detectors, gaseous detectors, e.g. multiwire proportional counters [16], are another commonly used type of tracking detectors. The choice of a detector type and its layout is driven by the requirements of the experiments. The frequent choice of silicon as a base material for tracking detectors is based on its excellent properties with respect to many of these requirements. To name some of these properties, loosely following [12] and [17]:

- **Spatial resolution:** In the context of tracking detectors track resolution is to be understood as the uncertainty on the spatial track parameters. It depends on properties like the hit resolution of single detector elements, the geometry of the tracking detector, its material budget (see below) and particle momentum.

- **Energy resolution:** The energy resolution is defined as the uncertainty on a measurement of the energy deposited in a given sensor.

- **Time resolution:** Time resolution is to be understood as the uncertainty of a time measurement.

- **Granularity:** Granularity is the density of readout elements in a plane or volume. It determines the two-track resolution, the capability to separate individual tracks for high local track density in e.g. boosted jets or high pileup experiments. It is strongly related to spatial resolution.

- **Rate capability:** Similar to granularity in space, the rate of bunch collisions constrains the time available for the formation of a signal in the sensor and its processing in the readout chain.

- **Material budget:** Charged particles passing matter experience elastic coulomb scattering, causing especially angular deviations from their original direction. This is a limiting factor to track resolution and quantified in terms of material budget.

- **Radiation tolerance:** The ionizing and non-ionizing radiation at high energy physics experiments causes aging effects in many detector components. Thus the chosen detector components must withstand these aging effects expected in the foreseen operation period.

- **Cost and scalability:** Monetary costs and many other practical aspects associated with the choice of a detector type need to be taken into account.

These properties are not solely related to the silicon sensor, but also to the design of e.g. the readout chip, data acquisition system, mechanics and cooling. In the following sections, an introduction to the physics of silicon detectors is given.

2.1. Basic Properties and Concepts

A comprehensive discussion of concepts related to the physics of semiconductor devices and the relevant properties of silicon is given in [18], serving as a basis for a brief summary.

Detector grade silicon is monocrystalline and has a lattice in diamond structure. In crystals, the discrete energy levels of the individual atoms degenerate due to the interaction between the atoms and form energy bands. The highest energy band occupied at a temperature $T = 0\,\mathrm{K}$ is referred to as the valence band, the next highest band is referred to as the conduction band. Silicon is classified as a semiconductor. In figure 2.1 schematic band diagrams of a conductor, semiconductor and insulator are shown. In conductors, the valence band is either partially filled or overlapping with the conduction band, permitting electrons to move between free states and contribute to an electrical current. In semiconductors and insulators, the valence and conduction band are separated by a gap in energy, the bandgap E_g. The difference is the magnitude of the bandgap, determining the probability of a thermal excitation from the valence to the conduction band. In

this case, an electron in the conduction band and an empty state in the valence band — defining a hole — can contribute to an electric current. In semiconductors, the bandgap is on the order of $1\,\text{eV}$. In high purity silicon, it is $1.12\,\text{eV}$, at room temperature. This is to be compared to the thermal energy at room temperature, which is on the order of $k_B T \approx 0.025\,\text{eV}$, with k_B being the Boltzmann constant.
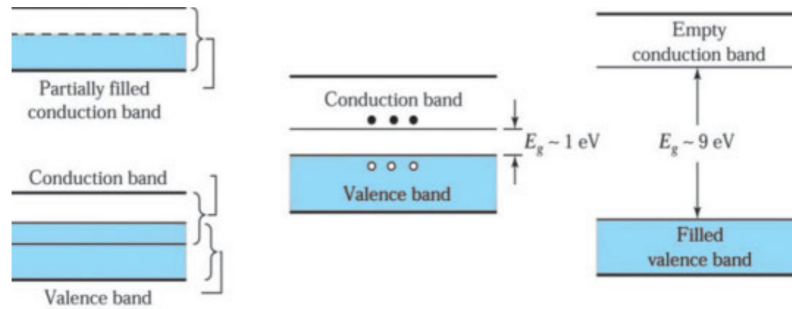

Figure 2.1.: Schematic band diagrams in a conductor (left), semiconductor (center) and insulator (right). The full and open circles indicate thermally excited electrons and empty states in the valence band (holes), respectively. Taken from [18]

The number of free charge carriers in semiconductors — electrons in the conduction band and holes in the valence band — can be manipulated by introducing particular impurities to the crystal. This procedure is known as doping. Regarding the impurities, donors and acceptors are distinguished. Atoms like arsenic or phosphorus are used as donors in silicon and offer additional states in the bandgap, close beneath the edge of the conduction band. In case of phosphorus, the measured ionization energy of the additional state is $0.046\,\text{eV}$ [19] in silicon. They are ionized with a high probability at room temperature. Thus additional negative charge carriers are *donated* to the semiconductor and the material is called n-type. Similarly acceptors, like boron and aluminum in silicon, introduce additional empty states close to the valence band. These additional states are typically filled at room temperature, leaving holes in the valence band. Electrons from the valence band are *accepted* and the material is called p-type.

In figure 2.2 the charge carrier concentrations n and p are shown schematically, for intrinsic, n-type and p-type semiconductors. They are derived from the product of the density of states and the Fermi-Dirac distribution $N(E)\cdot\text{F(E)}$, integrated over the conduction or valence band. The system is assumed to be in thermal equilibrium and non-degenerate, meaning that the doping densities are smaller than the effective densities of states in the valence and conduction band. The explicit calculations are given for example in [19].

Another important concept related to the physics of silicon devices is the p-n junction. Following [20], the p-n junction is an interface between an n-type and a p-type region inside a semiconductor. Due to the gradient in the concentrations of electrons, electrons diffuse from the n-type to the p-type region. In the p-type region, they recombine with holes. The same applies to holes, diffusing in the opposite direction and recombining with electrons. This way a space charge region builds up, which is positive in the n-type and
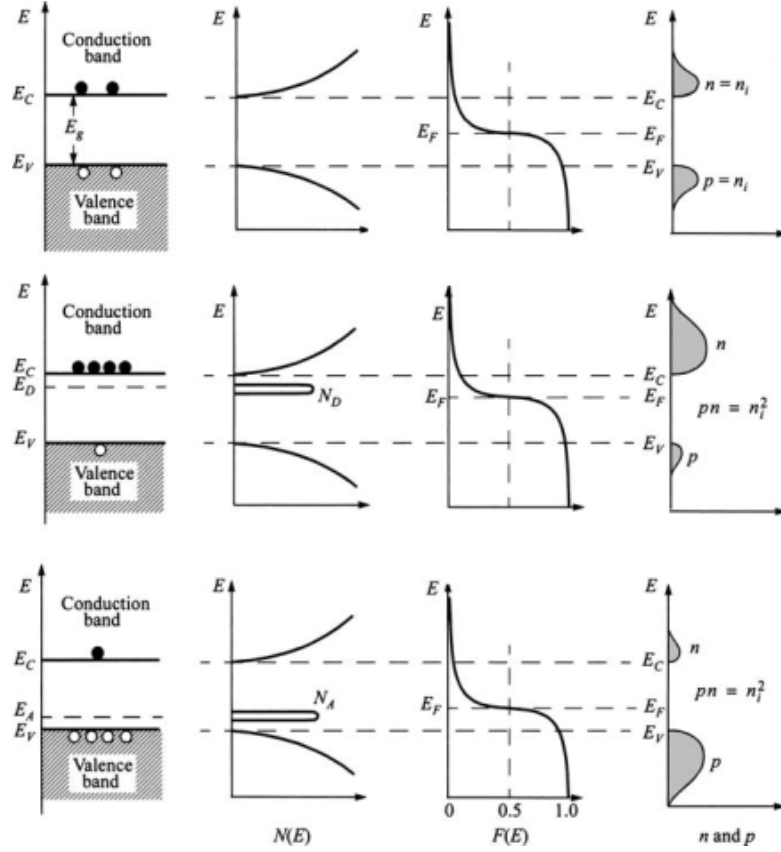
Figure 2.2.: Schematic band diagram, density of states $N(E)$, Fermi-Dirac distribution $F(E)$ and charge carrier concentrations n, p (left to right) in an intrinsic, n-type and p-type semiconductor (top to bottom). Taken from [19].

negative in the p-type material. This region is also called depletion region, as it is mostly depleted from free charge carriers. Due to the space charge, an electric field builds up, opposing diffusion, until equilibrium is reached.

In figure 2.3 the depletion region, electric field and electric potential are shown for an abrupt, one-dimensional p-n junction in equilibrium. The acceptor and donor densities are denoted as N_D and N_A. The width of the depletion region is labeled W_{Dp}, W_{Dn} in the p-type, n-type region, respectively. The potential difference between the p-type and n-type region is the build-in potential Ψ_{bi}.

The silicon sensors investigated in this work contain a junction between e.g. a highly doped n-type region, denoted as n^+ region, and p-type material. For an abrupt junction and $N_D \gg N_A$, the total width $W = W_{Dp} + W_{Dn}$ of the depletion region is dominated by W_{Dp} and reads [20]

$$W \approx \sqrt{\frac{2\epsilon_s\epsilon_0}{eN_A}(\Psi_{bi} + V_{bias})}, \tag{2.1}$$

were e denotes the elementary charge, ϵ_0 is the vacuum permittivity, ϵ_s the relative permittivity of silicon and V_{bias} is an additional positive voltage applied on the n^+ side of the junction. For increasing V_{bias} the width of the depletion zone grows and the current through the p-n junction is small. This situation is referred to as reverse bias and the way
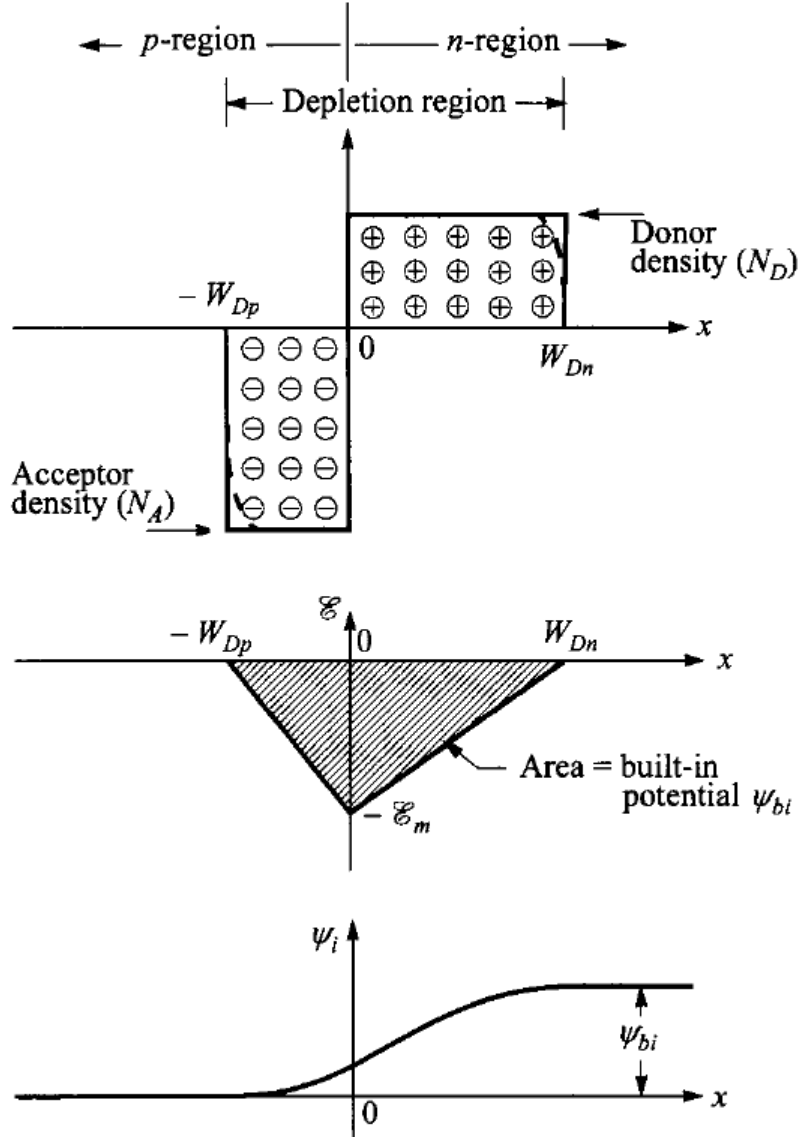
Figure 2.3.: Schematic depletion region, electric field and electric potential (top to bottom) for an abrupt p-n junction in equilibrium. Taken from [19] and modified.

silicon sensors are typically operated. For sufficiently large V_{bias}, W reaches the physical thickness d of the silicon sensor and further growth of the depletion region is usually constrained by a highly doped p$^+$ region. The voltage at which $W = d$ defines the full depletion voltage

$$V_{depl} = \frac{e|N_{eff}|d^2}{2\epsilon_s\epsilon_0},$$ (2.2)

neglecting the build-in potential Ψ_{bi}. Following [21], the density of acceptors N_A is replaced by the effective space charge $|N_{eff}|$, as this will prove handy for the discussion of irradiated silicon sensors. Note that this equation is only valid if N_{eff} is constant through the p-type (bulk) region.

2.2. Energy Loss in Silicon

The detection of charged particles in detectors is based on the fact that charged particles lose energy as they pass through matter. A fraction of the lost energy results in the generation of electron-hole pairs in semiconductor detectors, electrons and ions in gaseous detectors and photons in scintillators, generating detectable signals. A thorough discussion of the interactions between particles and matter is given in [22], and an overview is presented in [23], used as a basis for this section.
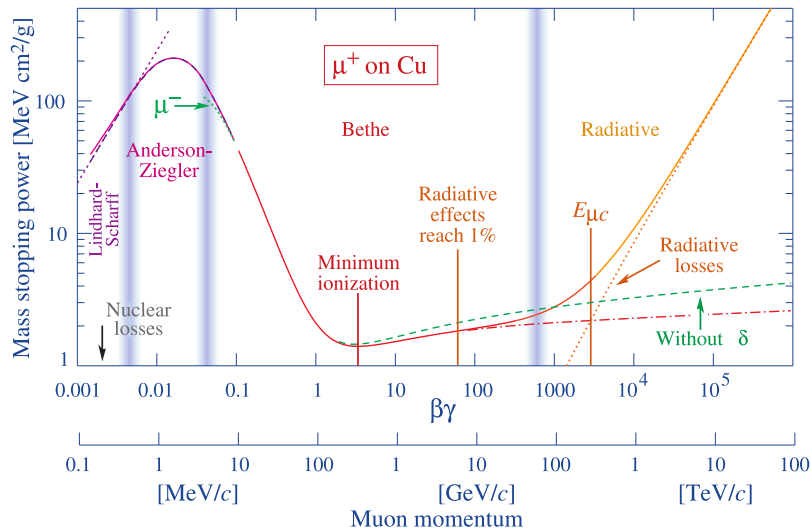

Figure 2.4.: Mass stopping power for antimuons in copper as a function of the antimuon momentum and $\beta\gamma$. Taken from [23].

For charged particles with masses larger than the electron mass m_e the "Bethe equation" describes the mean energy loss rate $\langle -dE/dx \rangle$, also called mass stopping power, approximately in the range $0.1 < \beta\gamma < 1000$. Here x is a distance and β is defined as

$$\beta = \frac{v}{c},\tag{2.3}$$

where v and c are the particles velocity and the speed of light in vacuum. The Lorentz factor γ is

$$\gamma = \frac{1}{\sqrt{1-\beta^2}}.\tag{2.4}$$

In said range, the energy loss is dominated by ionization and excitation of atoms in the traversed material. The "Bethe equation" is given for example in [23] and $\langle -dE/dx \rangle$ is shown in figure 2.4 for antimuons in copper. The approximate range given above is indicated in the figure. For lower momenta corrections, e.g. for atomic binding energies, need to be taken into account. See [24] for further discussion. For larger momenta radiative processes like electron-positron pair production and bremsstrahlung set in and dominate above a critical energy $E_{\mu c}$, as discussed in [23]. Both regions are indicated in the figure including the correction for the density effect (δ). At $\beta\gamma \approx 3$ the energy loss has

a minimum and particles experiencing a similar energy loss are called Minimum-Ionizing Particles (mip's). Typically the performance of particle detectors is characterized for the smallest possible signal using mip's.

The energy loss experienced by a single particle is subject to fluctuations. The corresponding energy loss distributions are called straggling functions and are highly skewed. In practice, the mean energy loss rate is of limited use, since rare large energy depositions introduce large fluctuations for small samples and make it sensitive to cuts [23]. In figure 2.5 straggling functions are shown for 500 MeV/c pions in silicon of different thicknesses.

Within this work, silicon sensors with a thickness of about 150 µm are investigated using a beam of electrons with a momentum of about 5 GeV/c, as discussed in chapter 5. For electron momenta exceeding a few 1 MeV/c, radiative processes need to be taken into account in energy loss calculations [22]. In any case, this effect is small in thin silicon sensors $O(100\,\mu m)$, according to Bichsel [25]. This is because most of the generated photons are hard and do not interact inside the silicon, thus their contribution to the generation of electron-hole pairs is negligible. It follows that the energy loss distributions calculated in [25] can be used to derive the number of electron-hole pairs expected for the above-mentioned experimental conditions. The Most-Probable Value (MPV) of the energy loss distributions Δ_p is reported to be

$$\Delta_p = d \cdot (190 + 16.3 \ln(d)), \tag{2.5}$$

where Δ_p is in keV and d is the thickness of a silicon absorber in µm. It is stated to be accurate within 1 % for electrons, pions and protons with $\beta\gamma > 100$. In addition, the full with half maximum of the calculated straggling functions are reported to agree within 1 % for the above-mentioned particles and $\beta\gamma > 100$. This motivates the use of pion cross-sections at 45 GeV/c in the simulation studies presented in chapter 8.

Evaluating equation 2.5 for a thickness of 150 µm yields a most probable energy loss of 40.8 keV. Taking into account the mean ionization energy in silicon[1]of 3.67 eV at room temperature, this corresponds to an expected MPV of 11.1×10^3 electron-hole pairs (11.1 ke). Evaluating figure 34.6 in [23] the most probable energy loss in 150 µm of silicon has a minimum of about 37.3 keV. Thus the energy loss for mip's is about 9 % smaller compared to 5 GeV/c electrons.

Another aspect regarding the interaction of charged particles in matter is the angular deflection of charged particles passing matter. The net deflection is dominated by many small-angle deflections due to Coulomb interaction with the nuclei — multiple Coulomb scattering. Infrequent large-angle deflections cause tails in the distribution of the scattering angle. In any case, a Gaussian representation is presented here, following the

---

[1]Different values are reported in literature. Owens *et al.* report a value of 3.62 eV [26], Scholze *et al.* determined 3.66 eV [27]. The value quoted here is from Groom [28], where results from various references, including measurements at cryogenic temperatures, are reviewed.
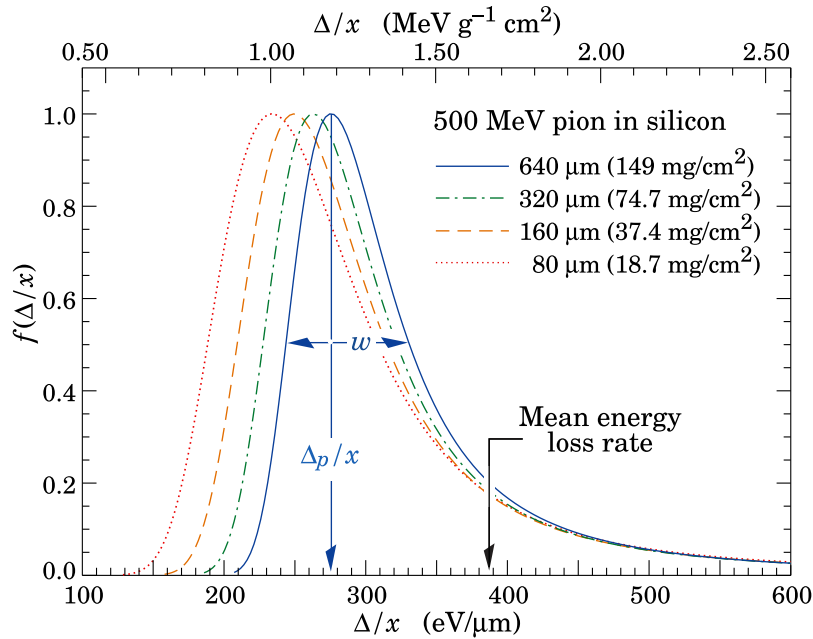
Figure 2.5.: Straggling functions f for 500 MeV pions in silicon of different thicknesses x. The energy loss is denoted as Δ, Δ_p is the most probable energy loss and w is the full width at half maximum. The functions are normalized to unity at the maximum. Taken from [23].

parametrizations given in [29]. A better description of the angular distributions is given by Molière [30] and further references in [29]. In the Gaussian representation, the distribution of the deflection angles in the two directions orthogonal to the initial direction of the incident particle has a Root Mean Square (RMS)

$$\theta_0 = \frac{13.6\,\text{MeV}}{\beta c |\vec{p}|} Z \sqrt{\frac{X}{X_0}} \left[1 + 0.088 \log_{10} \left(\frac{X Z^2}{X_0 \beta^2} \right) \right]. \tag{2.6}$$

Here $|\vec{p}|$ and Z denote the absolute momentum of the incident particle and its charge number. The thickness X of the scattering material is given in terms of the corresponding radiation length X_0. Tabulated values for X_0 can be found in [31]. It is the mean path over which the energy of an electron is reduced to $1/e$, where e is Euler's number, of its initial energy via emission of bremsstrahlung [23].

2.3. Working Principle of Silicon Pixel Sensors

A schematic sketch of a pixel detector module is shown in figure 2.6. It consists of a n$^+$-p silicon sensor and a readout chip. For its operation, a negative bias voltage is applied to the p$^+$ side of the sensor, referred to as backside. With increasing bias voltage, a depletion zone grows from the n$^+$ doped regions, the pixel implants, into the p-type region, also known as bulk region. An electric field builds up and at a sufficiently high voltage, the depletion region reaches the backside, as discussed in section 2.1. In a real sensor the

situation is more complicated. Further features like guard rings and additional implants to ensure inter-pixel isolation might be required. These are discussed thoroughly in [8], including further combinations of bulk and implant doping like n$^+$ implants in n-type material. Features of the sensors investigated in this work will be discussed in section 3.3.

Electron-hole pairs, generated by ionizing radiation as discussed in section 2.2, are separated in the electric field. The holes drift in the direction of the electric field towards the backside of the sensor, as indicated in the figure. Electrons drift towards the n$^+$ implants. The motion of the charge carriers induces a current signal in the n$^+$ pixel implants. Both, the charge carrier drift and the induction of the current signal will be further discussed later in this section. Via the metallization and the bump-bond connection, see for example [32], the pixel implant and readout chip have a conductive connection. In the readout chip, the current signal is processed and fed into a chain of readout electronics until it is stored. The readout chip and the readout chain are designed for a specific application. The readout system used in this work will be discussed in section 5.
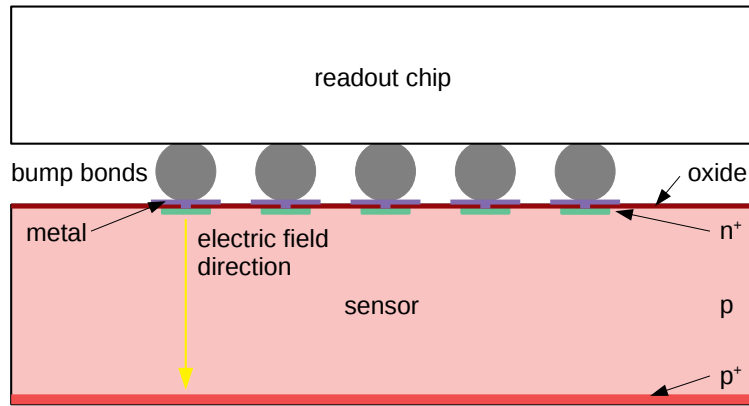

Figure 2.6.: Schematic n$^+$-p pixel detector module. The picture is not to scale.

Charge carrier drift in silicon can be described in terms of the equations of motion [33]

$$
\frac{d\vec{r}}{dt} = \vec{v} \tag{2.7}
$$
$$
\frac{d\vec{v}}{dt} = \frac{e}{m^*} \left[q\vec{E} + qr_H\vec{v} \times \vec{B} - \frac{\vec{v}}{\mu(|\vec{E}|)} \right],
$$

where $\vec{r}$ is the position, $\vec{v}$ the velocity, m^* the effective mass, q the sign of the charge, r_H the hall factor and $\mu(|\vec{E}|)$ the mobility of the corresponding electrons or holes. The electric and magnetic fields are denoted as $\vec{E}$ and $\vec{B}$, respectively and e is the elementary charge.

2. Physics of Silicon Pixel Sensors

In [19] the charge carrier mobility is introduced as the proportionality constant between the drift velocity and the electric field

$$\vec{v_d} = \mu \vec{E}. \tag{2.8}$$

For large electric fields, the mobility is a function of the absolute electric field $|\vec{E}|$ and several parametrizations are available in literature. Within this work, the parametrization presented in [34] is used. It is based on measurements of the drift velocity in the $\langle 111 \rangle$ direction and reads

$$\vec{v_d} = \frac{v_m/E_m}{\left(1 + \left(|\vec{E}|/E_m\right)^{\beta_m}\right)^{1/\beta_m}} \cdot \vec{E}. \tag{2.9}$$

The parameters v_m, E_m and β_m depend on the temperature and the charge carrier type and are explicitly given in [34]. In figure 2.7 electron and hole mobilities at $-20\,°\mathrm{C}$ are shown as a function of the electric field. Further measurements of the mobility and comparison between different parametrizations are presented in [35], focusing on measurements in the $\langle 100 \rangle$ direction.
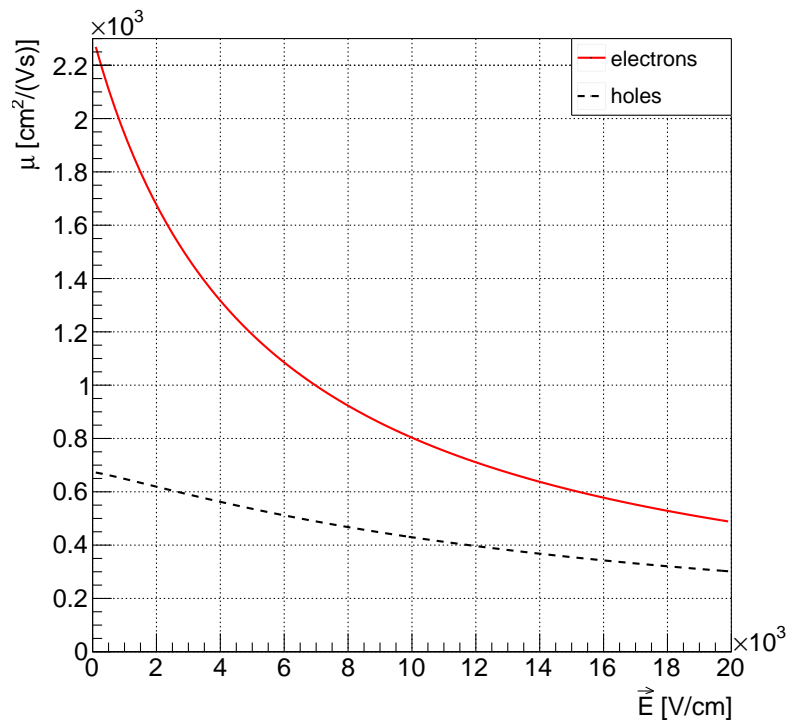
Figure 2.7.: Mobilities for electrons and holes at $-20\,°\mathrm{C}$ as a function of the electric field. Using equation 2.9 and parameters from [34].

In the absence of a magnetic field, the drift of holes follows the direction of the electric field and electrons drift in the opposite direction. In the presence of a magnetic field, the term $\vec{v} \times \vec{B}$ causes a deflection from that direction. This deflection is characterized by the

Lorentz angle θ_L following

$$\tan \theta_L = r_H \mu(|\vec{E}|) B_\perp, \tag{2.10}$$

where $B_\perp$ is the component of the magnetic field orthogonal to the velocity of the drifting charge carrier [8]. In figure 2.8a the deflection of electrons in a silicon sensor, simulated using Allpix^2 [36] is shown. The electron-hole pairs are generated along the z-direction and displaced in the x-direction. The largest displacement — the Lorentz shift — occurs for electrons generated at the backside, drifting through the entire thickness of the sensor. Assuming a constant electric field, a magnetic field of 3.8 T, a thickness of 150 μm and using the above-mentioned parametrization of the mobility at a temperature of $-20\,°C$, equation 2.10 is used to estimate the Lorentz shift as a function of the electric field. The result is shown in figure 2.8. It is found to be 50 μm for an average electric field of about $10 \times 10^3\,\mathrm{V\,cm^{-1}}$ and 25 μm for an average electric field of about $26 \times 10^3\,\mathrm{V\,cm^{-1}}$, corresponding to a bias voltage of 150 V and 390 V in a sensor of said thickness. As discussed later, this consideration is important to match the Lorentz shift to the pitch p of a pixel sensor. The pitch is the distance between the centers of two neighboring pixel implants.

(a)

(b)
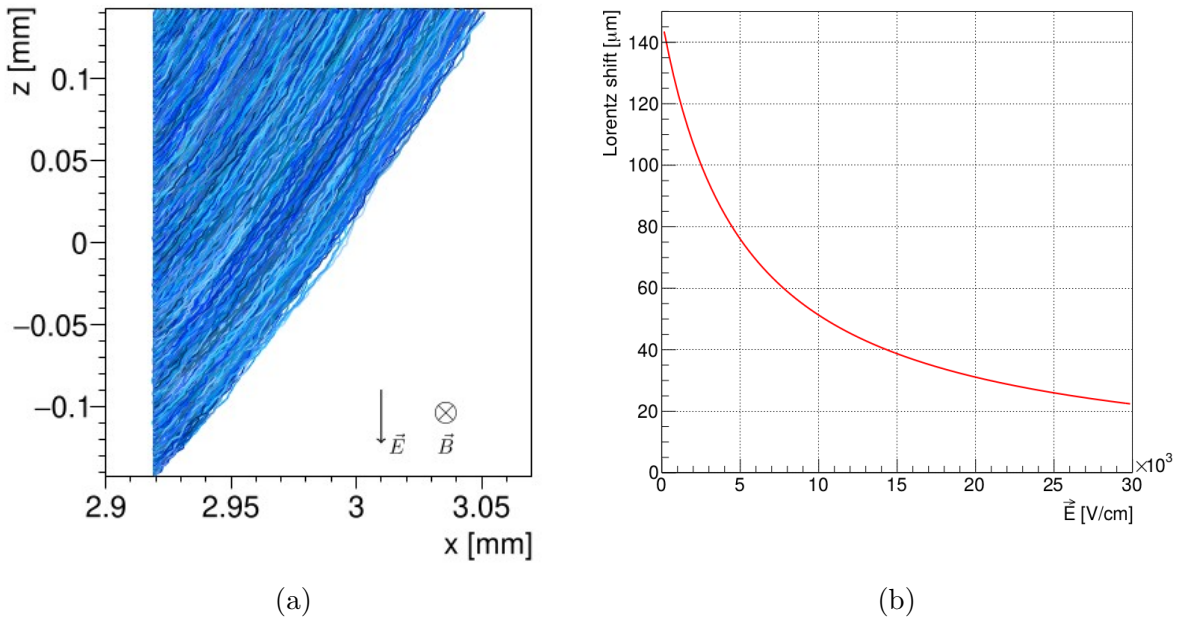
Figure 2.8.: Allpix^2 [36] simulation of the electron drift in silicon in the presence of a magnetic field (a). The electrons are generated along the z-direction, at $x = 2.92\,\mathrm{mm}$. The direction of the electric and magnetic fields are indicated in the figure. Taken from [37].

Lorentz shift for electrons drifting through 150 μm of silicon (b). The directions of the electric and magnetic fields and the shift correspond to those indicated in (a). The magnetic field is assumed to have 3.8 T and the electron mobility is the same as shown in figure 2.7. The hall factor of electrons is assumed to be 1.12.

2. Physics of Silicon Pixel Sensors

The transport of charge carriers in silicon is not solely due to drift, but also due to diffusion. As discussed in [8], the diffusion current for electrons and holes can be described by Fick's first law

$$\vec{j}_{e,\text{diff}} = -D_e \nabla n, \quad \text{and} \tag{2.11}$$
$$\vec{j}_{h,\text{diff}} = D_h \nabla p,$$

where $\vec{j}_{e,\text{diff}}$ and $\vec{j}_{h,\text{diff}}$ is the electron or hole diffusion current per unit area, D_e and D_h are the corresponding diffusion constants and ∇n and ∇p are the gradients of the electron and hole concentrations. Using the Einstein relation, the diffusion constant can be derived from the mobility

$$D = \mu \frac{k_B T}{e}. \tag{2.12}$$

Considering a single charge carrier, it will experience a Brownian motion due to interactions within the solid. The probability to find it at a given point in space after a time t will follow a Gaussian distribution centered around its initial position if there is no drift due to an electric field. The width of this Gaussian distribution (in one dimension) is

$$\sigma_{e,\text{diff}} = \sqrt{2 D_e t} \quad \text{for electrons} \tag{2.13}$$
$$\sigma_{h,\text{diff}} = \sqrt{2 D_h t} \quad \text{for holes.} \tag{2.14}$$

As mentioned above, the signal in the pixel implants is a current induced through the movement of a charge Q inside the silicon sensor. Quantitatively this current can be derived through the Shockley-Ramo theorem [39] [40], thoroughly discussed e.g. in [41]. With the weighting field $\vec{E}_W$ the induced current is

$$j_i = -Q\vec{v} \cdot \vec{E}_W. \tag{2.15}$$

The weighting field describes the geometry of a sensor, considering charge collection at a specific electrode. It is related to the weighting potential ϕ_W as the electric field to the electric potential, namely $\vec{E}_W = -\nabla \phi_W$, and derived by setting the potential of the considered electrode to $1\,\text{V}$ and all others to $0\,\text{V}$. In the presence of charge carrier trapping, see section 2.4, charge carriers generated at $\vec{r}_1$ might be trapped at $\vec{r}_2$. The charge induced by a charge carrier drifting between two positions is calculated as

$$Q_i = Q(\phi_W(\vec{r}_2) - \phi_W(\vec{r}_1)). \tag{2.16}$$

For illustrative purpose, the weighting potentials for two strip sensors with different geometries are shown in figure 2.9. It rises non-linearly towards the considered readout electrode. For the larger implants, the weighting field is smaller in the bulk region of the sensor and rises steeper close to the electrodes. Note that the rise is even steeper for pixels
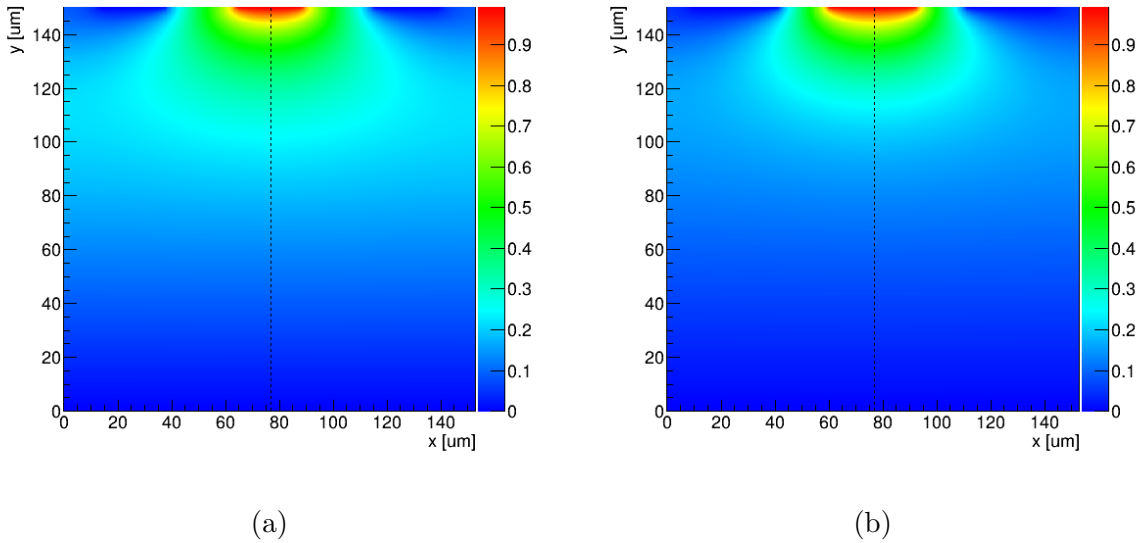
14

(a)   (b)

Figure 2.9.: Weighting potential for two strip sensors with a thickness of 150 μm, a pitch of 50 μm and implant widths of 24 μm (a) and 32 μm (b). The dashed line indicates the center of the read out implant at $y = 150$ μm. Derived using Weightfield2 [38].

sensors, as shown in [42], referred to as *small pixel effect* [12]. The fact that the charge carriers deposited by a single track induce a signal in more than one electrode is referred to as charge sharing. The number of electrodes with charge above a certain threshold is the cluster size. Charge sharing is typically dominated by the Lorentz shift and the track angle, as shown in figure 2.10. In addition effects of diffusion and the weighting field play a role.

The cluster size has a significant impact on the spatial resolution. In the simplest case, meaning the sensor is hit with an uniform distribution of particles and only one pixel fires and only if it is hit within $\pm p/2$ around the center of its implant, the position resolution is [8]

$$\sigma_{bin} = \frac{p}{\sqrt{12}}. \tag{2.17}$$

This is sometimes referred to as binary resolution. The assumption that only one pixel fires is usually violated and a certain fraction of particles generates a cluster size of two, even if the track angles are close to the sensor normal. Assuming these events occur in a region of width s, the resolution for binary readout becomes $(p - s)/\sqrt{12}$ in the region with cluster size one and $s/\sqrt{12}$ in the region with cluster size two [8]. So even for binary readout, the resolution is typically better than equation 2.17 suggests.

If information about the collected charge in each pixel electrode is available, the situation becomes more complicated. For cluster sizes larger than one, the additional information can be used to interpolate between the centers of the firing pixels. Several interpolation algorithms are discussed in literature [43][44]. The interpolation significantly improves the position resolution and yields the best results if the cluster size is
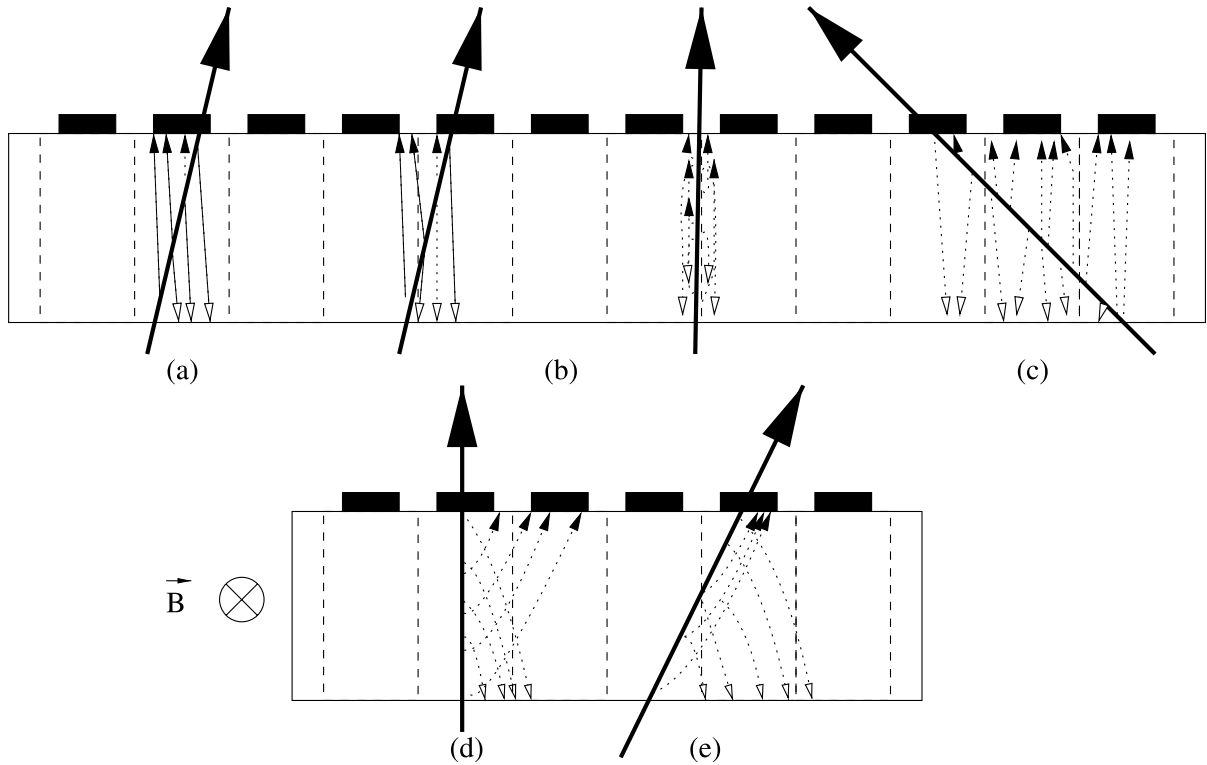
15

Figure 2.10.: Charge sharing in a silicon sensor for various track angles (solid arrows) without (a), (b) and (c), and with Lorentz shift (d) and (e) due to a magnetic field $\vec{B}$. The black boxes indicate n^+ implants collecting electrons (full dotted arrows). Taken from [8].

close to two. This is the case if $s \approx p$, neglecting threshold effects. Thus it is desirable to match the Lorentz shift and the pitch. Similarly, if charge sharing is dominantly due to the track angle, the best resolution is expected for track angles θ fulfilling $\tan(\theta) = p/d$. In this case, the spatial resolution is limited by the noise in each readout channel and energy loss fluctuations as discussed in [45].

2.4. Radiation Damage in Silicon Sensors

During operation, the components of particle detectors are exposed to a high flux of particles. The particles interact with the detector material and can alter its physical properties, which might lead to a degradation of the detector's performance. This degradation is referred to as radiation damage. In silicon devices two types of radiation damage — surface and bulk damage — are distinguished.

The mechanisms for the creation and main properties of surface damage effects are given in [46]. Surface damage is associated with the ionizing energy loss of particles, measured in terms of the total ionizing dose. Inside the bulk of the silicon material, ionizing energy loss leads to the generation of electron-hole pairs, as discussed in section 2.2. These charge carriers have a high mobility in silicon and are collected in the electrodes of a given sensor if they are generated in the depletion region. Otherwise, they simply recombine. In the

silicon-dioxide SiO_2 at the surface of silicon sensors though, holes have a low mobility and those which do not recombine can create radiation induced defects as detailed in [46] and [47]. The generation of defects begins with the slow transport of the holes towards the Si/SiO_2 interface. A fraction of them is trapped in long-lived states, oxygen vacancies concentrated close to the interface and eventually causes a rising density of positive oxide charges. Others create interface traps at the Si/SiO_2 interface by removing hydrogen atoms from hydrogen passivated dangling bonds, in an indirect process involving the formations of protons. The consequences are discussed in [48] and [49]. The oxide charge can lead to the formation of an electron accumulation layer between the pixel implants in p^+n sensors. For charge carriers generated in that region, this leads to longer drift times and makes them vulnerable to trapping effects. In addition, neighboring n^+ implants might be shorted through the electron accumulation layer. Further defects associated with surface damage, their generation and effects are discussed in [48] and [50]. It is to be mentioned that the interface traps contribute to the leakage current if the adjacent bulk region is depleted. Measurements of this surface generation current on gate-controlled diodes are presented in [51].

The second type of radiation damage is called bulk or displacement damage and due to the Non-Ionizing Energy Loss (NIEL) of particles. As discussed in [22] a fraction of the NIEL results in lattice vibrations, which are dissipated in the crystal. If the recoil energy of an interaction is larger than a threshold energy on the order of $20\,\text{eV}$ in silicon [22], a Frankel pair is created. A Frankel pair consists of two point defects, a vacancy and an interstitial, corresponding to one silicon atom displaced from its original position in the crystal lattice, hence the term displacement damage. If the energy transfer is significantly larger, localized clusters of point defects are generated through secondary interactions of the displaced atoms. These clusters are reported to have dimensions in the range of $100\,\text{Å}$ to $200\,\text{Å}$ for energy transfers on the order of $10\,\text{keV}$ [52] and line-like shapes (see figure 2.11).
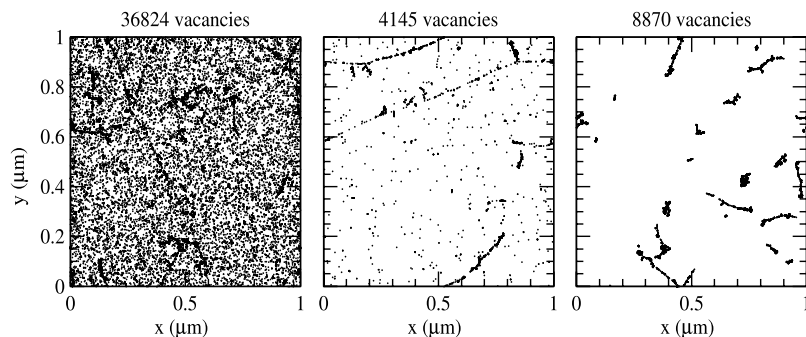
Figure 2.11.: Spatial distributions of vacancies projected over $1\,\mu\text{m}$ in the z-direction. Simulated for $10\,\text{MeV}$ protons, $24\,\text{GeV}$ protons and $1\,\text{MeV}$ neutrons (left to right) with a particle fluence of $10 \times 10^{14}\,\text{cm}^{-2}$ in each case. Taken from [54].

2. Physics of Silicon Pixel Sensors

The displacement damage of high energetic particles in silicon depends on the particle type and energy. It is expressed in terms of the damage function $D(E)$, shown in figure 2.12. The displacement damage of 1 MeV neutrons

$$D_n(1\,\text{MeV}) = 95\,\text{MeV}\,\text{mb} \tag{2.18}$$

is used to normalize damage functions, see figure 2.12, and radiation fields with mixed particle types and energies. To do so, a hardness factor is defined as [53]

$$\kappa = \frac{\int D(E)\phi(E)dE}{D_n(1\,\text{MeV}) \cdot \langle\phi\rangle}, \tag{2.19}$$

where $\langle\phi\rangle = \int \phi(E)dE$ and $\phi(E)$ is the energy spectrum of the corresponding radiation field. Consequently, the 1 MeV neutron equivalent fluence is defined as

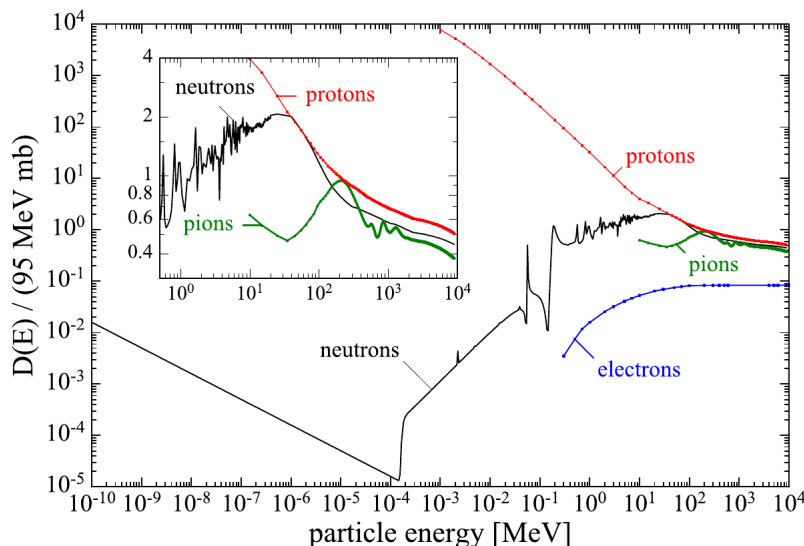$$\phi_{eq} = \kappa\langle\phi\rangle. \tag{2.20}$$

Figure 2.12.: Damage functions $D(E)$ for neutrons, protons, pions and electrons in silicon. Taken from [21].

This normalization neglects the fact, that the displacement damage is not uniformly distributed and particles like neutrons tend to generate clusters of displacements. This is illustrated in figure 2.11, where simulated spatial distributions of vacancies are shown after irradiation with protons of two energies and neutrons. These distributions are directly after the initial creation of the vacancies. The generated vacancies and interstitials are mobile at room temperature and might recombine or form point defects with long lifetimes and clusters thereof. Typical types of defects are combinations like e.g. two vacancies (V_2), a vacancy and an oxygen atom (V-O) or a vacancy and a phosphorus atom (V-P). In [54] simulations of the initial creation of vacancies and interstitials, their migration and combination are described, providing a better overview of the involved physics. It

should be mentioned that the formed defects can break up again, especially at higher temperatures. This leads to partial recovery of the initial material properties known as annealing.

Some of the defects or defect clusters are electrically active and introduce additional energy levels in the bandgap of silicon, similar to the energy levels introduced through doping. These energy levels alter also macroscopic properties of the silicon sensor, depending on their position in the bandgap. Following [21], Shockley-Read-Hall statistics can be used to derive these macroscopic changes if a few properties of the defects are known. These are their concentration, their capture cross sections for electrons and holes, their energy levels and whether they are donor or acceptor like. For their characterization methods like the Thermally Stimulated Current's (TSCs) method [55] or Deep-level Transient Spectroscopy (DLTS) [56] are employed. A summary of the observed macroscopic effects is given in [21]. They are:

- **Increased leakage current:** In irradiated silicons sensors an increase of the reverse current (dark current) is observed after irradiation, due to an increase of charge carrier generation. Energy levels close to the bandgap are most efficient in charge carrier generation. The increase in leakage current will be further discussed below.

- **Removal of donors and acceptors:** Some of the formed defects include the original donor or acceptor atoms. These defects can have electrical properties different from those of the original donor or acceptor so that the corresponding donor or acceptor level is effectively removed. This is known to be a problem in Low Gain Avalanche Diodess (LGADs) [57], as reported in [58].

- **Change of the effective space charge:** In addition to the removal of donors and acceptors, further charged defects are forming after irradiation, leading to a change of the space charge effective doping concentration N_{eff}. Due to the leakage current, the local densities of electrons and holes depend on the position inside the bulk and consequently also trap occupation and space charge depend on position. This can lead to the formation of a double junction and an electric field with two local maxima on the front and backside of a silicon sensor [59]. The change of the effective space charge will be further discussed below.

- **Charge carrier trapping:** Charge carrier trapping refers to the fact that free charge carriers can be captured in defect states so that the lifetime of free charge carriers and in consequence the collected charge are reduced. Measurements of the trapping times after irradiation with protons, neutrons and pions are presented in [60]. Parametrizations of the fluence and temperature dependence and the annealing behavior are given.

In principle properties of radiation-induced defects can be implemented in device simulators like Synopsys TCAD [61] to predict the performance of irradiated devices. In

2. Physics of Silicon Pixel Sensors

practice, not all introduced defects are fully characterized. In addition numerical calculations become exceedingly complex, if the number of considered defects becomes too large. Thus effective models like the Hamburg Penta Trap Model (HPTM) [62] need to be used to predict the performance of irradiated devices.

As discussed above, the number of initially created point defects scales with the NIEL. This motivates the NIEL hypothesis, namely that the number of successively formed (semi) stable defects scales with NIEL. In consequence, one would expect certain macroscopic properties to have a linear dependence on ϕ_{eq}. In practice, this hypothesis is known to be violated. For example, are certain defects created via second-order processes, thus reported to have a quadratic fluence dependence [63]. Furthermore different concentrations of certain defects, like $E(30\,\text{K})$, are found after proton and neutron irradiation [63]. The $E(30\,\text{K})$ is known to contribute a positive space charge at room temperature. In any case, for observables like the leakage current and the effective doping concentrations linear models are found to be suitable for many applications. Since these models are applied in section 4, they are reported below.

A parametrization of the leakage current of a silicon sensor as a function of the neutron equivalent fluence it was exposed to and its annealing history is given in [53] and revised in [21]. Here a summary based on these two references is given. The radiation-induced change in leakage current ΔI, measured above full depletion, is proportional to ϕ_{eq} and the active volume V in the silicon detector

$$\Delta I = \alpha(t, T_a) \cdot \phi_{eq} \cdot V. \tag{2.21}$$

Here t denotes the annealing time and T_a the annealing temperature. The proportionality constant α is called current related damage factor [21]. It is parameterized as

$$\alpha(t, T_a) = \alpha_I \cdot \exp\left(-\frac{t}{\tau_I(T_a)}\right) + \alpha_0(T_a) - \beta \cdot \ln\left(\frac{t}{t_0}\right) \tag{2.22}$$

and describes the annealing at a temperature dependent rate. The values of the introduced constants are

$$\alpha_I = (1.23 \pm 0.06) \cdot 10^{-17}\,\text{A cm}^{-1}, \tag{2.23}$$

$$\beta = (3.07 \pm 0.18) \cdot 10^{-18}\,\text{A cm}^{-1}\ \text{and} \tag{2.24}$$

$$t_0 = 60\,\text{s}. \tag{2.25}$$

The value of α_0 depends on the annealing temperature

$$\alpha_0 = -(8.9 \pm 1.3) \cdot 10^{-17}\,\text{A cm}^{-1} + (4.6 \pm 0.4) \cdot \frac{1}{T_a} \cdot 10^{-14}\,\text{K A cm}^{-1}. \tag{2.26}$$

So does the decay time τ_I in the exponential term. It follows an Arrhenius relation

$$\frac{1}{\tau_I} = k_{0I} \cdot \exp\left(-\frac{E_I}{k_B T_a}\right), \tag{2.27}$$

with

$$k_{0I} = 1.2^{+5.3}_{-1.0} \cdot 10^{13}\,\mathrm{s}^{-1}, \tag{2.28}$$

$$E_I = (1.11 \pm 0.05)\,\mathrm{eV}. \tag{2.29}$$

This is understood to be an empirical parametrization. It was inferred from measurements taken at a temperature $T = 20\,\mathrm{°C}$ and the annealing temperatures T_a cover a range from $21\,\mathrm{°C}$ to $106\,\mathrm{°C}$. The annealing times were down to a time scale of $60\,\mathrm{s}$. In [21], this model is shown to hold for different base materials and fluences up to $\phi_{eq} = 1 \times 10^{15}\,\mathrm{cm}^{-2}$. One should note that for such high fluences the current does not saturate after full depletion and the definition of a full depletion voltage becomes increasingly vague. Results from capacitance-voltage measurements become frequency dependent and measurements of the charge collection efficiency do not saturate due to trapping effects, as discussed in [64].

Another important aspect concerning the leakage current is its temperature dependence. The parametrization above describes a leakage current I_{20} at a temperature of $20\,\mathrm{°C}$. Since irradiated silicon sensors are typically operated at temperatures well below $0\,\mathrm{°C}$ to limit the leakage current, a conversion is needed to account for this temperature difference. Based on the findings in [65] the current measured at a temperature T_m is derived as

$$I(T_m) = I_{20} \left(\frac{T_m}{293.16\,\mathrm{K}}\right)^2 \exp\left(\frac{-E_{eff}}{2k_B}\left(\frac{1}{T_m} - \frac{1}{293.16\,\mathrm{K}}\right)\right), \tag{2.30}$$

using an effective band gap $E_{eff} = 1.21\,\mathrm{eV}$.

Similar to the leakage current in silicon sensors, radiation-induced changes to the effective doping concentration N_{eff} are described in a parametrization widely known as the Hamburg model [53], again reviewed in [21]. Also this model is of importance for the studies presented in chapter 4 and summarized here. The radiation-induced change reads

$$\Delta N_{eff}(\phi_{eq}, t, T_a) = N_C(\phi_{eq}) + N_A(\phi_{eq}, t, T_a) + N_Y(\phi_{eq}, t, T_a) \tag{2.31}$$

and its three terms are referred to as stable (N_C), beneficial annealing (N_A) and reverse annealing (N_Y) components [21]. The stable term

$$N_C(\phi_{eq}) = N_{C0}(1 - \exp(-c\phi_{eq})) + g_c\phi_{eq} \tag{2.32}$$

shows no time and temperature dependence. It consists of two contributions. One describes the incomplete donor removal with a fluence coefficient c up to the final value N_{C0}. The other describes the introduction of stable acceptors at an introduction rate g_c. In a

similar way, the introduction rate g_a and g_y are introduced in the other two terms

$$N_A(\phi_{eq}, t, T_a) = g_a \phi_{eq} \exp\left(-\frac{t}{\tau_a(T_a)}\right) \text{ and} \tag{2.33}$$

$$N_Y(\phi_{eq}, t, T_a) = g_y \phi_{eq} \left(1 - \exp\left(-\frac{t}{\tau_y(T_a)}\right)\right). \tag{2.34}$$

In both cases, the time constants τ are temperature dependent and follow an Arrhenius relation of the form

$$\frac{1}{\tau} = k_0 \exp\left(-\frac{E_A}{k_B T_a}\right), \tag{2.35}$$

with an activation energy E_A and a frequency factor k_0.

As pointed out in [21] the parameters describing a given silicon sensor depend on the impurity content in the base material as well as the particle type causing the radiation damage. For the reverse annealing component N_Y different parametrizations are used by different authors. It should be noted that the space charge becomes a function of position inside the silicon sensor as deep trap occupations become relevant once ϕ_{eq} reaches orders of $1 \times 10^{14} \text{ cm}^{-2}$[59]. In this case, also equation 2.2 looses validity.

3. The CMS Experiment

The CMS experiment is one of the four experiments situated at the LHC, a particle accelerator and collider at CERN [66][67]. Most of the LHC's operation time is dedicated to proton-proton collisions, while collisions of lead ions complement the program. The other three experiments are ALICE, LHCb and ATLAS. ALICE is dedicated to lead-ion collisions andLHCb to physics related to b-mesons. ATLAS and CMS are general-purpose detectors with a broad physics program.

In the LHC, particles are accelerated in bunches. The nominal time between bunch crossings is 25 ns. So far, center of mass energies of 13 TeV were reached in Run 2 (2015 to 2018), 14 TeV are foreseen in the future. The LHC is designed for an instantaneous luminosity of $1 \times 10^{34} \, \mathrm{cm}^{-2} \, \mathrm{s}^{-1}$. In Run 2 peak luminosities of about $2 \times 10^{34} \, \mathrm{cm}^{-2} \, \mathrm{s}^{-1}$ were reached, amounting to delivered integrated luminosities of about $160 \, \mathrm{fb}^{-1}$ at 13 TeV in both ATLAS and CMS[68][69]. In both cases, the mean number of proton-proton interactions per bunch crossing, pileup, is found to be about 37.

In the mid-2020s, a major luminosity upgrade of the LHC, the High-Luminosity LHC (HL-LHC), is planned [70]. In the ultimate scenario, the instantaneous luminosity will be leveled at 7–$7.5 \times 10^{34} \, \mathrm{cm}^{-2} \, \mathrm{s}^{-1}$ to constrain pileup to an average of 200 [70] [71]. In this case, up to $4000 \, \mathrm{fb}^{-1}$ are expected to be collected in about 10 years of operation. The HL-LHC challenges the four experiments to conduct major upgrades of their instrumentation. The focus of this work is on the upgrade of the CMS tracking system, the Phase-2 Upgrade, discussed later in this section.

The CMS detector is situated in an underground cavern at LHC Point 5, one of the interaction points designed to deliver high luminosities. A broad overview of its physics program is given in [72], and in numerous publications from the CMS Collaboration issued since then. The CMS detector is dedicated to search for physics beyond the standard model, to precisely measure properties of standard model particles, since even top quarks are produced at high rates, and to find the postulated Higgs boson, which indeed was found in 2012 [73].

A brief summary of the detector concept is given here, based on information from [74] and [75], if not stated otherwise. The CMS detector has a cylindrical geometry, centered around the interaction point, thus cylindrical coordinates are well suited for its description. The origin of the coordinate system is at the interaction point. The z-axis points approximately west following the beam direction. The radial coordinate is r. The azimuthal angle ϕ is measured between the x-axis, pointing towards the center of the LHC

ring, and the upwards pointing y-axis. The polar angle θ is expressed in terms of the pseudorapidity $\eta = -\ln(\tan(\theta/2))$ and measured with respect to the z-axis. For particles with $|\vec{p}| \gg m$ the pseudorapidity converges towards the rapidity, for which differences are invariant under Lorentz transformations along the z-axis. It is a useful quantity since the interacting proton constituents carry variable fractions of the proton momentum so that their center of mass system is boosted in the beam direction.
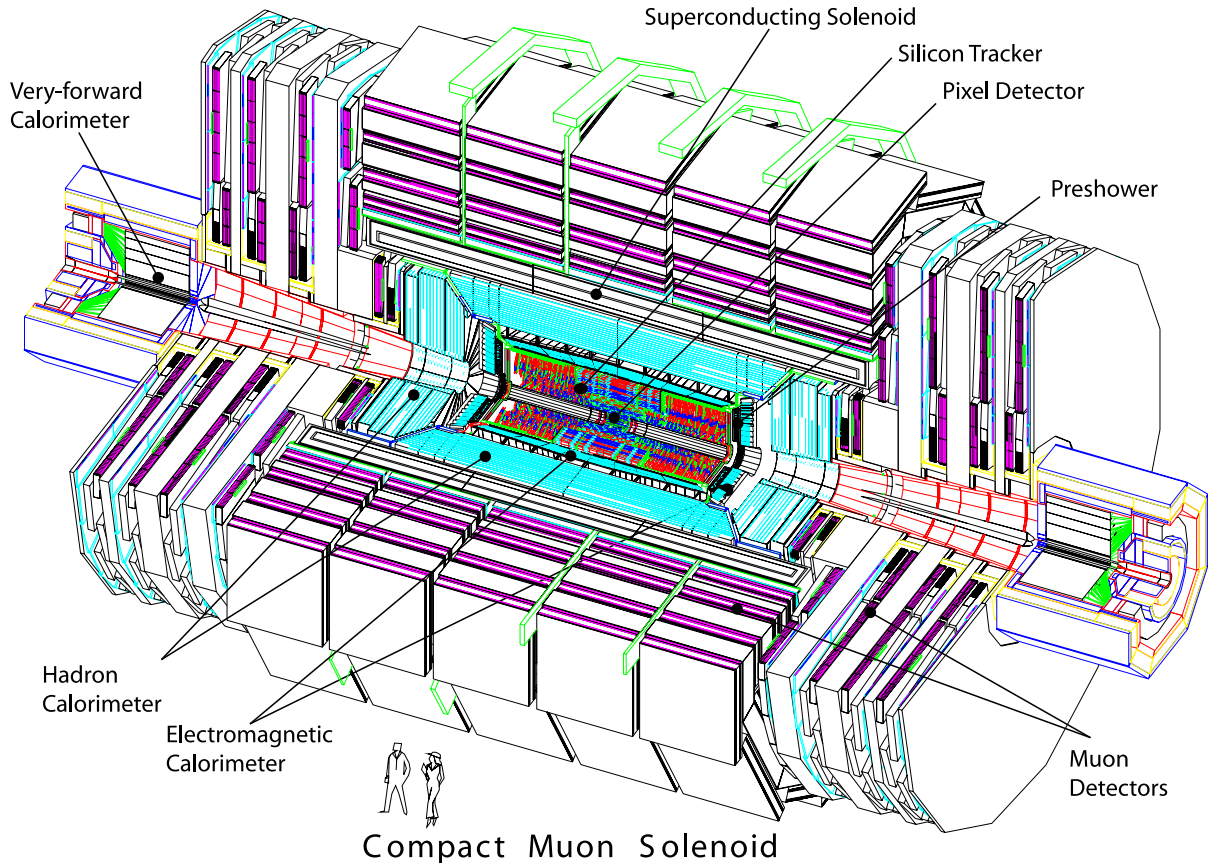
Figure 3.1.: The CMS detector, taken from [74].

The detector consists of several sub-systems, as indicated in figure 3.1. A brief description and discussion of their functionality is given here:

- **The superconducting solenoid:** The central element of the CMS detector is a superconducting solenoid with a length of $12.5\,\mathrm{m}$ and an inner radius of $3\,\mathrm{m}$. It is designed to provide a magnetic field of up to $4\,\mathrm{T}$ in its core. It is embedded in a layered steel yoke to confine the magnetic field and has a thickness of $3.9\,X_0$ (see section 2.2). It contains the inner tracker, the electromagnetic and the hadronic calorimeter. Its purpose is to bend the trajectories of charged particles, which allows to determine their momentum and the sign of their charge. For a uniform magnetic field $\vec{B}$ the relation between the particle momentum $p_\perp$ and the radius R in the transversal plane is [12]

$$R = \frac{p_\perp}{q|\vec{B}|}. \tag{3.1}$$

- **The inner tracker:** The essential purpose of the inner tracking system is to determine the trajectories of charge particles, to estimate their curvature and to find primary and secondary vertices (see section 2 for a broader discussion). It consists of a pixel detector with 3 barrel layers of cylindrical geometry and two disc layers at each end of the cylinder, surrounded by a strip detector with 10 barrel and 12 disc layers. For $\eta \approx 0$, a radiation length of about $0.4\,X_0$, a relative $p_\perp$ resolution of about $7\,\%$ and a transverse impact parameter resolution of about $20\,\mu\mathrm{m}$ (both for muons with a $p_\perp$ of $10\,\mathrm{GeV/c}$) are reported [74].

- **The electromagnetic calorimeter:** Similar to the inner tracker, the electromagnetic calorimeter consists of a barrel part of cylindrical and endcaps of disk-like geometry. It is dedicated to measure the energy of electrons and photons. The detector modules are lead tungstate scintillating crystals read out with photo detectors. In the barrel region, these are avalanche photodiodes [76]. In the endcaps vacuum phototriodes are used to account for the higher expected fluence ϕ_{eq} [77]. The total radiation length of the electromagnetic calorimeter is reported to be larger than $25\,X_0$. In test beams a relative energy resolution of

$$\left(\frac{\sigma_E}{E}\right)^2 = \left(\frac{2.8\,\%}{\sqrt{E}}\right)^2 + \left(\frac{12\,\%}{E}\right)^2 + (0.3\,\%)^2 , \qquad (3.2)$$

with energies in units of GeV, was found for barrel modules and electrons in the momentum range $20\,\mathrm{GeV/c}$ to $250\,\mathrm{GeV/c}$.

- **The hadronic calorimeter:** The hadronic calorimeter is dedicated to measure the energy of hadrons and especially jets. Jets are accumulations of hadronic particles, collimated due to the Lorentz boosts of the primary quarks or hadronically decaying τ-leptons. It is a sampling calorimeter with brass absorbers and plastic scintillators, again separated in a barrel and endcap region. In the barrel region, it is completed by a tail catcher outside of the solenoid. In the forward region, the geometrical coverage is extended through the hadron forward calorimeter, employing steel absorbers and quartz fibers, in which Cerenkov radiation is emitted by charged particles. The thickness of a hadronic calorimeter is measured in terms of the nuclear interaction length λ_l, which is typically an order of magnitude larger than the radiation length (see [23]). Including the tail catcher, it is reported to range $10\,\lambda_l$ to $15\,\lambda_l$. The relative energy resolution for pions was measured in a test beam setup with a barrel-like calorimeter configuration. It is found to be [78]

$$\left(\frac{\sigma_E}{E}\right)^2 = \left(\frac{115.3\,\%}{E}\right)^2 + (5.5\,\%)^2 , \qquad (3.3)$$
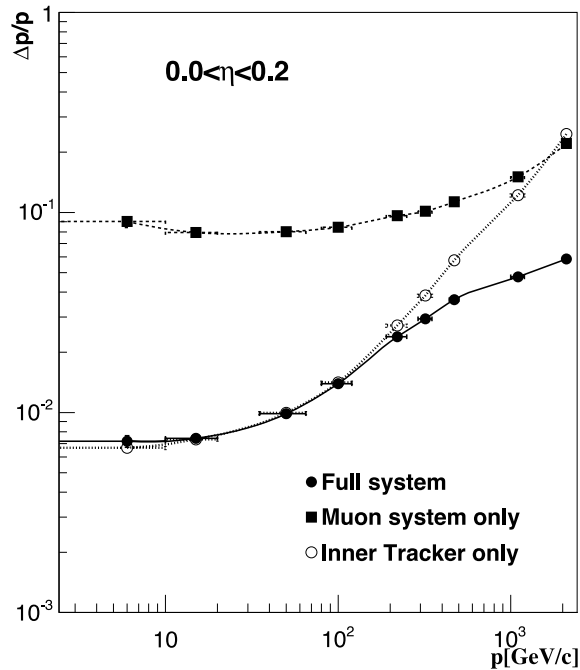
with energies again in units of GeV.

Figure 3.2.: Relative momentum resolution for muons as a function of their momentum. The muons are reconstructed using the muon system, the silicon tracker or both. Especially for large momenta, the combination improves the resolution significantly. Taken from [75].

- **The muon system:** The muon system is the outermost detector system and consists of several layers, which are embedded in the steel return yoke. Since charged particles other than muons are predominantly absorbed within the calorimeters (e.g. electrons and pions) or decayed (τ-leptons or b-mesons), the identification of muons in the muon system is comparably easy. Thus all-muon final states are excellent candidates for physics searches. The muon system employs different types of gaseous detectors, drift tubes in the barrel region and cathode strip chambers in the endcaps. In both cases, the system is completed by resistive plate chambers providing a dedicated trigger signal. The relative momentum resolution for muons is shown in figure 3.2.

- **The trigger system:** The sheer number of bunch crossings and signals from the readout channels in all sub-detectors amounts in a tremendous data rate. The trigger system is designed to select events (bunch crossings) such that the initial event rate of 40 MHz is reduced by a factor of 10×10^6 or more. The reduction is reached in two steps, the Level-1 and the High-Level Trigger. The Level-1 trigger is a hardware system and uses information from sub-detectors such as the calorimeters and the muon system. The high level trigger makes decision based on a fast event reconstruction and selection criteria applied on the reconstructed objects. The trigger selection contains different categories, like criteria dedicated to certain processes e.g. a Higgs boson decaying into two photons or four leptons, but also minimum bias

events are selected to study e.g. hadronic interactions [79].

Further sub-systems like the data acquisition system, powering and cooling infrastructure are discussed in [74] and [75] and references therein, including additional information on the presented systems. It should be noted that the given description is for the detector as it operated in Run 1 (2009 – 2013). Since then parts of the detector were or are foreseen to be upgraded. The Phase-1 [80] and Phase-2 upgrade [17] of the pixel detector will be discussed in section 3.1 and 3.2.
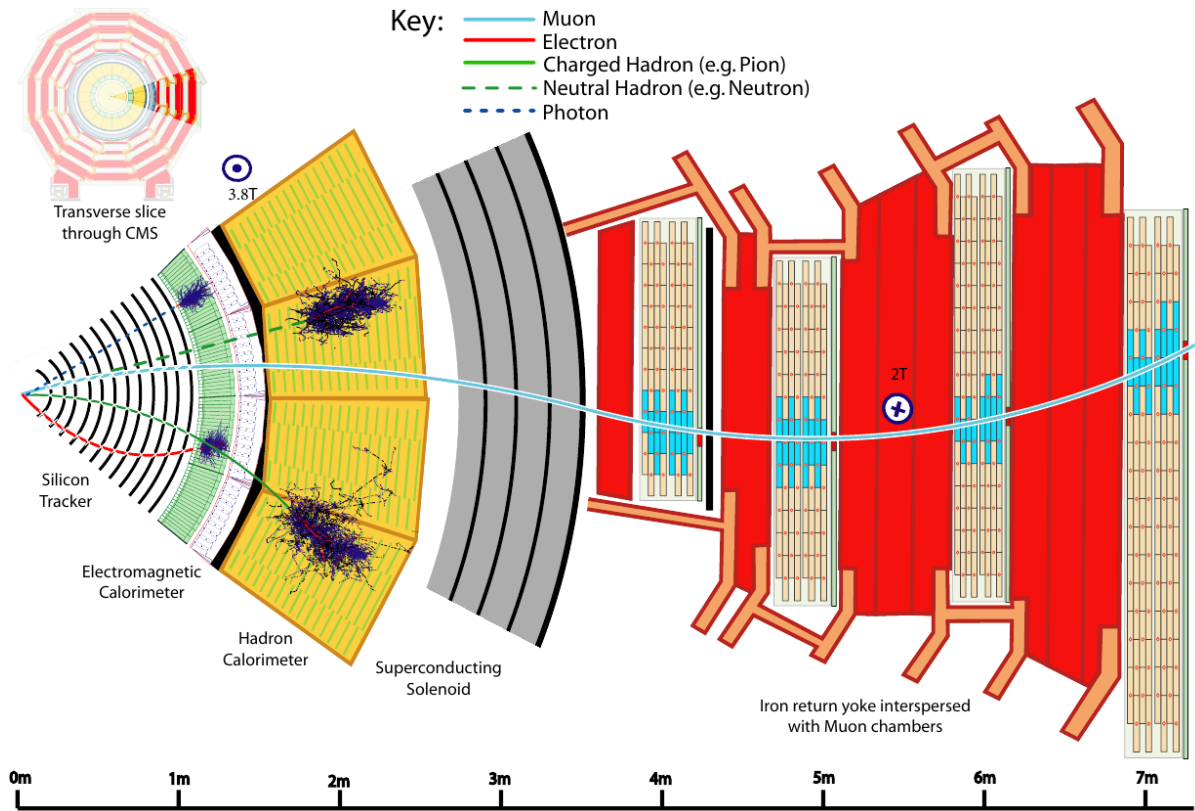
Figure 3.3.: Reconstruction scheme for different particle types in the CMS detector. Charged particles are identified as curved tracks in the silicon tracker and the muon system. Electrons and photons are stopped and deposit energy in the electromagnetic calorimeter, while hadrons interact predominantly in the hadronic calorimeter. Muons are typically reconstructed as long tracks in both the silicon tracker and the muon chambers. Taken from [13].

The total reconstruction of events in the CMS detector results in so called physics objects such as different particle candidates, as shown in figure 3.3, but include also hadronic jets. The reconstruction of physics objects correlates the information from different sub-detectors in a particle-flow approach [13]. The power of such an approach is impressively demonstrated in figure 3.2.

3.1. The CMS Pixel Detector for Phase-1

The CMS collaboration installed an upgraded pixel detector, the CMS Phase-1 pixel detector, between December 2016 and April 2017. This was part of a major upgrade, the Phase-1 upgrade, including also improvements of the muon system, the hadronic calorimeter, the trigger and the data acquisition system. Detailed descriptions of the new detector and studies on its performance are given in [81] and [80], providing the information quoted in this section, if not stated otherwise. The main reason for the upgrade is to render the detector capable of efficient tracking up to instantaneous luminosities of $2 \times 10^{34}\,\mathrm{cm^{-2}\,s^{-1}}$, a factor two above the design luminosity of the LHC. In the initial pixel detector, dynamic inefficiencies occur for high track densities and trigger rates as a result of high instantaneous luminosities, resulting for example in a drastic reduction of the tracking efficiency in $t\bar{t}$ events.
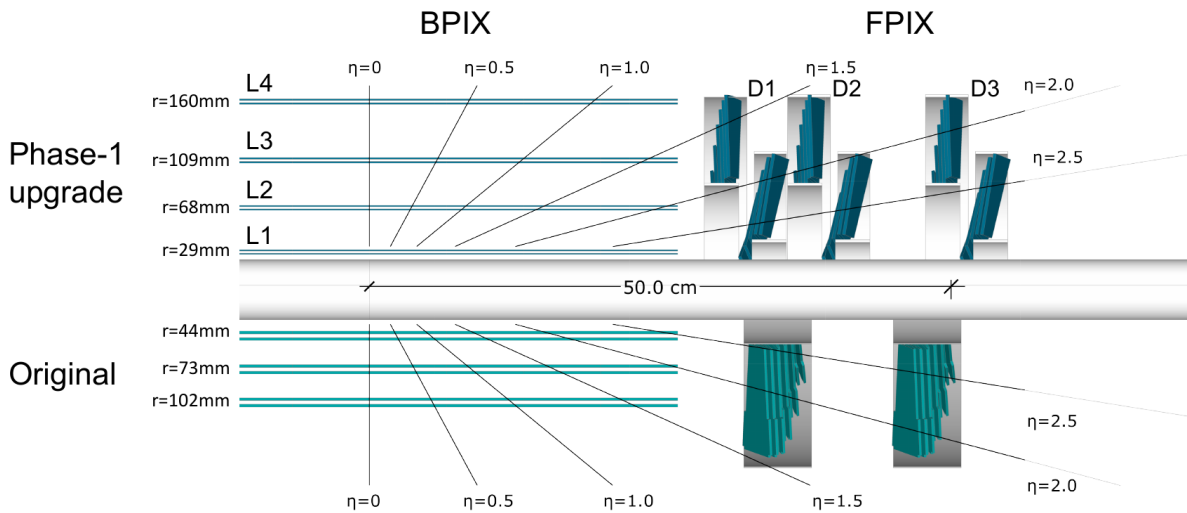

Figure 3.4.: Schematic layout of the original and Phase-1 pixel detector compared. Taken from [81].

In figure 3.4 the layout of the original and the Phase-1 pixel detector are compared. The main features are a new beam pipe with a smaller radius, additional layers and coverage for larger η in the Forward Pixel Detector (FPIX) and an additional layer in the Barrel Pixel Detector (BPIX). Measurements of the leakage current and the full depletion voltage of silicon sensors in BPIX are presented in chapter 4 and compared to model predictions, thus this section focuses on its properties. The mean radial positions of the modules in the BPIX layers are 28.98 mm, 67.57 mm, 108.725 mm and 159.805 mm for layer 1 to 4, respectively. Thereby a reduction of the radius for the innermost layer and an increase of the radius for the outermost layer is achieved.

In total, the pixel detector consists of 1856 modules, each consisting of a pixel sensor with 160×416 pixels and 16 readout chips. The readout chips needed to be upgraded in order to reduce the dynamic inefficiencies. The revised readout chips are the PSI46dig [82] and the PROC600 [83]. The former is designed for expected hit

rates f_h of up to $120\,\mathrm{MHz\,cm^{-2}}$, the latter is designed for the innermost BPIX layer, where rates of up to $600\,\mathrm{MHz\,cm^{-2}}$ are expected. Both readout chips have a power consumption of $41\,\mathrm{mW}$ in the analog part. For the digital part a power consumption of $70\,\mathrm{mW} + f_h \cdot 0.31\,\mathrm{mW\,cm^2\,MHz^{-1}}$ and $90\,\mathrm{mW} + f_h \cdot 0.20\,\mathrm{mW\,cm^2\,MHz^{-1}}$ is quoted. Thus the heat load in the innermost barrel layer is significantly larger compared to the other layers.
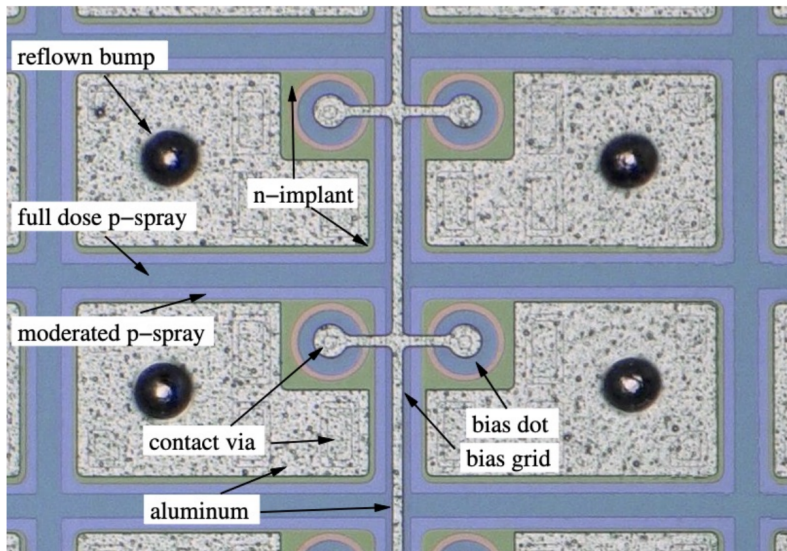
Figure 3.5.: Microscopic image showing 2×2 pixels of a sensor as it is used in the barrel region of the Phase-1 pixel detector. Taken from [81].

The pixel sensors in BPIX have an active area of $16.2 \times 64.8\,\mathrm{mm^2}$ and a thickness of $0.285\,\mathrm{mm}$ corresponding to an active volume of $0.299\,\mathrm{cm^3}$. The sensors are manufactured by CiS Forschungsinstitut für Mikrosensorik and SINTEF Microsystems and Sensors, receptively used for BPIX and FPIX. The CiS sensor design is shown in figure 3.5. The pixels have dimensions of $100 \times 150\,\mathrm{\mu m^2}$ and feature n+ implants in n-type bulk material. The inter-pixel isolation is ensured by a moderated p-spray technology and a combination of a bias grid and punch through bias dots allows to ground the pixel implants for pre-assembly tests. The full depletion voltage of non-irradiated CiS sensors is reported to be $55\,\mathrm{V}$.

To limit the leakage current in the pixel sensors — especially after irradiation — the pixel detector needs to be cooled. The cooling system employs an evaporative CO_2 cooling technology, capable of removing $15\,\mathrm{kW}$ of power in the entire pixel system [85]. The thermal load of BPIX is quoted to be on the order of $6\,\mathrm{kW}$. The coolant is fed into stainless steel tubes in contact with the carbon fiber support structure on which the modules are mounted, as shown in figure 3.6. The minimal temperature of the coolant is $-23\,^\circ\mathrm{C}$, but due to the thermal resistance between the cooling liquid and the silicon sensor the temperatures of the silicon sensors are much larger than that, as detailed in chapter 4.
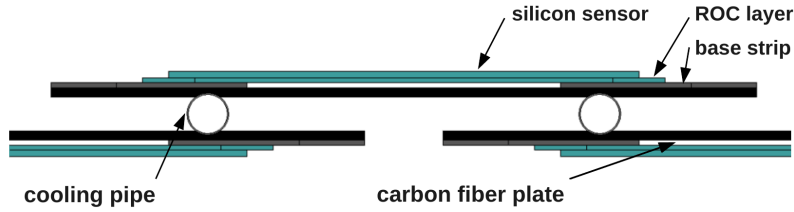
Figure 3.6.: Simplified cross section of a detector module as it is used in BPIX layer 2, 3 and 4. The cooling loops and the carbon fiber support structure are included. Taken from [84].

3.2. The Phase-2 Upgrade of the Pixel Detector

The Phase-2 upgrade of the CMS detector will render it capable to maintain its excellent performance after the upgrade of the LHC to the HL-LHC introduced above. The main challenges are twofold: The upgraded detector has to be capable to deal with the higher instantaneous luminosities, i.e. the higher pileup and consequently larger track densities. In addition, the collected integrated luminosity leads to significant radiation damage affecting components throughout the detector. A general discussion of the upgrade is given in [86] and details on the upgrade of the tracking detector are given in [17], both serving as basis for this section. The upgraded detector will employ new electromagnetic and hadronic calorimeters in the endcap region. The muon endcaps will be complemented by additional detectors capable of higher rates. Also the systems for radiation protection, luminosity measurements, triggering and data acquisition will be upgraded. Finally a replacement of the tracking system, including major upgrades, is foreseen.
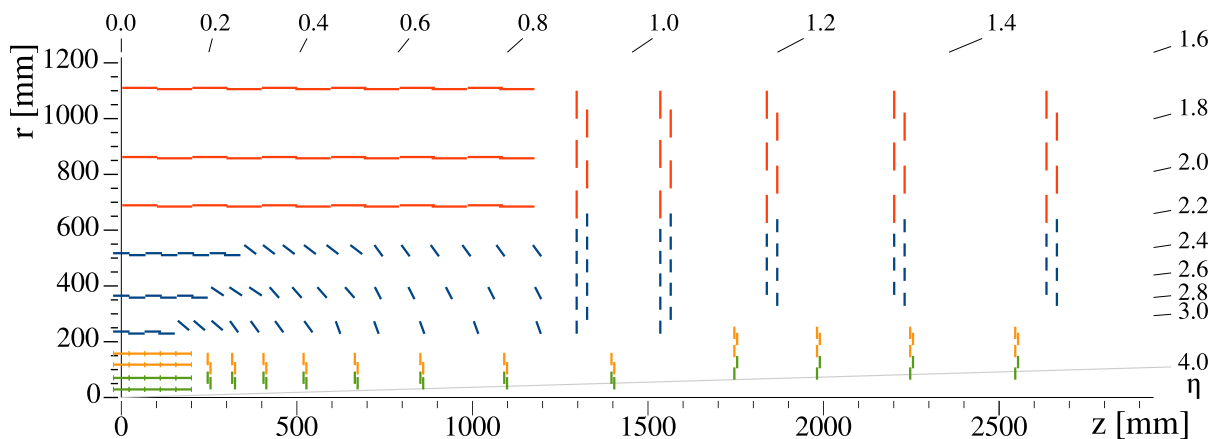

Figure 3.7.: Cross section through a quarter of the tracking system for the Phase-2 upgrade of the CMS detector. Pixel modules with two and four readout chips are represented by green and yellow lines, respectively. Modules of a strip and a macro-pixel sensor are drawn in blue, those with two strip sensors in red. Taken from [86].

The tracking system is separated into an inner and an outer tracker, schematically shown in figure 3.7. In the outer tracker modules of either two strip sensors or a macro-pixel and a strip sensor are used. The pitches of the strips and pixels are 90 µm or 100 µm

in ϕ-direction and the macro pixels have a length of approximately $1.5\,\text{mm}$ in either z-direction or r-direction to cope with high track multiplicities. The strips have lengths of about $24\,\text{mm}$ or $50\,\text{mm}$. A key feature of the new outer tracker is its capability to provide information to the trigger system in terms of stubs. Those are pairs of hits in the two layers of the outer tracker modules originating from tracks with a transverse momentum above approximately $2\,\text{GeV}$, reconstructed directly on the modules. In addition, the material budged of the outer tracker will be reduced and the sensors will be optimized to withstand fluences up to $\phi_{eq} = 1.4 \times 10^{15}\,\text{cm}^{-2}$ (updated with respect to [17]).

Since the sensors investigated within this work are foreseen for the inner tracker, it will be discussed in more detail. The inner tracker will be built from modules of either two or four readout chips bump bonded to one silicon sensor. The readout chip will be based on the prototype chip RD53A [87], using the $65\,\text{nm}$ CMOS technology and developed in collaboration with ATLAS. It features pixel cells of $2500\,\mu\text{m}^2$, radiation tolerance up to an ionizing dose of $5\,\text{MGy}$, a minimal in-time threshold of $1200\,\text{e}$, on-chip data sparsification and digitization of the time-over-threshold with $4\,\text{bit}$ resolution. The dimensions of the final readout chip, the CROC, correspond to an active area of $16.4 \times 22.0\,\text{mm}^2$.

The pixel detector provides coverage for $|\eta| < 4$ with measurements in three or more layers. The sensor modules will be mounted on a carbon fiber support structure, similar to the one described for the Phase-1 pixel detector. They will be powered in a serial approach, amounting to approximately $50\,\text{kW}$ of power in the entire pixel detector. To keep the modules at the foreseen operating temperature of $-20\,^{\circ}\text{C}$, an evaporative CO_2 cooling system will be employed, aiming for temperatures of about $-35\,^{\circ}\text{C}$ in the cooling pipes in contact with the carbon fiber support structure.

A general requirement to the upgraded detector is to at least maintain the track and vertex finding performance from Phase-1 for the harsher conditions in Phase-2. Figure 3.8 shows two examples comparing the performance of the Phase-1 and Phase-2 tracker in simulation. For high track densities, a significant improvement of the tracking efficiency is expected. The same holds for the impact parameter resolution for all track pseudorapidities.

One of the major parts of this work is to characterize the performance of planar pixel sensor prototypes for the Phase-2 pixel detector. These must fulfill a set of criteria in order to achieve the desired performance of the detector or to meet technical constraints, as discussed in [17] and [88]. The pixel density achieved in the readout chip constrains the area of the pixels to $2500\,\mu\text{m}^2$, leading to the choice of $25 \times 100\,\mu\text{m}^2$ and $50 \times 50\,\mu\text{m}^2$ sized pixels as options for the final sensor. The sensors are n^+p type, with n^+ pixel implants and p-type bulk material. These can be manufactured in a single-sided lithographic process, thus are potentially cheaper when compared to n^+n sensors. The reverse bias voltage is applied to the backside of the sensor, which is electrically connected to the edge region of the front side since the cut edge of the sensor is conductive. This creates the risk of sparkover between the sensor and the readout chip, so that a treatment for spark
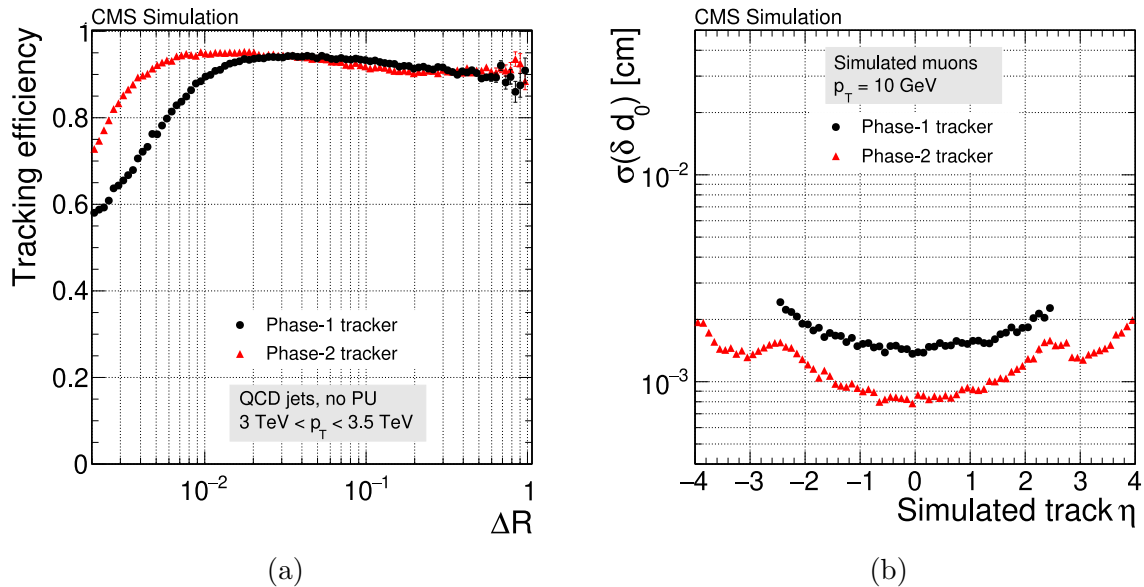
(a)   (b)

Figure 3.8.: Simulated tracking efficiencies as a function of the distance to the closest neighboring track $\Delta R = \sqrt{\Delta\eta^2 + \Delta\phi^2}$ for QCD jets in a $p_\perp$ range of $3\,\mathrm{TeV}$ to $3.5\,\mathrm{TeV}$ (a). The simulation did not include pileup events. In (b) the transverse impact parameter resolution from simulations is shown as a function of the track pseudorapidity η. These results are for isolated muons with a $p_\perp$ of $10\,\mathrm{GeV}$. Taken from [17].

protection is required. The active thickness is chosen to be $150\,\mu\mathrm{m}$, approximately half the thickness of the current pixel sensors. This is due to the fact, that larger electric fields at the same bias voltage potentially mitigate trapping effects in highly irradiated sensors, as shown for strip sensors in [17] and [89]. Further requirements are presented in table 3.1. The quoted fluence of $\phi_{eq} = 5 \times 10^{15}\,\mathrm{cm}^{-2}$ correspond to the fluences expected in barrel layer 2 after an integrated luminosity of $3000\,\mathrm{fb}^{-1}$, as presented in table 3.2. For the innermost layer, a replacement after half the operation time is foreseen, so the expected fluence is about $\phi_{eq} = 10 \times 10^{15}\,\mathrm{cm}^{-2}$. By now new values are discussed within the CMS Tracker group for the ultimate HL-LHC operation scenario, i.e. for an integrated luminosity of $4000\,\mathrm{fb}^{-1}$. In this case, the fluence ϕ_{eq} in the innermost layer is expected to reach $19 \times 10^{15}\,\mathrm{cm}^{-2}$, again including a replacement.

Next to planar pixel sensors, 3D sensors are another option considered for the innermost layer and ring of the upgraded detector. In 3D sensors the n^+ and p^+ electrodes are realized as columns perpendicular to the surface of the sensor, so that thickness (deposited charge) and drift path are decoupled [91]. This reduces their sensitivity to trapping effects and allows for much lower bias voltages, consequently also lower leakage currents, and renders them a promising choice in a high irradiation environment [92]. Since their fabrication is more complex, larger costs and lower production yields are expected for this sensor type.

Table 3.1.: Major requirements for planar pixel sensors for the Phase-2 Upgrade of the CMS detector [88]. The hit efficiency is defined in section 6.3.3.

Parameter	Requirement	State
polarity	n^+p	
active thickness	$150\,\mu m$	
pixel size	$25 \times 100\,\mu m^2$	
	$50 \times 50\,\mu m^2$	
breakdown voltage	$300\,V$	before irradiation
	$800\,V$	after $\phi_{eq} = 5 \times 10^{15}\,cm^{-2}$
leakage current		
at $V_{depl} + 50\,V$	$0.75\,\mu A\,cm^{-2}$	before irradiation
at $600\,V$	$45\,\mu A\,cm^{-2}$	after $\phi_{eq} = 5 \times 10^{15}\,cm^{-2}$
hit efficiency		
at $V_{depl} + 50\,V$	$> 99\,\%$	before irradiation
at $800\,V$	$> 99\,\%$	after $\phi_{eq} = 5 \times 10^{15}\,cm^{-2}$
at $800\,V$	$> 98\,\%$	after $\phi_{eq} = 10 \times 10^{15}\,cm^{-2}$

Table 3.2.: Radial positions of the barrel layers of the Phase-2 pixel detector. The quoted fluences ϕ_{eq} and ionizing doses are from FLUKA simulations [90] presented in [17] and correspond to an integrated luminosity of $3000\,fb^{-1}$ under HL-LHC operation conditions.

Layer	Radius [mm]	Φ_{eq} [$10^{16}\,cm^{-2}$]	Ionizing dose [MGy]
1	28	2.3	12
2	69	0.5	3
4	156	0.15	1

3.3. Planar Pixel Sensor Prototypes for the Phase-2 Upgrade

Strong requirements on the properties of pixel sensors for the Phase-2 Upgrade of the CMS detector call for an extensive R&D campaign. The test-beam measurements presented in this work are part of said campaign, covering prototypes manufactured by Hamamatsu Photonics K.K. (HPK) [93]. The information is this section is from [88], [94] and [95]. A comprehensive summary will be given in [96].

The investigated prototype sensors are bump bonded to the ROC4SENS readout chip (ROC4SENS) introduced in chapter 5. They are produced as part of a bigger submission containing also sensors for further readout chips like the RD53A and test structures, such as planar diodes of different sizes. Different sensor designs are included, featuring, among other variations, different pixel geometries:

3. The CMS Experiment

- **50×50 μm²:** This pixel size is the natural choice given the bump bond pattern dictated by the CROC. For large track angles the charge collection per pixel is determined by the pitch rather than the active thickness of a sensor. Since track angles above 80° will be present in the barrel region, the tracking efficiency for this condition is critical and needs to be studied with great care.

- **25×100 μm²:** Metal routing will be required to match the pitch of the sensor to the pitch of the readout chip. This results in crosstalk between neighboring pixels. The long side of the pixels will follow the z-direction in the barrel region and the radial direction in the endcaps. This way the finer pitch allows for a better hit resolution in traversal direction. The bias voltage needs to be higher to optimize the Lorentz shift as discussed in section 2.3.

The nominal active thickness of the investigated prototypes was specified to be 150 μm. The base material (substrate) is p-type float zone silicon in $\langle 100 \rangle$ orientation, with a resistivity ranging from $3\,k\Omega\,cm$ to $5\,k\Omega\,cm$ and an oxygen concentration between $1 \times 10^{16}\,cm^{-3}$ and $6.5 \times 10^{17}\,cm^{-3}$. Within these specifications three substrate options are investigated:

- **FTH:** The wafers are mechanically thinned from the backside after the front side is processed. The p^+ implantation at the backside is performed after thinning. The doping profiles, determined from capacitance-voltage measurements, indicate an active thickness of about 148 μm and a doping concentration around $4.4 \times 10^{12}\,cm^{-3}$ in the bulk.

- **FDB:** The base substrate is similar to FTH. After thinning, a low resistivity wafer is direct bonded to the backside. The active thickness is determined to be about 145 μm and the bulk doping concentration is around $3.3 \times 10^{12}\,cm^{-3}$. The physical thickness of the entire substrate is about 200 μm.

- **FDD:** Thinning is performed only down to a physical thickness of about 200 μm. A deep diffused backside implant reduces the depletable volume so as to match the specified active thickness. It turned out that the active thickness of sensors from this substrate is larger than 175 μm and that the doping profile is non-uniform in the bulk region so that this option was discarded.

The doping concentrations and active thicknesses are determined from capacitance-voltage measurements on planar diodes from the same wafers, correcting for edge effects [97]. Full depletion voltages from 55 V to 75 V are found. In the case of the FTH and FDB material, the measurements of the active thickness are confirmed by edge-on measurements on pixel sensors presented in [98]. A brief discussion of such measurements is given in section 7.3.2.

The presence of positive charges in the oxide at the surface of the sensor leads to an accumulation of electrons in the adjacent silicon bulk. Since electrons are the majority
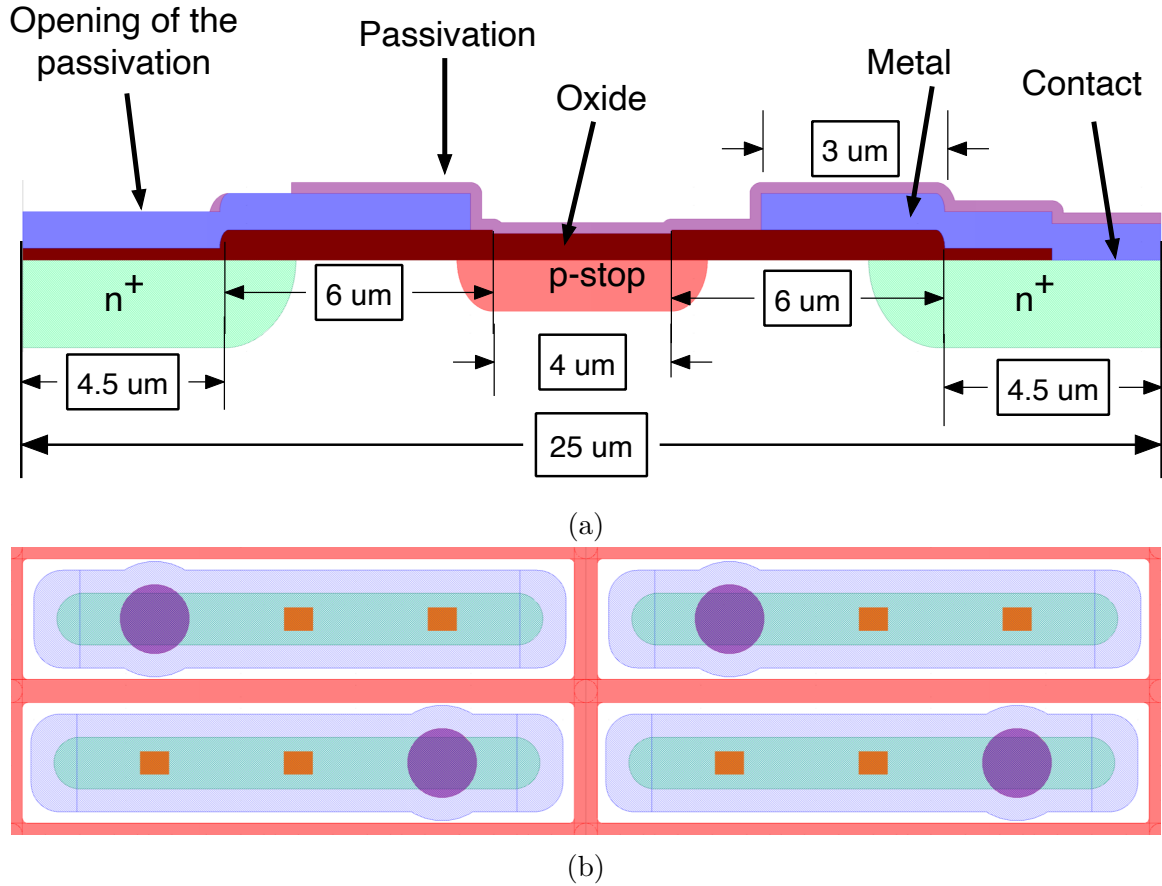
(a)

(b)

Figure 3.9.: Cross section (a) and top view (b) of the pixel layout with regular implants, p-stop inter-pixel isolation and $25 \times 100\,\mu m^2$ pixel geometry. The opening of the passivation is drawn as purple circle in (b), the contacts are drawn as orange squares. The other colors agree between the two figures.

charge carriers in the n+ implants, this accumulation layer can effectively short neighboring implants. To prevent this, a p-doped region is introduced to ensure inter-pixel isolation. Two distinct inter-pixel isolation technologies are implemented in the investigated prototypes:

- **p-stop:** The p-stop inter-pixel isolation technology introduces an additional p^+ implant between the pixels, as shown in the cross section in figure 3.9a.

- **p-spray:** The p-spray inter-pixel isolation technology employs a homogeneous p-type blanket, thus does not require an additional lithographic mask [99].

It appears that the passivation openings in figure 3.9 are directly above the pixel implants and no routing is needed, even for $25 \times 100\,\mu m^2$ pixels. This is due to the fact, that the ROC4SENS has a staggered bump-bond pattern — meaning every other column is shifted by half the pitch. In total, the R&D campaign includes prototype sensors with 29 different pixel designs compatible with the ROC4SENS. Among them are 17 designs with p-stop inter-pixel isolation. A selection is shown in figure 3.10 and 3.11. The p-spray designs are similar but have slightly larger pixel implants as discussed below. The basic
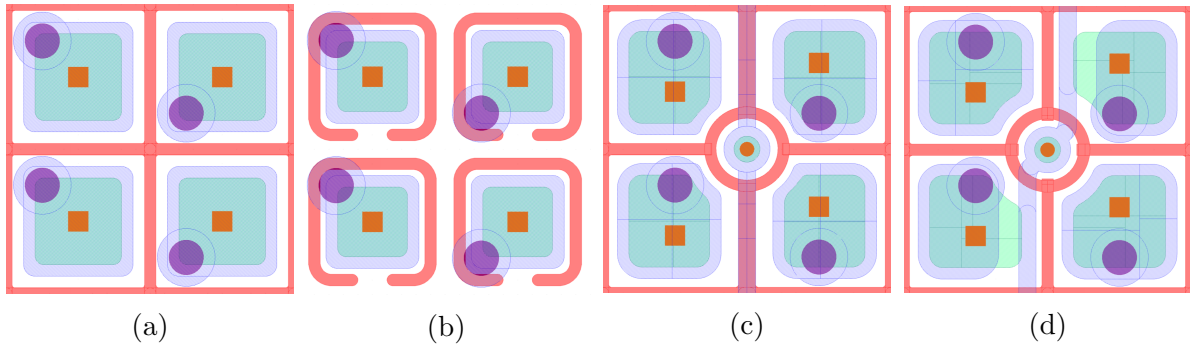
Figure 3.10.: Selection of sensor designs compatible with the ROC4SENS with $50 \times 50\,\mu m^2$ pixel geometry and p-stop inter-pixel isolation. Descriptions are given in the text.
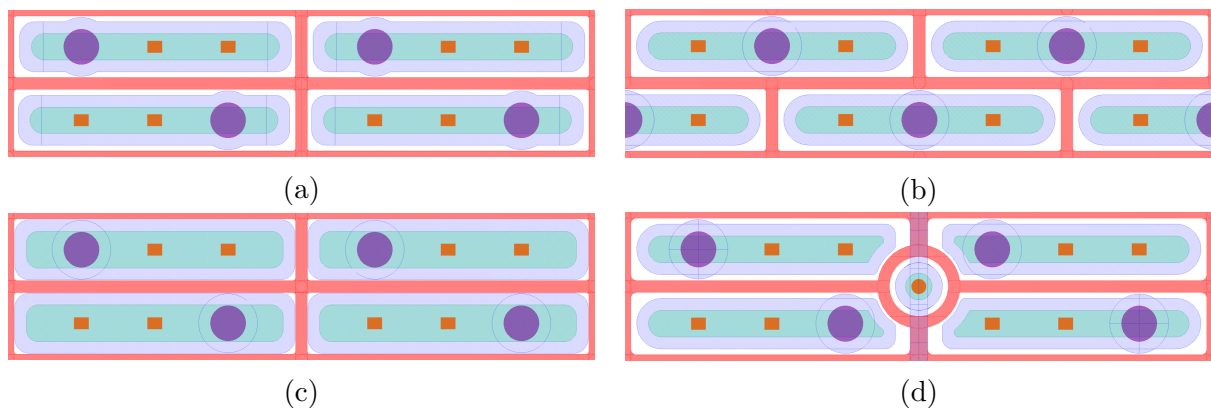

Figure 3.11.: Selection of sensor designs compatible with the ROC4SENS with $25 \times 100\,\mu m^2$ pixel geometry and p-stop inter-pixel isolation. Descriptions are given in the text.

concepts are:

- **Regular and enlarged implants:** The regular implant designs with p-stop inter-pixel isolation are shown in figure 3.9, 3.10a and 3.11a. Similar designs with enlarged implants are also studied. The implant sizes are compared in table 3.3.

- **Open p-stop:** For most of the sensor designs the p-stop implant is between two neighboring pixels. The sensor design in figure 3.10b features individual p-stop for each pixel with an opening on one side. This is to flatten the pixel potential in case of a faulty bump-bond connection or for quality tests before bump bonding (usually current-voltage measurements). For this design, the pixel implants have a width of $24\,\mu m^2$ neglecting lateral diffusion.

- **Bias dots:** Sensor designs featuring a common punch-through (bias dot) connected to a bias rail are shown in figure 3.10c, 3.10d and 3.11d. This allows to apply the same potential to all pixels for quality tests before bump bonding. Since the bias structure is known to interfere with the charge collection, bias dots of different sizes and variable routing schemes for the bias rail are tested.

- **Polysilicon resistors:** Another way to connect the bias rail to the pixel implants are polysilicon resistors.

- **Bricked:** The sensor design shown in figure 3.11b is referred to as bricked. A similar design exists with $50 \times 50\,\mu m^2$ pixel geometry.

Two options for the spark protection were considered for the final production. The chosen solution is parylene coating of the modules. Another considered option was benzocyclobutene deposition on the sensor or readout chip, which was used for the prototypes and proved to be insufficient. The investigated modules were covered with SYLGARD™ 184 Silicone Elastomer [100] to allow for operation at bias voltages up to 800 V.

Table 3.3.: Implant dimensions for selected sensor types. The numbers are those specified in the technical drawings (e.g. figure 3.9) and do not account for a lateral diffusion of about 1 µm per side in the production process.

Isolation	Geometry [µm²]	Design	Width [µm]	Width [µm]
P-stop	25×100	regular	9.0	84.5
P-stop	25×100	enlarged	12.5	87.5
P-spray	25×100	regular	10.5	85.5
P-spray	25×100	enlarged	15.5	90.5
P-stop	50×50	regular	30.0	30.0
P-stop	50×50	enlarged	33.5	33.5
P-spray	50×50	regular	34.0	34.0
P-spray	50×50	enlarged	40.5	40.5

List of Own Contributions The author's contributions to the results presented in this chapter include:

- Preparation of samples for irradiation with protons.

- Characterization of the non-uniform fluence profiles after proton irradiation.

This work has been performed under the supervision of Prof. Dr. Erika Garutti and Dr. Daniel Pitzl.

3.3.1. Irradiation and Dosimetry

The sensor modules, consisting of a sensor bump bonded to a ROC4SENS readout chip, were irradiated with protons or neutrons to study the impact of radiation damage on the performance of the sensors.

The neutron irradiation took place in the TRIGA Mark II reactor (TRIGA) in Ljubljana. The neutron spectrum of the reactor has a hardness factor $\kappa = 0.9$ [101]. The

3. The CMS Experiment

investigated fluences are ϕ_{eq} of 0.5, 3.6, 7.2 and $14.4 \times 10^{15}\,\mathrm{cm}^{-2}$ with a relative uncertainty of about 3 %, derived from the uncertainty of the reported hardness factor.

The proton irradiation took place at CERN in the PS-IRRAD Proton Facility (PS). The beam at PS provides protons with a momentum of $24\,\mathrm{GeV/c}$ [102], for which a hardness factor of $\kappa = 0.62$ is reported [103]. The beam has a Gaussian profile, monitored by a set of Beam Profile Monitors (BPMs) measuring the beam intensity in the two coordinates perpendicular do the beam axis. Following the approach in [92], the BPM data are used to obtain 2-dimensional beam profiles, e.g. shown in figure 3.12a. Their normalization in terms of a proton fluence is obtained from aluminum-foil dosimeters placed up- and downstream of the irradiated samples [104]. The hit efficiency map in figure 3.12b shows that the sensor modules were not centered with respect to the beam. The offset is found to differ between sensors, so they have received different net fluences. To take this into account, reconstructed quantities, such as fluence and hit efficiency, are quoted for the beam-spot region. The beam-spot region is defined as a circle with a radius of $2\,\mu\mathrm{m}$ centered around point at which the minimal hit efficiency is observed.

(a) (b)
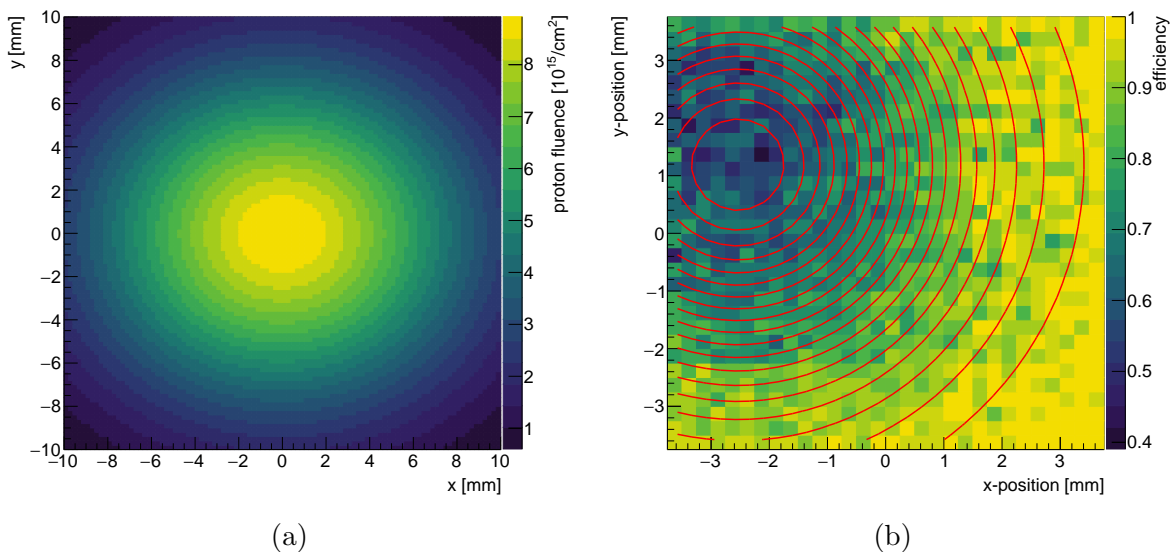
Figure 3.12.: Proton beam profile (a), determined from one-dimensional Gaussian fits to the BPM data, averaged over the period of irradiation.
Hit efficiency as a function of position reconstructed for a proton irradiated sample at a bias voltage of $150\,\mathrm{V}$ (b). The reconstruction of the hit efficiency is discussed in section 6.3.3. The origin corresponds to the center of the sensor, and the average fluence in the beam-spot region is $\phi_{eq} = 5.4 \times 10^{15}\,\mathrm{cm}^{-2}$.

The proton irradiation reached fluences ϕ_{eq} of about $3 \times 10^{15}\,\mathrm{cm}^{-2}$ and $5.3 \times 10^{15}\,\mathrm{cm}^{-2}$ in the beam-spot region. The precise values will be quoted in the corresponding sections and figures. The uncertainties on the quoted fluences are estimated to be 17 %, taking into account contributions from the dosimetry of the aluminum foils, the proton cross section, the width of the proton beam estimated from the BPM data, the position of the aluminum foil with respect to the beam and the position of the hit efficiency minimum.

4. Monitoring and Modeling of Pixel Sensor Properties

The CMS detector is exposed to a flux of high energetic particles during operation. These high energetic particles cause radiation damage to the detectors subsystems which changes their properties. The radiation damage effects in silicon pixel sensors are discussed in section 2.4. In the running experiment monitoring and modeling of radiation damage effects is important to optimize the operational parameters and temperature of the detector. Note that the temperature control is not limited to operation, that is when high voltage is applied, but also required during shutdowns etc., to control annealing effects.

From a practical perspective, two quantities of interest are the leakage current I_{leak} and the full-depletion voltage V_{depl} of the silicon sensors. The leakage current and the corresponding power consumption are required to stay within the limits given by the power supplies and the cooling system of the detector. The full depletion voltage is used to indicate the annealing state of the detector to utilize beneficial and avoid reverse annealing effects. In the following sections, a framework to model the development of these two quantities over the operation time will be described, followed by a comparison between the model predictions and measurements. Then a set of improvements and systematic studies on this modeling framework will be presented.

List of Own Contributions   The author's contributions to the results presented in this chapter include:

- Maintenance of the modeling framework in 2018 and 2019.

- Generation of and preapproval presentation for the figures presented in section 4.2, published in [105].

- Improved understanding of the sensor temperatures in the modeling framework.

- Investigation of systematic effects related to the tension between leakage current measurements and model predictions.

This work has been performed in collaboration with Dr. Jory Sonneveld, Dr. Benedikt Vormwald (both Hamburg University at that time) and Prof. Dr. Annapaola de Cosa

(ETH Zürich). Julia Alexandra Hunt (KIT) introduced the author to the modeling framework.

4.1. Modeling Framework

The basis for the presented framework are the fundamental studies on changes of the leakage current and the effective doping concentration given a certain irradiation and temperature (annealing) history in [53]. Based on these studies, a modeling framework for the CMS strip tracker was developed in [106] and extended for the CMS barrel pixel tracker in [107]. The development and maintenance of the latter are continued within this work, concentrating on the years 2017 through 2018 (Phase-1).

The development of leakage current as a function of the 1 MeV neutron equivalent fluence ϕ_{eq} a silicon sensor was exposed to and its annealing behavior can be modeled with the parametrization introduced in equation 2.21 to 2.30, as long as the surface generation current is negligible. The contribution from the surface generation current is discussed in section 4.3.4. The full-depletion voltage can be modeled in a similar way, by using the parametrization for the development of the effective doping concentration N_{eff} given in equation 2.31 to 2.35 and deriving the full-depletion voltage according to equation 2.2.

In both cases, the parametrizations are found for initial irradiation and subsequent annealing at a constant temperature. This does not hold for the operating CMS detector, where the irradiation extends over a period of years, with interruptions for technical stops, maintenance and shutdowns. The annealing takes place simultaneously and at varying temperatures. To account for that modeling is performed in time steps of one day. The fluence ϕ_{eq} deposited in one day is annealed in steps of one day, using an averaged annealing temperature, and the total change of the leakage current and the effective doping concentration on a given day is the sum of all annealed contributions from previous days.

For a better overview, the procedure is shown in a flow chart in figure 4.1. As discussed above, both parametrizations require the fluence ϕ_{eq} and the temperature history, labeled T_a in the above mentioned equations, since the irradiation. To compare the modeled leakage current to the measurement it needs to be corrected for the temperature offset between the temperature T_m at which the measurement was taken and 20 °C, for which α is parameterized. This correction is performed using a temperature dependent scaling factor introduced through equation 2.30. This way temperature needs to be considered twice in the leakage current model.
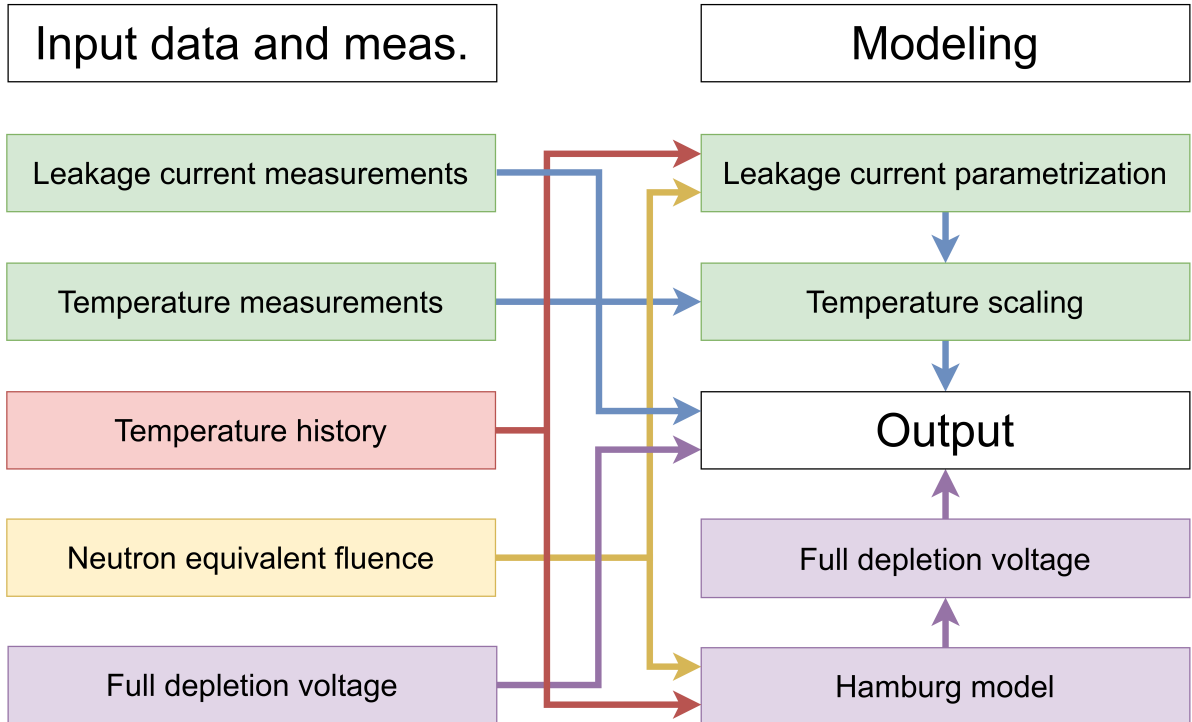
Figure 4.1.: Framework for modeling of the leakage current and the full-depletion voltage.

4.1.1. Input Data

The model framework requires a set of input data, displayed on the left half of figure 4.1. These data need to be acquired from the running experiment, comparable conditions need to be found and systematic effects need to be corrected for.

Leakage Current Measurements

The leakage current of each power group in the pixel detector is constantly measured during the operation of the experiment and stored in a database. Each power group contains several detector modules, increasing from 3 in layer 1 to 16 in layer 4, at different z-positions. To select leakage current measurements for comparable conditions, the measurements are taken once for each LHC fill, 20 min after the declaration of stable beam conditions. Short fills and those with a small number of bunches are excluded from this selection [108]. These current measurements are averaged over each layer, excluding 3 power groups with non-active modules. It should be noted that the leakage currents are measured at the operation voltage, which is typically chosen above the full depletion voltage of the sensors. The related systematic effects are discussed in section 4.3.3.

Temperature Measurements

In order to compare the modeled and measured leakage currents, the temperature T_m at which the measurements were taken needs to be known to perform the temperature scaling according to equation 2.30. Thus temperature measurements are selected with

the same criteria as the leakage current measurements discussed above, such that both measurements are taken at comparable points in time.

It should be noted, that the temperature sensors are placed on the carbon fiber support structure, at the beginning, center and end of each cooling loop. Thus there is no one-to-one correspondence between the temperature sensors and the power group and the temperature readings from all sensors are averaged for a given layer. In addition, there is a temperature offset between the temperature sensors and the silicon sensor due to the electrical power dissipated in the detector module and the finite thermal conductivity of the material between these two. This offset was quantified in a set of studies on a thermal mock-up [109], representing one half shell of the barrel layer 2, and simulations [84], summarized in [107]. The final values for the temperature offset are 3 °C in layer 1 to 3 and 4 °C in layer 4.

Taking into account this temperature offset, the average silicon temperatures at which the leakage current measurements are taken are -10 °C in layer 1, -11 °C in layer 2 and 4, and -12 °C in layer 3.

Temperature History

In the model for the development of the leakage current I_{leak} and the effective doping concentration N_{eff} an annealing temperature T_a is needed. Since annealing is a process continuous in time, in theory, the entire temperature history — the temperature at any time in the considered time frame — needs to be known. In practice, a trade off between accuracy on the one hand and computation time as well as simplicity, on the other hand, is made. The temperature history is acquired in day wise binning, by taking the median of the database entries for one day. This is considered a good approximation since temperature variations within one day and between the layers are typically small [107]. Two broken temperature sensors and one outlier are excluded from the calculation of the median.

These median temperatures are corrected for the temperature offset mentioned in the previous section if the detector is on. For the year end technical stop 2017/18 the detector was in the clean room and no temperature measurements were taken between mid of January 2018 and the end of February. For this phase, the temperature of the detector is assumed to be 20 °C. In figure 4.2 the annealing temperature used to model layer 4 is shown.

Neutron Equivalent Fluence

The 1 MeV neutron equivalent fluence ϕ_{eq} the silicon sensors were exposed to needs to be known in order to estimate the effects of radiation damage. Because ϕ_{eq} is not directly measured in CMS it is calculated from the LHC delivered luminosity.

Since the recorded luminosity is a crucial ingredient in the calculation of cross sections, it
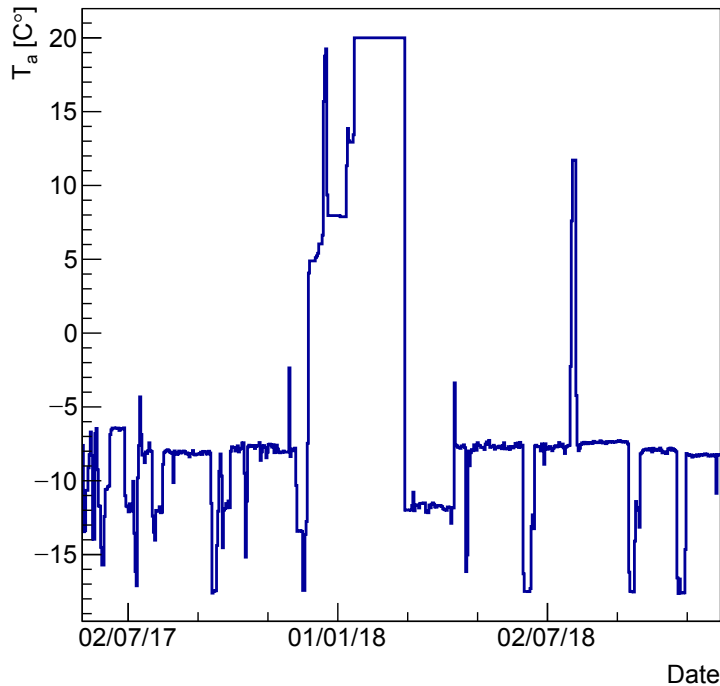
Figure 4.2.: Annealing temperature used to model layer 4.

is precisely measured within the Beam Radiation Instrumentation and Luminosity (BRIL) project of CMS. An overview of the results can be found in [69]. On that basis, the delivered luminosity per day is obtained and used for the calculation of ϕ_{eq}.

Within the BRIL group, FLUKA [90] simulations are used to derive the deposited fluence ϕ_{eq} per fb^{-1} as a function of the position within the detector. The results of such a study (v.3.13.0.0) are presented in [110]. They show the radial dependence of ϕ_{eq} for different z-positions and are split into the contributions of neutrons, protons and charged pions. For the presented results FLUKA study v.3.23.1.0 is used. At $z = 0\,$mm and the radial positions of the four barrel layers, the deposited ϕ_{eq} is calculated separately for charged and neutral particles, using the delivered luminosity on each considered day. The radial positions are 28.98 mm, 67.57 mm, 108.725 mm and 159.805 mm for layer 1 to 4, respectively. The split into charged and neutral particle contributions is due to the dependence of ΔN_{eff} on the particle type discussed in [21]. A more detailed discussion on the reconstruction of the fluence ϕ_{eq} can be found in [107].

Full Depletion Voltage

In contrary to the leakage current, the full-depletion voltage V_{depl} can not be measured directly in the running experiment. In laboratory measurements it is usually extracted from the voltage dependence of the sensor's capacitance, as long as the frequency dependence building up with increasing ϕ_{eq} is not dominating the results [111]. In the running experiment scans of the bias voltage are performed and the voltage dependence of quantities like

the cluster charge and cluster size is reconstructed. Since these bias scans interfere with the usual data acquisition, they are performed monthly on typically one representative power group per layer. Full scans, covering all power groups in the barrel pixel detector are performed about twice a year.

For the presented measurements all bias scans were performed after type inversion, predicted at $\phi_{eq} \approx 4.4 \times 10^{12} \, \text{cm}^{-2}$ within the applied model. For these comparably low fluences cluster charge and cluster size increase with voltage, as the depletion zone grows from the pn-junction to the backside of the detector, until the sensor is fully depleted. Once this has happened both quantities saturate. A small remnant slope with a positive or negative sign is explained by a combination of a reduction of the diffusion width and Lorentz angle with increasing voltage, threshold effects and reduced drift times in the presence of charge carrier trapping. For highly irradiated sensors the situation is more complicated due to double junction effects. In any case, the Hamburg model is applicable up to $\phi_{eq} < 5 \times 10^{14} \, \text{cm}^{-2}$ [21]. For a set of bias scans, taken in 2018, the reconstructed cluster charge in layer 2 is shown and discussed in [112].

The kink in the voltage dependence of either quantity can be determined in three ways: First, by fitting a straight line in both linear regions and finding the intersections. Second, by finding the minimum in the curvature of the curve. Third, by visual inspection. Since the former two approaches fail for certain shapes of the curves and are compatible with the results of the third method [107], results from the third method are used in this work.

4.2. Data and Model Comparison

At the end of 2018, the acquisition of collision data in the CMS experiment stopped due to a planned shut down of the LHC referred to as Long Shutdown 2 (LS2). On this occasion a set of plots from the operation of the experiment was pre-approved within the CMS collaboration, containing also a comparison of the measured and modeled leakage current I_{leak} and the full-depletion voltage V_{depl} in the barrel of the CMS pixel detector. These results are published in cite [105], where they are compared to results from other LHC experiments, and discussed below.

4.2.1. Leakage Current

A comparison of the measured and modeled leakage current for the years 2017 and 2018 and the four barrel layers is shown in figure 4.3. The leakage current is normalized to an active volume of $0.299 \, \text{cm}^3$, corresponding to one detector module. The fluences reached at the end of 2018 are $\phi_{eq} = 7.9 \times 10^{14} \, \text{cm}^{-2}$, $\phi_{eq} = 1.8 \times 10^{14} \, \text{cm}^{-2}$, $\phi_{eq} = 0.9 \times 10^{14} \, \text{cm}^{-2}$ and $\phi_{eq} = 0.5 \times 10^{14} \, \text{cm}^{-2}$ for layer 1 to 4, respectively.
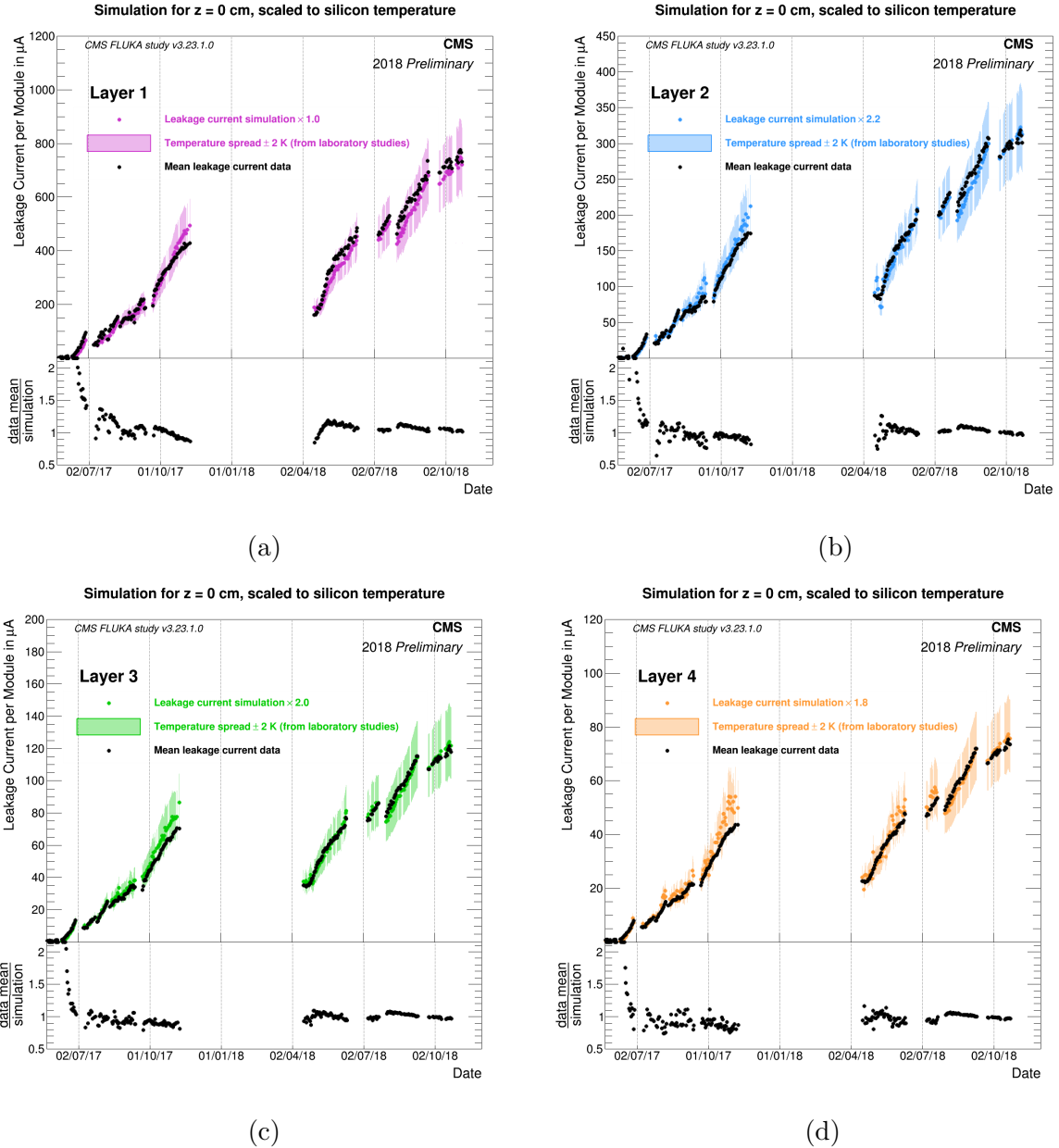
(a)

(b)

(c)

(d)

Figure 4.3.: Measured and modeled leakage current per detector module as a function of time, for the four barrel layers of the CMS detector. For layer 2 to 4 the simulation is scaled by a factor of about 2, specified in the figures. The errors on the simulation are from a temperature uncertainty of $\pm 2\,°C$, as found in the thermal mock-up of the detector.

Qualitatively the model follows the trend and features of the measurements. For layer 2 to 4 the modeled currents are scaled by a factor of about 2 to correct for a quantitative disagreement. The origin of this disagreement is not fully understood. In addition, systematic tensions on the order of $20\,\%$ are observed, for example in layer 1 around April 2018. The simulation significantly underestimates the leakage current at the beginning of 2017. A discussion on the systematic effects and their correction is presented in section 4.3.

4.2.2. Full Depletion Voltage

A comparison of the measured and modeled full-depletion voltages for the years 2017 and 2018 and the four barrel layers is shown in figure 4.4. The fluences reached at the end of 2018 are $\phi_{eq} = 7.9 \times 10^{14}\,\mathrm{cm}^{-2}$, $\phi_{eq} = 1.8 \times 10^{14}\,\mathrm{cm}^{-2}$, $\phi_{eq} = 0.9 \times 10^{14}\,\mathrm{cm}^{-2}$ and $\phi_{eq} = 0.5 \times 10^{14}\,\mathrm{cm}^{-2}$ for layer 1 to 4, respectively. Note that at the fluence ϕ_{eq} deposited in layer 1, the effects of charge carrier trapping and double junctions become relevant.
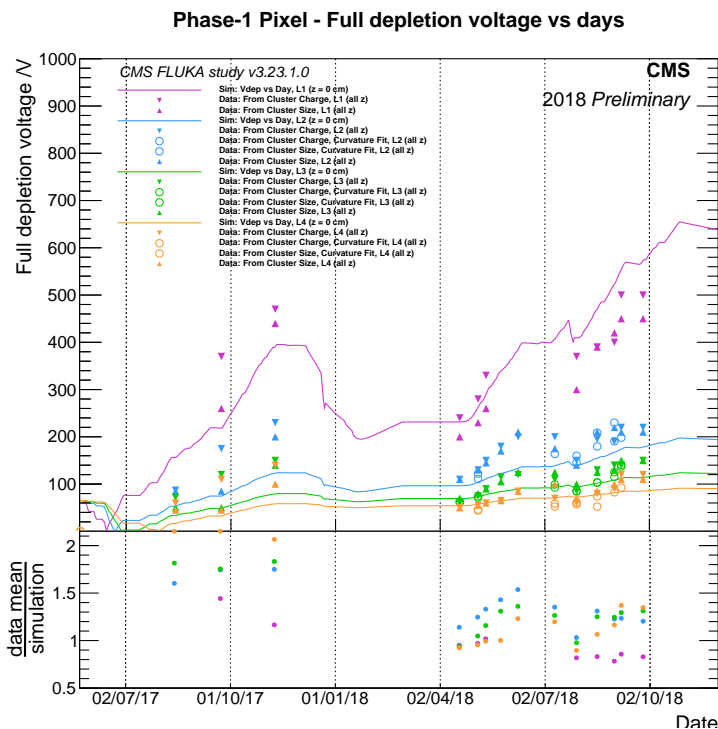
Figure 4.4.: Measured and modeled full-depletion voltage as a function of time, for the four barrel layers of the CMS detector. The data points are extracted from the kink in the voltage dependence of cluster charge or cluster size. The kink is estimated per visual inspection (full markers) or by finding the minimal curvature (open markers, limited number of points).

Qualitatively the model follows the trend and features of the measurements. The full-depletion voltages extracted from the voltage dependence of cluster charge or cluster size differ by typically $50\,\mathrm{V}$ for layer 1, for the other layers the differences are smaller. In addition, the points obtained from visual inspection and those from the minimal curvature do agree within that range. In general, the model underestimates the full-depletion voltages found in the measurements. Interestingly the agreement is best after the year end technical stop between 2017 and 2018, meaning no additional irradiation and storage at higher temperatures so that the short term annealing can take place. For layer 1 and the end of 2018, the model overestimates the measured values.

4.3. Improvements and Systematic Studies

The focus of this project is monitoring and modeling of leakage current and full-depletion voltage in order to predict the future behavior of these quantities for an assumed scenario of operation conditions. Typically these scenarios consist of an expectation on the integrated luminosity and temperature conditions as a function of time. The temperature conditions are varied, within operational constraints, to maximize the profit from beneficial annealing, while keeping reverse annealing effects as low as possible. Examples of such studies are discussed in [107], while the focus here is placed on a set of improvements to the modeling framework implemented within the scope of this work. In addition, some of the systematic effects mentioned in the previous sections are discussed and quantified.

4.3.1. Improved Temperature Measurements

As pointed out in section 4.1.1 temperature enters the model in two ways, as annealing temperature T_a and in order to perform temperature corrections to the modeled leakage current according to equation 2.30, using a temperature T_m. Initially, the temperature corrections of the leakage current were performed based on the temperatures T_a used to model annealing effects. These are derived as median (see section 4.1.1), covering measurements in all layers taken on the corresponding day. Since the investigated leakage current measurements are taken during data acquisition there is a systematic difference between the temperature at which the current is measured and these median temperatures. Thus a new set of temperature measurements matching the leakage current measurements, which was already introduced in section 4.1.1, is taken and used to apply temperature corrections to the simulated leakage current.

The effect of this improvement is shown in figure 4.5, where the results obtained with both approaches are compared for layer 1 and 3. For layer 1 the effect on the simulated leakage current is as large as 30 %, for layer 2, 3 and 4 the effect is typically below 10 %. This is due to the higher hit rate in layer 1, which leads to a higher temperature during operation caused by the larger digital activity. In addition, the local spread of the measurements is reduced, which is partially due to the use of the better temperature measurements, but also due to the removal of bad fills discussed in section 4.1.1.

4.3.2. Further Discussion of Temperature Issues

The annealing temperature has an effect on the output of the model for both leakage current and full-depletion voltage, but the model for the leakage current is more sensitive, due to the exponential temperature dependence introduced through equation 2.30. Thus it is necessary to discuss some systematic effects related to temperatures.

As introduced in 4.1.1, the temperature is averaged over all layers and the three positions of the temperature sensors along the cooling pipes. The latter can not be avoided,
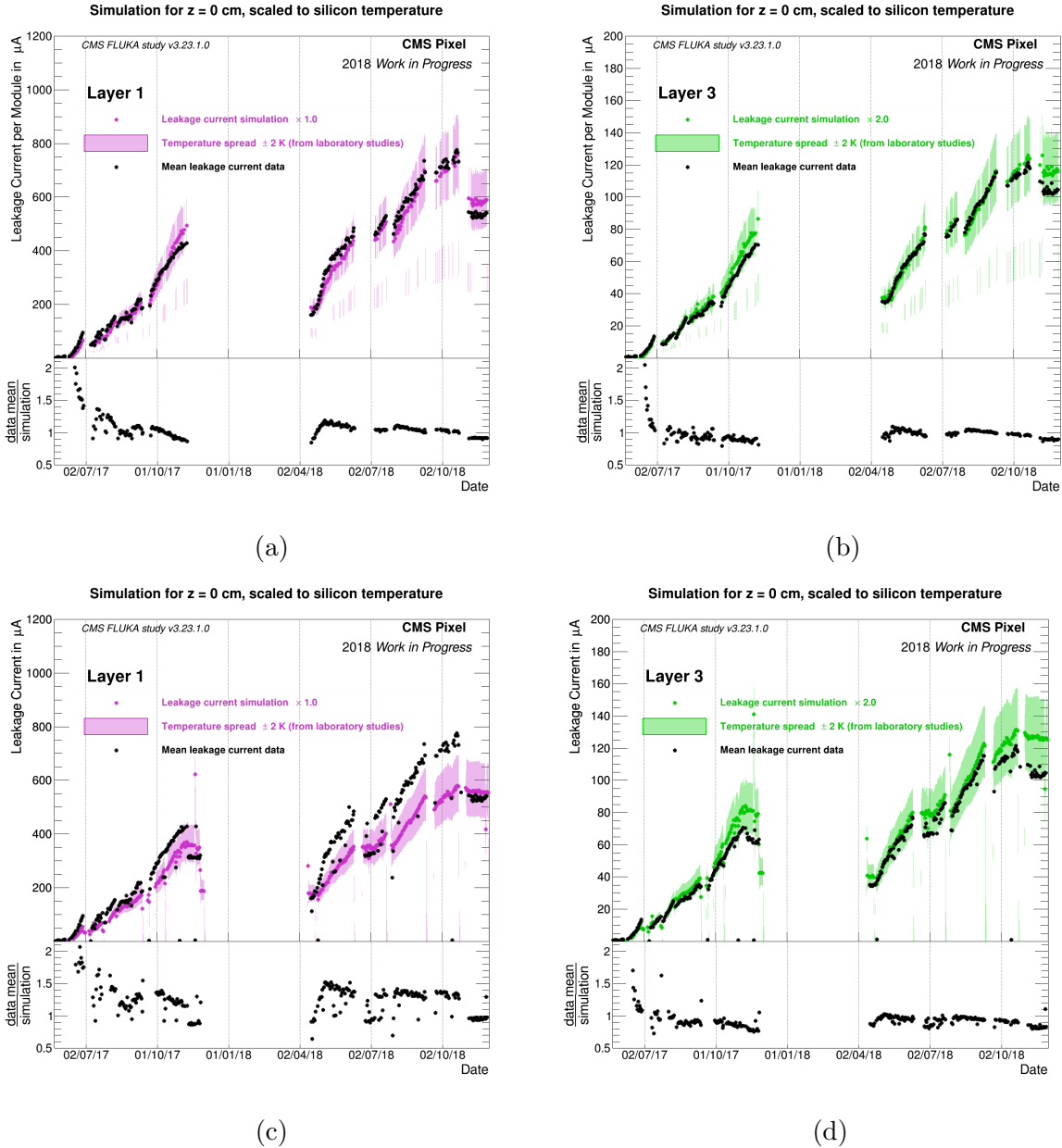
(a)

(b)

(c)

(d)
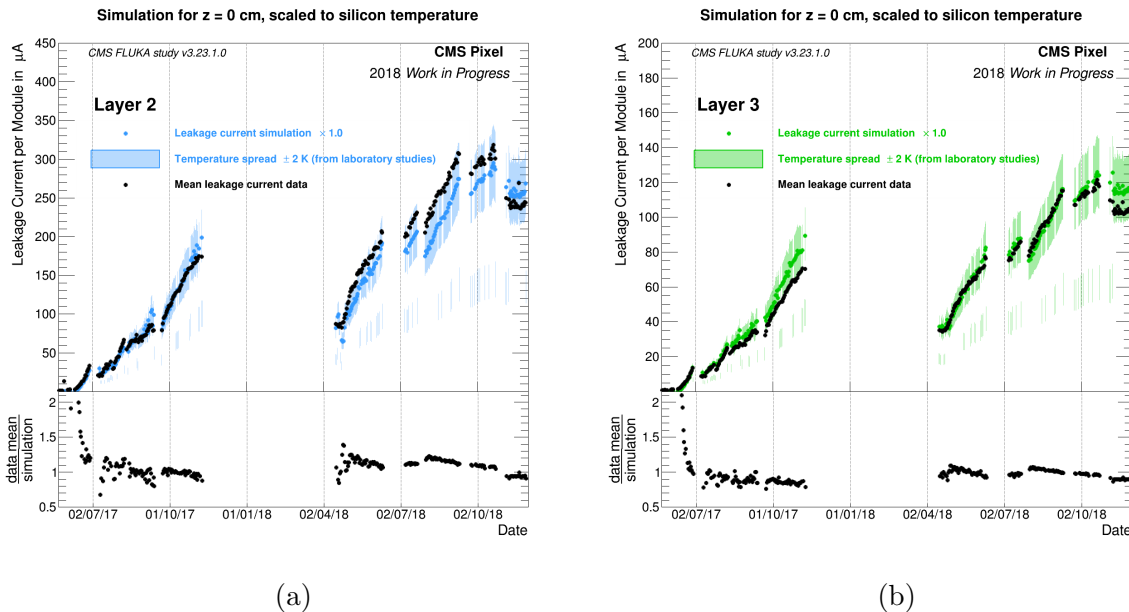
Figure 4.5.: Measured and modeled leakage current per detector module as a function of time, for barrel layer 1 and 3 of the CMS detector. For layer 3 the simulation is scaled by a factor of about 2, specified in the figures. The errors on the simulation are from a temperature uncertainty of $\pm 2\,°\mathrm{C}$, as found on the thermal mock-up of the detector.

In (a) and (b) the temperature correction of the modeled leakage current is performed based on temperature measurements taken 20 min into stable beam conditions, matching the conditions for the leakage current measurements. In (c) and (d) daily median temperatures are used. In addition, the set of irregular fills is not excluded from the presented data.

since the leakage current is measured for groups of modules so that the dependence of the leakage current on the position along the cooling loops can not be resolved. The temperature drop along a cooling loop is about $4\,°\mathrm{C}$ and since the leakage current is not linear in the silicon temperature, this causes a bias partially mitigated by the zigzag layout of the

cooling pipes. Still, assuming an average temperature of $-10\,°\mathrm{C}$ and a spread of $\pm2\,°\mathrm{C}$ a current of $100\,\mu\mathrm{A}$ at $20\,°\mathrm{C}$ scales into a current of $5.25\,\mu\mathrm{A}$ at the mean temperature. In contrast, the mean current, when scaling to a uniform distribution of temperatures between $-12\,°\mathrm{C}$ and $-8\,°\mathrm{C}$, amounts to $5.29\,\mu\mathrm{A}$. Thus the systematic effect of averaging the temperatures is about $1\,\%$ — negligible considering other systematic effects.

A similar systematic effect arises due to the day wise granularity of the temperature history. Temperature variations within one day are assumed to be on the order of $4\,°\mathrm{C}$. By successively adding and subtracting $2\,°\mathrm{C}$ to the daily temperatures shown in figure 4.2 and re-evaluating the model, the effect of such a temperature spread can be estimated while keeping the mean temperature constant. It is found that the effect is smaller than $7\,\%$ assuming temperature variations of $4\,°\mathrm{C}$ and smaller than $10\,\%$ assuming temperature variations of $10\,°\mathrm{C}$.

(a) (b)

Figure 4.6.: Measured and modeled leakage current per detector module as a function of time, for two of the four barrel layers of the CMS detector. The errors on the simulation are from a temperature uncertainty of $\pm2\,°\mathrm{C}$, as found on the thermal mock-up of the detector. Instead of scaling the modeled current, an offset of $8\,°\mathrm{C}$ is added to all temperatures used in the simulation.

Further systematic uncertainties need to be considered since the temperature is not measured directly on the silicon sensor, causing systematic uncertainties related to the temperature offsets discussed in section 4.1.1. With regard to the results presented in figure 4.3 it is obvious to ask which offset in temperature would be needed to explain the discrepancy between measurements and model. As presented in figure 4.6 the required offset amounts to $8\,°\mathrm{C}$ for layer 3. For layer 2 a higher and for layer 4 a lower offset is needed, in agreement with the higher and lower factors presented in figure 4.3. Considering equation 2.30 alone, $8\,°\mathrm{C}$ amounts to an increase of about a factor 2. Thus the annealing effects, in the considered range of time and temperature, are relatively robust with respect

to temperature uncertainties and the direct temperature dependence of the leakage current is the dominating contribution.

4.3.3. Voltage Offset

Another systematic effect to be discussed is the fact, that α describes the leakage current measured at the full-depletion voltage [53]. The leakage current measurements presented in section 4.2.1 are taken at the operation voltage V_{set}, which is typically larger than the full-depletion voltage V_{depl}. In table 4.1 the operation voltage and the full-depletion voltage of all four layers are given for a set of dates. Significant differences, even in excess of 100 V, are frequent.

Table 4.1.: Operation voltage V_{set} and full-depletion voltage V_{depl} of all four barrel layers for a selection of dates. The presented values for V_{depl} are those extracted from the voltage dependence of the cluster size, shown in figure 4.4. The values for V_{set} are extracted from the CMS-internal database. In addition, ratios r_I between the leakage currents measured at both voltages are given.

Dates	09.11.17	19.04.18	12.05.18	30.07.18	26.09.18
Layer 1					
V_{set}[V]	350	350	400	400	450
V_{depl}[V]	440	200	260	300	450
r_I[%]	88	109	110	108	100
Layer 2					
V_{set}[V]	250	250	250	300	300
V_{depl}[V]	200	110	145	140	210
r_I[%]	105	108	105	111	106
Layer 3					
V_{set}[V]	200	200	200	250	250
V_{depl}[V]	140	70	90	100	150
r_I[%]	113	107	107		108
Layer 4					
V_{set}[V]	200	200	200	250	250
V_{depl}[V]	100	50	60	70	110
r_I[%]	105	109	107		108

To estimate the effect of this voltage offset on the measured currents presented in figure 4.3, leakage current measurements taken during the scans of the bias voltage discussed in section 4.1.1 are extracted from the CMS-internal database. Two examples of these measurements are presented in figure 4.7. From these data it is straightforward to compare the current I measured at both voltages quantitatively, defining the ratio

$$r_I = \frac{I(V_{set})}{I(V_{depl})}.$$
(4.1)
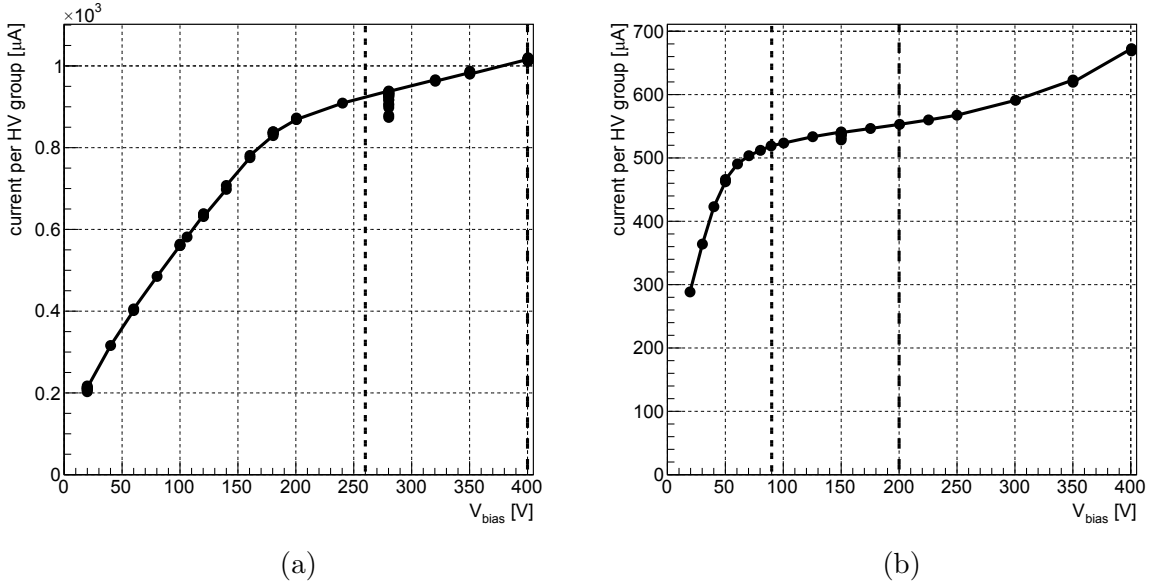
Figure 4.7.: Leakage current measurements taken during the scan of the bias voltage on 12.05.18. The measurements are taken on the HV groups *BPix_BmO_SEC2_PG1_channel002* and *BPix_BpO_SEC3_PG2_channel002* in layer 1 (a), 2 (b), respectively. The fine-dashed line indicates V_{depl} and the coarse dashed line indicates V_{set}.

For the selected dates these ratios are given in table 4.1. In all but one case (layer 1, 09.11.17) V_{set} is larger than V_{depl}, thus the measured current overestimates the current at the full-depletion voltage. Quantitatively this effect ranges between 5 % and 13 %. Although the saturation effects of the leakage current are still more pronounced for layer 2,3 and 4, as can be seen in figure 4.7, the effect is of similar size in all four layers, likely because the relative difference between the two voltages increases with the layer index.

4.3.4. Additional Effects

As discussed in [107], there is a small z-dependence in the FLUKA simulations of the flux of charged and neutral particles in the barrel region of the CMS pixel detector. For layer 1 this amounts to a reduction of about 15 % for charged and 9 % for neutral particles between $z = -3.7$ cm and $z = -23.7$ cm. The reduction of the leakage current is about 14 % between these two positions. This is qualitatively confirmed by z-dependent measurements taken at the end of 2018 [113]. As discussed in section 4.3.2, this can not be resolved in the measurements taken under operation conditions and also has a reduced effect on the final measurements since the average over all z-positions is taken. For the other 3 layers, the effect is negligible.

In addition to the current generation in the bulk of the silicon sensors due to the NIEL, the ionizing dose increases the density of traps at the Si-SiO$_2$ interface, increasing the surface generation current [51]. This contribution is not taken into account in the leakage current model. In [51] the surface current density, measured on gate-controlled diodes, is

presented as a function of the ionizing dose. The ionizing dose deposited in the four barrel layers at the end of 2018 was estimated from occupancy measurements and is shown in table 4.2. It is used to make a conservative estimate of the surface current density J_{surf}^{max} for each layer. The gaps between the implants correspond to approximately 30 % of the sensor surface. Assuming that the entire gap area contributes, a conservative estimate of the surface generation current I_{surf}^{max} is given, also in table 4.2. For layer 1 the contribution of the surface generation current amounts is less than 2 %. For layer 4 it is a contribution of up to 6 %.

Table 4.2.: The ionizing dose deposited in the four barrel layers at the end of 2018 was estimated from occupancy measurements. For the given doses a maximal surface-current density J_{surf}^{max} is estimated from the figure in [51]. This is used to derive a conservative estimate of the surface generation current I_{surf}^{max} in each layer.

Layer	Dose [kGy]	$J_{surf}^{max}[\mu A\,cm^{-2}]$	$I_{surf}^{max}[\mu A]$
1	410	4.5	14
2	86	2.5	8
3	53	0.5	6
4	29	0.4	5

The FLUKA simulations predict the radiation fields for different particle types and energies. Hardness factors, as defined in section 2.4, are used to scale these radiation fields into 1 MeV neutron equivalent fluences and subject to uncertainties. These uncertainties are estimated to yield a scale uncertainty of $\approx 30\,\%$ [105] on the simulated fluences ϕ_{eq}.

It is clear that the collision rate at the LHC has — through the occupancy — an impact on the digital activity and the power dissipation in the readout chips of the CMS pixel detector. This can be observed, in figure 4.5a. At the end of 2018, the LHC performed heavy ion runs, associated with lower pixel occupancies. The lower power dissipation causes a temperature drop, explaining the mismatch between data and model for these days. This effect is not taken into account in the framework of the model, but the discussed example shows that it is on the order of 10 % in extreme cases.

Finally, it should be noted that the applied model for the development of the leakage current is valid for $1 \times 10^{-17}\,A\,cm^{-1} < \alpha < 6 \times 10^{-17}\,A\,cm^{-1}$ [53]. The values occurring in this application are in the range $2 \times 10^{-17}\,A\,cm^{-1} < \alpha < 8 \times 10^{-17}\,A\,cm^{-1}$. It might be the case, that for these conditions further short-term annealing components need to be considered [53].

4.4. Conclusion

A framework to model the evolution of the full depletion voltage V_{depl} and the leakage current I_{leak} in the four barrel layers of the CMS pixel detector through the years 2017 and 2018 is introduced in [107]. Within the scope of this work, the framework is revised and systematic uncertainties are investigated.

For the results discussed in section 4.2 and published in [105], the shape of the measured and modeled I_{leak} as a function of time agrees well, provided that the modeled values are scaled by a factor of approximately 2. Also for V_{depl} the key features of the reconstructed values, presented versus time, are represented by the model. In any case, systematic deviations are observed, which can not be accounted for by simple scaling.

As presented in section 4.3.1, a dedicated set of temperature measurements is defined to scale the modeled I_{leak} to the temperature at which the measurements are taken. This significantly reduces fluctuations of the ratio between measurements and model, especially for layer 1 (see figure 4.5). It is shown that the factor 2 disagreement between measured and modeled I_{leak} can hardly be explained by an offset in temperature alone, which would have to be around 8 °C. Further systematic effects are quantified, ranging between 1 % and 14 % effect on the leakage current. An exception is the uncertainty on the hardness factors, yielding a scale uncertainty of $\approx 30\,\%$ on the fluence ϕ_{eq}, according to [105].

In general, it is to be concluded that the deviations between measurements and model are not fully understood. Other experiments make similar observations, presented in [105], although quantitatively the deviation between measured and modeled leakage currents is smaller. Despite these deviations, the presented framework is a valuable tool providing a fact base for operational decisions. Especially for the choice of temperature conditions in periods where the detector is off, to profit from beneficial annealing effects.

5. Materials and Methods for Beam Tests of Pixel Sensors

In order to identify the best pixel sensor design for the Phase-2 Upgrade, see section 3.2, of the CMS detector, a large number of sensors with different designs were tested in an extensive test-beam campaign. The tests were executed in several setups and for sensors bump bonded to different readout chips, namely the RD53A [87] and the ROC4SENS [114] readout chip where the majority of the results presented in this work were obtained with the latter.

In the following, the ROC4SENS readout chip and the corresponding readout system, the test-beam setup and the routine for online monitoring and data acquisition are introduced.

List of Own Contributions   The author's contributions to the results presented in this chapter include:

- Preparing and conducting test-beam measurements.

- Data quality assessment during test-beam measurements.

- Characterization, calibration, and pulse-shape optimization for sensor modules in the laboratory.

- Development and testing of a program for data acquisition and online monitoring.

This work has been performed under the supervision of Prof. Dr. Erika Garutti and Dr. Daniel Pitzl, and in collaboration with the test beam crew listed in [115].

5.1. Readout Chip

Hybrid pixel detector modules consist of a pixel sensor bump bonded to a readout chip. The energy depositions from charged particles generate electron-hole pairs in the sensor material. The drift of the electrons and holes induces a signal in form of current pulses on the sensor electrodes. The readout chip amplifies and shapes these signals for every pixel, stores them and facilitates the electrical circuits for the readout of all the pixels.

5. Materials and Methods for Beam Tests of Pixel Sensors

The ROC4SENS is a generic pixel readout chip and was developed at the Paul Scherrer Institute (PSI). Since it is of major importance for this work, a summary of its properties based on [114] is given in this section. A discussion of the Digital Test Board, used for data acquisition with the ROC4SENS, and the applied calibration procedures follows.

In general, the ROC4SENS is dedicated to sensor studies. Thus its key feature is the analog pulse-height measurement without zero suppression, which allows detailed studies of the charge collection in the sensor. It is not self-triggered, so a trigger signal needs to be generated externally and provided to the chip. To avoid annealing during bump bonding, the sensors are irradiated thereafter together with the readout chip. Therefore the ROC4SENS is produced in the same 250 nm CMOS technology as the CMS-readout chip PSI46V2.1 [116], which is known to perform well after proton irradiation to ϕ_{eq} of $5.1 \times 10^{15}\,\mathrm{cm}^{-2}$ [117]. Another feature is the staggered bump bond pattern with 50 μm pitch. This allows for an elegant connection to both $50 \times 50\,\mathrm{μm}^2$ and $25 \times 100\,\mathrm{μm}^2$ pixel sizes, as discussed in section 3.3. Test pulses can be injected into each pixel via a dedicated capacitor. They are used for the discussed calibration procedures. For the measurements presented in this work, version V1.1 of the ROC4SENS is used.
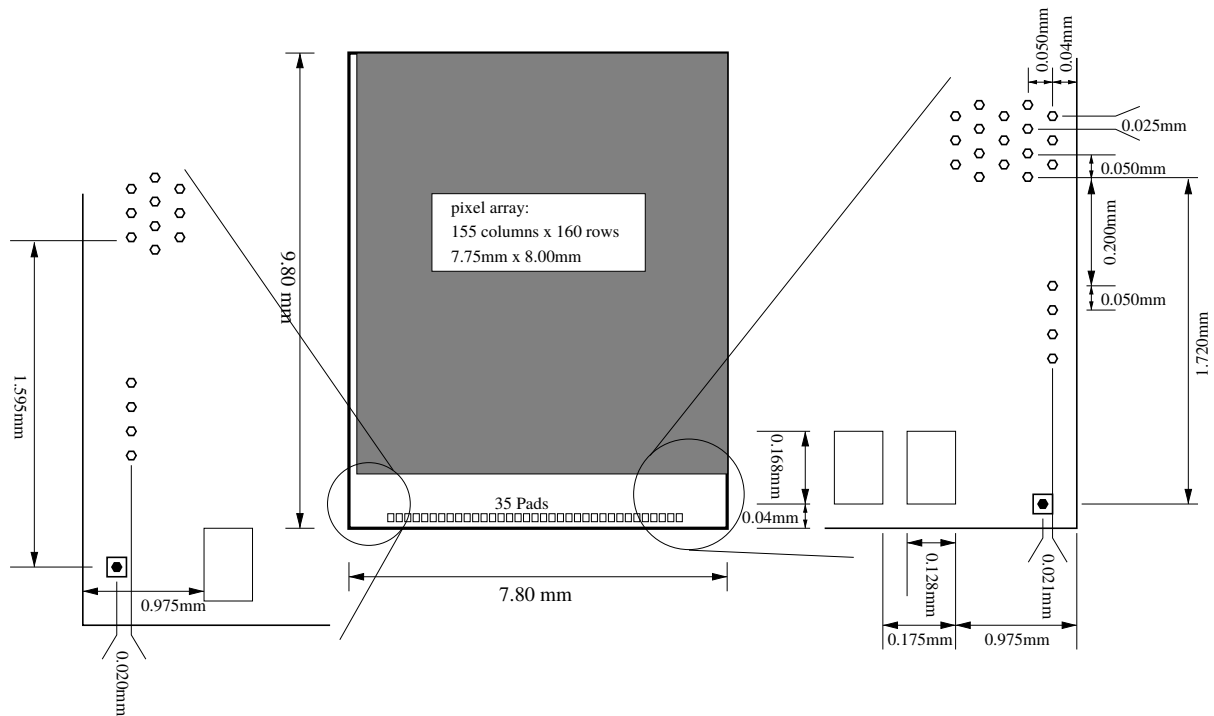
Figure 5.1.: Geometric layout of the ROC4SENS readout chip. Taken from [114].

5.1.1. Geometry

The pixel matrix of the ROC4SENS consists of 24 800 pixels organized in 155 columns and 160 rows, as indicated in the geometric layout in figure 5.1. Taking into account the pitch of 50 μm this sums up to an active area with a width of 7.75 mm and a height of 8 mm. Pixel counting starts in the bottom left corner with pixel index (0,0). In every odd

56

column, the bump bond pad is shifted down by half the pitch ($25\,\mu m$) yielding a staggered bump bond pattern. This allows for the use of sensors with pixel sizes of $50 \times 50\,\mu m^2$ and $25 \times 100\,\mu m^2$ without the necessity of putting bump bond pads on the pixel boundaries, shown in section 3.3, which would potentially increase crosstalk.

Outside of the pixel array, the chip periphery hosts additional logic elements, infrastructure and wire-bond pads to make connections for power supply and communication with the chip. Including the periphery, the ROC4SENS has a width of $7.8\,mm$ and a height of $9.8\,mm$. The ROC4SENS readout chips used in this work were produced on wafers with a thickness of $700\,\mu m$ and not thinned.

5.1.2. Readout Chain

The drift of charge carriers induces current pulses in the pixel electrodes of a silicon sensor. Over the bump bond connection, this pulse is transmitted to a pixel of the readout chip. The circuit diagram of a pixel of the ROC4SENS is shown in the top left corner of figure 5.2. A capacitor for test-pulse injection is close to the bump bond pad but not shown in this figure.
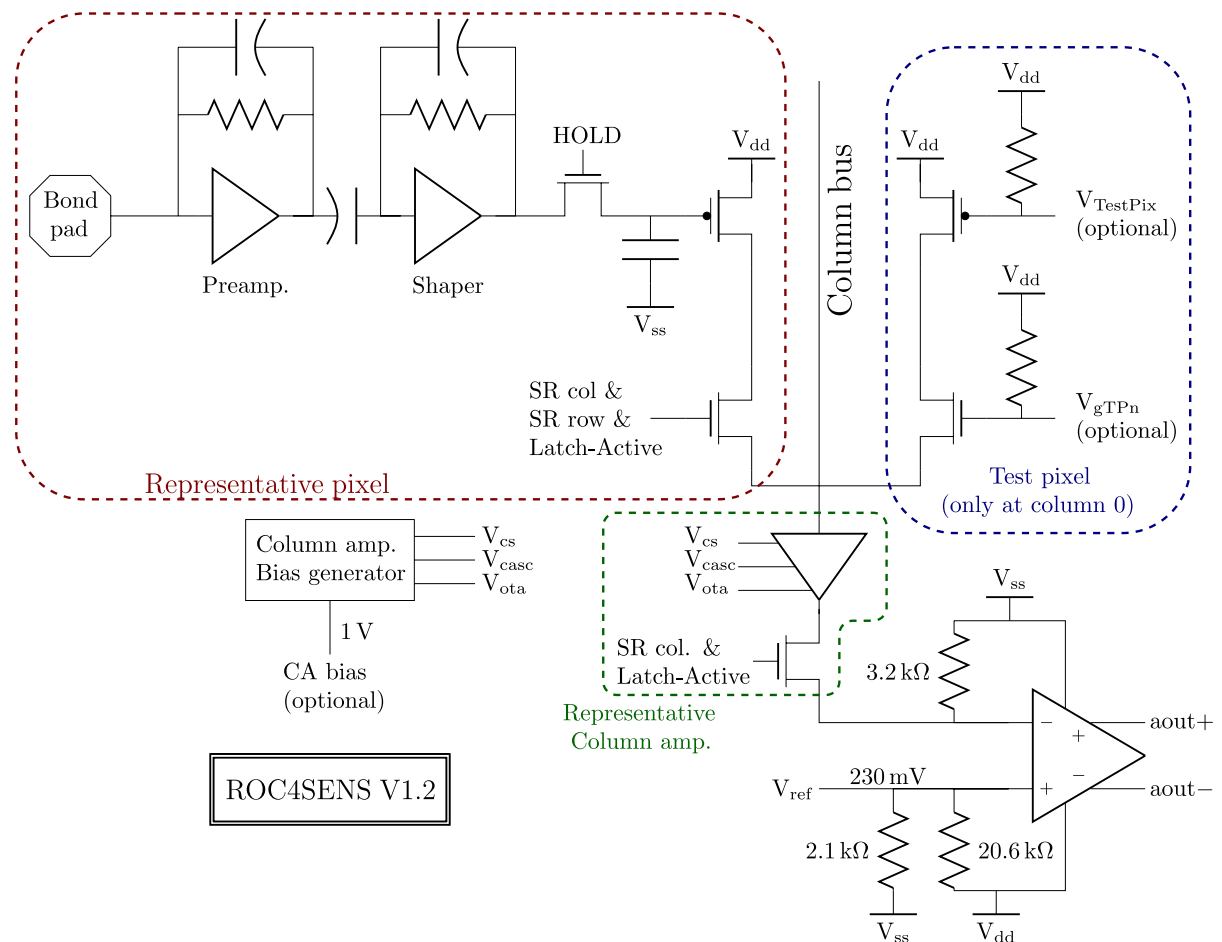
Figure 5.2.: Simplified circuit diagram of the ROC4SENS readout chain. The circuit within the dashed red line represents one of the 24 800 pixels. The circuit within the dashed green line represents the 155 columns. Taken from [114][1].

Each pixel has two integrating feedback amplifiers, named pre-amplifier and shaper. The rise and fall time of their output pulses are controlled via their respective feedback resistances. The resistances are in turn steered by setting the gate voltages on the corresponding transistors (PFETs) V_{gpr} and V_{gsh}, respectively. For pulses with negative polarity — as is the case for signals induced on the electrodes of n$^+$p-pixel sensors — decreasing V_{gpr} decreases the slope of the falling edge and decreasing V_{gsh} decreases the slope of the rising edge. This way the time to reach the peak of the signal, the peaking time, can be adjusted. Another way to change the peaking time is to change the analog power shared between the two feedback amplifiers via the analog voltage V_{ana}, where lower values yield a larger peaking time.

At the arrival of an external trigger signal, the HOLD switch is opened. This samples the output of the shaper by storing a corresponding charge on a capacitor. To read out the signal of a given pixel, it needs to be selected with the two shift registers SR col and SR row. If the respective pixel is selected, the stored charge is passed on to the column amplifier in the periphery upon arrival of the Latch-Active signal.

The column amplifiers resemble a critically damped harmonic oscillator and improve the readout speed of the ROC4SENS. A logic switch ensures that the column amplifier of the column selected by the column shift register is coupled to the positive input of the differential output amplifier of the ROC4SENS. The negative input of the output is connected to a constant voltage V_{ref} which can be used to tune the signal range.

The differential output signal of the ROC4SENS is digitized with 12 bit resolution on a Digital Test Board (DTB), further discussed in the next section 5.1.3. In total, the frame rate possible with this readout procedure is better than 1 kHz. In practice, the frame rate is limited to approximately 150 Hz due to the limitation of the USB2.0 connection between the DTB and the computer steering the data acquisition and storing data to disc.

5.1.3. Digital Test Board

The DTB is designed for data acquisition with readout chips and pixel modules for the CMS pixel detector in laboratory or beam tests. For obvious reasons, the ROC4SENS is designed such that it is compatible with the DTB [114]. Detailed descriptions of the hardware and software for the DTB can be found in [118][119]. The way it is used for the presented measurements is described in the following. A simplified block diagram is shown in figure 5.3.

---

[1]Note that ROC4SENS V1.1 is used for this work. Changes for V1.2 reduce the crosstalk between signal and clock and between output and selected row. Also the column amplifier was reworked. For details see change log in [114].
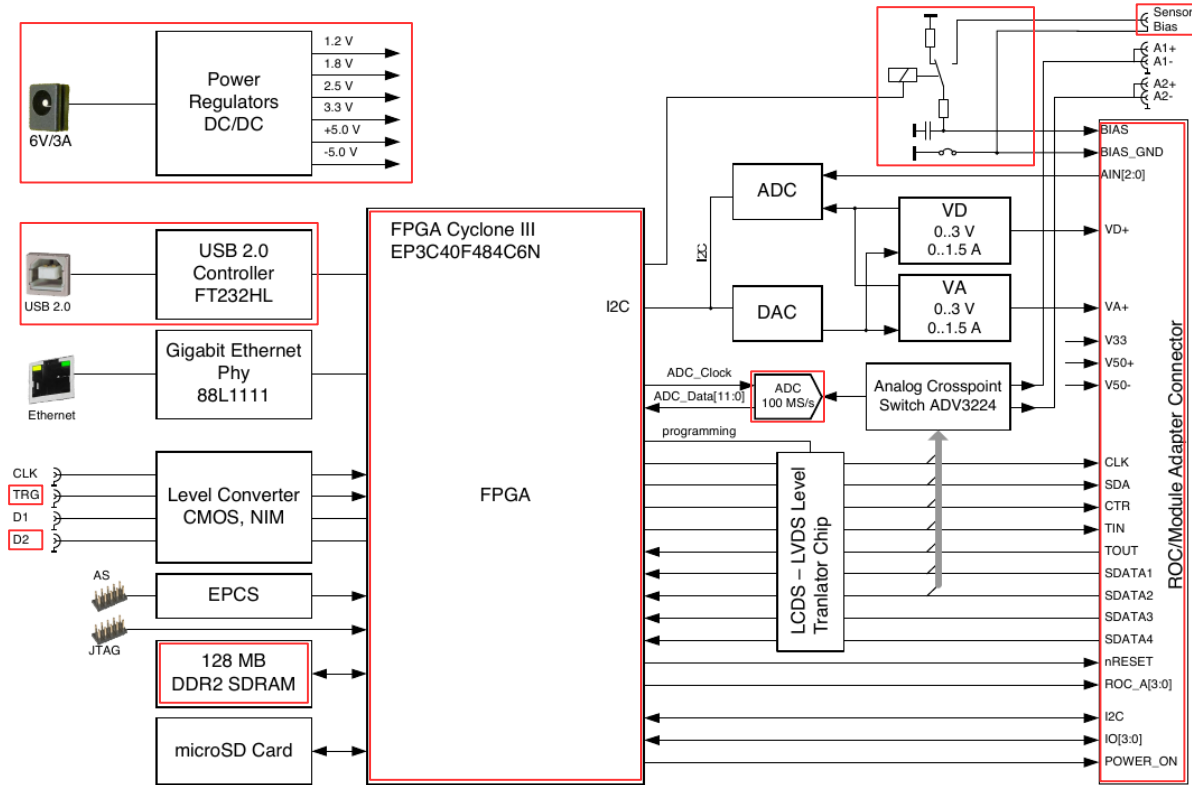
Figure 5.3.: Simplified block diagram of the Digital Test Board. Essential parts are highlighted in red and discussed in the text. Taken from [118].

The DTB is operated with custom-written software on a computer, sending commands to and receiving data from the DTB via USB2.0 connection. The Altera Cyclone III FPGA is the core of the DTB. It receives and executes the commands and from a computer to control the board and the connected readout chip.

The board is powered with $6\,\mathrm{V}$ at $3\,\mathrm{A}$ and features power regulators to supply the power levels needed for its subcomponents and the connected readout chip. For the operation of a ROC4SENS additional regulators are needed to provide the right power levels. Those are placed on a custom adapter card depicted in figure 5.4. The bias voltage for the silicon sensor V_{bias} needs to be provided via an additional LEMO connector and can be safely switched on and off with the DTB. For safety reasons, no bias voltage above $800\,\mathrm{V}$ is used. The current through the sensor is limited with a series resistance of $102\,\mathrm{k\Omega}$ on the DTB.

The DTB features additional LEMO connectors for input and output signals. One of them is to receive an external trigger signal with TTL level. The other one is to send out a busy signal, also with TTL level.

To pass the high voltage, steering signals and data between the ROC4SENS and the DTB, the ROC4SENS is glued and wire bonded to a custom Printed Circuit Board (PCB) as shown in figure 5.5. The PCB is inserted into a custom adapter card connected to the DTB via a ribbon cable and SCSI Type II connectors, depicted in figure 5.4.

For each trigger, the analog pulse height information of each pixel on the ROC4SENS

is digitized with 12 bit resolution on the DTB with an Analog to Digital Converter (ADC) operating at a sampling rate of 100 MHz. The sampling point of the ADC was optimized in order to limit the dependency between a signal and the preceding one. The sampled pulse height information for up to 200 trigger signals is stored on the DTB (128 MB of DDR2 RAM) before the data are sent to the computer. This procedure is faster than sending each event individually. On the computer, the data are further processed by the routine for online monitoring and data acquisition further treated in section 5.3.
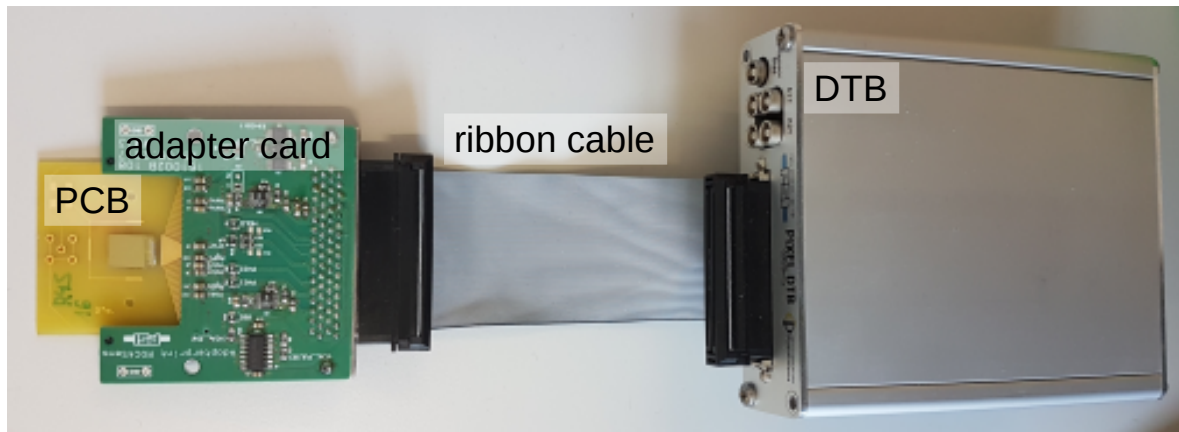
Figure 5.4.: ROC4SENS readout chip on a PCB similar to figure 5.5 connected to the DTB, via a custom adapter card and a ribbon cable. Taken from [114].
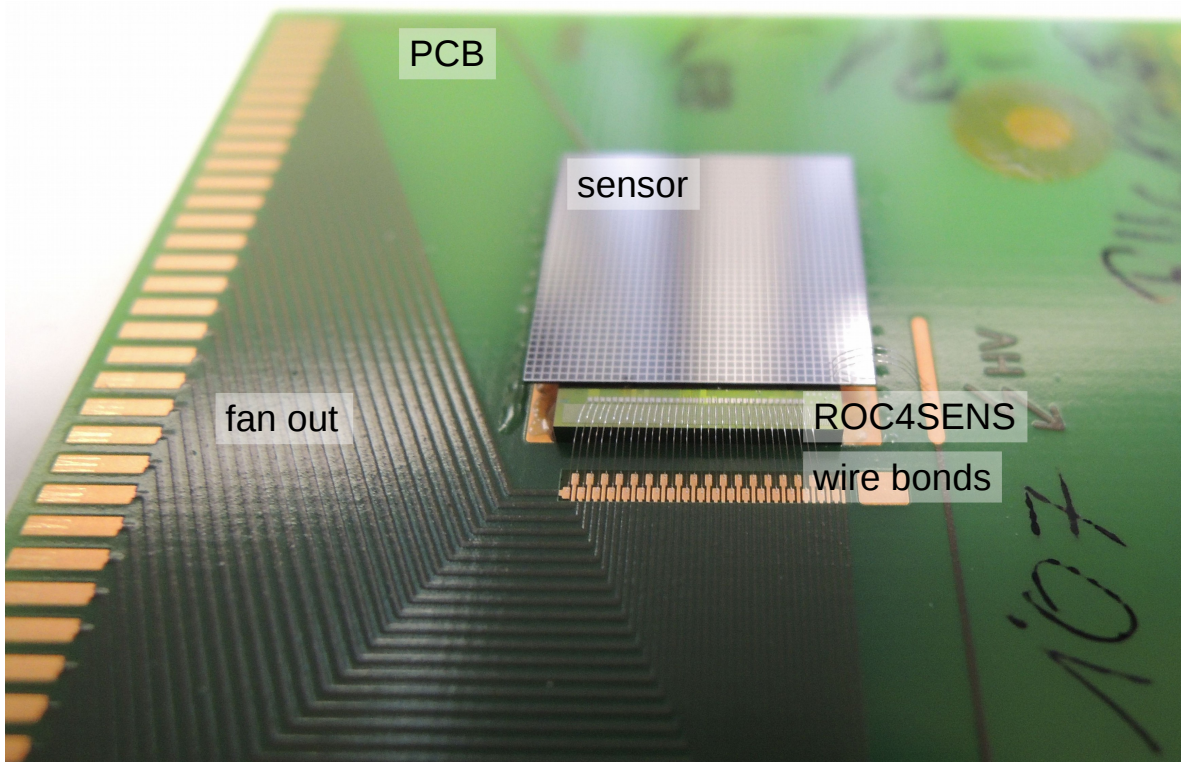
Figure 5.5.: ROC4SENS readout chip with a bump bonded pixel sensor on top. The ROC4SENS is glued and wire bonded to a custom PCB with fan out.

5.1.4. Calibration Procedures

Before a ROC4SENS readout chip can be used, the shape of the output pulse of the pixel pre-amplifiers and shapers (analog pulse shape) needs to be adjusted. Furthermore, the response of each pixel is measured as a function of the input-signal amplitude, which is crucial to account for the gain variations between the pixels. Both procedures make use of test-pulse injections to the pixels and are described in the following.

It has to be noted that also an absolute charge calibration of the readout chip in terms of electrons would be desirable. Typically this is done by using the characteristic X-ray fluorescence lines of metals [89]. Unfortunately, this is challenging with the ROC4SENS, since it requires an external trigger signal which is in general not provided by setups with an X-ray tube. X-rays in the required energy range either pass the silicon sensor without interaction or are fully absorbed, preventing the usage of trigger scintillators. Instead, for the non-irradiated sensors, the absolute charge is calibrated to have its MPV at 11 ke, expected for a Minimum-Ionizing Particle (MIP) in 150 µm of silicon as discussed in section 2.2. Details on the absolute calibration are treated in 6.3.1.

Pulse Shape Adjustment

After the arrival of an external trigger signal, the HOLD switch, see figure 5.2, is opened and the output of the shapers in the pixel cells is stored on a capacitor. Hence, the output pulse of the shapers is effectively sampled at a given point in time. To optimize the signal-to-noise ratio this needs to happen at the maximum of the output pulse. The trigger delay is defined as the time between the passage of a particle and moment when the signal is sampled. The shortest trigger delay obtained with the used setup, further discussed in 5.2.2, is around 250 ns. Thus, the output pulse of the pre-amplifiers and shapers needs to reach its maximum at this point in time or later. This is achieved by adjustment of the analog current I_{ana} via the analog voltage V_{ana} and the feedback of the pre-amplifiers and shapers regulated via V_{gpr} and V_{gsh}, respectively.

For measurements of the analog pulse shape, a test pulse is injected into an individual pixel cell. With a certain delay (hold delay) with respect to the test-pulse injection, the hold switch is opened, sampling the analog pulse. By scanning the hold delay, the analog pulse shape can be measured for each pixel. The decision for the settings for test-beam operation is based on the average analog pulse shape of all pixels. To account for the variations between individual readout chips and the measurements conditions (especially temperature), this adjustment is repeated prior to any set of measurements on a given module.

In figure 5.6 the analog pulse shape, averaged over all pixels, is shown for several readout chips and settings, before and after irradiation. More details on the used settings are summarized in table 5.1, where V_{cal} denotes the amplitude of the test pulse. For the recommended value of I_{ana}, between 120 mA and 125 mA, the peak of the analog pulse
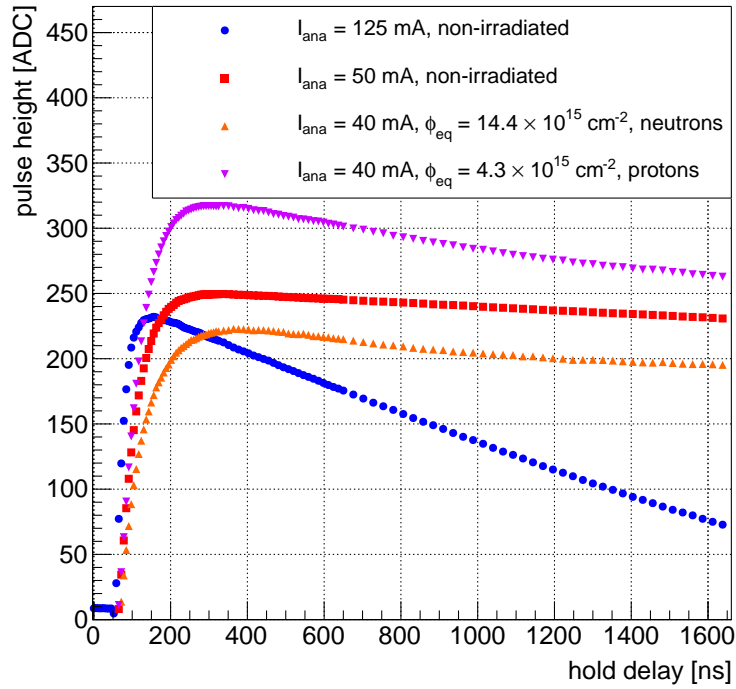
Figure 5.6.: Measurements of the analog pulse shape averaged over all the pixel cells of the ROC4SENS readout chip. The pulse height is pedestal corrected and given in units of ADC counts. The measurements were taken with test pulses of different amplitudes V_{cal} and scaled to an amplitude of $300\,\mathrm{mV}$ for better comparability. More details on the used settings are given in table 5.1.

is at approximately $150\,\mathrm{ns}$ which is too early compared to the trigger delay. Instead, I_{ana} between $40\,\mathrm{mA}$ and $50\,\mathrm{mA}$ is used and yields peaking of the analog pulse at $250\,\mathrm{ns}$ even after proton and neutron irradiation to the highest fluences. For all the presented measurements, the relative deviation of the pulse amplitude at $250\,\mathrm{ns}$ from the respective maximum of the pulse is below $5\,\%$, while it is usually much less for the setting with a lower analog current.

Table 5.1.: Details on the irradiation state of the readout chips and the settings used for the measurements of the analog pulse shape shown in figure 5.6.

chip no.	$I_{ana}[\mathrm{mA}]$	$V_{gpr}[\mathrm{mV}]$	$V_{gsh}[\mathrm{mV}]$	$V_{cal}[\mathrm{mV}]$	$V_{bias}[\mathrm{V}]$	$\phi_{eq}[10 \times 10^{15}\,\mathrm{cm}^{-2}]$
144	125	900	670	300	120	0
144	50	900	670	300	120	0
197	40	700	570	250	800	14.4, neutrons
174	40	700	600	400	200	4.3, protons

It has to be mentioned that the biggest effect of the irradiation on the readout chip performance is due to the increased leakage current in the connected silicon sensor. As discussed in section 3.3.5 of [114], the leakage current alters the analog pulse shape and

it is suggested to keep the leakage current below $1\,\mathrm{nA}$ per pixel corresponding to $25\,\mathrm{\mu A}$ for the entire sensor. For the measurements presented here is assured by cooling of the sensor.

Gain Equalization

Once the analog pulse shape is tuned to reach its maximum around $250\,\mathrm{ns}$, the hold delay in return is set to $250\,\mathrm{ns}$. Now, the amplitude of the test pulse V_{cal} is scanned between $0\,\mathrm{mV}$ and $2400\,\mathrm{mV}$ and the response of each pixel is measured individually. The result of such a single pixel measurement is shown in figure 5.7 for readout chip no. 144 at $I_{ana} = 50\,\mathrm{mA}$ (see table 5.1). The saturation of the curve for V_{cal} values above $800\,\mathrm{mV}$ is due to the saturation of the amplifiers. The curve is fitted with a logistic function of the form

$$f(V_{cal}) = \frac{a}{(1 + \exp(-\frac{V_{cal}-x_0}{w}))} + c, \tag{5.1}$$

where a, c, x_0 and w are the free parameters of the fit. The fit range excludes the first two points, because the pulse height shows no response to the calibration pulse for such low values of V_{cal}, and ends at $V_{cal} = 800\,\mathrm{mV}$. The fit parameters are stored for each pixel. The function f is inverted and shifted, such that

$$g(ph) = f^{-1}(ph) - f^{-1}(0), \tag{5.2}$$

where ph denotes the pulse height. Thereby, the missing response for low values of V_{cal} is taken into account and $g(0) = 0$ is assured. Now, the function g is used to correct for non-linearities and pixel to pixel gain variations.

5.2. Test-Beam Setup

The general idea of test-beam measurements is to test detector components in an environment close to their foreseen application in a high-energy physics experiment. Particle type and momentum as well as time structure and intensity of the beam have to be chosen to suit the needs of the intended tests. For tracking detector components the beam momentum is usually chosen to be close to the minimum of the particles ionizing energy loss to study the performance for the smallest possible signal or at the highest available energy to reduce effects of multiple Coulomb scattering. Depending on the intended tests additional equipment like scintillators, beam telescopes or magnets are needed to provide trigger signals, reference tracks or magnetic fields.
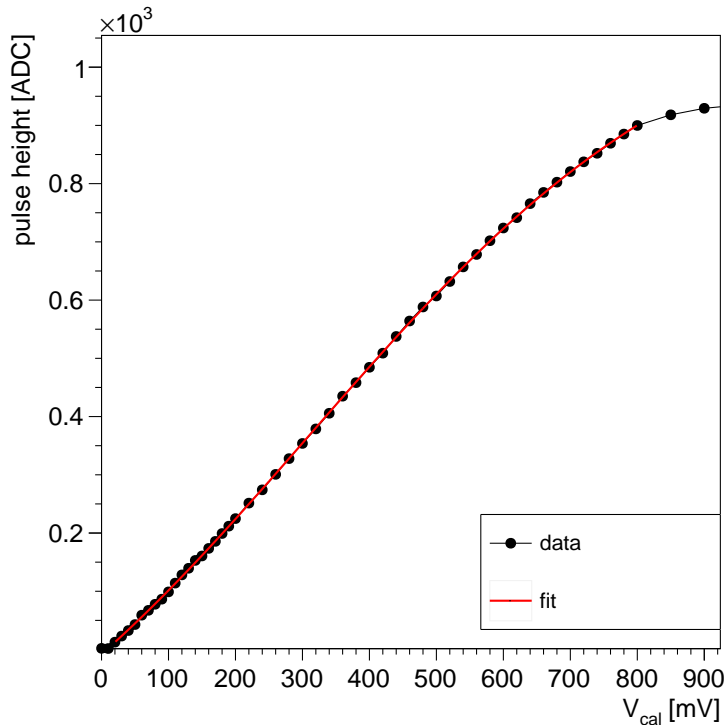
Figure 5.7.: Measurement of the response of a single pixel in a ROC4SENS readout chip as a function of the test-pulse amplitude V_{cal}. The pulse height is pedestal corrected and given in units of ADC counts. The data are fitted with a logistic function 5.1, excluding the first two points, up to $V_{cal} = 800 \, \text{mV}$.

The test-beam measurements described in this work were taken at Beam line 21 (TB21) of the DESY II synchrotron (DESY II). An overview of the beam line, infrastructure and software is given in the following. In addition, the special features of the setup for measurements with the ROC4SENS readout chip are discussed.

5.2.1. DESY II Test-Beam Facility

The heart of the DESY II test-beam facility is the successor of the synchrotron giving name to the research institute Deutsches Elektronen-SYnchrotron (DESY), DESY II. The synchrotron has a radius of 46.6 m and a circumference of 292.8 m. It accelerates positrons or electrons for PETRA III and three test-beam areas TB21, TB22 and TB24. A detailed description of the DESY II Test Beam Facility is given in [120], while this section aims to summarize the aspects essential to this work with focus on the EUDET-type Pixel Beam Telescope DATURA.

Beam Line

Pre-accelerated electron or positron bunches with momenta of 0.45 GeV/c are injected into DESY II and further accelerated to momenta of 6.3 GeV/c (even 7 GeV/c). Usually, an electron bunch is used for two acceleration cycles before it is dumped after a total of

160 ms in the synchrotron.

The generation of a test beam from these electron bunches is shown in figure 5.8 on the example of beam line 21. It starts with the conversion of the electrons or positrons into photons via bremsstrahlung. Therefore a carbon wire with a thickness of 7 µm can be moved into the DESY II beam orbit. The thin wires ensure that the bunch steadily loses intensity producing photons at a rate of $\approx 1.02\,\text{MHz}$, since one rotation in the cyclotron takes $\approx 0.98\,\text{µs}$. The photons leave the vacuum, tangential to the beam orbit, through an aluminum window. A secondary target converts the photons into electron-positron pairs, just before another vacuum line starts. The secondary targets are made of aluminum or copper. Different target thicknesses between 1 mm and 5 mm are available. For the presented measurements the 5 mm copper target was chosen to optimize the electron rate. A magnet with a maximum field of 1.38 T spreads the beam according to momentum and charge of the incoming particles. The current through the magnet can be adjusted such that the primary collimator, tungsten with a thickness of 100 mm, selects electrons or positrons with an average momentum between $1\,\text{GeV/c}$ and $6\,\text{GeV/c}$.
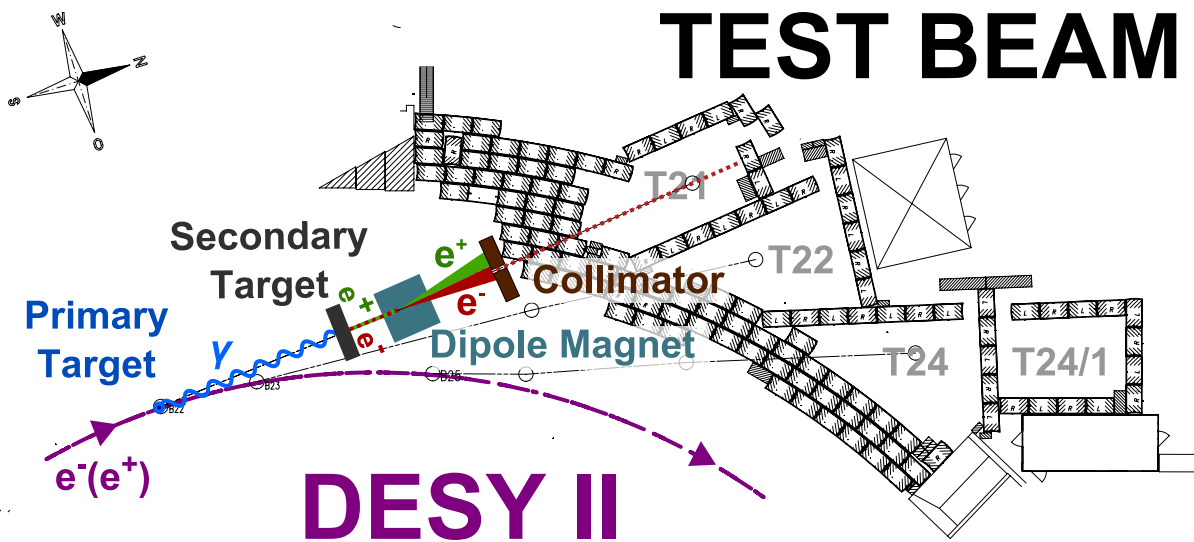
Figure 5.8.: Beam line 21 for test-beam generation at DESY II. Taken from [120].

The test-beam measurements are performed in the so-called test-beam areas. An additional, secondary collimator inside the test-beam area is the last element of the beam line outside of the beam vacuum. Secondary collimator with different sized openings between $5 \times 5\,\text{mm}^2$ and $20 \times 20\,\text{mm}^2$ are available and define the final shape of the beam. The momentum spread of the beam depends on the width of the primary and secondary collimator but is typically around $0.16\,\text{GeV/c}$. Inside the test-beam area, the beam is used for the intended experiments penetrating e.g. scintillators, several planes of the beam telescope and the tested detector components before it is stopped in a combination of lead blocks and a concrete wall.

A beam shutter, coupled to an interlock system, can stop the beam to allow for safe access to the test-beam area for human interaction. A spill counter inside the synchrotron

and a beam monitor in front of the secondary collimator provides information about the operational state of the accelerator and particle rate inside the test-beam area.

Beam Telescope

A beam telescope is one of the key elements to investigate the spatial resolution of modules for tracking detectors in high-energy physics since it provides the measurements needed for tracking the incoming particles. The hit resolutions of the modules are on the order of several µm, thus the track resolution of the beam telescope needs to be comparable or better. The DATURA beam telescope, provided at TB21, is an EUDET-type pixel beam telescope consisting of 6 individual planes, where each plane is a MIMOSA 26 sensor. A detailed description and performance study of the beam telescope can be found in [121], a summary is given here.

The MIMOSA 26 [122] sensor is a monolithic active pixel sensor produced in an AMS 350 nm CMOS process with a pixel size of $18.4 \times 18.4\,\mu m^2$. The pixels are arranged in an array of 1152 columns and 576 rows covering an area of $21.2 \times 10.6\,mm^2$. The average physical thickness is $54.5 \pm 3.6\,\mu m$. The sensors are read out with an integration time of 115.2 µs with the rolling-shutter method and provide binary hit information per pixel. The intrinsic hit resolution of a single plane is $3.24 \pm 0.9\,\mu m$ for normal particle incidence at a threshold of 6 times the pixel noise. Each of the six MIMOSA 26 sensors is mounted on an aluminum frame, as shown in figure 5.13, and covered with light tight, 50 µm thick Kapton foil. Thus the material budget of one telescope plane ϵ_{M26} sums up to 0.00076 (in units of the radiation length X_0), where the radiation length and densities are taken from [23]. The aluminum frames are water-cooled to typically 18 °C. Usually, the telescope is used such that three planes form a triplet, illustrated in figure 5.9. One triplet is placed upstream, one downstream with respect to the position of the investigated detector module, also called Device Under Test (DUT). The spacing dz of the planes can be no smaller than 20 mm, due to the thickness of the aluminum frames, and no larger than 150 mm at equidistant spacing, as the rail on which a triplet is mounted, is 300 mm long. For the presented measurements, the distance between the closest plane and the DUT dz_{DUT} is typically around 40 mm or larger, due to mechanical constraints. The minimal material budget is given by the summed thickness of sensor and readout chip, which is approximately 850 µm or 900 µm. The former corresponds to a material budget ϵ_{DUT} of 0.0091, again using [23].

As demonstrated in figure 5.10 the track resolution of the beam telescope at the position of the DUT depends on dz, dz_{DUT} and ϵ_{DUT}. Even for the minimal values of dz_{DUT} and ϵ_{DUT} given above, the track resolution for $dz = 150\,mm$ is better compared to $dz = 20\,mm$, thus the large telescope spacing is used in the following. The track resolution also depends on the particle momentum, which is chosen to be close to 5 GeV/c as a compromise between particle rate and track resolution. For the selected spacing and conditions, the

track resolution of the telescope at the position of the DUT is on the order of $3\,\mu m$.
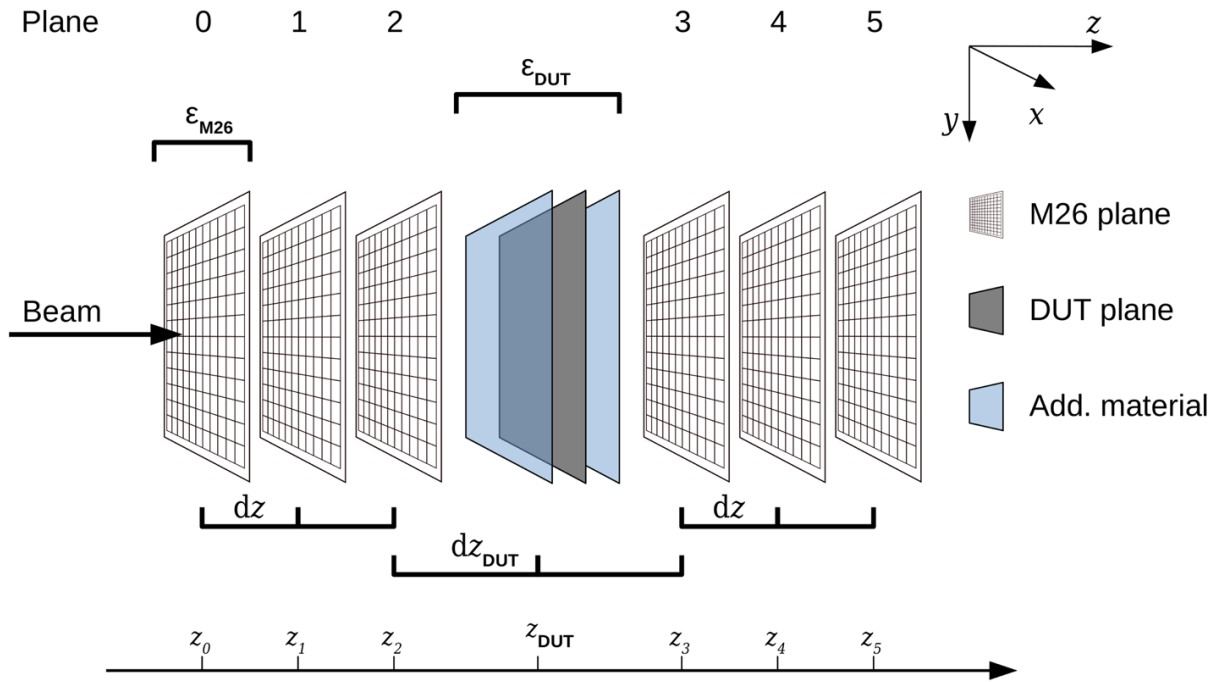
Figure 5.9.: Typical setup for test-beam measurements with the DATURA beam telescope. The telescope planes have equal spacing dz, while dz_{DUT} denotes the distance between the closest telescope plane and the DUT. The material budget of a MIMOSA 26 plane and the DUT are indicated as ϵ_{M26} and ϵ_{DUT} respectively. Taken from [121].

(a)

(b)
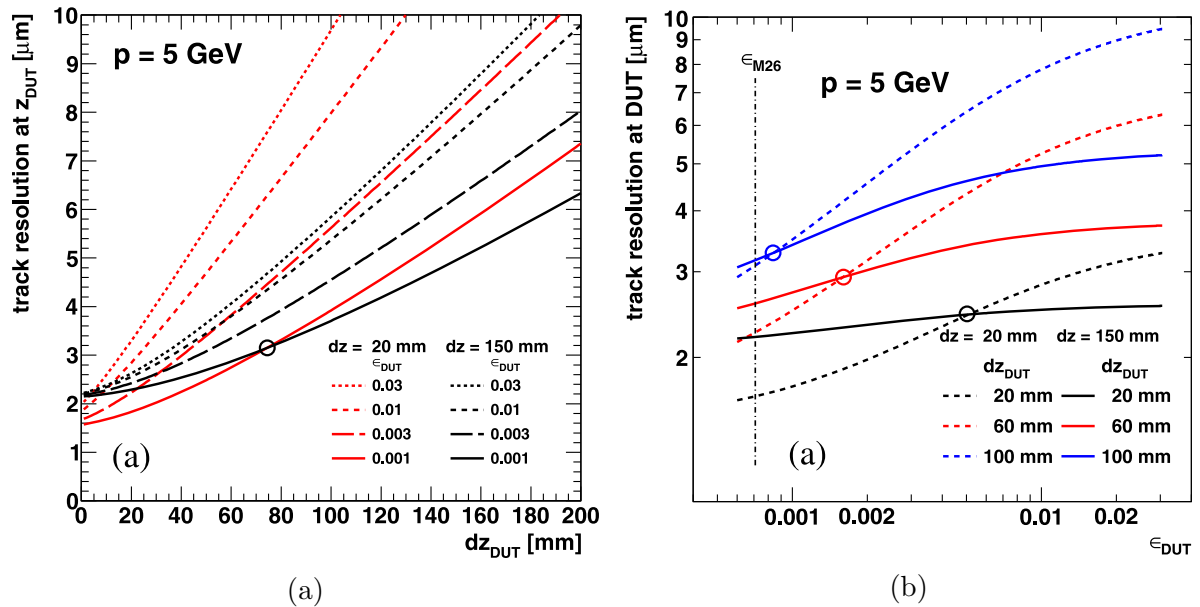
Figure 5.10.: Track resolution of the DATURA beam telescope at the position of the DUT for different spacing dz of the beam telescope triplets. Predicted using the General Broken Lines formalism, as a function of the position (a) and the material budget of the DUT (b). Taken from [121].

5. Materials and Methods for Beam Tests of Pixel Sensors

Additional Infrastructure

On top of the particle beam and the beam telescope, additional infrastructure is needed to perform studies on modules for tracking detectors in high-energy physics experiments.

To start the readout sequence once an "interesting" event happened, many detector components require a trigger signal. The definition of interesting depends on the experiment. For the presented measurements it is sufficient to have a particle passing within a certain window of acceptance, such that it passes the active area of the DUT. To provide a trigger signal, four scintillators, each with an acceptance of $10 \times 20\,\mathrm{mm}^2$, are coupled to PhotoMultiplier Tubes (PMTs) via light guides.

The output signals of the PMTs are fed into a Trigger Logic Unit (TLU), which is another important piece of test-beam infrastructure. The TLU provides the supply voltage for the PMTs, discriminates the PMT signals, and applies a configurable AND or OR logic to up to four PMT signals to issue a trigger. The trigger signal is provided with NIM or TTL level on LEMO RJ45 ports.

Another key aspect of the TLU is the so-called handshake mechanism. The basic idea is to prevent the TLU from sending trigger signals while one detector component is still in the readout sequence of a previous trigger. Therefore the TLU accepts a so-called busy signal from each detector component. These busy signals are used to veto further trigger signals until all detectors finished their readout sequence. Further information on the TLU and the handshake mechanism can be found in [123]. In addition, two linear stages and a rotation stage are available to steer the position and inclination of the DUT with precision of $0.1\,\mathrm{\mu m}$ and $50\,\mathrm{\mu rad}$ respectively [124]. The linear stages are primarily used to center the DUT with respect to the beam axis. The rotation stage is used to rotate the DUT with respect to the beam axis, in order to study DUT properties as a function of the particles' incidence angle.

Further information on the test-beam infrastructure can be found online [124].

Software

Another important aspect of test-beam measurements is the software framework for the data acquisition with the beam telescope and other detector components. The software framework EUDAQ [121][125] is native to the EUDET-type beam telescopes but allows for the integration of other devices. For the presented measurements EUDAQ is used to steer and read out the beam telescope and the time reference plane which is further discussed in section 5.2.2. In contrast, the investigated detector module is operated with its own software framework described in section 5.3.

The integration of a detector in the EUDAQ framework requires a producer as interface between the detector's data acquisition and the EUDAQ Run Control. It receives commands from the Run Control and sends data to the Data Collector which combines data from all detectors and writes them to disk. The EUDAQ Run Control is a user

interface and provides the possibility to configure the detectors and start and end the data acquisition. EUDAQ also provides online monitoring and collects log messages from all integrated detectors for data quality control.

5.2.2. Setup for Measurements with ROC4SENS

The setup for test-beam measurements with the ROC4SENS readout chip is adapted to the beam line and infrastructure at the DESY II test-beam facility — especially the beam telescope — covered in the previous section 5.2.1. For the presented measurements electrons with a momentum close to $5\,\text{GeV/c}$ are selected with the primary collimator. The electrons enter the test-beam area of TB21 and pass the detectors, set up as sketched in figure 5.11.
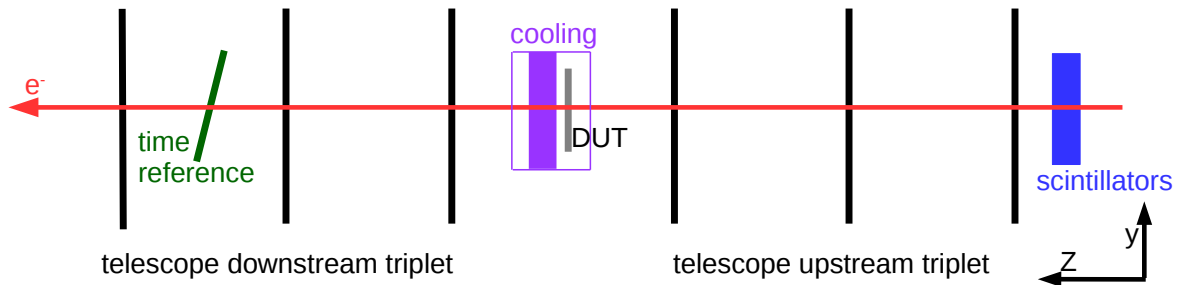
Figure 5.11.: Detector arrangement used for the test-beam measurements.

The trigger scintillators are placed upstream of the setup, the direction facing the beam. The six MIMOSA 26 sensors of the beam telescope are grouped in an upstream and a downstream triplet. The triplets are placed upstream and downstream of the investigated module, labeled DUT. Due to the long integration time of $155\,\text{µs}$ for the MIMOSA 26 planes, tracks in-time with the readout cycle of the DUT are selected with a CMS Phase-1 pixel module [81], serving as time reference plane. The time reference plane is placed between the fourth and the fifth plane of the beam telescope (counting from zero). It is inclined by $\theta_x \approx 19°$ and $\theta_y \approx 28°$, were θ_x and θ_y correspond to a rotation around the x- and y-axis respectively, to improve the spatial resolution. Additional information on the used CMS Phase-1 pixel modules is given at the end of this section.

In figure 5.12, a simplified block diagram of the setup displays how the detectors are integrated into a system of devices and how these devices steer/influence each other. A photo of the detector setup is shown in figure 5.13. In the block diagram, the devices are grouped into types according to functionality. Some operation conditions are to be kept constant for an entire run or even sets of runs, referred to as environmental control parameters. For simplicity, the group of environmental control devices controlling these parameters is shown only for the DUT. The DUT requires cooling to limit the leakage current for highly irradiated modules which in return demands thermal isolation as well as a flow of dry air to prevent condensation on critical electrical components. To characterize
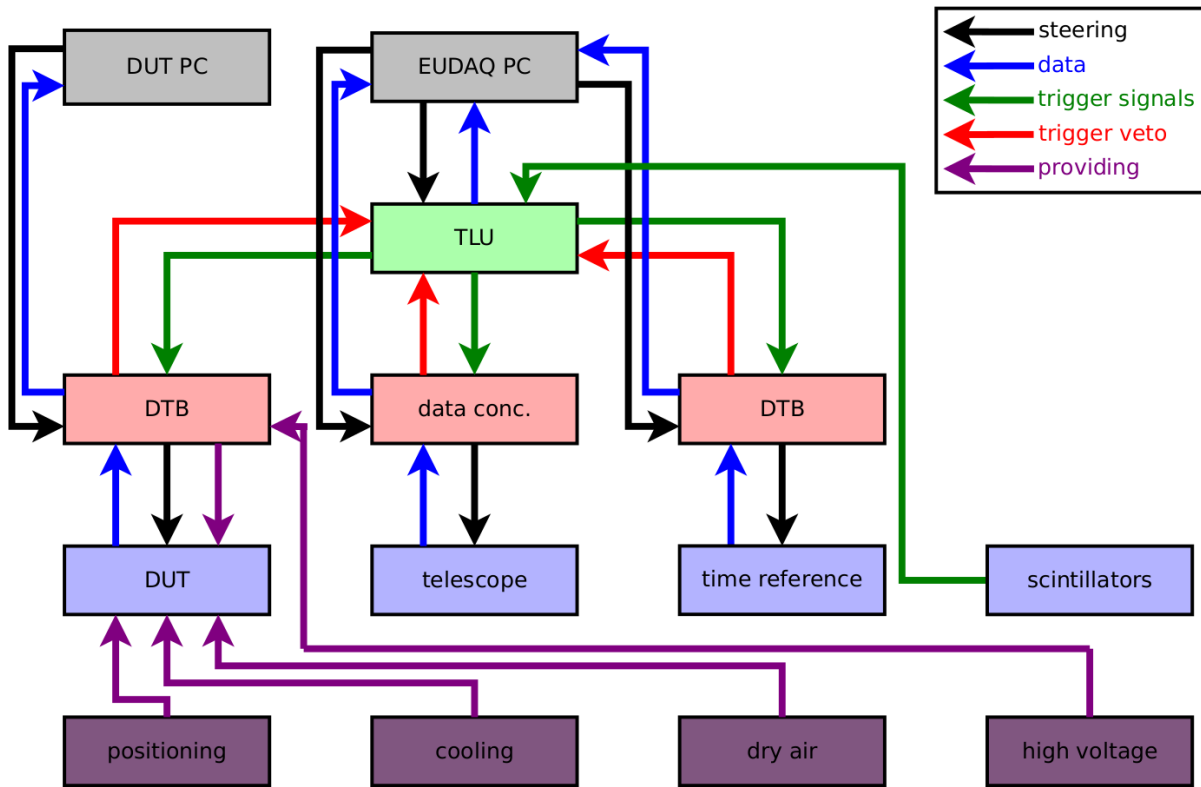
Figure 5.12.: Simplified block diagram of the test-beam setup. The blocks represent physical devices, colored according to their type. The types are PCs (gray), trigger level (green), data acquisition (light red), detector (light blue) and environmental control (purple). The arrows indicate the flow of signals or influence.

the DUT as a function of the particle's incidence angle and the bias voltage applied to the silicon sensor, the position and high voltage need to be adjustable.

Once the environmental control parameters are set to the desired values, human interaction in the test-beam area is finished and the beam interlock is set, a run is started by starting the data acquisition software on the DUT PC and the EUDAQ PC. The former steers and reads out the DUT via its DTB as discussed in 5.1.3. The latter runs EUDAQ, see section 5.2.1, which steers and reads out the six MIMOSA 26 planes, the TLU and the time reference plane. Note that the actual data-acquisition and steering programs for telescope and TLU run on an additional computer connected to the EUDAQ PC, which is not shown in figure 5.12.

For each passing electron, The trigger signal from the scintillators is passed to the TLU. Operated in handshake mode, the TLU transfers the trigger signal to the data-acquisition devices respecting their busy signals, as discussed in 5.2.1. The data-acquisition devices initiate the readout sequence of the corresponding detectors and transmit the data to the computers.

As the run start in EUDAQ starts the TLU, the DUT receives no triggers as long as the run is not started in EUDAQ. Thus, the data acquisition of the DUT is started first. This way, the event numbers in the data files on the DUT PC and the EUDAQ PC are

synchronized for a given run. In the following, the trigger line, the setup for environmental control and the time reference plane are discussed in more detail.
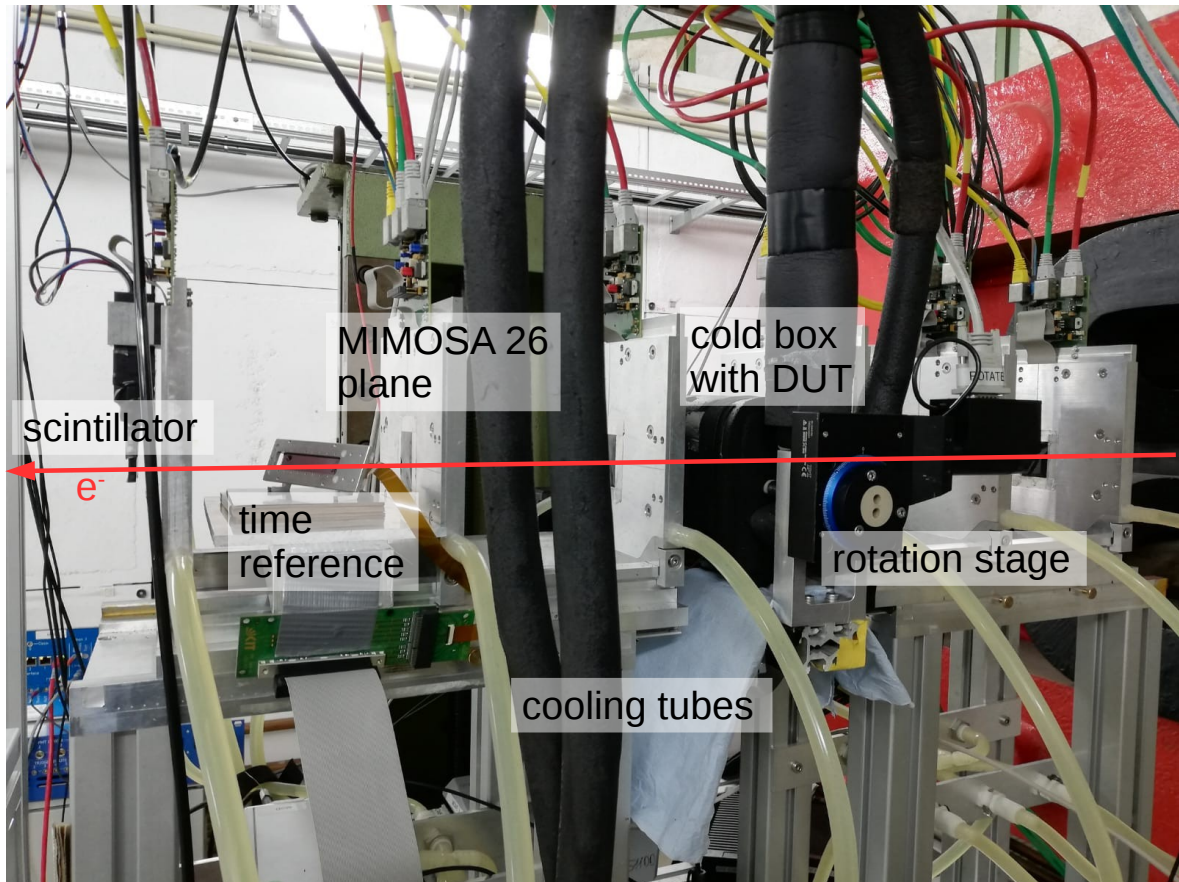
Figure 5.13.: Photo of the test-beam setup at TB21. The aluminum frame and the entrance window (black Kapton foil) of the MIMOSA 26 planes can be seen. The label scintillator is actually not in use, the used ones are hidden behind the MIMOSA 26 plane on the right.

Trigger Line

Initially the trigger signal is generated by assemblies of scintillators and PMTs as discussed in section 5.2.1. To define an acceptance window of $10 \times 10\,\mathrm{mm}^2$ — slightly bigger than the active region of the ROC4SENS — two trigger scintillators in a cross configuration are placed upstream of the beam telescope. The output signals of the two PMTs are passed to the TLU. The TLU is configured to send out a trigger on a coincidence of the two scintillator signals (respecting the handshake condition).

The trigger signal sent for the DUT and the time reference plane is chosen to be a NIM level signal. A NIM module is used to discriminate the trigger signal issued by the TLU to suppress occasional double pulses by choosing a sufficiently long gate. The discriminated signal is converted to TTL standard, split using a fan out and passed to the two DTBs for the DUT and the time reference plane. To optimize the efficiency of the time reference plane, its trigger signal needs an additional delay of several ns.

The internal delays of the electronic devices on the trigger line cumulate to about 112 ns. However, delay scans, performed by inserting additional cable delays to the trigger line, have shown that the actual delay corresponds to approximately 250 ns. Therefore the pulse analog pulse shape of the single pixels in the ROC4SENS is tuned to peak around the latter value.

Environmental Control

Environmental control parameters are to be kept constant for an entire run or even sets of runs. The essential environmental control parameters are temperature and position of the DUT and the bias voltage applied to the silicon sensor.
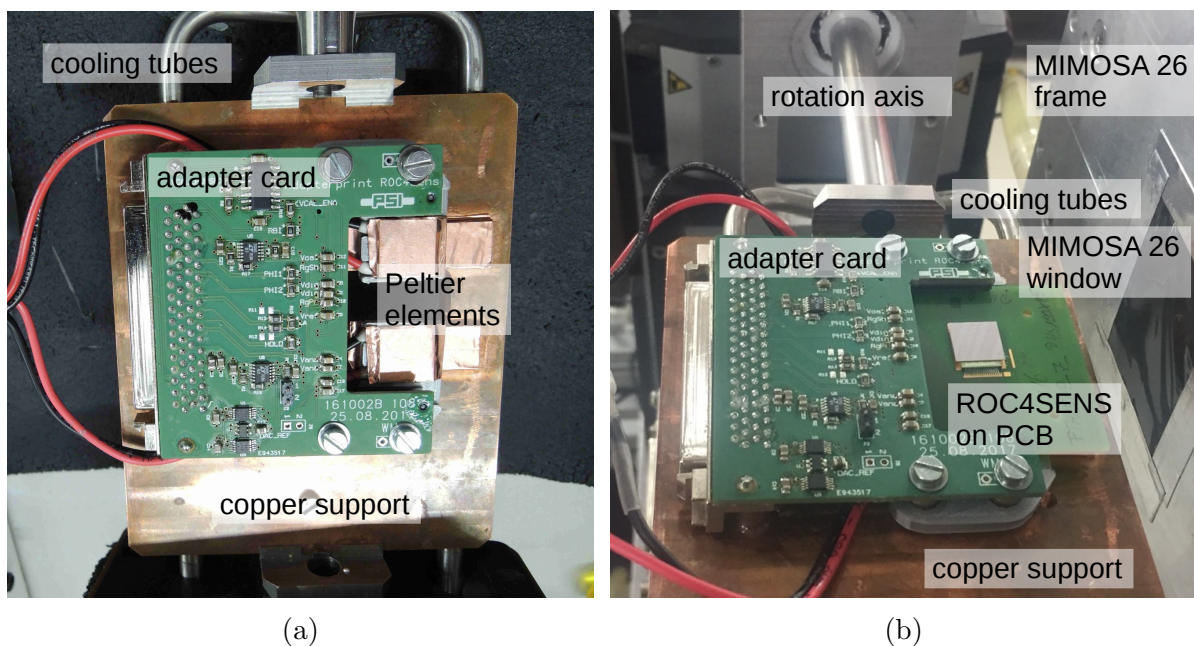
Figure 5.14.: Adapter card for the ROC4SENS mounted on the cooled copper support structure without (a) and with (b) ROC4SENS on a PCB. The Peltier elements in (a) are covered with copper-coated tape for better heat conductivity. In (b) the assembly is mounted on the positioning stage inside the beam telescope but rotated by approximately 90° for better visibility.

A two-stage cooling system is used to keep the leakage current through irradiated sensors below the limit of 25 µA motivated in section 5.1.4. The first stage is an ethanol chiller operated at a set point between $-20\,°C$ and $-26\,°C$ cooling a copper support structure. The second stage are two Peltier Elements operated with 5 W to 7 W in direct contact with the PCB holding the DUT as shown in figure 5.14. The temperature on the DUT is not directly measured. From measurements with a thermistor, directly attached to one of the modules, the temperature is estimated to be around $-24\,°C$. For thermal isolation and to prevent condensation the copper support structure is placed in a plastic box, referred to as cold box, wrapped with ArmaFlex insulation and flushed with dry air. To limit the amount of material in the beam, the plastic box features openings and is not used for

non-irradiated samples.

The position of the investigated module needs to be within the acceptance window $(10 \times 10 \, \text{mm}^2)$ defined by the trigger scintillators to take advantage of the provided particle rate. The two linear stages introduced in section 5.2.1 are mounted such that the DUT can be moved in the x- and y-direction (see figure 5.11). Sub-millimeter precision on the placement is achieved by online adjustments employing the pulse-height weighted hit maps introduced in 5.3.3.

An ISEG SHQ high-voltage power supply provides the high voltage for the pixel sensor. The power supply is placed inside the counting room (where people sit to run the test-beam experiment) to allow for changes of the bias voltage without human intervention inside the beam area. The bias current is monitored and noted for every run to make sure it stays below $25 \, \mu\text{A}$ for the entire sensor. At $25 \, \mu\text{A}$ the voltage over the resistance of $102 \, \text{k}\Omega$, introduced in section 5.1.3, is $2.55 \, \text{V}$ and neglected in comparison to the applied bias voltages of up to $800 \, \text{V}$.

Time Reference Plane

Several particles might pass the setup within the $155 \, \mu\text{s}$ integration time of the MIMOSA-26 readout chips. The time reference plane is needed to select the subset of corresponding telescope tracks which are in-time with the readout cycle of the DUT.

A CMS Phase-1 pixel module [81], as used in layer 3 and 4 of the barrel pixel detector, serves as time reference plane. The silicon sensor has a thickness of $285 \, \mu\text{m}$ and the pixels have a size of $100 \times 150 \, \mu\text{m}^2$. The sensor is read out by a PSI46digv2.1-respin readout chip with 52×80 pixels. The module consists of 2×8 readout chips and the gaps between the individual readout chips are covered by pixels of doubled pitch. It is operated at a bias voltage of $150 \, \text{V}$, whereas the full depletion voltage is $70 \, \text{V}$. Charges above a threshold of $1500 \, \text{e}^-$ are digitized with 8 bit resolution. The obtained position resolutions are about $9 \, \mu\text{m}$ and $6 \, \mu\text{m}$ in the x- and y-direction, respectively. The efficiency is about $85 \, \%$, as the internal $40 \, \text{MHz}$ clock is asynchronous with respect to the DESY bunch.

5.3. Data Acquisition and Online Monitoring

As an introductory work to the subject of this thesis a routine for data acquisition and online monitoring, to be used in test-beam measurements with the ROC4SENS readout chip, was developed.

For each event, the digitized response of the 24,800 pixels is recorded and sent from the DTB to the PC. Storing it for all those pixels would require a large amount of storage. Thus responses indicating a particle hit are identified and stored together with the position of the corresponding pixels. In addition, response and position of a group of neighboring pixels are stored as well. This way the amount of stored data is reduced drastically while

the key feature of the ROC4SENS — it has no zero suppression — is used to full capacity. Within this data-acquisition routine, a set of observables is derived from the acquired data and displayed during data taking to allow for a first assessment of the data quality.

The routine complements the efforts of Dr. Aliakbar Ebrahimi and Dr. Daniel Pitzl to enable test-beam measurements with the ROC4SENS. It is integrated into the ROC4SENS client software from Dr. Beat Meier (PSI) written in C++. The client software establishes communication between a PC and a DTB via USB2.0 as an interface to the ROC4SENS itself.

5.3.1. Hit Identification

Before pixel responses indicating a particle hit can be identified, a series of corrections is applied to the incoming data. In total, the procedure for the identification of hits contains the following steps:

1. The pedestal is calculated.

2. The pixel response is corrected for the pedestal.

3. Baseline oscillations are corrected for.

4. The significance of the response is calculated.

5. A threshold cut is applied.

All details are given in the paragraphs hereafter.

As discussed in section 5.1.3, the analog signal of each pixel sent from the ROC4SENS is digitized with 12 bit resolution in an ADC on the DTB and sent to the computer in blocks of a programmable number of events. For the presented measurements this is set to 200 events per block. The first step towards hit identification is a baseline correction, also referred to as pedestal correction, to shift the average pixel response in absence of a particle interaction to 0. The raw response is denoted as RAW and the pedestal as PED. Using the first N_{PED} events (typically 200), the initial pedestal is calculated as the average response of a pixel

$$PED_{ijN_{PED}} = \sum_{n=0}^{N_{PED}-1} \frac{RAW_{ijn}}{N_{PED}}, \tag{5.3}$$

where the indices i, j and n label column, row and event number. The effect of impinging particles within these N_{PED} events is negligible, following from occupancy considerations. For $n > N_{PED}$ the pedestal is calculated as a running average. It is updated every event using

$$PED_{ijn+1} = \frac{PED_{ijn} \times (N_{PED} - 1) + RAW_{ijn}}{N_{PED}}, \tag{5.4}$$

if there is no indication for a particle hit in a given pixel. The condition for the hit identifications is given later in this section. The pedestal corrected pixel response, pulse height PH, is calculated as

$$PH_{ijn} = RAW_{ijn} - PED_{ijn}. \tag{5.5}$$

The next correction applied to the pixel response mitigates the effect of a base line oscillation common to all pixels. The base line oscillation becomes apparent in figure 5.15. It has a period of about 200 pixels, corresponding to $5\,\mu s$ at a readout speed of $25\,ns$ per pixel. As the period of this oscillation is much larger than $25\,ns$, consecutively read out pixels experience a similar baseline shift. Thus the pulse height of a given pixel is corrected using the pulse height of the pixel preceding in the readout sequence. The correction reads

$$\Delta PH_{ijn} = PH_{ijn} - PH_{i-1jn} \text{ or } \Delta PH_{ijn} = PH_{ijn} - PH_{ij-1n}, \tag{5.6}$$

where ΔPH_{ijn} is called differential pulse height. The former option $(i-1)$ is used for the column-wise, the latter $(j-1)$ for the row-wise readout sequence. In the column-wise readout sequence, each pixel of the first column is read out from the lowest to the highest row index, followed by the next column until all pixels are covered. The row-wise readout sequence is defined following the same logic. Both sequences were used for the measurements presented in this work, their advantages and disadvantages are discussed later in this section.
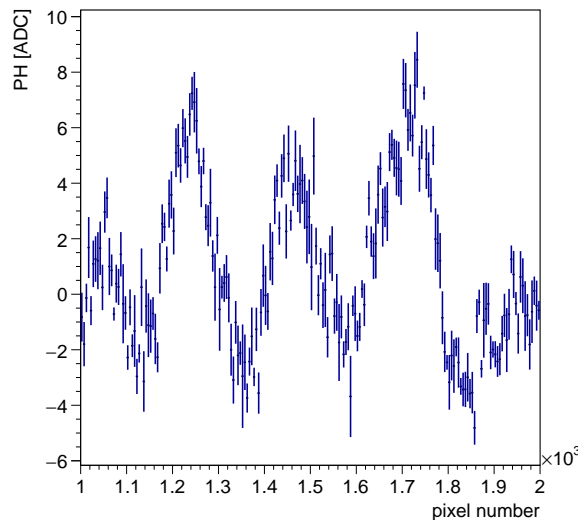
Figure 5.15.: Pixel pulse height PH as a function of the pixel number in the readout sequence indicating a baseline oscillation. Recorded for an arbitrary event with test-pulse injection to a pixel outside the displayed range. Each bin contains an average of 5 pixels.

A map of the pedestal and distributions of the raw pixel response, pulse height and differential pulse height are shown in figure 5.16. The corresponding measurements are taken on a non-irradiated, bare ROC4SENS using the row-wise readout sequence and test-pulse injection. The amplitude of the test pulse (signal) corresponds to about $-100\,\mathrm{ADC}$, roughly one half of the signal expected from a MIP. The pedestal variations are on the order of $500\,\mathrm{ADC}$. The pattern in the pedestal map is explained by the different pedestal contributions of the column amplifiers, introduced in section 5.1.2. After the pedestal correction, the responses of pixels without test pulse injection (noise) fluctuate around $0\,\mathrm{ADC}$. Compared to PH the width of the noise peak is reduced for ΔPH, which enhances signal-to-noise separation. For ΔPH also positive entries around $100\,\mathrm{ADC}$ occur as a consequence of the difference in equation 5.6, which is to be considered for hit identification.
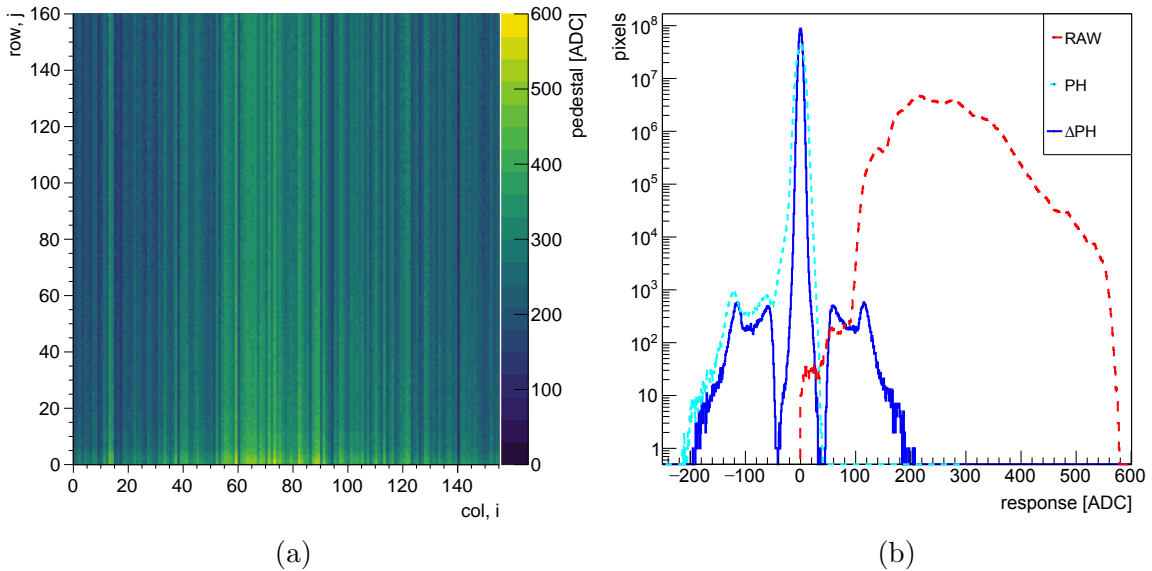
Figure 5.16.: Pedestal map (a) and pixel response distributions for different quantities (b). The analyzed measurements were taken with test-pulse injection on a non-irradiated, bare ROC4SENS using the row-wise readout sequence.

For the identification of particle hits the significance α_{ijn}, defined as

$$\alpha_{ijn} = \frac{\Delta PH_{ijn}}{\mathrm{RMS}(\Delta PH_{ij})}, \tag{5.7}$$

is used as discriminator. The root mean square of the differential pulse height $\mathrm{RMS}(\Delta PH_{ij})$ is initially set to a value of $10\,\mathrm{ADC}$, which is above the typical value. Thereafter it is calculated and updated every N_{up} events, while hit pixels are vetoed in the calculation. The update period N_{up} is initially set to 200 and increased to 500, 2000 after 2000, 10000

triggers respectively. The conditions to mark a pixel i, j, n as hit are:

$$\alpha_{ijn} < -th_{roi} \text{ and} \tag{5.8}$$
$$\alpha_{i+1jn} > th_{roi} \text{ or}$$
$$\alpha_{ij+1n} > th_{roi},$$

were usually a threshold $th_{roi} = 4$ is used. Here again, the former option $(i + 1)$ applies for the column-wise, the latter $(j + 1)$ for the row-wise readout sequence. With a fixed threshold the use of α instead of ΔPH is advantageous, as effects of gain variations are mitigated and noisy pixels are automatically suppressed. The two conditions are needed to deal with clusters of hit pixels, especially if several consecutively read out pixels are hit.

In figure 5.17 schematic hit patterns are shown. While it looks just as expected for the pulse height PH the hit pattern is "differentiated" for the significance α due to the difference in equation 5.6. It becomes apparent that the condition 5.8 identifies the leading and trailing hit of a cluster. The inner pixels of a cluster are not marked in the first place. But since a group of surrounding pixels is stored for each marked pixel, those inner pixels are usually also stored. For exceedingly long clusters though, occurring when the angle between sensor normal and particle beam axis is large, this might not be the case. Therefore the readout direction is chosen to be orthogonal to the direction of long clusters. If not stated otherwise, the column-wise readout sequence is used in the following. This is advantageous since the pixels in a column share the same column amplifier. Thus one source of the gain variations between consecutively read out pixels is eliminated, reducing the width of the noise peak for ΔPH. In addition, frequently switching the column amplifiers, which is done after each pixel in the row-wise readout sequence, increases the width of the noise peak.
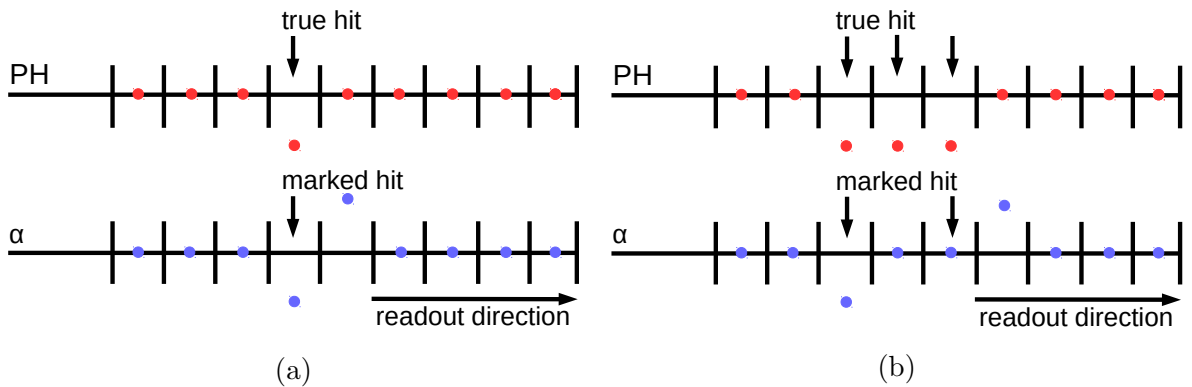
Figure 5.17.: Schematic hit patterns in pulse height PH and significance α for 1 (a) and 3 (b) hit pixels. The pixels marked as hit by the condition 5.8 are indicated.

Distributions of the significance, for the test pulse measurements discussed above and for test-beam measurements on a non-irradiated sensor are shown in figure 5.18. For the test-beam measurements, the particle incidence was parallel to the sensor normal and the peaks at $\alpha \approx \pm 70$ correspond to the peak of a Landau distribution for a minimum ionizing particle. For the test pulse measurements, an excellent separation between signal and noise is apparent. The peaks at $\alpha \approx \pm 20$ and $\alpha \approx \pm 40$ are due to spatial variations of the test pulse amplitude over the area of the readout chip. For the test-beam measurements, there is no clear separation due to charge sharing. In any case, also those fractional charges are stored for later analysis due to the region of interest approach.

(a) (b)
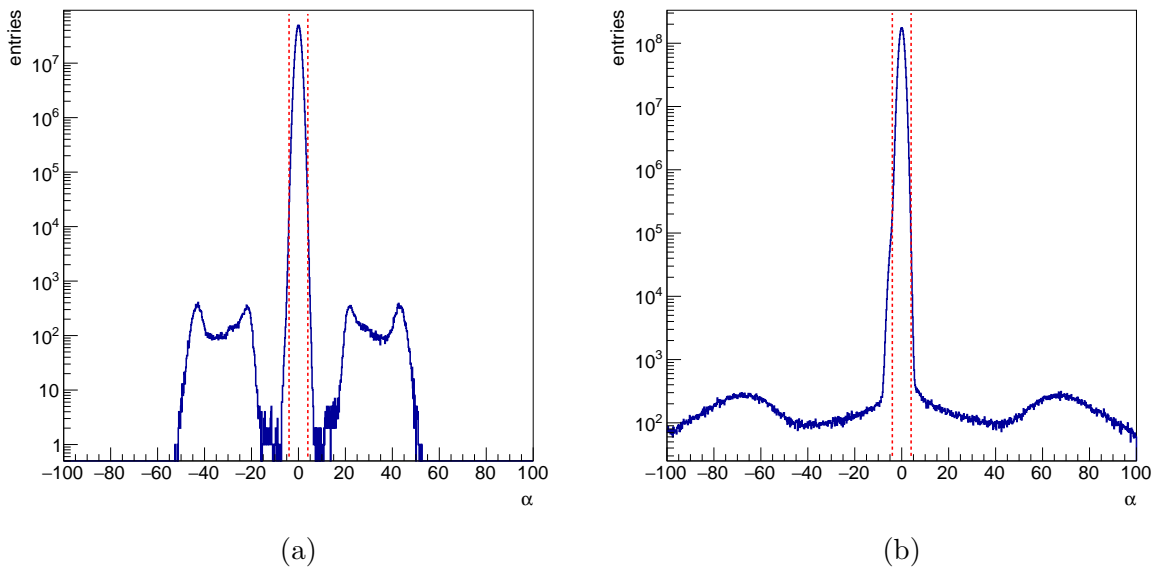
Figure 5.18.: Distributions of the significance α, measured with test pulse injection (a) and in the test beam (b). The dashed red line indicates a threshold at $\alpha = \pm 4$.

5.3.2. Data Storage

The data from the ROC4SENS are stored in a so-called Region Of Interest (ROI) approach, illustrated in figure 5.19. Pixels with a response indicating a particle hit are identified as described in the previous section and trigger the placement of a ROI. For the presented measurements a ROI contains 7×7 pixels and is centered around a hit. The positions and pulse heights of the pixels in the ROI are stored for offline analysis. For each stored pixel a flag is raised to avoid doubling entries in the case of overlapping ROIs, as indicated in the figure.

The pixel data are stored in a simple ASCII format. The header of the data file contains the run number and some parameters of the data taking routine like the applied threshold th_{roi}. For each event, the event number n, a flag indicating if at least one hit was found, a number indicating to which block of data the event belongs and a time stamp

are printed to the data file. It is followed by the ROI-pixel data. For the selected pixels the column, row index i, j and the pulse height PH_{ijn} are stored. This way the required disc space per event is reduced from $\approx 100\,\mathrm{kB}$ (storing all pixels pulse height) to $\approx 2\,\mathrm{kB}$ at $th_{roi} = 4$.
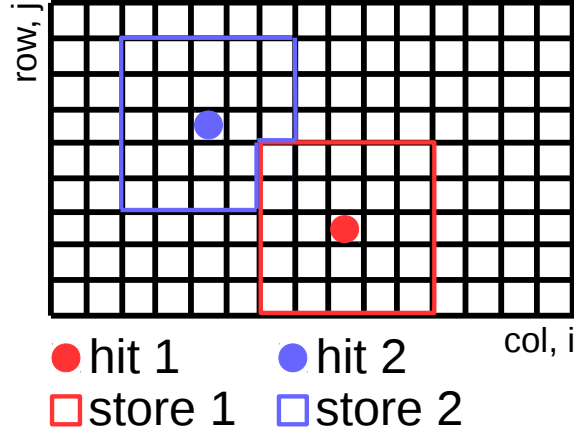
Figure 5.19.: Sketch of the ROI storage pattern. Data are stored for a group of pixels around each identified hit.

Efficiency and Purity of the Region of Interest Selection

The hit-identification and data-storage routine were tested before the first test-beam measurements. Therefore raw data samples were taken on non-irradiated, bare ROC4SENS readout chips, as chips with a sensor were not yet available. These raw data samples were recorded using the row-wise readout sequence and test-pulse injection. They are available with various hit patterns and signal amplitudes.

For the characterization of the routine, the efficiency ϵ_{roi} and purity ρ_{roi} are defined. They measure the probability to store a true signal and the fraction of true signals in the stored signals, respectively. False signals usually arise from baseline fluctuations in the pixel cell (noise). For data with test-pulse injection, it is known which pixel in an event (one readout of the ROC4SENS) received a test pulse, thus the truly hit pixels are known. The efficiency denotes the fraction of truly hit pixels contained in a ROI and therefore marked for data storage. It reads

$$\epsilon_{roi} = \frac{N(\text{true and stored})}{N(\text{true})}, \tag{5.9}$$

where N denotes the number of pixels in the data set fulfilling the condition in parenthesis. In a similar way, the purity is defined as the fraction of ROIs triggered due to pixels correctly identified as hit by the hit-identification routine. It reads

$$\rho_{roi} = \frac{N(\text{identified})}{N(\text{true and identified})}. \tag{5.10}$$

In figure 5.20, ϵ_{roi} and ρ_{roi} are shown as a function of the threshold th_{roi} used in the hit-identification routine. The raw data sample contains mostly two pixel clusters generated by test-pulse injection to neighboring pixels. The total response of these clusters roughly corresponds to one third of the signal expected from a MIP. The signal is equally distributed between the two pixels. Such low signals occur in irradiated sensors and, due to charge sharing, also in non-irradiated sensors. In non-irradiated sensors though, this effect is not critical as the small charges are neighbored by bigger ones thus likely to be contained in a ROI. It becomes apparent that for these conditions $th_{roi} < 5$ is needed for $\epsilon_{roi} > 99\,\%$. On the other hand, ρ_{roi} starts to drop for $th_{roi} < 5$ thus the required disc space increases. As a consequence $th_{roi} = 4$ was chosen as a tradeoff.
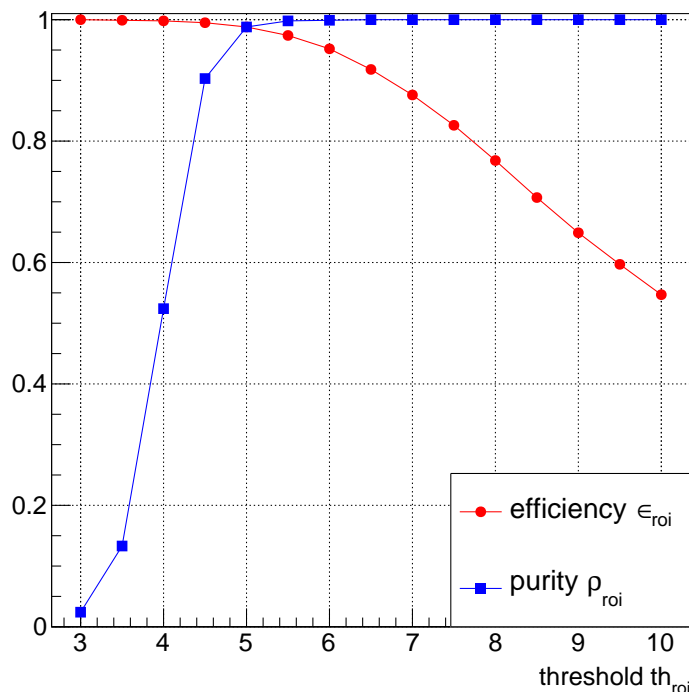
Figure 5.20.: Efficiency and purity as a function of threshold. Measured on a raw data sample taken with test-pulse injections on a bare ROC4SENS.

Additional tests were performed on samples with different cluster sizes, cluster charges and asymmetric pixel charges. In addition, these test measurements were used to check the set of monitoring plots defined in the following section. The promising results of these tests are confirmed by the excellent efficiencies observed in the test-beam measurements discussed in chapter 7. Finally, the ROI approach permits in-depth studies on the physics of silicon sensors, e.g. the edge-on tomography measurements presented in [98].

5.3.3. Monitoring

The characterization of sensors and readout chips for the Phase-2 Upgrade of the CMS detector requires a lot of test-beam measurements. However, time available at test-beam

facilities is limited. Therefore it is crucial to monitor the data acquisition and to spot and solve problems affecting the data quality as soon as possible. On this account, a set of monitoring plots is defined. This set splits into graphs, showing time developments, histograms, showing distributions and maps, where each pixel of the ROC4SENS is represented in a 2D-matrix. A minimal subset (**bold below**) is shown live and updated every N_{up} events (compare 5.3.1) as the online visualization is computationally expensive. This way the time required for the updates is limited to a few seconds every N_{up} events. The other plots are available as soon as a run is stopped. The set contains the following monitoring plots, grouped according to the displayed quantity:

- Pedestal: The pedestal of each pixel is calculated according to equation 5.3 and 5.4.

  - **Graph:** To monitor its time development, the average pedestal of all pixels is calculated every N_{up} events and displayed as a function of the event number.

  - Map: To monitor the spatial distribution of the pedestal, each pixel's pedestal value is displayed on a map updated every N_{up} event.

- Number of pixels over threshold: Every time one of the hit conditions in equation 5.8 is met a counter is incremented.

  - **Graph:** Every N_{up} events the average number of counts per event is calculated for the last N_{up} events and displayed as a function of the event number.

  - Histogram: For every event, the number of counts is filled into a histogram.

  - **Map:** A pixel which is marked as hit due to the conditions in equation 5.8 gets an entry in the hit map. This is a very powerful tool to see if the placement of the DUT is within the scintillator acceptance while the data acquisition is running.

- Raw pixel response: The raw pixel response RAW_{ijn} corresponds to the signal of a pixel digitized by the ADC on the DTB.

  - Histogram: For every event and every pixel RAW_{ijn} is filled into a histogram.

- Pulse height: The pulse height PH_{ijn} is the pedestal corrected raw pixel response and defined in equation 5.5.

  - Histogram: For every event and every pixel PH_{ijn} is filled into a histogram.

  - Map: The pulse height PH_{ijn} for a given pixel is averaged over all events and displayed on the map. This severs the same purpose as the hit map but is less sensitive to noise.

- RMS of the pulse height: For each pixel the RMS of its pulse height $\text{RMS}(PH_{ij})$ is recalculated every N_{up} events. Apart from those where a pixels was marked as hit, all events since the last update are considered.

- Map: To monitor its spatial distribution, each RMS(PH_{ij}) is displayed on a map updated every N_{up} events.

- Differential pulse height: The differential pulse height ΔPH_{ijn} is defined in equation 5.6.

    - **Histogram:** For every event and every pixel ΔPH_{ijn} is filled into a histogram.

- RMS of the differential pulse height: For each pixel the RMS of its differential pulse height RMS(ΔPH_{ij}) is recalculated every N_{up} events. Apart from those where a pixels was marked as hit, all events since the last update are considered.

    - **Graph:** Every N_{up} events RMS(ΔPH_{ij}) is averaged over all pixels and displayed as a function of the event number.

    - **Histogram:** Every N_{up} events RMS(ΔPH_{ij}) is filled into a histogram for each pixel.

    - Map: To monitor also the spatial distribution of RMS(ΔPH_{ij}), each pixels value is display on a map updated every N_{up} events.

- Pulse height significance: The pulse height significance α_{ijn} is defined in equation 5.7,

    - **Histogram:** For every event and every pixel α_{ijn} is filled into a histogram.

Full sets of these monitoring plots, recorded at the test beam for a non-irradiated and an irradiated sensor module, are shown in appendix A.

5.4. Conclusion

The ROC4SENS readout chip, introduced in this chapter, offers analog pulse-height measurements without zero suppression, rendering it an excellent choice for studies on the physics of silicon pixel sensors in test-beam experiments. To capitalize from the capabilities of the ROC4SENS a set of experimental techniques was developed and presented within the scope of this work. This includes the routine for data acquisition and online monitoring, presented in the previous section. The key characteristic of this routine is the ROI approach for data storage, permitting data sparsification while keeping locally threshold-less information around particle hit candidates, for in-depth studies of sensor physics.

6. Analysis of Test-Beam Data

The key observables characterizing the investigated pixel sensors are position resolution and hit efficiency. Their determination from test-beam measurements requires the reconstruction and a clean selection of particle tracks with the beam telescope.

The track reconstruction for the detector setup introduced in section 5.2.2 is described in the following, starting from single pixels and their clustering. Pixel clusters represent possible particle intersections with one of the detector planes and are further used to reconstruct particle track candidates based on a priory assumptions on position and orientation of the detector planes. In an iterative alignment procedure, these tracks are used to correct position and orientation, in return yielding higher quality tracks. Then the definition and reconstruction of position resolution, hit efficiency and further observables characterizing the investigated sensor modules are discussed. Finally, a set of selection criteria is introduced, selecting track candidates likely originating from real particle interactions, to reduce background contributions to the investigated observables.

List of Own Contributions   The author's contributions to the results presented in this chapter include:

- Development of the procedures to correct for the baseline oscillations and crosstalk affecting the pixel response.

- Reconstruction of the pixel noise from monitoring figures.

- Development of a procedure to reconstruct the spatial resolution of the investigated modules.

- Revision of the hit efficiency definition.

- Definition of a robust set of selection criteria and development of the residual pairing method.

This work has been performed under the supervision of Prof. Dr. Erika Garutti and Dr. Daniel Pitzl. It builds on the reconstruction software developed by Dr. Daniel Pitzl [126]. The developments on the reconstruction of the spatial resolution were done in collaboration with Irene Zoi.

6.1. Clustering and Position Reconstruction

Due to charge sharing, see section 2.3, the charge deposited by a single particle intersection with a pixel sensor might be distributed over several pixels. In a first step, the pixels containing the deposited charge need to be selected. These pixels are grouped into a cluster by applying a clustering algorithm. Once the clustering is done, the position at which said particle penetrated the detector plane is reconstructed to be used in the track reconstruction.

In general, the response of each of the pixels in the eight detector planes is measured if a trigger signal is issued. Only a small fraction of these responses actually corresponds to a charge deposition. The selection of this fraction is done by applying a threshold on the pixel response. The threshold choice represents a compromise between efficiency and purity. On one hand, there is a finite probability to miss a signal issued by a real electron interaction, on the other hand, there is a finite probability to include a noise fluctuation in the signal selection. The threshold can be applied online, on the readout chip or in the data acquisition software, or offline in the reconstruction software. The way the thresholds are applied differs between the three used types of pixel modules:

- **DUT:** Each pixel is read out. In the data acquisition software pixels with a pulse height more than 4 times their noise are selected. The pixel position and digitized response are stored for a ROI of 7×7 pixels (details given in 5.3). In the offline reconstruction a fixed pixel threshold th_{pix}, optimized for the spatial resolution of each individual module, is applied. The response is corrected for gain variations and non-linearity as described in section 5.1.4.

- **Time reference:** A CMS Phase-1 pixel module [81] is used as time reference plane. The response of pixels above a threshold of $1500\,e^-$ is digitized with 8 bit precision and stored together with the pixel positions. A correction for gain variations and non-linearity is performed in a similar way as for the DUT.

- **MIMOSA 26:** For the six MIMOSA 26 sensors in the beam telescope, the threshold is applied on the chip and only the positions of the pixels exceeding the threshold are stored. This means only binary charge information is available for the analysis. A threshold of 5 or 6 times the individual pixel noise is used. The differences in performance between the two threshold settings are negligible as shown in [121].

For each event and detector plane, the clustering algorithm is applied to the subset of pixels above the respective threshold. It starts with one pixel and adds pixels to the cluster as long as another pixel fulfilling the clustering condition can be found. Once no further pixel can be added to the cluster the procedure starts over, ignoring pixels already assigned to a cluster. This continues until all pixels are clustered. The clustering

conditions reads

$$|\Delta i| \leq 1 \text{ and} \tag{6.1}$$
$$|\Delta j| \leq 1,$$

where Δi and Δj are the difference in column and row index between any pixel in the cluster and any pixel not yet assigned to a cluster. Examples of allowed cluster topologies are shown in figure 6.1.
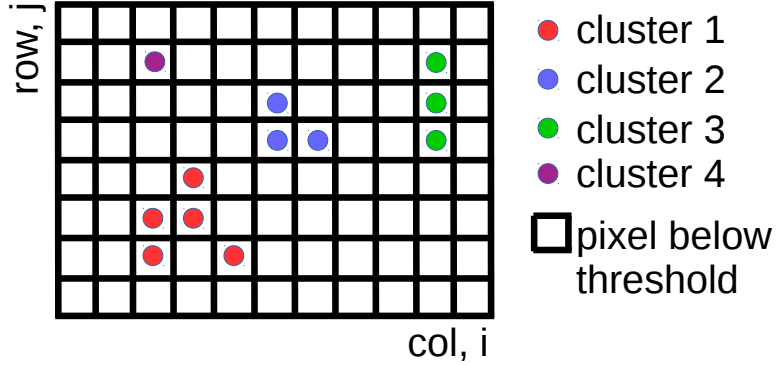
Figure 6.1.: Examples of cluster topologies allowed by the clustering condition 6.1.

For a given cluster the cluster position x_{cl} (y_{cl} analog) is calculated via

$$x_{cl} = p_x \frac{\sum_{k=0}^{S_{cl}} Q_k \cdot i_k}{\sum_{k=0}^{S_{cl}} Q_k}, \tag{6.2}$$

where p_x is the pitch in x-direction, S_{cl} is the number of pixels in the cluster, i_k is the column index of a given pixel and Q_k is the pixel charge defined in section 6.3. For the alignment of the telescope, Q_k is set to the number of neighboring pixels. This is usually referred to as weighted algorithm or center-of-gravity algorithm. Other algorithms are discussed in literature [44] and yield better performance especially for small (η-algorithm) or large (head-tail algorithm) incidence angles. However, the scope of this work is to compare the performance of different sensor designs, thus a decision for a simple and robust algorithm has been made.

The cluster charge is defined as the sum over the charges of all pixels in a cluster.

6.2. Track Reconstruction and Alignment

The cluster positions, estimated according to equation 6.2, are calculated in the local coordinates of each telescope plane. The first step towards the reconstruction of telescope tracks is the transformation from the local to global coordinates. The global, right-handed coordinate system has its origin in the center of telescope plane 0 (up to an alignment correction), the z-direction is parallel to the beam and the y-direction points upwards

6. Analysis of Test-Beam Data

(compare figure 5.11). The transformation reads

$$\vec{x}_g = (\vec{x}_{lp} + \vec{x}_{ap}) \cdot \bar{\mathbf{R}}_z(\theta_{zp}), \tag{6.3}$$

where $\vec{x}_g$, $\vec{x}_{lp}$ corresponds to a position in global and local coordinates, respectively. The rotation matrix $\bar{\mathbf{R}}_z(\theta_{zp})$ corresponds to a rotation around the z-axis $\mathbf{R}_z(\theta_{zp})$, applying the small-angle approximation. A first estimation of the alignment vector $\vec{x}_{ap}$ and the rotation angle θ_{zp} is based on direct measurements or prior knowledge from previous runs. The track-based correction of these alignment parameters is described later in this section. Rotations around the x- and y-axis are not considered for the telescope planes, as the angles are close to zero due to sufficient mechanical precision.

Once the global positions are calculated, triplet tracks are reconstructed in the upstream and downstream triplet of the telescope. In figure 6.2 the procedure is illustrated for the upstream triplets. Each cluster in plane 0 is combined with each cluster of plane 2 and the corresponding track angles are calculated. For each combination, a triplet track candidate is defined as a straight line between the two cluster positions. For 3 particles — a typical number for pile up within the telescope integration time — this yields 9 combinations. Two conditions are applied to select the correct combinations:

- **Slope:** To reduce the number of combinations, triplet track candidates with a slope $|dx_{02}/dz_{02}|$ or $|dy_{02}/dz_{02}| > 0.005$ are rejected. For typical settings, and particle tracks $\mathrm{RMS}(dx_{02}/dz_{02})$ and $\mathrm{RMS}(dy_{02}/dz_{02}) < 0.001$.

- **Residual:** The triplet track candidates are interpolated to plane 1 (x_{02}, y_{02}). The residuals $\Delta x_{tri} = x_{02} - x_{g1}$ and $\Delta y_{tri} = y_{02} - y_{g1}$ are calculated and tracks with $\Delta x_{tri}, \Delta y_{tri} > 50\,\mu\mathrm{m}$ are rejected.

The remaining combinations are defined as triplet tracks and their parameters are stored for further analysis steps.
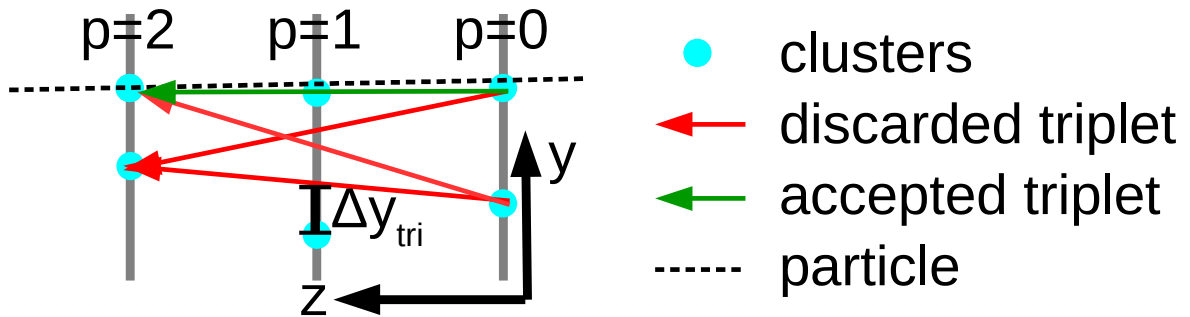
Figure 6.2.: Schematic for triplet track reconstruction. All combinations between plane 0 and plane 2 are considered. Triplet candidates with large slopes or residuals Δy_{tri} are rejected.

For the downstream triplet, triplets tracks are defined in a similar way. The time reference plane between telescope plane 4 and 5 causes additional multiple scattering of the beam electrons. This is taken into account by changing the cut on the residual from $50\,\mu\text{m}$ to $100\,\mu\text{m}$ and by re-calculating the track parameters for the selected triplets based on the clusters on plane 3 and 4.

To represent a full particle trajectory through the setup, the tracks in the upstream and downstream triplet are combined. All possible combinations between tracks in the two parts are considered in a first step. The residuals

$$\Delta x_{TEL} = x_{utri} - x_{dtri} \text{ and } \Delta y_{TEL} = y_{utri} - y_{dtri} \tag{6.4}$$

are calculated, where (x_{utri}, y_{utri}) and (x_{dtri}, y_{dtri}) are derived from the extrapolation of the upstream and downstream triplet to the z-position of the DUT. A combination is defined as telescope track if it fulfills the following condition:

- **Residual:** The residuals Δx_{TEL} and Δy_{TEL} must be smaller that $30\,\mu$m.

The quality of the telescope tracks depends on the precision of the detector alignment. As the position resolution of silicon detectors exceeds the mechanical precision of the setup, alignment corrections are calculated and applied in software. This is done by recursively correcting the alignment parameters in equation 6.3 using the reconstructed tracks. In the following, two examples are discussed to illustrate the correction procedure.

To align the downstream triplet with respect to the upstream triplet in the x-direction, the distribution of the residual Δx_{tel} is used. In figure 6.3a such residual distributions are shown in a misaligned and aligned situation. In the aligned case, the distribution peaks at zero. In the misaligned case, the peak is displaced and wider. By fitting the sum of a Gaussian function and an offset, the peak position is estimated and determines a correction for the alignment parameters x_{ap} of the three downstream telescope planes.

In figure 6.3b the average residual $\text{AVG}(\Delta x_{tel})$ is shown as a function of the y-coordinate of the corresponding triplet track. It appears, that the average residual in the misaligned case is not only shifted but shows a slope indicating a rotation around the z-axis. The rotation angle is calculated from the slope of a linear fit to the data points and again determines a correction for the alignment parameters θ_{zp} of the three downstream telescope planes.

The entire set of alignment parameters for the telescope planes is estimated in that fashion, apart from two exceptions. First, the alignment parameters for plane 1 are zero by definition. Second, z_{ap} is estimated only for plane number 2 and 5, as corrections in the z-direction are weakly constrained due to the small angular dispersion of the electron beam.
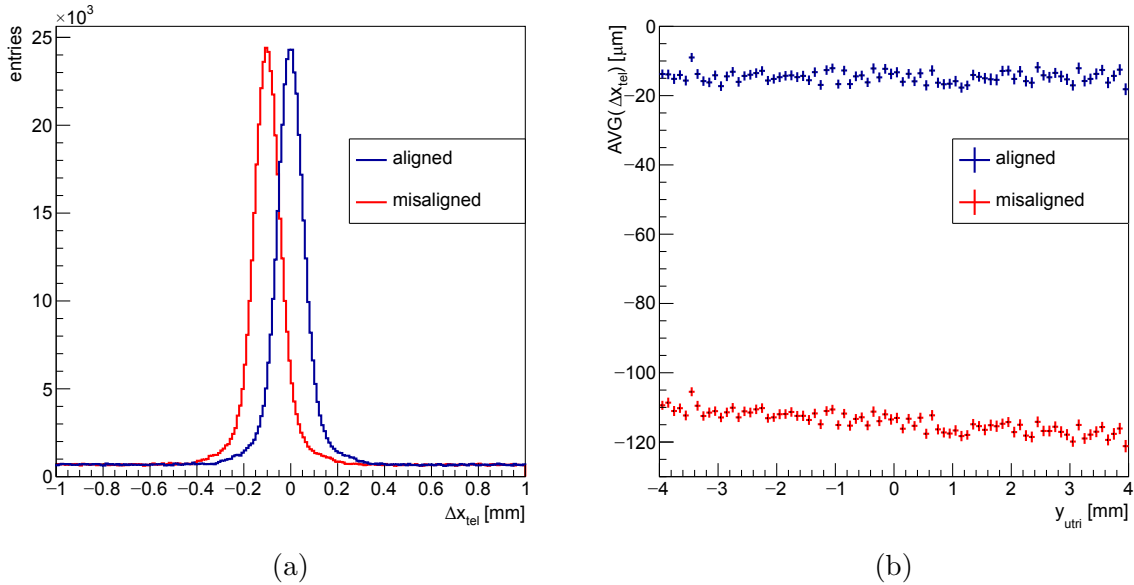
Figure 6.3.: Examples of the Δx_{tel} residual distribution (a) and its mean as a function of the y-coordinate y_{utri} (b) in an aligned and misaligned case. The upstream and downstream triplet planes have an equidistant spacing of ≈ 150 mm and the distance between the closest planes of the two triplets is ≈ 80 mm. The misaligned scenario corresponds to an intentional shift of ≈ -0.1 mm in the y-direction and a rotation of ≈ 1 mrad around the z-axis for demonstrative purpose. Before the alignment procedure misalignments are larger and the residual distributions are significantly wider.

To include or evaluate measurements from the time reference plane and the DUT, these detectors also need to be aligned with respect to the beam telescope. In addition to the alignment parameters introduced in equation 6.3, rotations around the x- and y-axis need to be taken into account. The alignment procedure is the same for both detectors. For simplicity, the DUT alignment will be discussed in the following.

Similar to the alignment of the telescope planes, the alignment of the DUT is based on residuals. The first step to calculate this residual is to derive the intersections between the extrapolated upstream triplet tracks and the DUT plane, taking into account the z-position and orientation of the DUT. The second step is to extrapolate the corresponding downstream triplet tracks to the z-positions of said intersections and to combine the x- and y-coordinates of the two extrapolated tracks by taking their average. This step is skipped for modules on rotated PCBs. For those modules, there is a significant overlap between the DUT and the cooled copper support structure. The additional material budget deteriorates the pointing resolution of the downstream triplet. In the case of the time reference plane, only the downstream triplet tracks are considered for the alignment. The third step is to transform these points of intersection into local DUT coordinates $\vec{x}_{lD}$ using

$$\vec{x}_{lD} = \vec{x}_g \cdot \mathbf{R}_y(\theta_{yD}) \cdot \mathbf{R}_x(\theta_{xD}) \cdot \mathbf{R}_z(\theta_{zD}) + \vec{x}_{aD}. \tag{6.5}$$

DUT coordinates refers to a coordinate system where the x- and y-axis are parallel to the columns and rows and the origin is in the center of the DUT pixel matrix. This is convenient since properties of the DUT are best expressed in a coordinate system with fixed DUT orientation. The alignment parameters θ_{yD}, θ_{xD}, θ_{zD} and $\vec{x}_{aD}$ are estimated in the same fashion as discussed above. The used residuals are

$$\Delta x_{DUT} = x_{DUT} - x_{TEL}, \text{ and } \Delta y_{DUT} = y_{DUT} - y_{TEL}, \tag{6.6}$$

where x_{DUT}, y_{DUT}, x_{TEL} and y_{TEL} denote the position of a DUT cluster and the point of intersection of a telescope track in DUT coordinates, respectively. The z-component of the alignment vector $z_{aD} = 0$, because the correction of the DUT z-position is already taken into account in the first step of the residual calculation.

6.3. Definition of Observables

For the characterization of the investigated pixel sensors, a set of observables is defined in the following. While hit efficiency and position resolution are important performance benchmarks, further observables, like cluster size and charge, offer additional insight into the physics of silicon pixel sensors.

6.3.1. Charge

The charge collected at the readout electrodes of a silicon sensor can decrease after the sensor has been exposed to a flux of particles, as discussed in section 2.4. Since the charge collection has a direct impact on the performance, its degradation with neutron equivalent fluence is interesting to study. Within this work, the absolute collected charge of the non-irradiated modules is calibrated to the expected MPV of 11 ke, as discussed in section 2.2. For the irradiated modules, it is reconstructed up to a calibration constant, thus no studies on the charge collection as a function of the neutron equivalent fluence are shown. In any case, it proves to be a helpful observable. For example, it is used to derive a signal-to-noise ratio, to improve the comparability of the efficiency measurements on different samples. In total the charge is calculated in four steps:

1. The pedestal is subtracted from the pixel response, using equation 5.5.

2. The pixel response is corrected for baseline oscillations.

3. It is corrected for crosstalk between consecutively read out pixels.

4. For non-irradiated sensors, a correction for gain non-linearity and pixel-to-pixel gain variations is applied before the response is scaled into a number of collected charge carriers.

6. Analysis of Test-Beam Data

The details of these steps are given in the paragraphs hereafter.

The offline analysis starts with the digitized, pedestal corrected pulse height PH as a measure for the charge (see equation 5.5). It is provided for all pixels in the stored ROIs, as introduced in section 5.3. Not only is this a non-linear, measure of the charge in arbitrary ADC units, but also it is subject to baseline oscillations, crosstalk and varies as a function of position on the sensor (gain variations). The treatment of these flaws is discussed in the following.

The correction for the baseline oscillations is

$$DPH_{ijn} = PH_{ijn} - \frac{1}{2} \times (PH_{ifn} + PH_{iln}), \tag{6.7}$$

where DPH_{ijn} denotes the corrected pulse height and f, l are the row indices of the first and last in column i, stored for the given event. The correction is different from the one in equation 5.6. This is to avoid deformations of the hit pattern like in those figure 5.17, as this would spoil the calculation of the cluster position (equation 6.2). The effect of the correction is shown in figure 6.4a. While the responses above $100\,\mathrm{ADC}$ agree within errors, the width of the peak at $0\,\mathrm{ADC}$ (noise) is reduced significantly.

(a) (b)
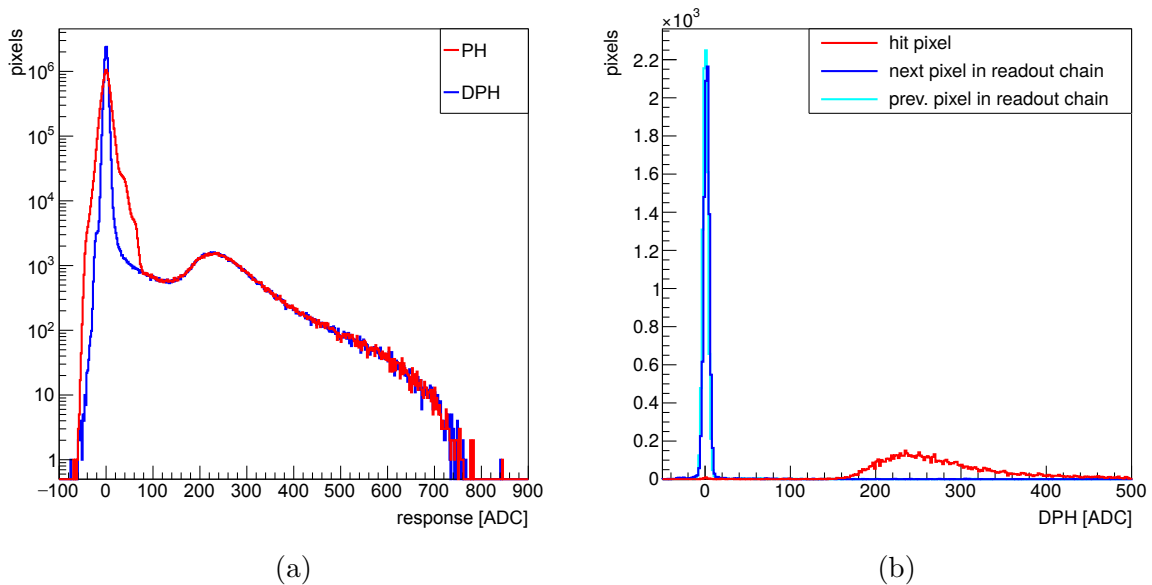
Figure 6.4.: Distributions of the responses PH and DPH (see equation 5.5 and 6.7). Measured on a non-irradiated sensor, with $50 \times 50\,\mathrm{\mu m^2}$ pixel size for vertical beam incidence. In (a) the response is shown for all stored pixels. In (b) hit pixels are selected with the beam telescope to study the response in the neighboring pixels.

For some of the investigated samples, crosstalk occurs between pixels read out consecutively. Likely because the discharge on an electrical component is too slow and leaks into the readout of the following pixel. To visualize this phenomenon, the beam telescope is used to select pixels hit within their central $30 \times 30\,\mathrm{\mu m^2}$ (for $50 \times 50\,\mathrm{\mu m^2}$ pixel size).

By comparing the signal of the neighboring pixels, the previous and next pixel in the column-wise readout sequence, this crosstalk becomes apparent. An example is shown in figure 6.5a, where the pedestal peak for the next pixel is widened and shifted to 10 ADC, 4 % to 5 % of the charge deposited in the hit pixel. For the affected samples a correction function

$$C(PH_{ijn}) = PH_{ijn} - c_x \times PH_{i-1jn} \tag{6.8}$$

is applied prior to equation 6.7. The correction factor c_x is estimated for each sample separately. The correction is applied in figure 6.5b. It successfully shifts the pedestal peak to 0 ADC but does not recover the original width of the distribution. For a sample which is not affected by said crosstalk, the same distributions are shown in figure 6.4b. Note that for the samples used in the resolution studies, presented in chapter 7, the effect is below 2.5 % and neglected.

(a)   (b)
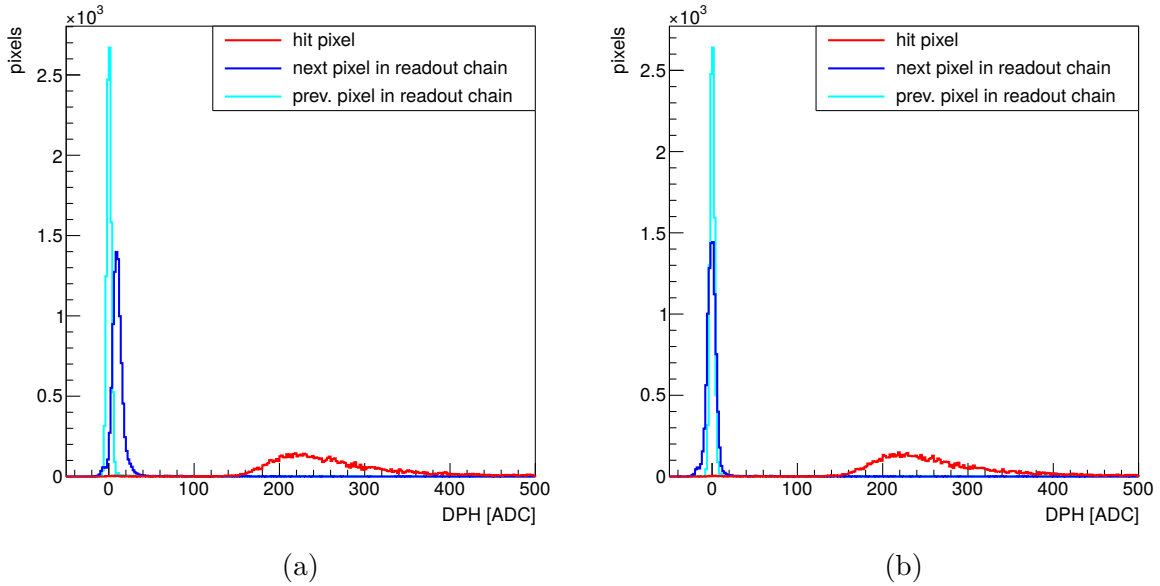
Figure 6.5.: Distributions of DPH. Measured on a non-irradiated sensor, with $50 \times 50\,\mu m^2$ pixel size for vertical beam incidence. Hit pixels are selected with the beam telescope to study the response in the neighboring pixels. In (a) crosstalk between the hit pixel and its upper neighbor is apparent. In (b) crosstalk is corrected for, by applying the correction function C.

To correct for the gain non-linearity and pixel-to-pixel gain variations the preparative test-pulse measurements described in section 5.1.4 are used. The correction function for each pixel $g_{ij}(DPH_{ijn})$ is determined from these test pulse measurements to correct for said effects. The last missing step to an absolute charge calibration is a conversion factor k for each module. Thus the absolute pixel charge

$$Q_{ijn} = k \times g_{ij}(DPH_{ijn}). \tag{6.9}$$

6. Analysis of Test-Beam Data

As pointed out in section 5.1.4 an independent, absolute charge calibration using x-ray fluorescence lines is not possible. Instead, k is chosen such that the MPV of the charge distribution is at the expected value of 11 ke, see section 2.2. In figure 6.6 distributions of the non-calibrated (DPH) and calibrated (Q) responses are shown for clusters generated in different regions of the same module. Note that the definition of the cluster response in terms of DPH is analog to the definition for Q. It appears that the peaks in the two distributions of DPH are shifted by about 10 ADC due to gain differences between the respective regions. For Q the two distributions overlap and have an MPV of 11 ke.
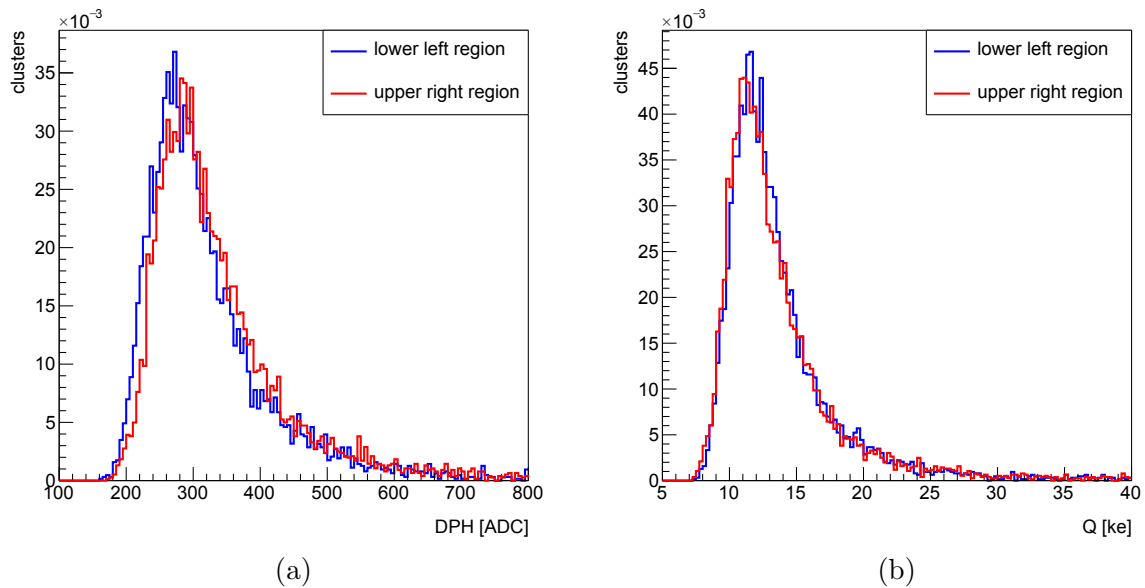
Figure 6.6.: Distributions of the responses DPH and Q for DUT clusters linked to a telescope track, measured on a non-irradiated sensors, with $50 \times 50 \, \mu m^2$ pixel size at vertical beam incidence. The distributions are shown for two regions of $3 \times 3 \, mm^2$, one in the lower left and one in the upper right region of the sensor.

The spread on the conversion factor k between different non-irradiated modules is smaller than 5 %. Assuming that gain changes in the readout chip are compensated by the gain equalization procedure, one could use an averaged conversion factor k for the calibration of the irradiated modules to study charge loss due to trapping after irradiation. However, the charge measurements obtained with this approach turned out to be inconsistent regarding their fluence dependence. For modules irradiated with protons to $\phi_{eq} = 5.1 \times 10^{15} \, cm^{-2}$ the shaping found in test pulse measurements and in trigger delay scans with beam particles were different. Thus the compensation of the gain changes with the test pulse calibration is faulty and this approach was discarded. Instead, for the irradiated sensors, the charge is expressed in either DPH or as signal-to-noise ratio defined later.

6.3.2. Noise

With higher deposited neutron equivalent fluences, the leakage current through the silicon sensor increases. This yields increasing shot noise[1], one contribution to the noise of the sensor module. While the leakage current increases several orders of magnitude, the noise increases by a factor 2 to 3 after irradiation and is independent of the applied bias voltage (see figure 7.12b). Thus the leakage current is considered to be a sub-dominant contribution and the increase in noise can be associated with radiation effects in the readout chip. Its change is still considerable since also the signal degrades with irradiation.

In the following, the noise is calculated for DPH. The noise of each pixels ΔPH is defined as $\mathrm{RMS}(\Delta PH_{ij})$, calculated online and stored (see section 5.3.1 and 5.3.3). The corresponding map is retrieved in the offline analysis and the noise of each pixel $\sigma(DPH)_{ij}$ is calculated as

$$\sigma(DPH)_{ij} = \frac{\sqrt{3}}{2} \times \mathrm{RMS}(\Delta PH_{ij}). \tag{6.10}$$

This is derived through error propagation of equation 5.6 and equation 6.7, assuming that the noise $\sigma(PH)$ is equal for all pixels within one column.

For the subsequent analysis steps, each pixel's x- and y-position are calculated. This way it is straightforward to calculate the average noise in the same region of the sensor used to calculate the average efficiency and signal. A consistent comparison between these quantities is achieved also for the proton irradiated samples with a nonuniform fluence distribution.

6.3.3. Hit Efficiency

The hit efficiency of the DUT is defined as

$$\epsilon = \frac{N(\text{hit on track})}{N(\text{track})}, \tag{6.11}$$

where $N(\text{track})$ denotes the number of selected telescope tracks and $N(\text{hit on track})$ is the subset of those tracks matched with a hit in the DUT. Although this definition is fairly simple, careful selection of the considered telescope tracks is crucial to obtain meaningful results. The selection criteria are discussed in section 6.4.

In this context, DUT hits are pixels fulfilling the hit finding condition 5.8. So only pixels triggering a ROI are selected. This is more meaningful than e.g. using a fixed, resolution-optimized threshold, which is typically lower and increases the probability for false-positive efficiency entries.

---

[1]Shot noise refers to the fluctuations on the number of charge carriers contributing to the leakage current. Its spectral density is $i_n^2 = 2eI$, where e is the elementary charge and I is the average current [41].

6. Analysis of Test-Beam Data

The matching between telescope track and DUT hits is performed by applying a cut on the radial distance r_{min} between a telescope track and the closest hit

$$r_{min} = \sqrt{(x_{min} - x_{TEL})^2 + (y_{min} - y_{TEL})^2} < 0.2\,\mathrm{mm}, \tag{6.12}$$

where x_{min} and y_{min} denote the position of the closest DUT hit in DUT coordinates. In figure 6.7 an example of the inefficiency as a function of the cut on r_{min} is shown. The inefficiency is defined as $1 - \epsilon$ and shown occasionally because it is convenient to examine on a logarithmic scale. The cut on r_{min} is chosen to be well above the steep rise up to $\approx 0.1\,\mathrm{mm}$ to include even rare events with poor resolution.

The error on the hit efficiency is

$$\sigma_\epsilon = \frac{1}{\sqrt{N(track)}} \cdot \sqrt{\epsilon(1 - \epsilon)}, \tag{6.13}$$

referred to as Binomial Error in [127].
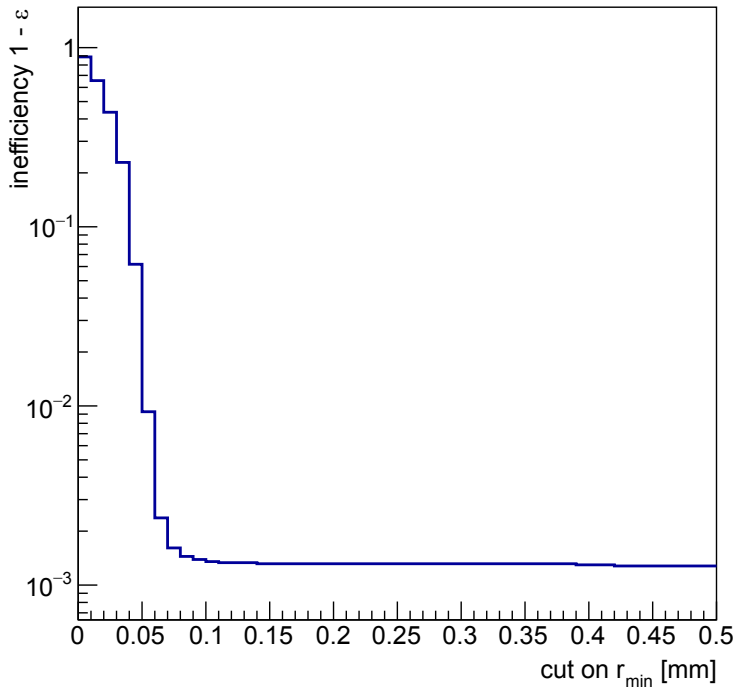
Figure 6.7.: Inefficiency as a function of the cut on r_{min} for a sample with a pixel size of $25 \times 100\,\mathrm{\mu m}^2$, neutron irradiated to $\phi_{eq} = 14.4 \times 10^{15}\,\mathrm{cm}^{-2}$, operated at $V_{bias} = 800\,\mathrm{V}$. Apart from the cut on r_{min} the selection is the same as for the results shown in chapter 7.

6.3.4. Spatial Resolution

In the context of tracking detectors, the word spatial resolution can be ambiguous. In this work, it is to be understood as the uncertainty on a position measurement in one

of the investigated sensor modules — a single plane resolution — and also referred to as hit resolution. The position is measured in the sensor plane, independent of the sensor orientation with respect to the beam telescope.

The resolution in x- and y-direction is defined as the width of the distribution of the residuals Δx_{DUT} and Δy_{DUT}, both defined in equation 6.6. In the following, the resolution in the y-direction will be discussed. The same procedure applies to the x-direction. Apart from a need for careful selection of the considered tracks, the extraction of the resolution faces two difficulties: consistent quantification of the residual width and the unfolding of the telescope track contribution to the residual width. The analysis procedure presented in the following addresses these issues.
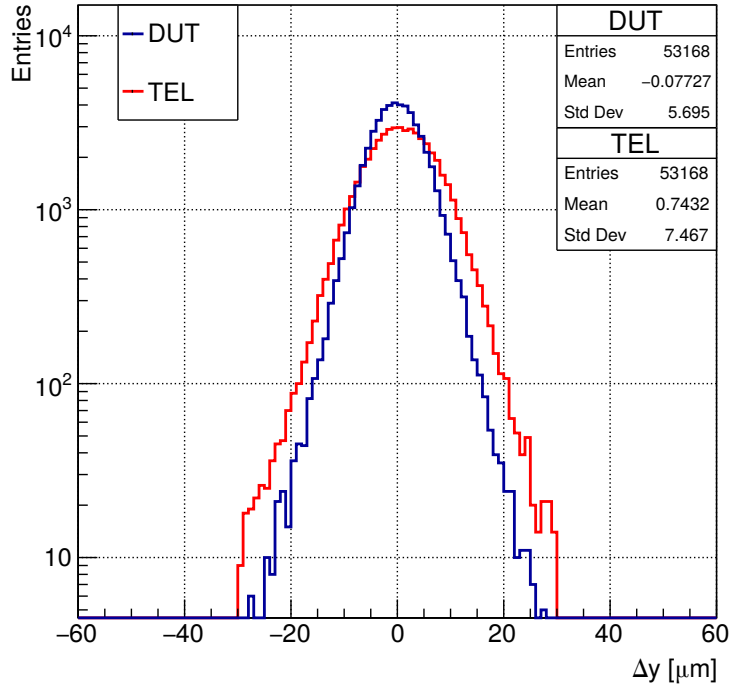
Figure 6.8.: Residual distributions for Δy_{DUT} and Δy_{TEL}. The DUT is a non-irradiated sensor with a pixel size of $50 \times 50\,\mathrm{\mu m}^2$ operated at $V_{bias} = 120\,\mathrm{V}$. The spacing of the planes in the beam telescope triplets is $\approx 150\,\mathrm{mm}$ and the closest planes of the two triplets are $80\,\mathrm{mm}$ apart with the DUT half the way between them. The DUT is rotated around the x-axis, such that $\theta_{xD} = 18.4°$.

The final event selection for the resolution studies is presented in section 7.1. For this selection, an example of the residual distribution Δy_{DUT} is shown in figure 6.8. A method to characterize the width of this distribution should fulfill three requirements:

1. Respect the non-Gaussian nature of the distribution for incidence angles close to 0°, due to the physics of energy loss and multiple Coulomb scattering (tails), demonstrated in figure 6.9. Another effect is due to asymmetries caused e.g. through biases in the reconstruction algorithm.

95

6. Analysis of Test-Beam Data

2. Maintain comparability with other publications, frequently quoting a Gaussian σ.

3. Stability, especially with respect to outliers originating from δ-electrons and track selection criteria.
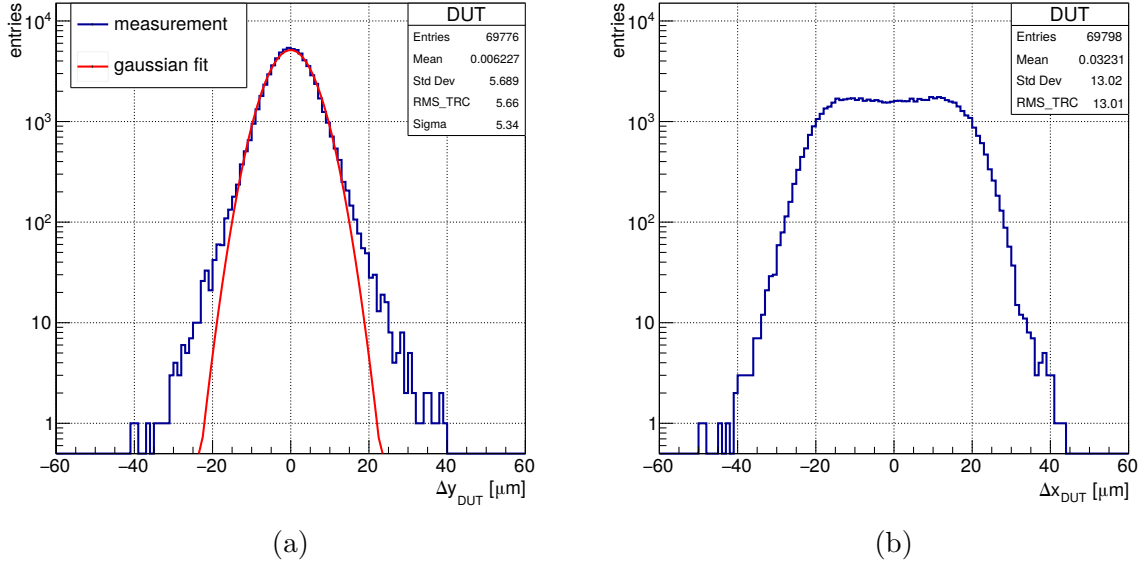
Figure 6.9.: Residual distributions for Δy_{DUT} and Δx_{DUT} for the same run as shown in figure 6.8. In (a) a Gaussian distribution, fitted to the measured distribution, clearly illustrates the non-Gaussian tails. The standard deviations of the measured distribution and the fitted Gaussian distribution (labeled Sigma), as well as the truncated RMS (labeled RMS_TRC), are given in the upper right boxes. The distribution of Δx_{DUT} in (b) is box-like, as $\theta_{yD} = 0°$.

To meet these requirements, the width is extracted using a truncated RMS denoted as $\mathrm{RMS}_{trc}(\Delta y_{DUT})$. For a Gaussian distribution, the RMS is equivalent to its σ, hence the comparability to other publications is assured without making assumptions on the shape of the distribution. To suppress the influence of outliers on the RMS it is recalculated in an iterative approach, discarding values outside of $\pm 6 \cdot \mathrm{RMS}_{trc}$. The considered range converges after few iterations and contains more than 99.95% of the events in the residual distributions for the presented data.

The finite track resolution of the beam telescope implies a certain error on x_{TEL} and y_{TEL}. Thus also x_{TEL} and y_{TEL} contribute to the width of the DUT residual. To quantify this contribution, the residuals Δx_{TEL} and Δy_{TEL} are used. They are defined in equation 6.4 and an example is shown in figure 6.8. The width of the residual is extracted as $\mathrm{RMS}_{trc}(\Delta y_{TEL})$. The effective telescope resolution, defined as the error on y_{TEL}, is

$$\sigma_{yTEL} = \frac{\mathrm{RMS}_{trc}(\Delta y_{TEL})}{2\cos\theta_{xD}}. \tag{6.14}$$

The factor $\cos\theta_{xD}^{-1}$ takes into account that the residual Δy_{TEL} is calculated in global coordinates, whereas Δy_{DUT} is calculated in DUT coordinates. For studies of σ_{yDUT} the

rotation around the y-axis $\theta_{yD} = 0$. The factor $\frac{1}{2}$ consist of two contributions $\frac{1}{\sqrt{2}}$. The first arises when the error σ_{ytri} on y_{utri} and y_{dtri} is derived from the residual width, assumed to be equal for the upstream and downstream triplet. The second is due to the error propagation through the term $\frac{1}{2}(y_{utri} + y_{dtri})$ contained in the calculation of y_{TEL}. The full calculation is presented in appendix B. Note that σ_{yTEL} is an effective resolution, derived for a given telescope geometry, DUT material budget and event selection. Thus it might differ from results presented in [121].

Once the effective telescope resolution is known, the resolution of the DUT is

$$\sigma_{yDUT} = \sqrt{\mathrm{RMS}_{trc}(\Delta y_{DUT})^2 - \sigma_{yTEL}^2}. \tag{6.15}$$

The statistical error on σ_{yDUT} is derived from the statistical errors on $\mathrm{RMS}_{trc}(\Delta y_{DUT})$ and $\mathrm{RMS}_{trc}(\Delta y_{TEL})$, propagated respecting equation 6.14 and 6.15. The errors on both $\mathrm{RMS}_{trc}(\Delta y_{DUT})$ and $\mathrm{RMS}_{trc}(\Delta y_{TEL})$ are estimated using pseudo experiments as discussed in [128], with some minor changes. In summary, the measured distribution is smeared by replacing each bins content by a random number drawn from a Poisson distribution with the original bin content as mean. This procedure is repeated 1000 times and each time the truncated RMS of the smeared distributions is calculated. This way the distribution of truncated RMS is generated from pseudo experiments and the uncertainty on the truncated RMS is defined as the RMS of this distribution.

6.3.5. Cluster Size

The cluster size is straightforward to reconstruct and gives insight into the physics of charge sharing, a mechanism with a large impact on the spatial resolution, discussed in section 2.3. In section 6.1, clusters are defined as a group of neighboring pixels above threshold, likely generated by a single particle. A clustering algorithm is used to group these pixels applying the clustering condition given in equation 6.1.

For a given cluster, the cluster size n_{px} is defined as the number of pixels forming it. Additionally, it is convenient to define n_{col} and n_{row} as the projection of the cluster size on the column or row direction. All three definitions are illustrated in figure 6.10.

6.3.6. In-Pixel Position

The layout of a single pixel cell varies between the investigated sensor designs. To study the influence of these different layouts, it helps to study observables like cluster size, cluster charge and efficiency as a function of the in-pixel position. This is possible due to the excellent track resolution of the DATURA beam telescope — being much smaller than the pitch of the investigated samples — but also requires sufficient statistics. To limit the required number of events, the periodicity of the sensor structure is utilized and regions of typically $100 \times 100\,\mu\mathrm{m}^2$ size are overlaid using a modulo operation (remainder

of a devision). Thus the variables x_{mod} and y_{mod} are defined as

$$x_{mod} = x_{TEL} \text{ modulo } 100\,\mu\text{m and} \tag{6.16}$$

$$y_{mod} = y_{TEL} \text{ modulo } 100\,\mu\text{m}.$$
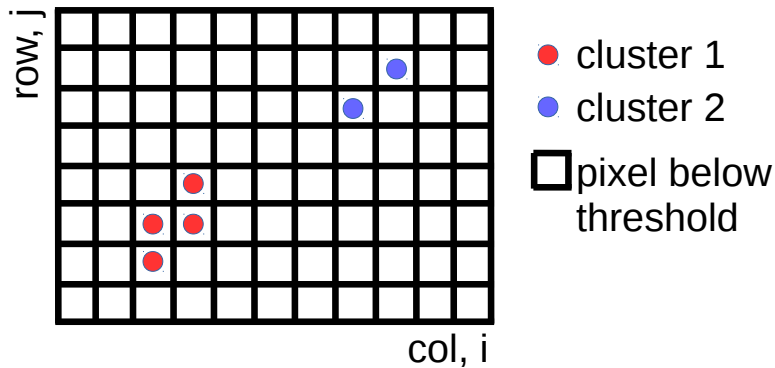
Figure 6.10.: Illustration of the cluster size definitions. For cluster 1 (red) $n_{px} = 4$, $n_{col} = 2$ and $n_{row} = 3$. For cluster 2 (blue) $n_{px} = n_{col} = n_{row} = 2$.

6.4. Selection Criteria

The methods and algorithms for the reconstruction of telescope tracks and observables characterizing the investigated pixel sensors are not perfect and may be affected by background processes. For example, noisy pixels or broken clusters can mimic particle hits in the planes of the beam telescope. With a certain probability, combinations of those fake hits with further fake or real hits fulfill the track requirements and result in a fake track. As there was no corresponding real particle hit in the investigated sample this could be interpreted as false zero efficiency measurement. To limit the influence of such processes on the reconstructed observables a set of selection criteria, defined below, is applied on the reconstructed objects. Some of these selection criteria are applied to all reconstructed quantities. An additional set of cuts is applied to study the spatial resolution and related quantities. A comprehensive overview is given in section 7.1.

6.4.1. Time-Reference Link

The planes of the beam telescope, the MIMOSA 26 sensors, are read out with an integration time of 115.2 µs. In contrast, the shaping of the ROC4SENS corresponds to an integration time on the order of some µs. Usually, the particle rate at TB21 is higher than $(115.2\,\mu\text{s})^{-1} = 8.7\,\text{kHz}$, so that several particles may pass the acceptance of the setup within one integration cycle of the MIMOSA 26 sensors. Typically just one of those particles caused the trigger signal and is contained in the effective integration time of the ROC4SENS. Thus these pileup tracks, corresponding to the additional particles, can

not be linked to measurements in the DUT which would again cause false zero efficiency entries, to give an example.

To exclude the pileup tracks, all telescope tracks are linked to the time reference plane introduced in section 5.2.2. The time reference has an integration time comparable to the integration time of the ROC4SENS, so it can be used to confirm that a track has correct timing with respect to the DUT. To link a telescope track to a hit in the time reference plane, the crossing point between the track and the time reference plane is calculated and transformed into the local coordinate system of the time reference plane. To do so, the same procedure as for the DUT, discussed in section 6.2, is applied. The residuals between the track intersections and cluster positions in the time reference plane Δx_{REF} and Δy_{REF} are calculated. A track is considered as in time with the DUT if it fulfills

$$|\Delta x_{REF}| \leq 150\,\mu m \text{ and} \tag{6.17}$$
$$|\Delta y_{REF}| \leq 150\,\mu m.$$

6.4.2. Track Isolation

As discussed above, it is possible that several telescope tracks are reconstructed. If these tracks intersections with the DUT or the time reference plane are too close to each other, ambiguities may follow. For example, only one of those tracks might be in time, but both point to the same cluster in the time reference plane (fulfill equation 6.17). To prevent such ambiguities, track isolation criteria are used.

To define track isolation at the DUT the upstream triplet tracks are extrapolated to the z-position of the DUT. For each upstream triplet track, the radial distance to the other upstream triplet tracks is calculated and the smallest distance r_{min} is stored. A track is considered isolated at the DUT, if

$$r_{min} < 600\,\mu m. \tag{6.18}$$

Track isolation at the time reference plane is defined for downstream telescope tracks, interpolated to the z-position of the time reference plane. The criterion on the minimal radial distance is the same as for isolation at the DUT.

6.4.3. Fiducial Region

For various reasons it is required to constrain the reconstruction of a quantity to a certain spatial region on the investigated sample, referred to as fiducial region. This is nicely illustrated on the efficiency map in figure 6.11. The physical dimension of the sensor corresponds to a fiducial region of $\approx \pm 3.9\,mm$ in the x- and y-direction. In addition, this sensor has an inefficient region in the upper right corner, likely due to defect bump bond connections, and a row of dead pixels at $y \approx 3.2$. Including these regions in an efficiency

analysis would spoil the comparison to other samples without such defects. Therefore the corresponding area is excluded from the fiducial region.

For most investigated samples, the fiducial regions is constraining the analysis to the physical dimensions of the sample or to the beam-spot region defined in section 3.3.
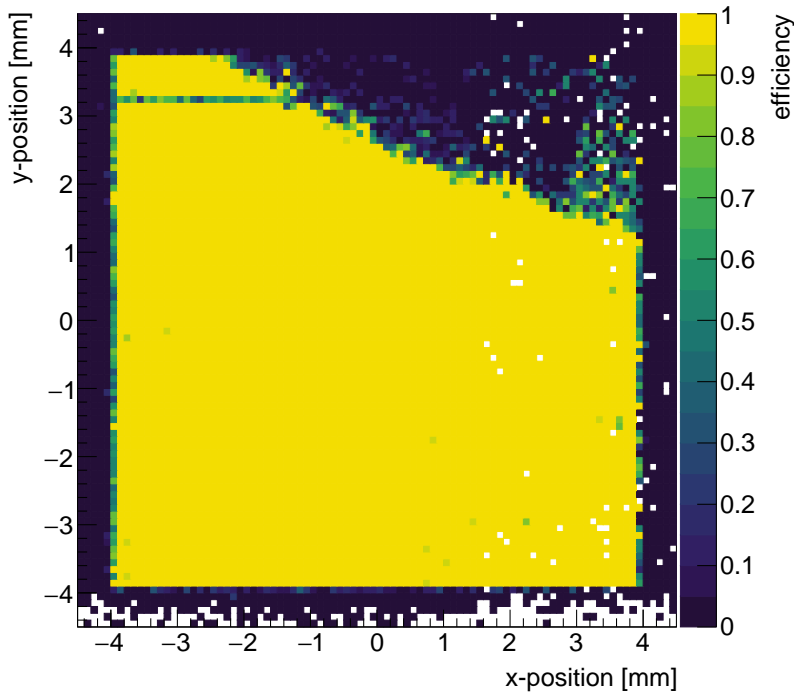
Figure 6.11.: Efficiency as a function of the position on the DUT. The investigated sample is proton irradiated to $\phi_{eq} = 2.4 \times 10^{15}\,\text{cm}^{-2}$ in the beam-spot region and operated at $V_{bias} = 800\,\text{V}$. The measurements are taken at vertical beam incidence. Apart from the fiducial selection, the selection criteria are the same as in chapter 7.

6.4.4. Timing Cut

The TLU and the DTB provide a time stamp for each event. The time passed since the previous event is calculated for each time stamp and denoted as t_{TLUi} and t_{DTBi}. To assure synchronization between the events recorded by the two devices a timing criterion is defined by

$$|t_{TLUi} - t_{DTBi}| < 20\,\mu s. \tag{6.19}$$

Events fulfilling this criterion are considered in time. Typically more than $99.8\,\%$ of the events pass this selection.

6.4.5. Residual Pairing

To study their resolutions, residuals are calculated between the position measurements provided by two devices. Whenever there is more than one position measurement in at least one of the two devices there are ambiguous combinations. This occurs for example if multiple particles pass the setup within the integration time of (one of) the devices or if noise fluctuations fake particle hits. The situation is illustrated in figure 6.12. The question is: Which combinations of those measurements correspond to one particle?

One solution is to request exactly one measurement in each device. Another solution is to pair combinations fulfilling the following conditions:

1. The measurement j on device 1 is closest to measurement k on device 2.

2. The measurement k on device 2 is closest to measurement j on device 1.

Pairs fulfilling this condition are circled in figure 6.12. Residual distributions obtained applying these two methods (requesting exactly one measurement and the pairing approach), are shown in figure 6.13. While the shape of the two distributions agrees within errors, the latter approach yields 8.5 times more entries, owing to the fact that most events have more than one telescope track or DUT hit. Typically the procedure is applied for the DUT residual, where one position measurement is provided by the DUT and the other is derived from the extrapolation of telescope tracks.
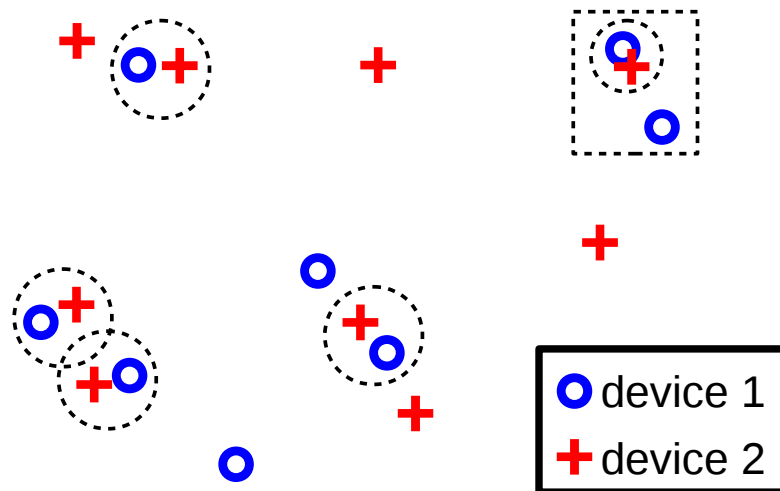
Figure 6.12.: Sketch of several position measurements provided by two devices. Combinations fulfilling the pairing condition are indicated by dashed circles.
Note that the two matching conditions are not redundant. Considering e.g. the measurements in the dashed box, the first condition is fulfilled only for the measurements in the dashed circle, while the second condition is fulfilled for both measurements on device 1.
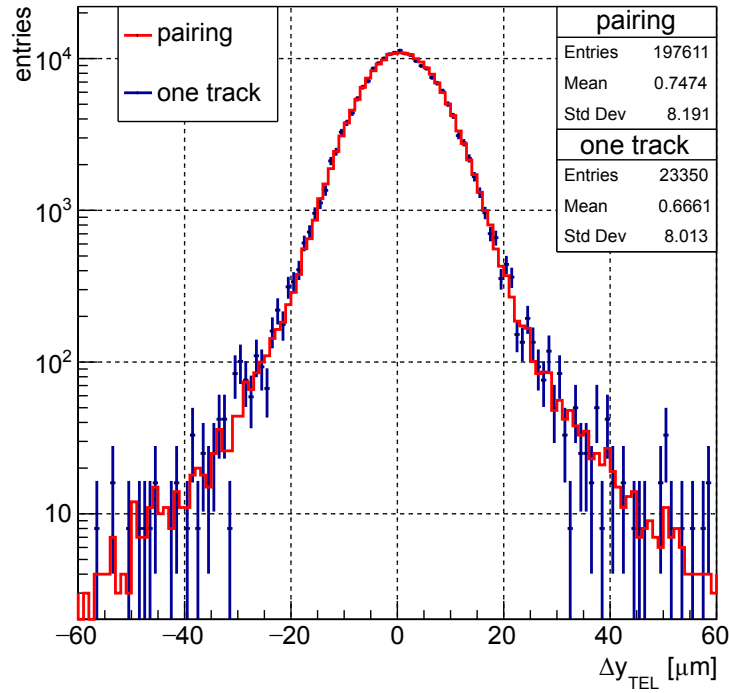
Figure 6.13.: Distributions of Δy_{TEL} for the run also presented in figure 6.8 applying fewer track selection criteria. Track isolation at the DUT and the time reference plane are requested and the tracks are to pass the fiducial region of the investigated sensor. In one case, track combinations fulfilling the pairing requirement are selected (pairing). In the other case, the number of tracks in the upstream and downstream triplet is restricted to one. The latter distribution is scaled for better comparability.

6.4.6. Residual Cut

When quantities like the cluster charge or cluster size are investigated it is crucial to remember that not all pixels above threshold indicate real particle hits. Noise fluctuations may fake hits and thereby affect reconstructed quantities. Telescope tracks are used to confirm the origin of e.g. a cluster to suppress fakes. In practice, this is implemented as a cut on the residuals

$$\Delta x_{DUT} < c_x \text{ and} \tag{6.20}$$
$$\Delta y_{DUT} < c_y.$$

The numbers for c_x and c_y correspond to two times the RMS of a typical residual and are given in table 6.1. They are adapted to the pitch of the investigated sample in the respective direction.

Additionally, these cuts are used to obtain cleaner residual distributions. A cut on Δx_{DUT} is applied to study Δy_{DUT} and vice versa, assuming that Δx_{DUT} and Δy_{DUT} are uncorrelated. The effect is that ambiguous combinations are geometrically constrained to a small corridor, thus suppressed.

Table 6.1.: Values for c_x and c_y, chosen for the corresponding pitch.

Pitch [µm]	25	50	100
c_x and c_y [µm]	14.4	28.9	57.7

6.4.7. Charge Cut

Particle hits with large energy depositions — associated with the generation of δ-electrons — can yield large residual values. This is due to the fact that the additional charge deposition of the δ-electrons can shift the "center-of-gravity" of the deposited charge with respect to the trajectory of the primary particle, as discussed in [129] and demonstrated experimentally in [45]. For the presented measurements this correlation is illustrated in figure 6.14, where distributions of the cluster charge and the mean of $|\Delta y_{DUT}|^2$ as a function of the cluster charge are shown.

These rare, large charge depositions have a great influence on the RMS of Δy_{DUT}. In practice this effect is frequently suppressed due to saturation of amplifiers, digitization (large depositions populate the overflow bin) or by explicit truncation of large charges. In this work events above a certain charge limit are excluded for resolutions studies. This charge limit is chosen such that 10% of the events are discarded (see figure 6.14).

6.5. Conclusion

In this chapter, the reconstruction of tracks in the beam telescope, the definition of observables in the DUT and the applied event selection criteria are described. The corrections of the measured signal for baseline oscillations and crosstalk between consecutively read out pixels, shown in section 6.3.1, are to be emphasized. These techniques are fundamental for this work and form a foundation for edge-on measurements in [98] and the resolution studies on sensors with pixels sizes of $25 \times 100 \, \mu m^2$ in [115]. Another challenge was the development of a procedure to estimate the hit resolution of a sensor module, where the truncated RMS, introduced in 6.3.4, and the residual pairing method, in sec-

---

[2]The mean of $|\Delta y_{DUT}|$ is strongly correlated with the RMS of Δy_{DUT} (resolution) but is more robust with respect to outliers since they do not contribute quadratically. This becomes significant if the resolution is investigated e.g. differential in cluster charge or in-pixel position, since the events are distributed over several bins.

tion 6.4.5, are to be emphasized. These procedures were developed in collaboration with
Irene Zoi [115] [130].
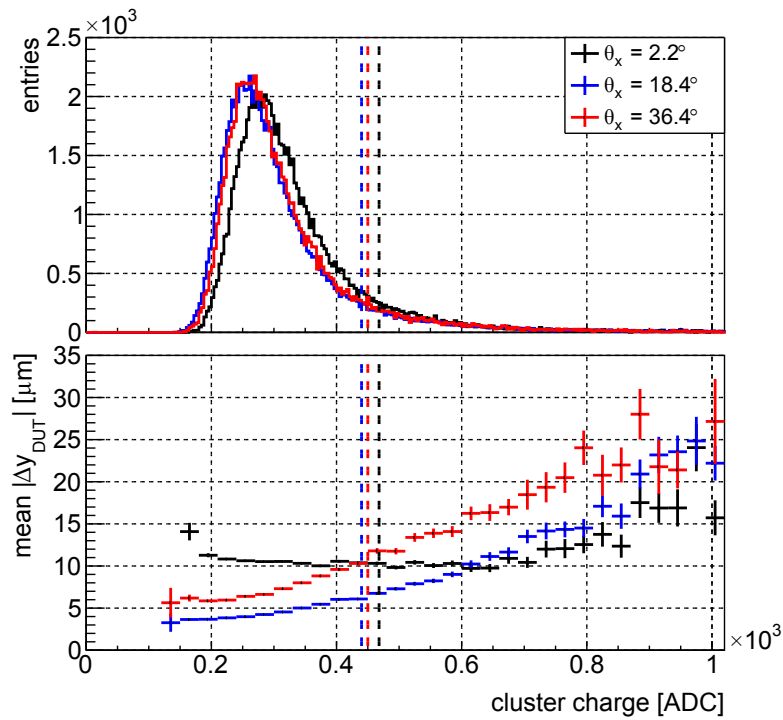
Figure 6.14.: Distributions of the cluster charge (upper panel) and the mean of $|\Delta y_{DUT}|$
as a function of the cluster charge (lower panel). The cluster charge is
scaled by $\cos(\theta_{xD})^{-1}$ to correct for the larger charge deposition for larger
θ_x. The measurements are taken on a non-irradiated sensor with a pixel
size of $50 \times 50\,\mu\text{m}^2$ operated at $V_{bias} = 120\,\text{V}$. The dashed line separates
$90\,\%$ and $10\,\%$ of the entries on their left, right respectively. Note that the
measurements at 2.2° are taken with different ROC4SENS settings, yielding
a slightly higher gain.

7. Pixel Sensor Characterization

The results of the test-beam measurements on planar sensor prototypes for the CMS Phase-2 Upgrade, bump bonded to ROC4SENS readout chips are presented in this chapter. First, some general information on the measurements and reconstruction is summarized. Then the results on the non-irradiated, neutron irradiated and proton irradiated samples are discussed with focus on hit efficiency and resolution. Two key questions are answered:

- Do these sensors permit a hit efficiency sufficient for operation in the layer 2 of the CMS Phase 2 Inner Tracker after proton irradiation?

- Which of the prototype designs has the best performance and would be a promising candidate for the upgrade of the detector?

List of Own Contributions   The author's contributions to the results presented in this chapter include:

- Comprehensive analysis of the presented test-beam measurements.

- Quality assessment of the analyzed data with respect to alignment and the corrections applied to the pixel response and the reconstructed quantities.

- Investigation of the systematic effects.

A subset of the presented results is published in [131] and [88]. A third publication with more detail and including more results is prepared at the time of writing [96]. This work has been performed under the supervision of Prof. Dr. Erika Garutti and Dr. Daniel Pitzl.

7.1. Samples, Conditions and Selection Criteria

The presented results depend on the design of the investigated sensor, its irradiation and annealing state, the measurement conditions and the selection criteria applied in the analysis. Some of these aspects are common to many of the presented results and are summarized here, for a better overview.

7. Pixel Sensor Characterization

The various sensor designs are introduced in section 3.3. The comparison of their performance and its degradation after irradiation are the main focus of this work, thus the design differences are discussed alongside the results. However, there are several common aspects:

- **Inter-Pixel Isolation:** Most of the sensors have p-stop inter-pixel isolation. If a sensor has p-spray inter-pixel isolation this is explicitly mentioned.

- **Substrate Options:** There are three substrate options for the investigated sensors, FTH, FDB and FDD, introduced in section 3.3. If not stated otherwise one of the first two options is used. Between them no significant differences are observed.

Changing measurement conditions add to the systematic uncertainties of the results, therefore, measurement conditions are usually kept the same if not explicitly sketched. Typically the measurements are taken for the following conditions:

- **Temperature:** The non-irradiated sensor modules are measured at room temperature and the irradiated sensor modules are measured at about $-24\,°C$. In both cases, temperature variations are estimated to be on the order of $1\,°C$. The temperature dependence of the pulse height DPH is found to be negligible when the analog voltage V_{ana} is adapted to compensate for the change of the analog current I_{ana}.

- **Bias Voltage:** Measurements on non-irradiated sensors are taken at $V_{bias} = 120\,V$. For irradiated samples, $V_{bias} = 800\,V$ is used.

- **Track Angle:** Most of the measurements are taken for DUT inclinations of $\theta_x = \theta_y = 0$, meaning that the plane of the DUT is parallel to the planes of the beam telescope and vertical to the electron beam axis. Spatial resolutions are studied as a function of the track angle θ_x, ranging from 0° to 40°.

- **Beam Momentum:** The momentum of the electron beam is $5.2\,GeV/c$.

- **Analog Current:** The analog current I_{ana} of the ROC4SENS is set to values between $40\,mA$ and $50\,mA$.

A common set of selection criteria, defined in 6.4, is used for all the investigated quantities. Those common criteria are:

- **Time Reference Link:** Telescope tracks have to be linked to the time reference plane.

- **Track Isolation:** Track isolation at the time reference plane is requested.

- **Timing Cut:** The timing cut constrains the time difference between the TLU and DTB time measurements.

- **Fiducial Cut:** In general the fiducial region corresponds to the active region of the investigated sensor modules. Additionally, regions with dead pixels are excluded from the fiducial region.

Additional selection criteria are applied to study the resolution and resolution related quantities like the cluster size n_{px} and the projected cluster sizes n_{col} and n_{row}. This is due to the fact that cluster size and resolution are strongly related and otherwise comparison might be misleading. The additional criteria are:

- **Residual Cut:** The residual cut is applied on either Δx_{DUT} or Δy_{DUT}. For n_{px} the cut is on Δy_{DUT}. No significant differences are observed if instead a cut on Δx_{DUT} is used. The projected cluster sizes n_{col} and n_{row} are usually shown as a function of x_{mod} or y_{mod}. The cut is applied in the orthogonal direction.

- **Residual Pairing:** The residual pairing method is used.

- **Charge Cut:** The charge cut is used to discard $10\,\%$ of the events with the highest charge deposition in the DUT.

It should be noted, that this last set of selection criteria is related to the investigated observables. Their effects on the distribution of Δy_{DUT} and DPH are shown in figure 7.1.

(a) (b)
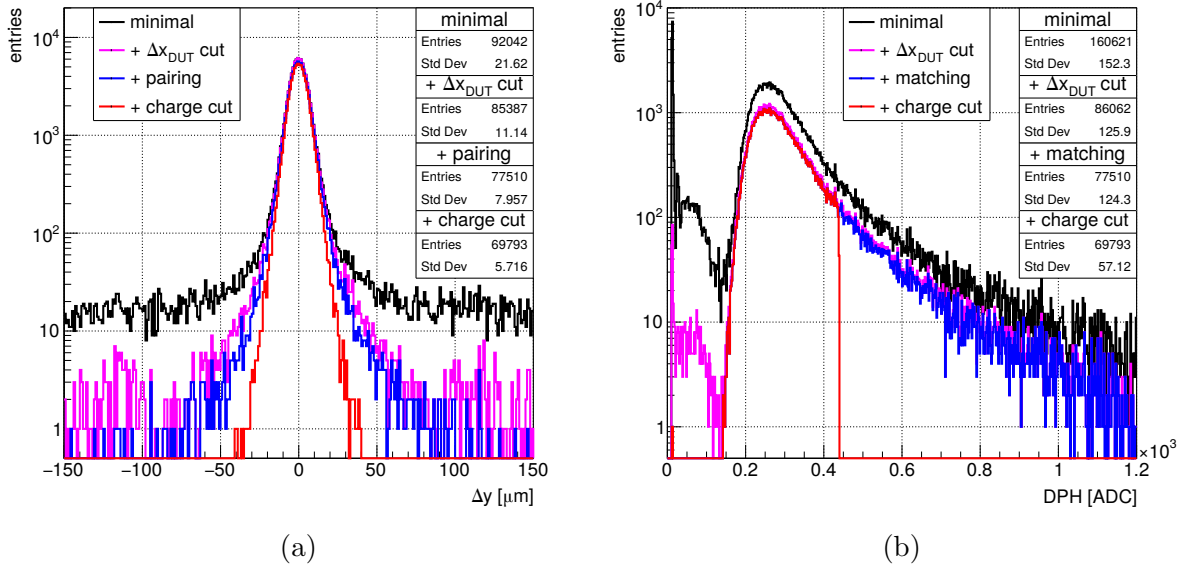
Figure 7.1.: Distributions of the residual Δy_{DUT} (a) and cluster charge DPH (b) successively adding the selection criteria for resolution studies. The DUT is a non-irradiated sensor with a pixel size of $50 \times 50\,\mathrm{\mu m}^2$ operated at $V_{bias} = 120\,\mathrm{V}$. The spacing of the planes in the beam telescope triplets is $\approx 150\,\mathrm{mm}$ and the closest planes of the two triplets are $80\,\mathrm{mm}$ apart with the DUT half the way between them. The DUT is rotated around the x-axis, such that $\theta_{xD} = 18.4°$.

7.2. Non-Irradiated Sensors

The characterization of non-irradiated pixel modules gives first valuable insights into the properties of the investigated pixel sensors. To begin, measurements of the cluster size as a function of the in-pixel position illustrate the differences between the sensor designs and wafer material. It follows a discussion of general properties like signal, noise and efficiency. Finally, the resolution as a function of the incidence angle is studied for a sensor with a pixel size of $50 \times 50\,\mu\mathrm{m}^2$ and one with $25 \times 100\,\mu\mathrm{m}^2$ and bricked implants. The latter reveals surprising properties, rendering it an interesting, non-baseline design option for the CMS Phase 2 Upgrade.

7.2.1. Cluster Size

The effect of charge sharing has a large impact on the hit resolution of pixel modules. The amount of charge sharing has a direct impact on the cluster size and depends on the track angle with respect to the sensor plane, the magnetic field, diffusion and shape of the electric field in the sensor. The design of the pixel cell and inter-pixel isolation technology have an impact on this electric field and may alter the observed cluster size.

The cluster size is reconstructed using the same selection as for the reconstruction of the spatial resolution. The cut on the pixel charge corresponds to $5\,\%$ of the MPV, as discussed in section 7.2.4. In figure 7.2a the cluster size is shown as a function of the in-pixel position for a group of four pixels. A representative picture of these four pixels is shown in figure 7.2b. For a better quantitative assessment, the projected cluster sizes n_{col} and n_{row} are shown in figure 7.2c. The average cluster size is about one if the central area of a pixel is hit and ideally reaches two and four in a region around the edges and corners respectively. Due to the finite telescope track resolution, these regions are smeared and lower values, 1.8 and 3, are observed.

In figure 7.2d n_{col} is shown as a function of x_{mod} for four sensors with different pixel cell designs. The comparison yields three observations. First, there is no significant difference between the regular (implant width $30\,\mu\mathrm{m}$) and the enlarged implant design (implant width $33.5\,\mu\mathrm{m}$). This does not hold for irradiated samples, where efficiency losses are different between the two designs, as shown in section 7.3.1 and 7.4.1. Second there is more charge sharing for sensor with open p-stop, which has the smallest implants (implant width $24\,\mu\mathrm{m}$). Third, for the sensor with large bias dots, the peaks at $0\,\mu\mathrm{m}$ and $100\,\mu\mathrm{m}$ are slightly higher than the peak at $50\,\mu\mathrm{m}$. This is due to the efficiency loss at the bias dot discussed in section 7.2.3.

A similar comparison is shown in figure 7.3, for different sensor substrate instead of different sensor designs. It appears that for the FDD substrate there is more charge sharing at the pixel boundaries, hence the larger cluster size in that region. This is due to the larger active thickness of the sensors made on FDD substrate — found to be larger
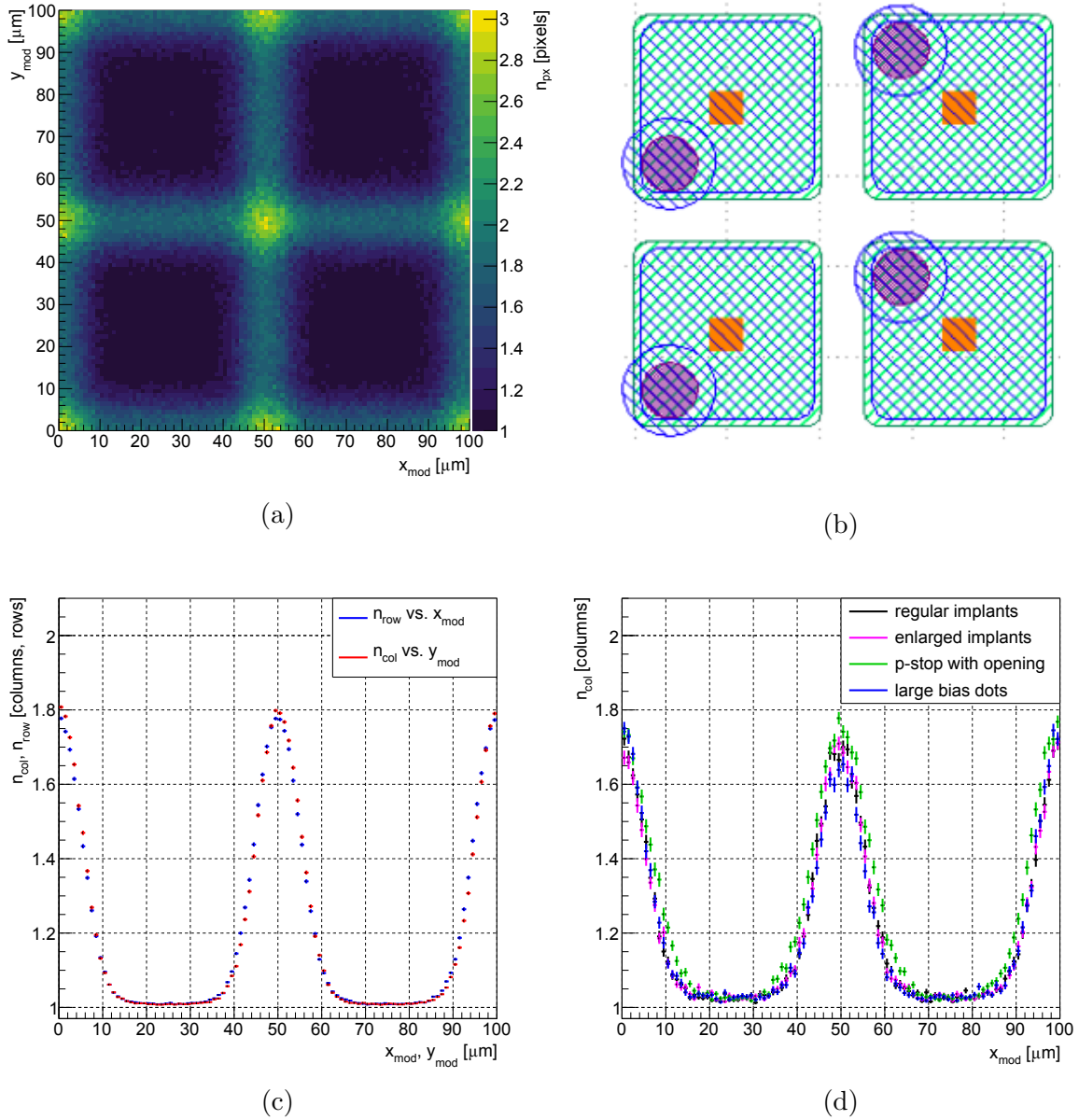
Figure 7.2.: Average cluster size as a function of the in-pixel position for non-irradiated samples with a pixel size of $50 \times 50\,\mu m^2$. In (a) the cluster size is shown as a function of the in-pixel position, measured on a sample with p-spray inter-pixel isolation and enlarged implants. The corresponding design scheme is shown in (b). In (c) the projected cluster sizes are shown for the same measurement. Both figures ((a) and (c)) contain more than 750 k entries. In (d) results for different sensor designs are compared for shorter runs (about 70 k entries), hence the larger errors. All measurements are taken at $I_{ana} \approx 125\,mA$. The beam momentum is $5.6\,GeV/c$ in (a) and (c) and $4.8\,GeV/c$ in (d).

than $175\,\mu m$ in capacitance-voltage measurements, as discussed in section 3.3. Larger active thickness leads to lower electric fields at the same voltage and longer drift paths. Both results in longer drift times and thus stronger diffusion effects.
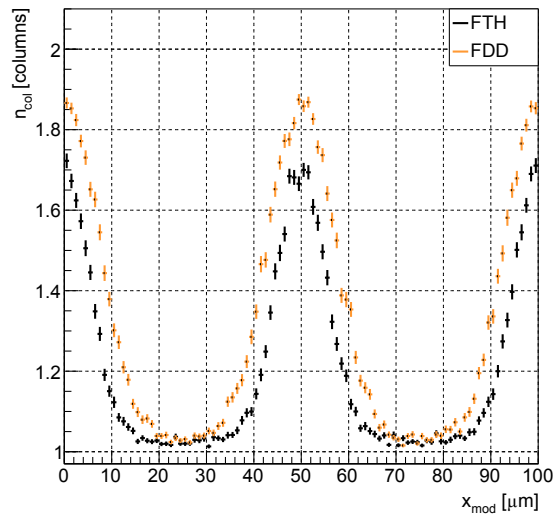
Figure 7.3.: Projected cluster size as a function of the in-pixel position. The black curve corresponds to the black curve in figure 7.2d. The orange curve is measured under the same conditions. The sensor design is the same for both curves but the substrate is FDD instead of FTH.

7.2.2. Signal and Noise

To define a signal-to-noise ratio, first, the signal is derived from the distribution of cluster DPH presented in figure 7.4a. The selection criteria are those also applied to the reconstruction of the efficiency. The convolution of a Landau- and a Gaussian distribution is fitted to the measured distribution using the method of least squares, constrained to the range with more than 20 entries per bin. The signal is defined as the MPV of the Landau distribution. For comparison, the distribution of the cluster charge is shown in figure 7.4b including an analog fit.

Second, the noise is defined as the arithmetic mean of $\sigma(DPH)$ over all pixels, the distribution of which is presented in figure 7.5a.

Using these definitions the signal-to-noise ratio is calculated for a set of sensors measured under the same conditions. The result is presented in figure 7.5b and yields a mean signal-to-noise ratio of 85 with a spread of 8.6 %. While this signal-to-noise ratio is the reason for the excellent results for efficiency and resolution, discussed in the following two sections, its reduction after irradiation is the driving factor for the worse performance of irradiated sensors.

(a) (b)
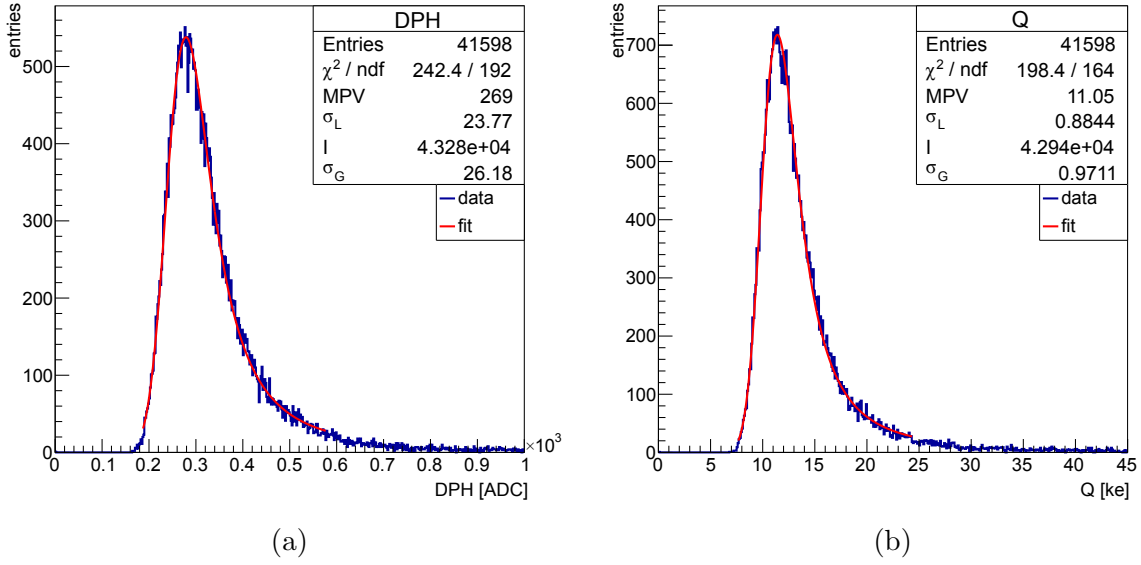
Figure 7.4.: Cluster charge distributions in DPH and Q, measured on non-irradiated samples with a pixel size of $50 \times 50\,\mu m^2$, are shown in (a) and (b). All measurements are taken at $I_{ana} \approx 50\,mA$. The convolution of a Landau- and a Gaussian distribution is fitted to the data. The MPV, width σ_L and integral I of the Landau distribution are given in the figure, together with the width σ_G of the convoluted Gaussian distribution.

(a) (b)
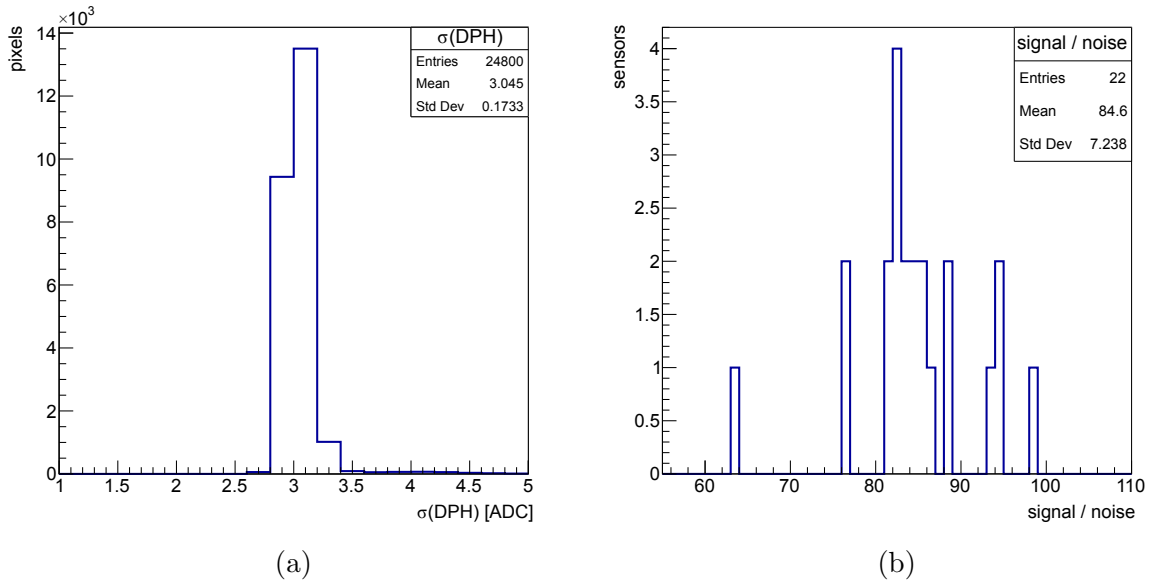
Figure 7.5.: In (a) the distribution of the pixel noise $\sigma(DPH)$ is presented for the same measurement as presented in figure 7.4. For a set of measurements taken under the same conditions, the signal-to-noise ratios are derived from the distributions of DPH and $\sigma(DPH)$. The distribution of these signal-to-noise ratios is shown in (b). Samples produced on FDD material are excluded.

7.2.3. Hit Efficiency

A hit efficiency above 99 % is a benchmark for the investigated pixel modules. The measurements on the non-irradiated pixel modules are taken at $V_{bias} = 120\,\text{V}$. For non-irradiated pixel modules at this voltage, the hit efficiency is typically well above the benchmark. The only exception are sensors with a bias dot and those with polysilicon resistors, the latter being excluded from further tests at an early stage of the test-beam campaign [96].

(a)

(b)
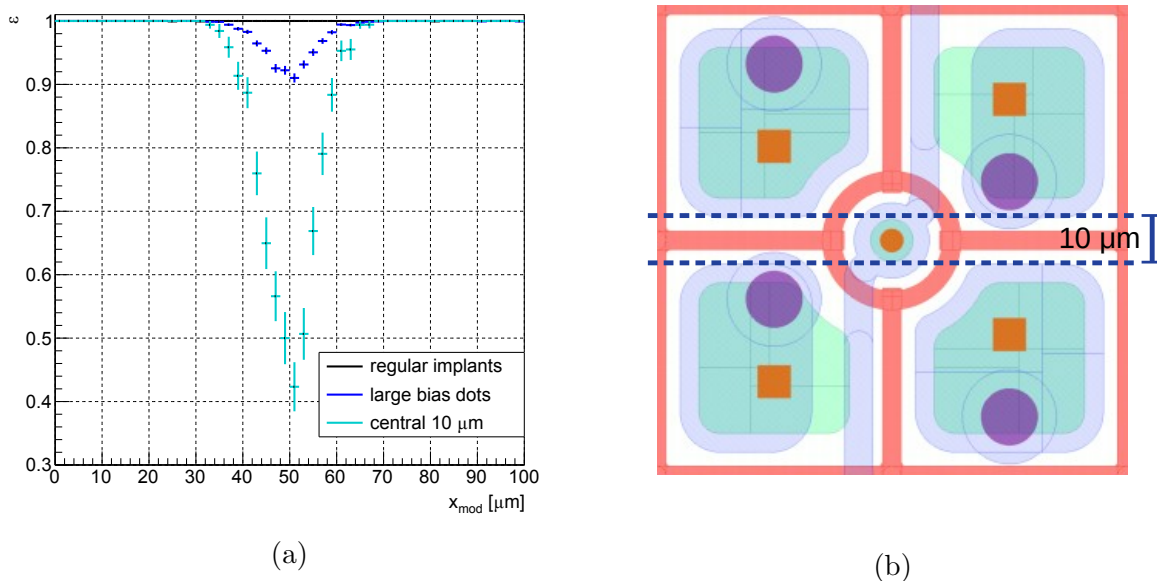
Figure 7.6.: In (a) the hit efficiency as a function of the in-pixel position is shown for two pixel modules. Both samples are non-irradiated with a pixel size of $50 \times 50\,\text{µm}^2$. The measurements are taken at $V_{bias} = 120\,\text{V}$, $I_{ana} \approx 125\,\text{mA}$ and a beam momentum of $4.8\,\text{GeV/c}$. For the sensor with regular implant design no significant efficiency losses are observed. For the sensor with bias dots, representative picture in (b), the projected efficiency drops to 92 %. Considering only the central 10 µm, indicated in (b), the efficiency at the bias dot drops to 40 %.

For sensors with a bias dot, significant efficiency losses are observed at the bias dot position, as shown in figure 7.6 (compare [132]). These losses could possibly be reduced if the bias grid potential is left floating instead of being set to ground. This can not be changed for assembled sensor modules, which is why further studies on these charge losses are not shown here. Additionally, these losses depend on the applied bias voltage, the track angle and the neutron equivalent fluence the sensor has been exposed to. Conclusive studies are performed with the RD53A readout chip and ongoing at the time of writing. First results as a function of the bias voltage and track angle are presented in [133]. Further results will be presented in [134].

It should be noted that bias voltages below 120 V would be sufficient to reach the efficiency benchmark and desirable considering power consumption. On the other hand,

even larger voltages might be needed in practice to reach the regime of mobility saturation so as to reduce the Lorentz angle in the magnetic field of the CMS detector. Especially for the sensors with $25 \times 100 \, \mu m^2$ pixel size, this needs to be considered to constrain charge sharing in the direction of $25 \, \mu m$ pitch, as discussed in section 2.3.

7.2.4. Spatial Resolution

Next to the hit efficiency the spatial resolution is a key characteristic of the investigated pixel modules. Its definition — as a single plane resolution — and reconstruction are discussed in section 6.3.4. Residual distributions for selected angles are presented in chapter 8 and compared to simulations.

The hit resolution of a sensor module depends on operational parameters like track angle, magnetic field (Lorentz angle) and the applied bias voltage. Additionally, it is affected by radiation damage (see section 7.3 and 7.4), depends on the applied algorithms for clustering and position reconstruction (see [44], and [135]) and properties of the readout chip like signal-to-noise ratio [45], gain-linearity and thresholds.

In a first step, the threshold dependence of the resolution is analyzed for a sensor with a pixel size of $50 \times 50 \, \mu m^2$ and enlarged implants at a track angle $\theta_x = 18.4°$. Therefore the threshold th_{pix} (see 6.1) is scanned to find the optimal threshold setting. The result is shown in figure 7.7a. The scanned range of $6 \, ADC$ to $30 \, ADC$ corresponds to 2.4% to 12% of the signal (Landau MPV). The variation on the resolution in this range is 10%. The optimal threshold is at $12 \, ADC$ corresponding to 5% of the signal.
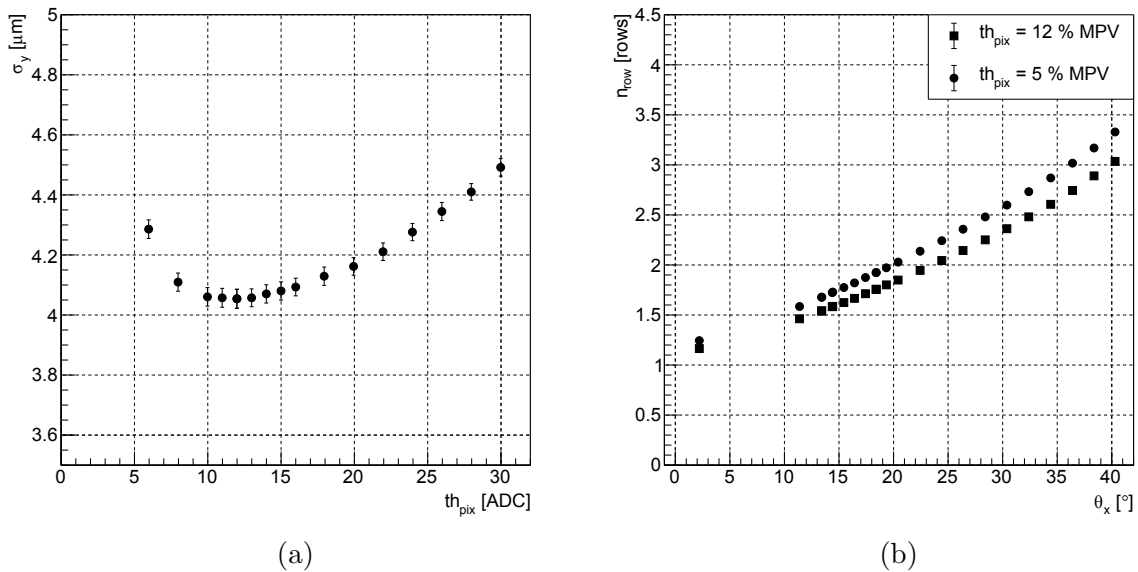
Figure 7.7.: Spatial resolution as a function of the pixel threshold (a) and projected cluster size as a function of the track incidence angle (b). The investigated sensor has a pixel size of $50 \times 50 \, \mu m^2$ and enlarged implants. The tracks hit the sensor at an angle $\theta_x = 18.4°$.

7. Pixel Sensor Characterization

The dependence of the resolution on the track incidence angle, studied on the same sensor module, is shown in figure 7.8. In general, one expects the resolution to have a minimum around $18.4° = \arctan(p/d)$, with pitch $p = 50\,\mu\text{m}$ and thickness $d = 150\,\mu\text{m}$. At this angle, the (projected) cluster size is expected to be approximately two, which allows for charge weighted position interpolation between the pixels. Note that the measured cluster size is smaller than two at that angle, due to threshold effects as figure 7.7b emphasizes. For angles larger than $18.4°$ the charge is distributed over more pixels, so the signal-to-noise ratio (per pixel) and likewise the resolution degrade. Also the effect of energy loss fluctuations becomes larger [45]. For smaller angles, one pixel clusters become increasingly frequent, for which interpolation between two pixel positions is not possible and the resolution approaches $\frac{p}{\sqrt{12}} = 14.4\,\mu\text{m}$. In both cases, for angles smaller and larger than the optimal one, biases in the reconstruction algorithm (equation 6.2) increase [136]. This qualitative behavior is indeed observed in the measurements, but comparing the curves for the two thresholds shows that not only the values but also the shape of the curve and the position of the minimum depends on threshold. In addition to thresholds, charge sharing by diffusion has a significant impact on the resolution, as discussed in 7.4.2.

For the threshold of $5\,\%$ of the MPV, the best resolution is observed for the measurement at $17.4°$ and reads

$$4.02\,\mu\text{m} \pm 0.03\,\mu\text{m}.$$
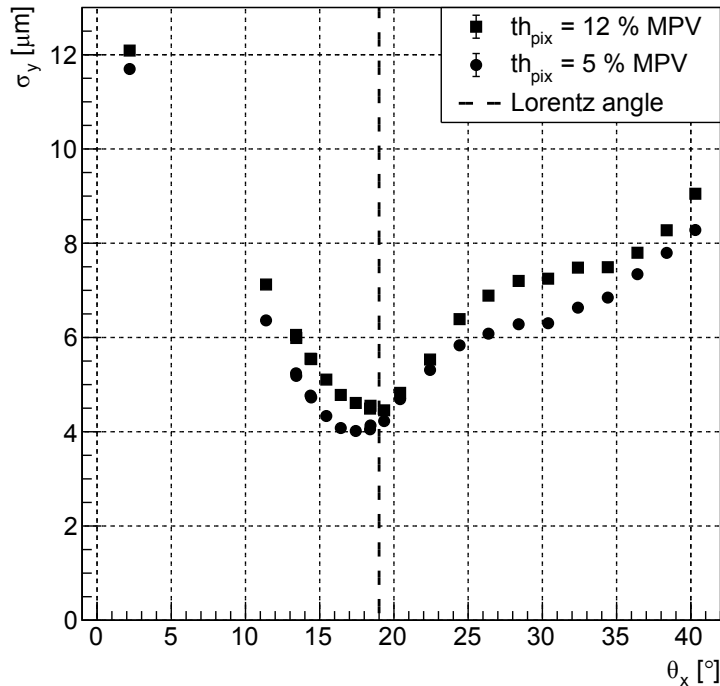
Figure 7.8.: Spatial resolution as a function of the track incidence angle, measured on a sensor with pixel size of $50 \times 50\,\mu\text{m}^2$ and enlarged implants. The Lorentz angle expected in the barrel region of the CMS pixel detector is indicated.

Thus the minimum is reached close to the Lorentz angle expected in the barrel region of the CMS pixel detector, as discussed in section 2.3. The quoted error includes only statistical uncertainties. Systematic uncertainties are discussed in section 7.5.

Given the experimental constraints, the measured telescope track resolution at the position of the DUT is about 4 µm at best. This is achieved for non-irradiated samples and $\theta_x < 20°$. For larger angles, the spacing of the telescope planes needs to be adjusted and for irradiated DUTs cooling infrastructure adds to the material budget and deteriorates the telescope track resolution. To measure the resolution of sensors with pixels sizes of $25 \times 100 \,\mu m^2$ a different setup is used based on the triplet method. The results are discussed in [115]. However, an explorative study on the resolution of sensors with bricked implants is presented in the following, as it reveals remarkable results.

The measurements for this study are taken for different track incidence angles by rotating the investigated module around its x-axis. This way charge sharing in the y-direction is increased. The y-direction corresponds to the direction of 25 µm pitch, as shown in figure 7.9. The residual distributions for these measurements are presented in figure 7.10. The corresponding resolutions are given in tabular 7.1.
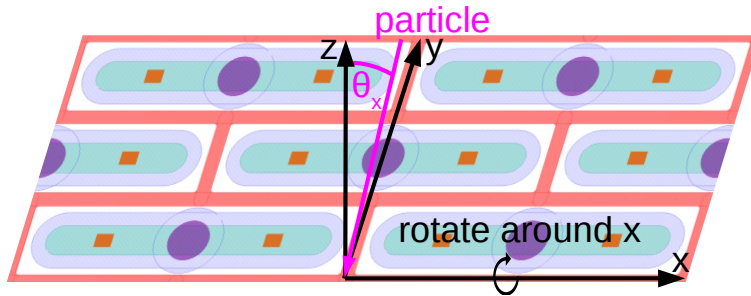
Figure 7.9.: Sensor design with bricked implants and a pixel sizes $25 \times 100 \,\mu m^2$. For the measurements the sensor is rotated around the x-axis, so there is increased charge sharing in the y-direction.

Qualitatively the residuals Δy behave as observed in [115]. The width of the residual is smallest around 9°, as expected for pitch $p = 25 \,\mu m$ with $\arctan(p/d) = 9.5°$, and increases towards smaller and larger angles. At $\theta_x = 0°$ the residual distribution is found to be similar for both sensor designs.

For the regular implants, changes of the resolution with θ_x are expected to be negligible. This does not hold for the bricked implants, due to the fact that the effective pitch is actually 50 µm instead of 100 µm if a particle deposits charge in two or more rows (2-pixels clusters in the y-direction). Comparing the residuals for the regular and bricked design at $\theta_x = 0°$ shows that even at this angle there is a significant effect, since diffusion causes a significant amount of such 2-pixel clusters. For larger θ_x this effect increases and is supposed to saturate around 18.4°, where the resolution is improved by a factor of 2.

These observations render the sensor design with bricked implants a favorable option for the Phase-2 Upgrade of the CMS pixel detector, thus it is included in the next submission

of prototype sensors. Additionally, this design choice proves to be helpful at dealing with crosstalk observed in the pixel modules with the RD53A readout chip. Further investigations concerning the resolution and radiation hardness of these sensors are ongoing at the time of writing.

(a) (b)
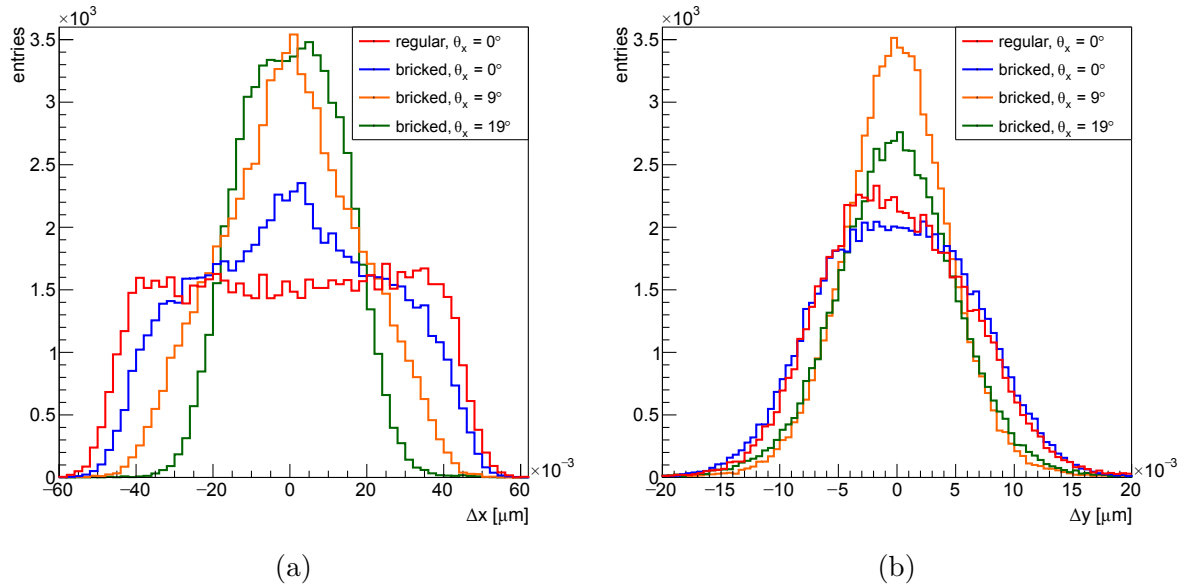
Figure 7.10.: Distributions of Δ_x (a) and Δ_y (b) measured on two sensors with pixel sizes of $25 \times 100\,\mu\text{m}^2$, one with regular implant design, the other with bricked implants as shown in figure 7.9. The measurements on the sensor with bricked implants are taken at a beam momentum of $5.6\,\text{GeV/c}$.

Table 7.1.: Resolutions σ_x and σ_y derived from the measurements presented in figure 7.10. Note that for resolutions below $4\,\mu\text{m}$ the residual width is dominated by the track resolution of the beam telescope so that there is a caveat to these values. In the last row results from [115] are added for comparison. Those are measured on a sensor with test routing.

θ_x [°]	0	9	19
bricked σ_x [µm]	23.2	17.3	12.4
bricked σ_y [µm]	5.2	2.5	3.4
regular σ_x [µm]	27.0		
regular σ_y [µm]	5.1		
test routing σ_y [µm]	5.6	3.3	4.3

7.3. Neutron Irradiated Sensors

A subset of the investigated sensor modules was irradiated with neutrons to $1\,\mathrm{MeV}$ neutron equivalent fluences ϕ_{eq} of 0.5, 3.6, 7.2 and $14.4 \times 10^{15}\,\mathrm{cm^{-2}}$. The irradiation was performed in the TRIGA. More details on the irradiation are discussed in section 3.3.

Beam test measurements on these sensor modules were performed for a set of bias voltages V_{bias}. The hit efficiencies are determined from these measurements and their dependency on V_{bias} is presented in this section. The benchmark efficiency of $99\,\%$ is reached at $V_{bias} < 800\,\mathrm{V}$ even for the highest fluence evaluated. Additionally, signal and noise are reconstructed for each of those measurements to show the dependence of the efficiency on the signal-to-threshold ratio. Studies of the spatial resolution are presented for samples irradiated to the two intermediate fluences ϕ_{eq}. It is shown that the depth dependence of the charge collection — more pronounced for neutron irradiated samples — has a significant impact on the track angle required to optimize the spatial resolution.

7.3.1. Hit Efficiency

The method for the reconstruction of hit efficiency is discussed in 6.3.3. The applied track and event selection criteria are given at the beginning of this section 7.1 and also applied for the reconstruction of other quantities in this section. As pointed out in the definition, only pixels fulfilling the hit finding condition 5.8 are considered for the efficiency studies. This is based on the significance of the signal in a pixel with respect to the pixel noise. This allows for fair comparison of samples for all conditions, as the efficiency is measured at a roughly constant fake rate.

In figure 7.11 the efficiency as a function of V_{bias} is shown for measurements taken on four sensor modules irradiated to all four fluences ϕ_{eq}. All sensors have p-stop inter-pixel isolation and a pixel size of $25 \times 100\,\mathrm{\mu m^2}$. The required bias voltages for an efficiency of $99\,\%$ are about 25, 85, 250 and $500\,\mathrm{V}$ from the lowest to highest fluence respectively, showing the degradation of the sensor performance with irradiation. Note that $25\,\mathrm{V}$ is below the full depletion voltage of the non-irradiated samples, which ranges from $55\,\mathrm{V}$ to $75\,\mathrm{V}$ as discussed in section 3.3.

There are two reasons for that: First, the signal decreases with irradiation, since the probability for trapping of charge carriers increases. Additionally, changes of the space charge density can cause the formation of low-field regions, thus reduce the charge collection further. Second, the noise increases with fluence leading to a higher threshold which is defined as four times the noise on ΔPH. This amounts to a reduction of the signal-to-threshold ratio, as shown in figure 7.12a. The variation on the signal-to-threshold ratio is dominated by the voltage dependence of the signal and its reduction with fluence ϕ_{eq}. The noise doubles from the lowest to the highest fluence and is within $5\,\%$ constant as a function of the bias voltage, as shown in figure 7.12b. Note that the definition of the
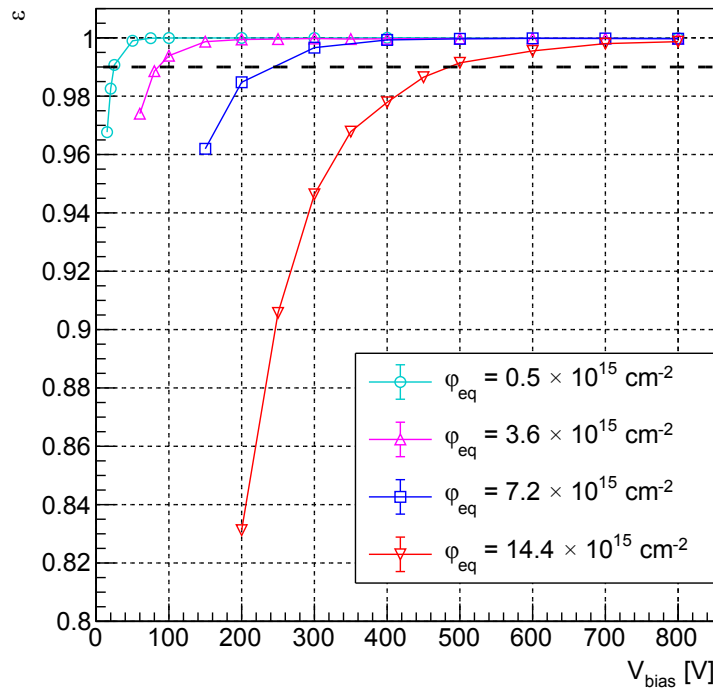
Figure 7.11.: Hit efficiency ϵ as a function of the bias voltage V_{bias}. The measurements are taken on four samples, neutron irradiated to four fluences ϕ_{eq}. All sensors have a pixel size of $25 \times 100\,\mu m^2$ and the samples irradiated to the lower three fluences have the regular implant design. The sensor irradiated to the highest fluence has enlarged implants.
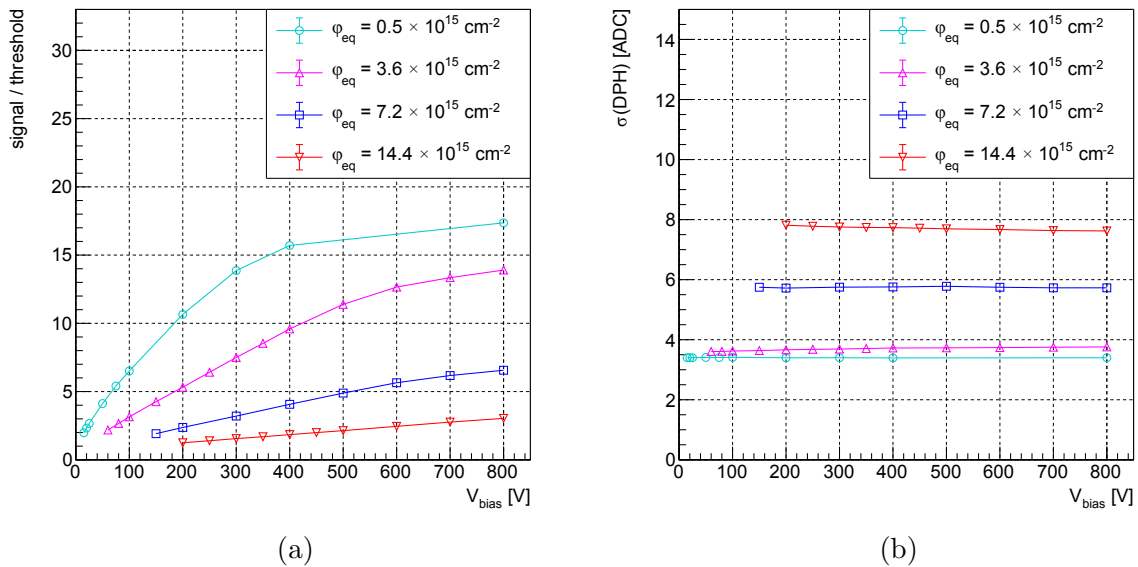
Figure 7.12.: Signal-to-threshold ratio (a) and noise (b) as a function of the bias voltage V_{bias}. The measurements are taken on four samples, neutron irradiated to four fluences ϕ_{eq}. All sensors have a pixel size of $25 \times 100\,\mu m^2$ and the samples irradiated to the lower three fluences have the regular implant design. The sensor irradiated to the highest fluence has enlarged implants.

signal is chosen to be consistent with the definition for the proton irradiated samples, discussed in section 7.4.

In figure 7.13 the inefficiency is shown as a function of the signal-to-threshold ratio. The three samples with default sensor design (lower three fluences) reach an efficiency of 99 % at a signal-to-threshold ratio of about 2.6. The sensor with maximum implant size reaches 99 % at a signal-to-threshold ratio about 2. This is due to the fact that the efficiency losses at the pixel edges are smaller for samples with larger implants. This is further discussed in 7.4.
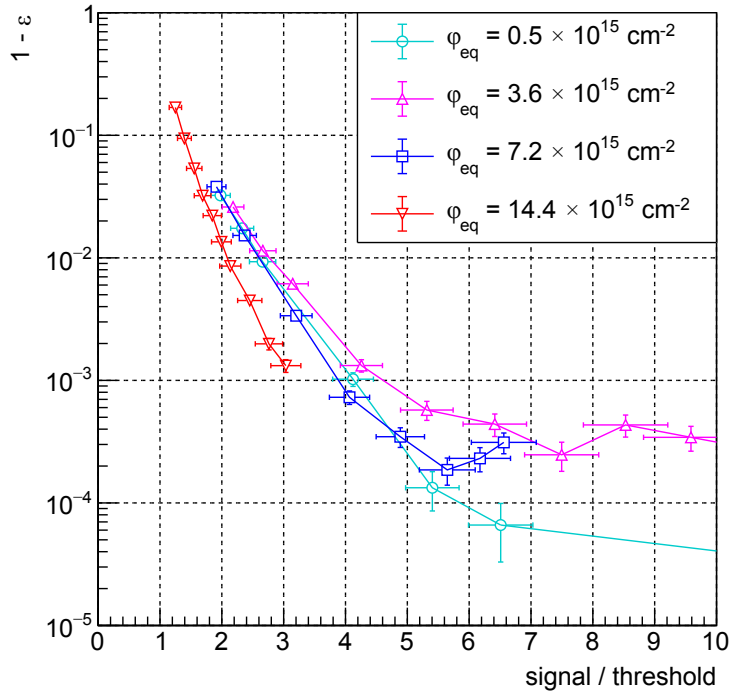
Figure 7.13.: Inefficiency as a function of the signal-to-threshold ratio. The measurements are taken on four samples, neutron irradiated to four fluences ϕ_{eq}. All sensors have a pixel size of $25 \times 100 \, \mu m^2$ and the samples irradiated to the lower three fluences have the regular implant design. The sensor irradiated to the highest fluence has enlarged implants.

An additional set of measurements was taken with several samples irradiated to fluences $\phi_{eq} = 7.2 \times 10^{15} \, cm^{-2}$ and $\phi_{eq} = 14.4 \times 10^{15} \, cm^{-2}$ to compare different sensor designs and track incidence angles.

In figure 7.14 four measurements are compared for the former fluence ϕ_{eq}. Two of the sensors have a pixel size of $25 \times 100 \, \mu m^2$, one of them with p-stop inter-pixel isolation and regular implant design, the other with p-spray inter-pixel isolation and enlarged implants. A third sample has a pixel size of $50 \times 50 \, \mu m^2$, p-stop inter-pixel isolation and the regular implant design. The third sample was measured at two track incidence angles $\theta_x = 0$ and 19°. Comparing the efficiencies as a function of the bias voltage allows for three observations. First, it occurs that the track angle has no significant impact on the

efficiency for the studied angles.

(a)   (b)
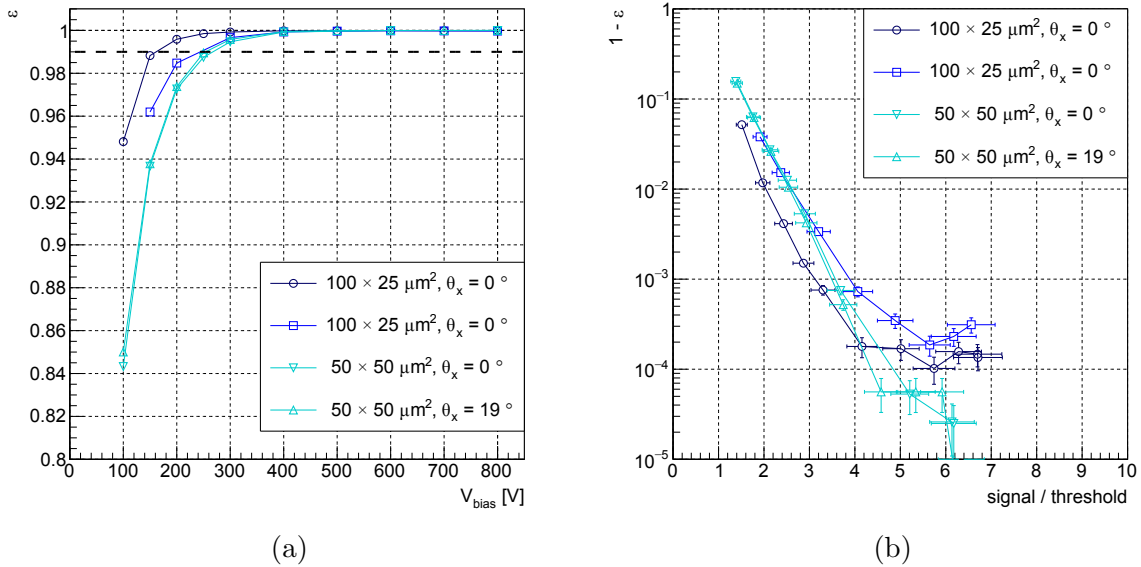
Figure 7.14.: Efficiency ϵ as a function of the bias voltage V_{bias} (a) and inefficiency as a function of the signal-to-threshold ratio (b). The measurements are taken on samples neutron irradiated to $\phi_{eq} = 7.2 \times 10^{15}\,\mathrm{cm}^{-2}$. The measurements marked by the cyan triangles are taken on the same sample. The dark-blue circles mark measurements taken on a sample with p-spray inter-pixel isolation and enlarged implants.

For larger angles, significant effects are expected. The deposited charge increases, since the distance a particle passes in silicon increases with $1/\cos(\theta_x)$. However, the charge is collected on a larger number of pixels due to charge sharing. For example, the MPV of the deposited charge is $11\,\mathrm{ke}$ for $\theta_x = 0°$ and about $14\,\mathrm{ke}$ for $\theta_x = 40°$. In the latter case though, the charge is shared between typically 3 pixels so that the signal-to-noise ratio is smaller. Systematic studies on the efficiency as a function of the track incidence angle will be presented in [134].

Second, the bias voltage for an efficiency of $99\,\%$ is about $250\,\mathrm{V}$ independent of the pixel size, although there are significant differences at lower bias voltages. Third, there is a significant difference between the measurements on the sensor with the maximized implants and the others, again likely due to the lower efficiency losses at the pixel boundaries for samples with larger implants.

These observations are confirmed in figure 7.14b, where the sensor with the maximum implant design requires a signal-to-threshold ratio of about 2 and the others require approximately 2.5 to reach an efficiency of $99\,\%$. This is in agreement with the observations in figure 7.13.

A similar comparison is presented in figure 7.15, where efficiency and inefficiency are shown as a function of the bias voltage and the signal-to-threshold ratio, respectively. The corresponding measurements are taken on two sensors with pixel size of $25 \times 100\,\mathrm{\mu m}^2$,

irradiated to $\phi_{eq} = 14.4 \times 10^{15}\,\mathrm{cm}^{-2}$. One sensor has p-stop inter-pixel isolation and enlarged implants, the other p-spray inter-pixel isolation and the regular implant design. The relative differences in implant size for this combination of sensor designs is about 20 % in the short and 2 % in the long direction. This difference is small compared to the difference between a sensor with p-stop inter-pixel isolation and the regular implant design and a sensor with p-spray inter pixel isolation and enlarged implants, where the differences are 70 % and 7 % respectively (see section 3.3). Comparing the efficiency curves, the sensor module with the regular implant design performs better, reaching an efficiency of 99 % at about 400 V, compared to 500 V for the other sensor module. In contradiction, the sensor module with the enlarged implants reaches an efficiency of 99 % at a signal-to-threshold ratio of about 2, while the other sensor module requires about 2.5, in agreement with the results presented in figure 7.13 and 7.14b. This can be explained by the fluctuations of the signal-to-noise ratio described in 7.2.2, causing systematic uncertainties in the efficiency measurements.

(a) (b)
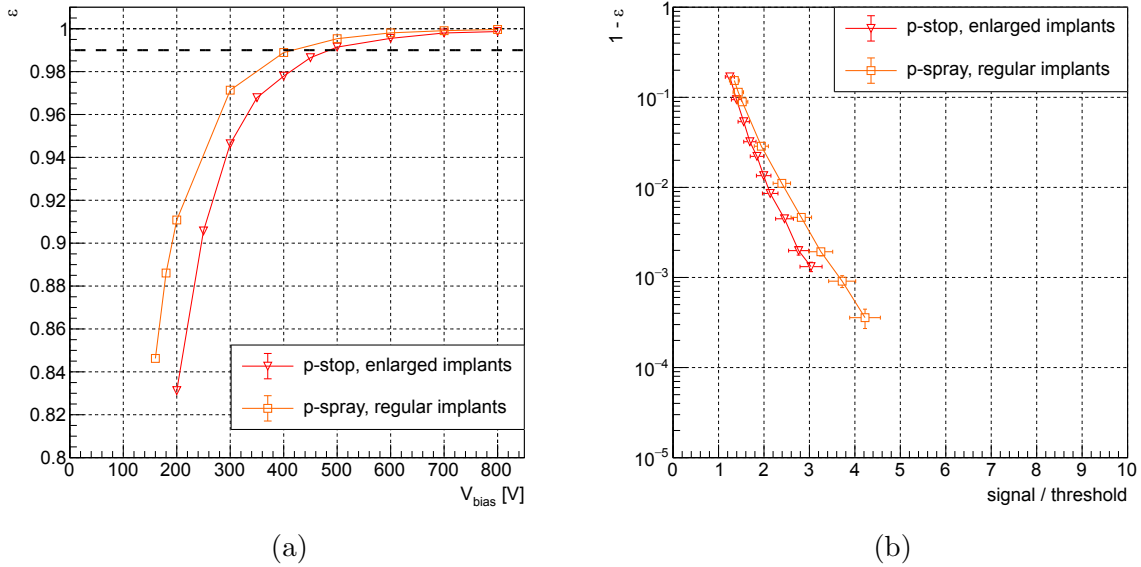
Figure 7.15.: Efficiency ϵ as a function of the bias voltage V_{bias} (a) and inefficiency as a function of the signal-to-threshold ratio (b). The measurements are taken on sensor modules neutron irradiated to $\phi_{eq} = 14.4 \times 10^{15}\,\mathrm{cm}^{-2}$ with a pixel size of $25 \times 100\,\mathrm{\mu m}^2$, different inter-pixel isolation technologies and different implant designs.

7.3.2. Spatial Resolution

The spatial resolution for the neutron irradiated sensor is studied for two sensors with a pixel size of $50 \times 50\,\mathrm{\mu m}^2$, irradiated to $\phi_{eq} = 3.6 \times 10^{15}\,\mathrm{cm}^{-2}$ and $7.2 \times 10^{15}\,\mathrm{cm}^{-2}$. The measurements are taken at $V_{bias} = 800\,\mathrm{V}$ to maximize the charge collection. The reconstruction of the spatial resolution is discussed in 6.3.4 and follows the same line as

for the non-irradiated sample. The selection criteria are those introduced for resolution studies and also applied for the reconstruction of other observables presented in this section.

In a first step, the threshold dependence of the spatial resolution is investigated for both samples using the measurements at $\theta_x = 17.5°$ and $20.9°$, corresponding to the best angles as observed in figure 7.17. The results are presented in figure 7.16a. Compared to the non-irradiated sample, studied for $\theta_x = 17.4°$, the dependence of the hit resolution on the threshold is stronger and a higher threshold is required to optimize the resolution. This is due to the increase in noise and decrease in charge collection discussed in the previous section. The optimal threshold values are at $18\,\mathrm{ADC}$ and $20\,\mathrm{ADC}$ for the lower and higher fluence respectively. They correspond to $8\,\%$ and $11\,\%$ of the Landau MPV.

(a)   (b)
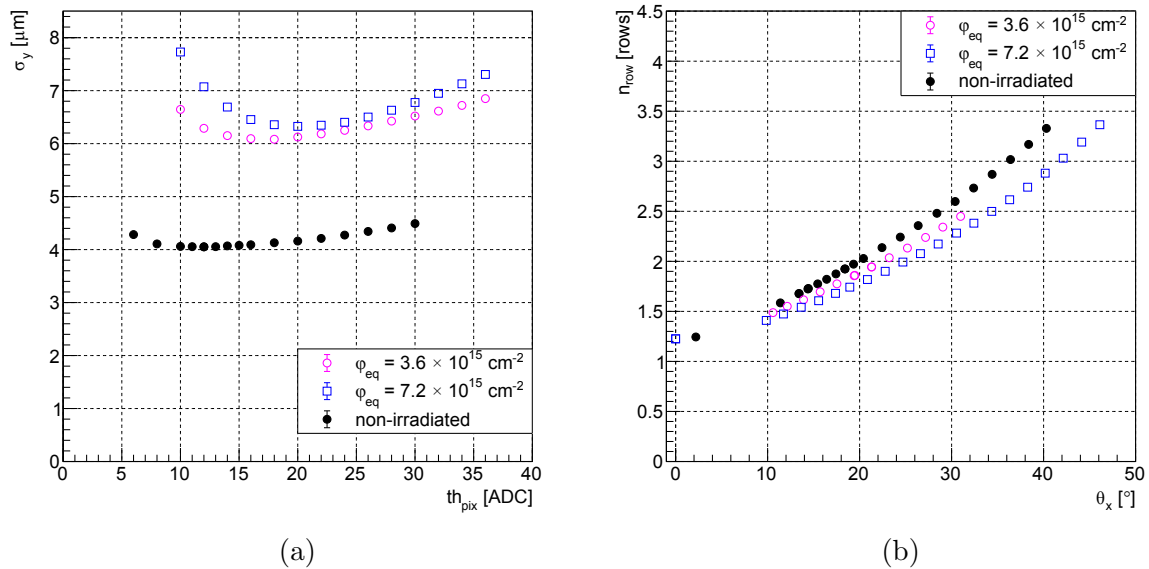
Figure 7.16.: Spatial resolution as a function of the pixel threshold (a), measured at $\theta_x = 17.5°$ (open circles) and $20.9°$ (open squares). Projected cluster size as a function of the track incidence angle (b) using the optimal threshold values, which correspond to $5\,\%$, $8\,\%$ and $11\,\%$ of the Landau MPV, increasing with ϕ_{eq}. The investigated sensors are neutron irradiated, have a pixel size of $50 \times 50\,\mathrm{\mu m}^2$, the regular implant design and p-spray and p-stop inter-pixel isolation for the lower and higher fluence, respectively.
The measurements on the non-irradiated sensor are shown for comparison and discussed in 7.2.4. The measurement in (a) is taken for $\theta_x = 18.4°$.

In figure 7.17 the spatial resolution as a function of the track incidence angle θ_x is shown for the two neutron irradiates sensor modules. The results from the non-irradiated sample are included for comparison. The first observation is that the qualitative shape of the curve is similar after irradiation. The resolution at the best angle degrades from

4.02 µm to

$$6.08\,\mu\text{m} \pm 0.06\,\mu\text{m at } \phi_{eq} = 3.6 \times 10^{15}\,\text{cm}^{-2} \text{ and}$$
$$6.33\,\mu\text{m} \pm 0.05\,\mu\text{m at } \phi_{eq} = 7.2 \times 10^{15}\,\text{cm}^{-2}.$$

The quoted errors include only statistical uncertainties. Systematic uncertainties are discussed in section 7.5. The best resolutions are found at $\theta_x = 17.5°$ and $20.9°$, for the lower and higher fluence respectively. For the higher fluence this angle is significantly larger. This is supposedly due to the fact that the depth dependence of the charge collection increasingly reduces the effective thickness of the pixel sensor with increasing fluence, which is further discussed towards the end of this section. For track angles $\theta_x \approx 0$ the differences in resolution appear to be smaller, but a lack of measurements permits further conclusions.
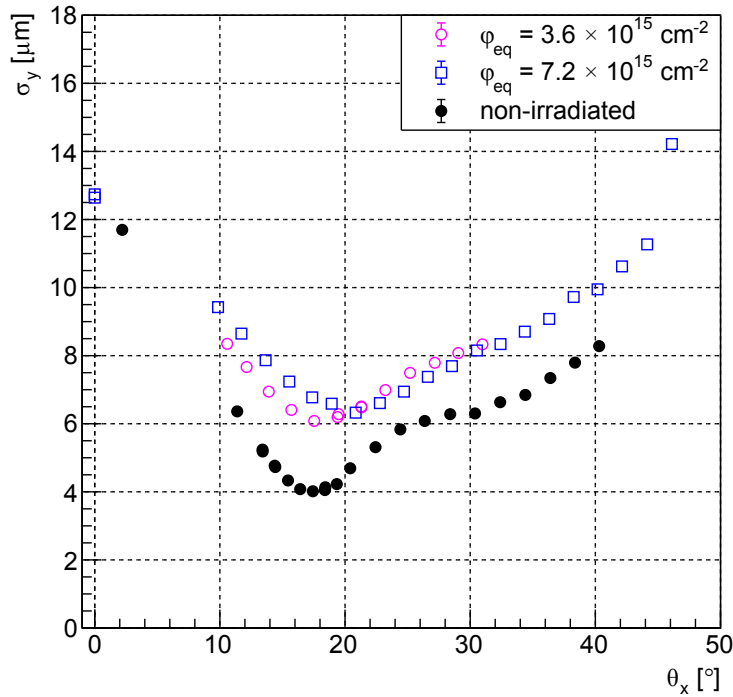
Figure 7.17.: Spatial resolution as a function of the track incidence angle. The investigated sensors are neutron irradiated, have a pixel size of $50 \times 50\,\mu\text{m}^2$, the regular implant design and p-spray and p-stop inter-pixel isolation for the lower and higher fluence, respectively. The measurements are taken at $V_{bias} = 800\,\text{V}$. The measurements on the non-irradiated sensor are shown for comparison and discussed in 7.2.4.

The corresponding dependence of the projected cluster size n_{row} on the track incidence angle θ_x is shown in figure 7.16b. The angle at which $n_{row} = 2$ increases with fluence, since the signal-to-threshold ratio increases and the effective thickness decreases with fluence.

The depth dependence of the charge collection is measured in a similar test-beam setup.

7. Pixel Sensor Characterization

The sensor module is positioned such that the beam axis is parallel to the surface of the sensor. The depth at which the particle passes the sensor is reconstructed using the beam telescope and corresponds to the y-coordinate as defined in figure 5.2.2. The charge collection is derived from the signal measured in the investigated sensor module and studied as a function of the reconstructed depth. Such edge-on measurements are presented in [98]. A subset of the results is shown in figure 7.18. The measurements are taken on the same set of sensors as the measurements presented in this work and for similar operation conditions, hence the comparability is assured. Note that electrons drift towards the n^+ implants, which are at an approximate depth of $-0.75\,\mu m$, so that the signal in this region is dominated by hole drift. The backside is at $0.75\,\mu m$, where the signal is dominated by electron drift. Since these are pixel sensors, the weighting field is non-uniform, as discussed in section 2.3.

Comparing the charge collection profiles at $800\,V$ for the two fluences reveals a stronger depth dependence for the higher fluence. This reduces the relative weight of charge deposited towards the backside of the sensor and thereby the effective thickness, which explains the shift of the minimum with fluence observed in figure 7.17.

(a) (b)
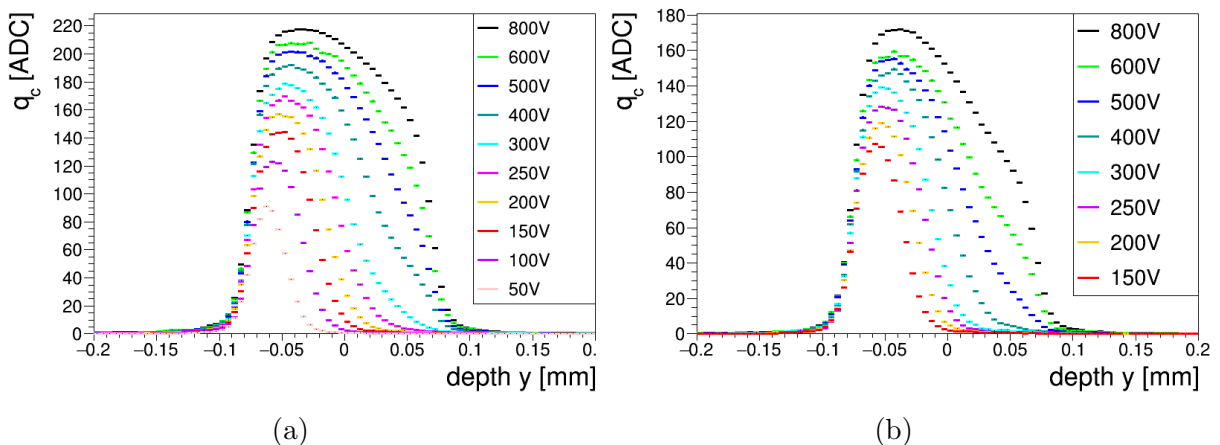
Figure 7.18.: Depth dependence of the charge collection, measured on sensors neutron irradiated to $\phi_{eq} = 3.6 \times 10^{15}\,cm^{-2}$ (a) and $7.2 \times 10^{15}\,cm^{-2}$ (b). The n^+-implants (front side) are at $y = -0.075\,mm$, the p^+-implants (back side) are at $y = 0.075\,mm$. Taken from [98].

7.4. Proton Irradiated Sensors

Another set of the investigated sensor modules was irradiated with protons at the PS. The reached $1\,MeV$ neutron equivalent fluences ϕ_{eq} are about 2.4 and $5.4 \times 10^{15}\,cm^{-2}$. The actual fluence depends on the investigated region on the sensor modules, due to non-uniformity of the irradiation, and the irradiation run (2018 and 2019). The precise numbers are quoted in the figures or captions. For more details on the irradiation and dosimetry see section 3.3.

Like for the neutron irradiated samples two studies are performed on the proton irradiated samples, one on the hit efficiency as a function of the applied bias voltage and one on the spatial resolution as a function of the track incidence angle. A first aim of these studies is to test the suitability of these sensors for the CMS Phase 2 Inner Tracker, where a flunce of up to $\phi_{eq} = 5 \times 10^{15}\,\mathrm{cm}^{-2}$ is expected in layer 2 and hit efficiencies $> 99\,\%$ are required for bias voltages below $800\,\mathrm{V}$. Additionally signal-to-threshold ratios and cluster size are investigated and the reconstructed quantities are compared for different sensor designs to choose the best sensor design for the upgraded pixel detector.
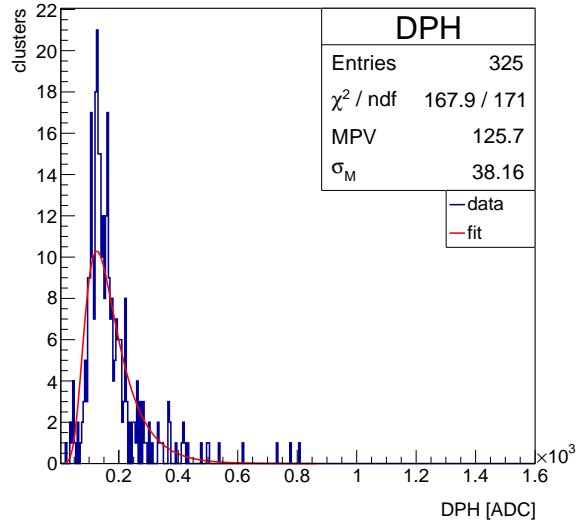
Figure 7.19.: Cluster charge distributions in DPH for one bin of $0.5 \times 0.5\,\mathrm{mm}^2$. The bin is in the beam-spot region, which is irradiated to an average fluence $\phi_{eq} = 5.4 \times 10^{15}\,\mathrm{cm}^{-2}$. The measurement is taken at a bias voltage of $800\,\mathrm{V}$. The likelihood fit of a Moyal distribution is shown and the resulting MPV and width σ_M are given. The integral of the Moyal distribution and the fit range are constrained to the number of entries and $DPH = 0$ to 5 times the mean of the distribution, respectively.

7.4.1. Hit Efficiency

In general, the methods to reconstruct the hit efficiency and further investigated observables are discussed in section 6.3.3. The criteria for the track and event selection are given in section 7.1. To take into account the non-uniformity of the irradiation two changes are applied to the selection criteria and reconstruction procedure.

First, the fiducial region is further constrained to the beam-spot region, defined as a circle with a radius $r = 2\,\mathrm{mm}$ centered around the point of highest irradiation, to limit the effect of spatial variations of the fluence. The reconstructed quantities and fluences are quoted for that region. Second, the MPV of DPH, used to calculate the signal-to-threshold ratio, is not determined from the fit of the convolution of a Landau- and a Gaussian distribution, since the spatial variation of the fluence increases the width of the

charge distribution. Instead, the sensor area is segmented in bins corresponding to an area of $0.5 \times 0.5 \, \text{mm}^2$ containing typically several hundred entries. The likelihood fit of a Moyal distribution to the distribution of the cluster DPH is used to estimate the MPV in each bin. This procedure minimizes the variance for small samples, as demonstrated in [137]. An example of the fit is shown in figure 7.19. The signal is calculated as the average of the MPVs over all bins in the beam-spot region.
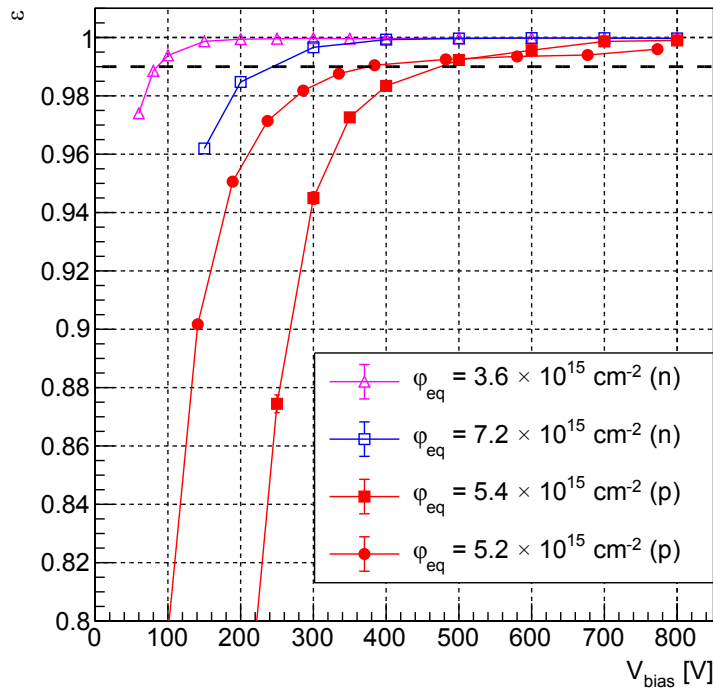
Figure 7.20.: Hit efficiency ϵ as a function of the bias voltage V_{bias}. The measurements are taken on four samples, two of them irradiated with neutrons (n) and two with protons(p). All sensors have a pixel size of $25 \times 100 \, \mu\text{m}^2$ and the regular implant design. The sensor irradiated to $\phi_{eq} = 5.2 \times 10^{15} \, \text{cm}^{-2}$ is bump bonded to an RD53A readout chip, details are given in [88].

In figure 7.20 the hit efficiency as a function of the bias voltage is shown for one of the sensor modules irradiated to an average fluence $\phi_{eq} = 5.4 \times 10^{15} \, \text{cm}^{-2}$ in the beam-spot region. An efficiency of $99 \, \%$ is reached at $V_{bias} \approx 480 \, \text{V}$, compliant with the requirement for a sensor in layer 2 of the CMS Phase 2 Inner Tracker. Two measurements from figure 7.11, taken at the two intermediate neutron fluences, are included for comparison. The bias voltage required for an efficiency of $99 \, \%$ is between $200 \, \text{V}$ and $400 \, \text{V}$ lower for the neutron irradiated sensor modules. One reason is the different bulk damage after irradiation with charged compared to neutral particles, as discussed e.g. in [138] and [139], although similar charge collection efficiencies are reported in [140] for strip sensors with a thickness of $300 \, \mu\text{m}$. The other reason is the sensitivity of the ROC4SENS with respect to the deposited ionizing dose, which is about a factor of 30 higher for the proton irradiation. To illustrate the dose sensitivity, an efficiency measurement performed on a similar sensor,

bump bonded to an RD53A readout chip — with a higher radiation tolerance — is included in the same figure. It reaches an efficiency of 99% at $V_{bias} \approx 380\,V$ but saturates at a lower efficiency since about 0.5% of masked pixels are not excluded from the analysis. Further details on the investigation of pixel sensor prototypes with the RD53A readout chip are given in [88] and will be published in [134].

A set of measurements taken on samples irradiated to the lower proton fluence is shown in figure 7.21 and 7.22. Generally speaking, all sensors modules show acceptable performance, requiring a bias voltage between $150\,V$ and $250\,V$ and a signal-to-threshold ratio between 2 and 3.5 for an efficiency of 99%.

Regarding the results of the measurements on samples with a pixel size of $25 \times 100\,\mu m^2$ in figure 7.21, the inefficiency as a function of the signal-to-threshold ratio is in agreement with the results on the neutron irradiated samples. For the sensor module with enlarged implants, an efficiency of 99% is reached at an signal-to-threshold ratio of about 2.2. For the other two samples, which have the same implant sizes the required signal-to-threshold ratio is approximately 2.5. Looking at the efficiency as a function of the bias voltage, the performance is in turn clearly better for the design with regular implants, which is possibly due to systematic effects like uncertainties on the fluence and the performance of the readout chip.

(a)   (b)
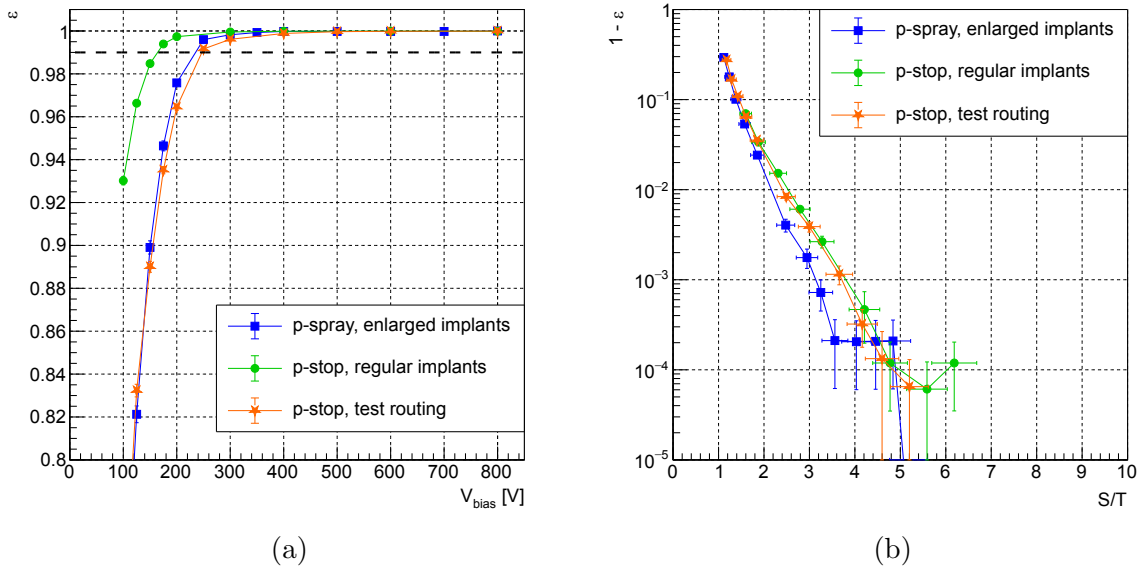
Figure 7.21.: Efficiency ϵ as a function of the bias voltage V_{bias} (a) and inefficiency as a function of the signal-to-threshold ratio (b). The measurements are taken on sensor modules with a pixel size of $25 \times 100\,\mu m^2$, different inter-pixel isolation technologies and implant designs. The samples are proton irradiated to $\phi_{eq} = 2.4 \times 10^{15}\,cm^{-2}$.

The results of two of the measurements on samples with a pixel size of $50 \times 50\,\mu m^2$ in figure 7.22 show the same trend. The smaller the implant width the larger the signal-to-threshold ratio required for an efficiency of 99%. Again the required signal-to-threshold

ratio is about 2.5 for the sensor module with regular implants (no. 2) and about 3 for the sensor module with open p-stop inter-pixel isolation. The third sensor module, which also has regular implants (no. 1) behaves differently and requires a signal-to-threshold ratio of about 3.5 for an efficiency of 99 %, on the other hand, it shows the best performance in efficiency as a function of the bias voltage.

(a)   (b)
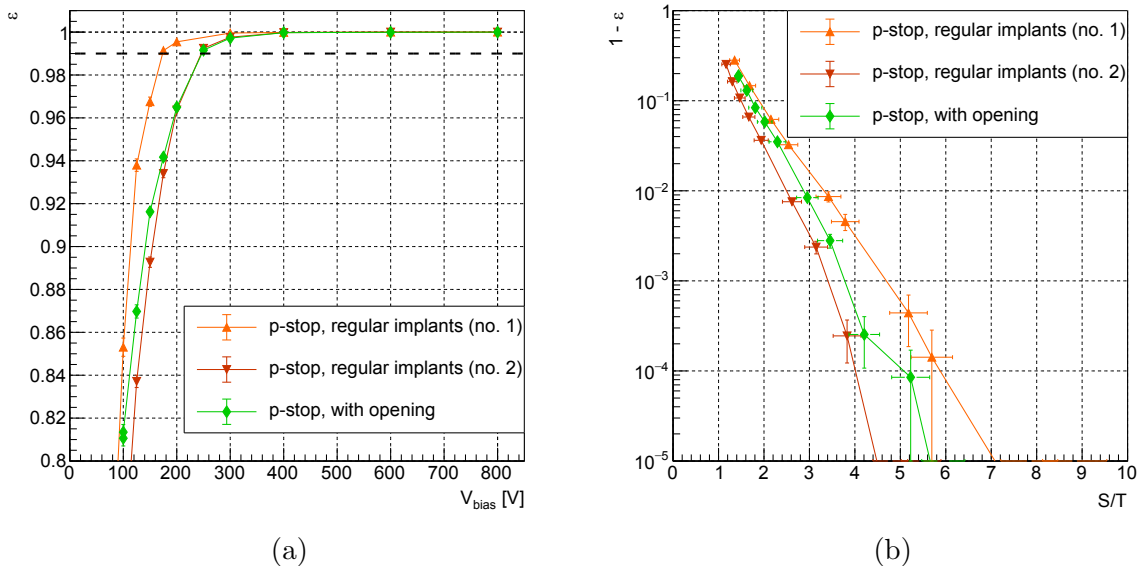
Figure 7.22.: Efficiency ϵ as a function of the bias voltage V_{bias} (a) and inefficiency as a function of the signal-to-threshold ratio (b). The measurements are taken on sensor modules with a pixel size of $50 \times 50 \, \mu m^2$ and different implant designs. The samples with regular implants are proton irradiated to $\phi_{eq} = 2.4 \times 10^{15} \, cm^{-2}$. The sample with the opening in the p-stop inter-pixel isolation are proton irradiated to $\phi_{eq} = 3.0 \times 10^{15} \, cm^{-2}$.

For sensor modules irradiated to $\phi_{eq} = 5.4 \times 10^{15} \, cm^{-2}$ and with a pixel size of $25 \times 100 \, \mu m^2$, efficiency as a function of the bias voltage and inefficiency as a function of the signal-to-threshold ratio are shown in figure 7.23. There is one sensor module with regular implants and two with enlarged implants. The bias voltages required for an efficiency of 99 % are between 100 V and 150 V smaller for the samples with enlarged implants. Also the needed signal-to-threshold ratio is about 2 for the two sensor modules with enlarged implants and about 2.4 for the sensor module with regular implants.

To further investigate the relationship between required bias voltage, accordingly the required signal-to-threshold ratio, and the implant design, the efficiency is shown as a function of the in-pixel position in figure 7.24. The figure shows measurements at 300 V and 800 V, from samples with both implant designs. At 800 V the efficiency is close to 100 % for both samples. At 300 V the efficiency in the central region, between 20 μm and 80 μm, is better than 99 % for both sensor modules. Towards the boundaries of the pixel cell at 0 μm and 100 μm, the efficiency drops to about 96 % for the sensor module with enlarged implants and 92 % for the sensor module with regular implants.

The interpretation is that charge losses at the pixel boundaries are more severe, the larger the distance between the n$^+$-implants is.

(a)   (b)
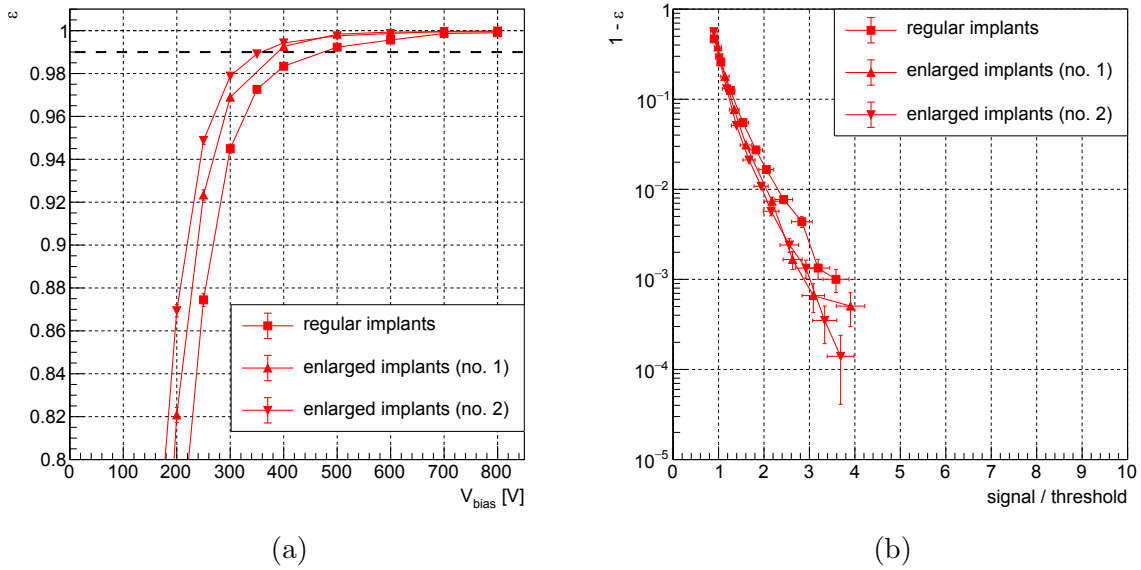
Figure 7.23.: Efficiency ϵ as a function of the bias voltage V_{bias} (a) and inefficiency as a function of the signal-to-threshold ratio (b). The measurements are taken on sensor modules with a pixel size of $25 \times 100\,\mu m^2$ and different implant designs. The samples are proton irradiated to $\phi_{eq} = 5.4 \times 10^{15}\,cm^{-2}$.
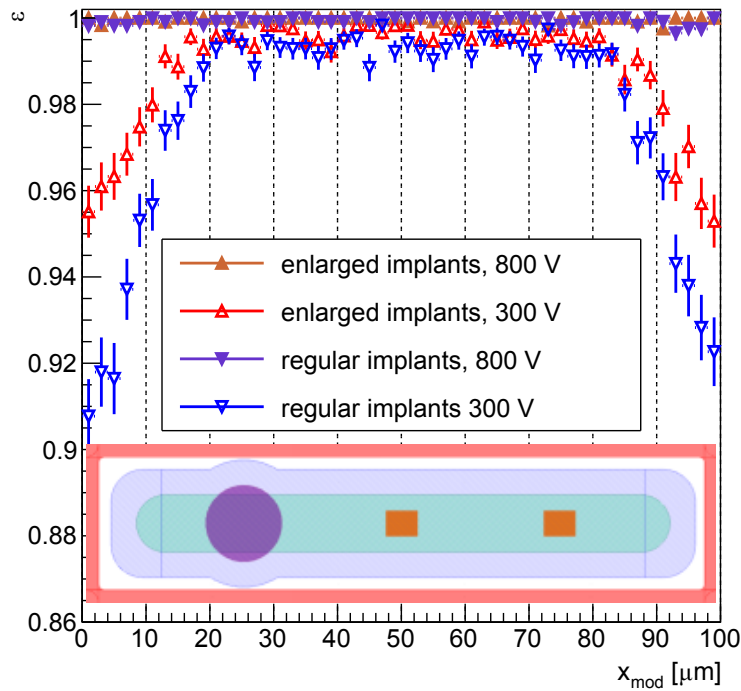
Figure 7.24.: Efficiency ϵ as a function of the in-pixel position x_{mod} for two bias voltages, corresponding to the measurements presented in figure 7.23. The samples are proton irradiated to $\phi_{eq} = 5.4 \times 10^{15}\,cm^{-2}$.

7. Pixel Sensor Characterization

In [141] similar measurements of the hit efficiency as a function of the in-pixel position are presented for sensors with implant sizes of $35 \times 35\,\mu m^2$ and $39 \times 39\,\mu m^2$. The sensors modules are neutron irradiated to $\phi_{eq} = 8 \times 10^{15}\,cm^{-2}$ and the efficiency at the pixel boundaries is smaller for the sensor with the smaller implants, in agreement with the presented results.

7.4.2. Spatial Resolution

After proton irradiation, the spatial resolution is studied for two sensor modules with a pixel size of $50 \times 50\,\mu m^2$, irradiated to $\phi_{eq} = 2.3 \times 10^{15}\,cm^{-2}$. Both samples have p-stop inter-pixel isolation, one the design with opening, the other one has enlarged implants. The selection criteria for resolution studies are applied for all observables discussed in this section. The reconstruction of the observables is discussed in 6.3.4. The measurement conditions are the same as for the other irradiated sensor modules, in particular, the bias voltage is set to 800 V.

(a) (b)
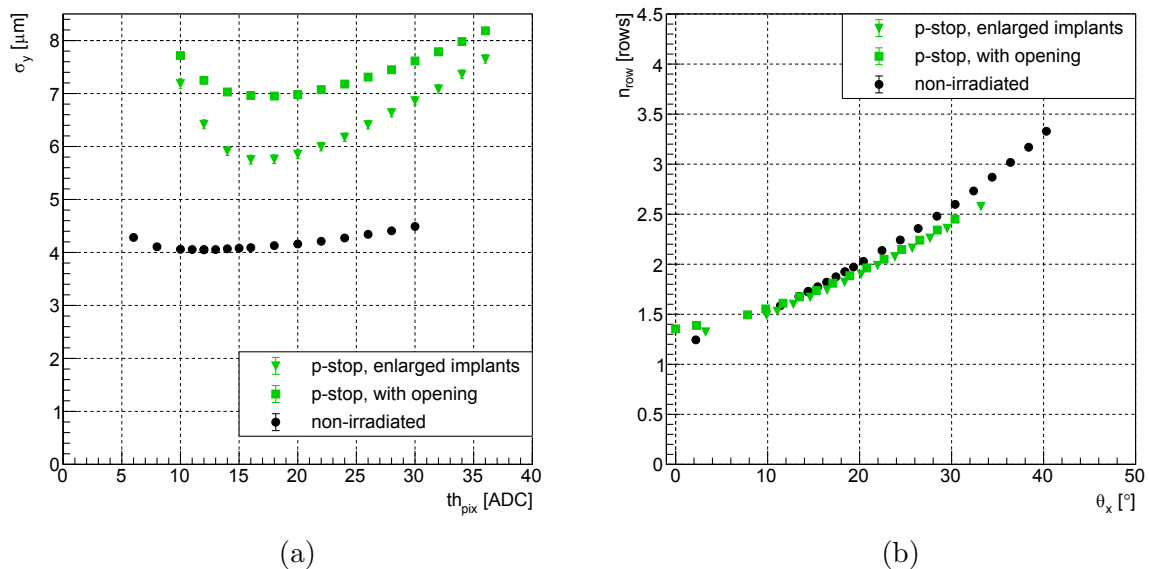
Figure 7.25.: Spatial resolution as a function of the pixel threshold (a), measured at $\theta_x = 18.4°$ (squares) and $18.9°$ (triangles). Projected cluster size as a function of the track incidence angle (b). The investigated sensors modules have a pixel size of $50 \times 50\,\mu m^2$ and are proton irradiated to $\phi_{eq} = 2.3 \times 10^{15}\,cm^{-2}$. The measurements on the non-irradiated sensor module, with p-stop inter-pixel isolation and enlarged implants, are shown for comparison and discussed in 7.2.4. The measurement in (a) is taken for $\theta_x = 18.4°$.

To optimize the pixel threshold, it is scanned for the measurements at $\theta_x = 18.4°$ and $\theta_x = 18.9°$ for the sample with the enlarged implant and open p-stop design, respectively. The resulting spatial resolutions as a function of the pixel threshold are shown in figure 7.25a. For the sample with the enlarged implants, a stronger threshold dependence of the spatial resolution is observed, with a minimum at a threshold of 16 ADC. The

optimal threshold for the sample with open p-stop is 18 ADC. In both cases, the optimal threshold corresponds to 10 % of the Landau MPV.
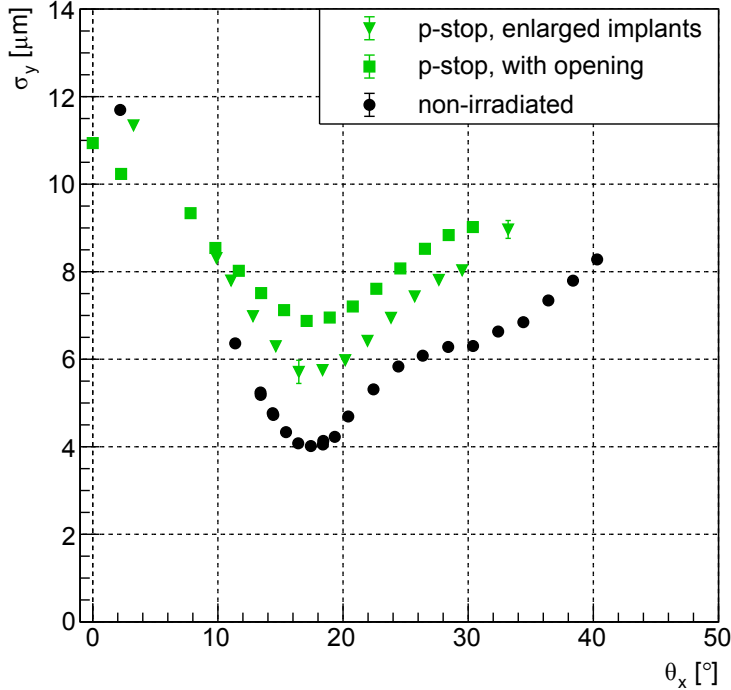
Figure 7.26.: Spatial resolution as a function of the track incidence angle. The investigated sensors modules have a pixel size of $50 \times 50\,\mu m^2$ and are proton irradiated to $\phi_{eq} = 2.3 \times 10^{15}\,cm^{-2}$.

The measurements on the non-irradiated sensor module, with p-stop interpixel isolation and enlarged implants, are shown for comparison and discussed in 7.2.4.

In figure 7.25b the projected cluster size for these measurements is shown as a function of the track angle. For the irradiated sensor modules, the differences in the cluster size are smaller than 5 %, but systematically larger for the sensor module with the open p-stop design. With respect to the non-irradiates sensor module, the cluster sizes are larger for angles below 14° and smaller for angles above. Note that the cluster size has a strong threshold dependence, as shown in figure 7.7b. Thus the small differences in cluster size are due to the fact that the threshold is optimized for each sensor module separately.

The hit resolution as a function of the track angle is shown in figure 7.26. The degradation of the resolution at the best angle after irradiation is about 2 µm for the sensor module with the enlarged implant design and about 3 µm for the sensor module with the open p-stop design. The resolutions are

$$5.71\,\mu m \pm 0.26\,\mu m \text{ and}$$

$$6.88\,\mu m \pm 0.04\,\mu m,$$

respectively. The quoted errors include only statistical uncertainties. Systematic uncertainties are discussed in section 7.5. The best spatial resolutions are observed at $\theta_x = 16.5°$ and $\theta_x = 17.1°$. Although the sensor with the open p-stop design has a worse resolution at the best angle, its resolution is better for small track angles, breaking even at about $10°$ and being even better than the non-irradiated sample at $\theta_x \approx 2°$.

(a)   (b)
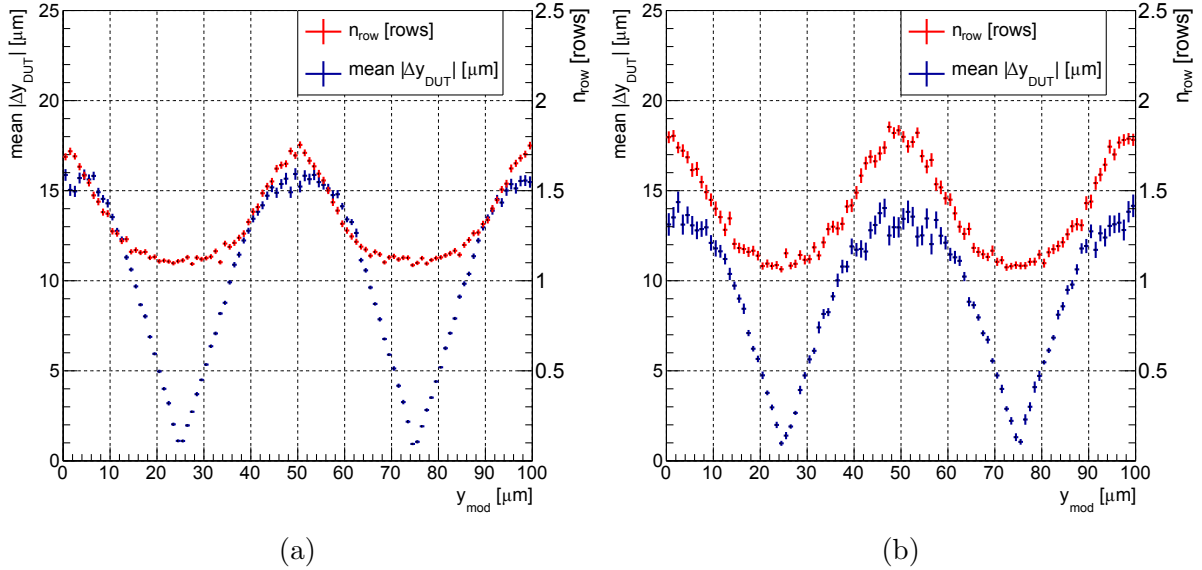
Figure 7.27.: Projected cluster size and mean $|\Delta y_{DUT}|$ as a function of the in-pixel position for two sensor modules with a pixel size of $50 \times 50\,\mu m^2$, proton irradiated to $\phi_{eq} = 2.3 \times 10^{15}\,cm^{-2}$, measured at $\theta_x \approx 2°$. The measurement presented in (a) is taken on the sensor module with enlarged implants. The measurement presented in (b) is taken on the sensor module with the open p-stop design.

To further investigate this observation, the projected cluster size and the mean of $|\Delta y_{DUT}|$ are studied as a function of the in-pixel position. In figure 7.27 these quantities are shown for both irradiated samples at $\theta_x \approx 2°$. In the center of a pixel, at $y_{mod} = 25\,\mu m$ and $y_{mod} = 75\,\mu m$, the projected cluster size is about 1.1 for both sensor modules. Towards the pixel boundaries, at $y_{mod} = 0\,\mu m$, $y_{mod} = 50\,\mu m$ and $y_{mod} = 100\,\mu m$, the cluster size increases, more so for the sensor module with the open p-stop design, in agreement with figure 7.25b. The mean of $|\Delta y_{DUT}|$ is close to 0 at the center of the pixel and increases linearly — expected by definition — until the effects of charge sharing by diffusion contribute close to the pixel boundaries. The effects of charge sharing decreases $|\Delta y_{DUT}|$, thus improve the spacial resolution, which is a smaller effect for the sensor module with enlarged implants.

With increasing track angle, the situation becomes more complicated, as the charge carriers are deposited in a certain range in the y-direction. It seems like charge sharing by diffusion perturbs the linearity of the relation between charge deposition and collection implicitly presumed in the applied center-of-gravity algorithm for position reconstruction. This possibly explains the worse resolution of the sensor with the open p-stop design for

track angles $\theta_x \geq 10°$.

7.5. Systematic Uncertainties and Effects

The findings of this work are based on the comparison of the hit efficiencies and spatial resolutions for different sensor designs, as discussed in the previous sections. The uncertainties quoted therein are of statistical nature and typically very small. This section addresses the systematic uncertainties of the quoted results and their sensitivity to the applied selection criteria.

Especially for low bias voltages, the hit efficiency is sensitive to the signal-to-threshold ratio. Three factors with impact on the signal-to-threshold ratio are to be emphasized, the fluence ϕ_{eq} a module was exposed to, the annealing state of said module and its gain. For the neutron irradiated modules, the uncertainties on the fluence are expected to be around 3 %, as discussed in section 3.3. For the proton irradiated modules the uncertainties are estimated to be 17 % in the beam spot region. These uncertainties are not investigated with respect to their effect on the hit efficiency, since the fluence dependence of the charge collection depends on the sensor thickness and on the type and combination of bulk and implant doping, as shown in [142], and was not studied for the investigated sensors. The annealing state of the sensors is estimated to be on the order of days at room temperature, accumulated during irradiation, shipment and handling. Studies on the annealing behavior of the signal on sensors with n-type implants and p-type bulk [143], indicate a dependence on the fluence, thickness and substrate and also not known for the investigated sensors. Due to the small number of modules with comparable sensors and irradiation conditions a quantitative assessment of these effects is not possible, but the difference between the two sensors with enlarged implants in figure 7.23a provides an estimate for the effect. To mitigate the effect of these uncertainties on the final conclusions the inefficiency is studied as a function of the signal-to-threshold ratio, for example in figure 7.23b. In this representation, the curves for the same sensor design overlap.

The systematic effects on the spatial resolution are investigated for a subset of the presented measurements. It contains measurements at three angles for each of the samples discussed in section 7.3.2 and 7.4.2. The angles are given in table 7.2, containing also the results of the systematic studies. To investigate the effect of the alignment precision, a Gaussian smearing is applied to the DUT alignment parameters and the measurements are re-analyzed iteratively. The RMS of the Gaussian distributions corresponds to the uncertainty of the considered alignment parameter. For each of the iterations the resolution is calculated and the RMS of these resolutions relative to the unperturbed measurement is given in the table. Around $\theta_x = 0°$ the effect is negligible, for the larger two angles variations up to 4 % are found. To evaluate the effect of the signal-to-noise ratio, the pixel noise is artificially increased by 10 %. This is achieved by smearing the pixel re-

7. Pixel Sensor Characterization

Table 7.2.: Systematic effects on the spatial resolution, quoting the percental variation or change of the spatial resolution with respect to the results presented in section 7.3.2 and 7.4.2. The variations applied to the corresponding parameters are discussed in the text. For the irradiated samples, the particle type (tp.) is given.

$\phi_{eq}[10^{15}\,\mathrm{cm}^{-2}]$	tp.	design	$\theta_x[°]$	align.	noise	charge cut	res. cut	RMS_{trc}
0.0		enlarged	2.2	0.0	0.0	3.6 -5.3	0.2 -0.2	0.4 0.0
			18.4	2.2	2.5	4.3 -6.8	0.6 -0.4	0.9 -0.4
			40.3	0.2	0.1	0.0 0.2	0.0 0.0	0.0 0.0
2.3	p	enlarged	3.2	0.2	0.6	-0.1 0.0	0.0 0.0	0.0 0.0
			18.4	2.5	3.5	2.9 -4.6	0.0 -0.4	0.5 0.0
			29.5	1.6	3.1	2.3 -4.2	0.2 -0.3	0.7 -0.2
2.3	p	open	2.3	0.1	0.6	0.3 -0.1	0.2 0.0	0.0 0.0
			18.9	0.4	1.7	1.8 -3.4	0.4 -0.2	0.3 -0.2
			30.3	1.7	2.1	1.8 -3.7	0.3 -0.1	0.3 -0.2
3.6	n	regular	10.6	0.4	0.6	0.3 -1.3	0.2 -0.1	0.2 -0.2
			19.4	1.6	2.3	1.8 -4.5	0.2 -0.4	2.9 -1.0
			30.1	1.3	0.7	2.0 -3.9	0.5 -0.3	1.0 -0.6
7.2	n	regular	0.0	0.1	0.0	-0.2 0.0	0.1 -0.1	0.0 0.0
			18.9	0.3	4.1	2.5 -4.3	0.5 -0.3	0.4 0.0
			46.1	2.0	1.2	2.4 -3.9	0.3 0.2	0.4 -0.1

sponse with a Gaussian distribution of the corresponding width. The effect is largest at the optimal angle and goes up to 4 %. Further investigated systematic effects are related to the reconstruction method. The charge cut, see section 6.4.7, is varied such that 85 % and 95 % instead of 90 % of the events with the largest charge are excluded. The residual cut, see section 6.4.6, is varied by ±10 %. Finally, the truncated RMS, see RMS_{trc} in section 6.3.4, is re-calculated discarding values outside of $\pm 5 \cdot \mathrm{RMS}_{trc}$ and $\pm 7 \cdot \mathrm{RMS}_{trc}$ instead of $\pm 6 \cdot \mathrm{RMS}_{trc}$. The relative decrease and increase of the spatial resolution is

also presented in table 7.2. The charge cut has the biggest impact on the result, yielding reductions up to about 4 % and increases by up to 7 % at around 18°, where the highest sensivity is observed. It should be noted, that the variations of the cuts are arbitrarily chosen, to give an estimate of the sensitivity. In general the systematic effects are found to be on the order of 5 % or smaller. Systematic effects due to biases of the reconstruction algorithm, discussed for example in [136], are not investigated.

7.6. Conclusion

The key findings in the context of this work are the results on the performance of the planar sensor prototypes for the Phase-2 Upgrade of the CMS pixel detector, presented in the previous sections. First conclusions can be drawn from the results of the measurements on non-irradiated sensor modules:

- The FDD material option is no longer considered as a choice for the final sensor. The measurements presented in figure 7.3 show hints for an active thickness larger than $150\,\mu m$, which is confirmed in capacitance-voltage measurements discussed in [96].

- Severe efficiency losses are observed at the bias dot, when it is grounded via the readout chip, as shown in figure 7.6. Further investigations are needed on sensors with bias grid at floating potential, after irradiation and as a function of the track angle.

- Sensors with polysilicon resistors were excluded from further studies at an early stage of the test-beam campaign due to low efficiencies even before irradiation.

- At the optimal track angle $\theta_x = 17.4°$ a hit resolution of $4.0\,\mu m$ is found for sensor with a pixel size of $50 \times 50\,\mu m^2$ at a bias voltage of $120\,V$. A scan of the track angle is shown in figure 7.8 for two pixel thresholds.

- Explorative measurements on sensors with bricked implants and a pixel size of $25 \times 100\,\mu m^2$ are presented in figure 7.10. They show that the resolution in the direction of $100\,\mu m$ pixel pitch can be improved by a factor of ≈ 2 compared to non-bricked designs, if charge sharing in the direction of $25\,\mu m$ pitch is present, which will be the case for the operation conditions in the barrel of the CMS pixel detector.

The results of the efficiency measurements on the irradiated sensors are summarized in table 7.3. Additional conclusions can be drawn from the measurements on neutron irradiated sensors:

- The investigated sensor modules reach an efficiency benchmark of 99 % for bias voltages below $800\,V$ after irradiation to $\phi_{eq} = 14.4 \times 10^{15}\,cm^{-2}$ as shown in figure 7.11. This raises confidence that planar sensor might be operated in innermost layer of

7. Pixel Sensor Characterization

the CMS pixel detector, where a maximum fluence $\phi_{eq} = 11.5 \times 10^{15}\,\text{cm}^{-2}$ will be reached in case of a replacement after half the operation time. One has to appreciate the fact that this needs to be confirmed with the final chip and after proton irradiation since proton irradiation comes with a higher ionizing dose and the bulk damage after proton and neutron irradiation is different.

- For sensors irradiated to $\phi_{eq} = 7.2 \times 10^{15}\,\text{cm}^{-2}$ the efficiency is found to be independent of the pixel size and the track angle up to $\theta_x = 19°$, as shown in figure 7.14.

- The spatial resolution at the best angle is found to degrade to $\approx 6\,\mu\text{m}$ after neutron irradiation to $\phi_{eq} = 3.6 \times 10^{15}\,\text{cm}^{-2}$ and $7.2 \times 10^{15}\,\text{cm}^{-2}$. The scan of the track angle, presented in figure 7.17, reveals a shift of the best angle to 20.9° for the higher fluence, due to an increasing depth dependence of the charge collection.

Table 7.3.: Summary of the measurements of the hit efficiency ϵ for irradiated samples including the particle type (tp.), pixel size (sz.), implant design (design), inter-pixel isolation technique (iso.) and required voltage (V_{99}) and signal-to-threshold ratio (S/T_{99}) for $\epsilon = 99\,\%$.
The measurements are taken at a track angle $\theta_x = 0$, only the measurement in line 07 is measured at $\theta_x = 19°$. The measurement in line 10 is taken on a sensor bump bonded to an RD53A readout chip, details are given in [88].

	$\phi_{eq}[10^{15}\,\text{cm}^{-2}]$	tp.	sz. [μm^2]	design	iso.	V_{99}[V]	S/T_{99}	in figure
01	0.50		25x100	regular	p-stop	25	2.6	7.11, 7.13
02	3.60		25x100	regular	p-stop	85	2.6	7.11, 7.13, 7.13
03	7.20		25x100	regular	p-stop	250	2.6	7.11 to 7.14, 7.13
04	14.40	n	25x100	enlarged	p-stop	500	2.0	7.11, 7.13, 7.15
05	7.20		25x100	enlarged	p-spray	150	2.0	7.14
06	7.20		50x50	regular	p-stop	250	2.6	7.14
07	7.20		50x50	regular	p-stop	250	2.6	7.14
08	14.40		25x100	regular	p-spray	400	2.5	7.14
09	5.40		25x100	regular	p-stop	480	2.4	7.20, 7.23
10	5.20		25x100	regular	p-stop	380		7.20
11	2.40		25x100	enlarged	p-spray	250	2.2	7.21
12	2.40		25x100	regular	p-stop	150	2.5	7.21
13	2.40		25x100	routing	p-stop	250	2.5	7.21
14	2.40	p	50x50	regular	p-stop	150	3.4	7.22
15	2.40		50x50	regular	p-stop	250	2.5	7.22
16	3.00		50x50	open	p-stop	250	2.9	7.22
17	5.40		25x100	enlarged	p-stop	380	2.0	7.23
18	5.40		25x100	enlarged	p-stop	350	2.0	7.23

Finally, a set of measurements on proton irradiates sensor modules is presented in this work. As the radiation damage inside the CMS pixel detector is dominated by charged

particles, those are the results of highest relevance regarding the key questions formulated at the beginning of this chapter. The conclusions drawn from these measurements are:

- The measurements presented in figure 7.20 show that pixel detectors with planar sensors reach an efficiency of 99 % at a bias voltage of about 480 V after proton irradiation to $\phi_{eq} = 5.4 \times 10^{15} \, \text{cm}^{-2}$. This suffices the requirements in layer 2 of the upgraded CMS pixel detector.

- As figure 7.24 demonstrates, larger n$^+$-implants reduce the efficiency losses at the pixel boundaries. This is confirmed by the findings in [141]. Additionally one can take a closer look at table 7.3. In general, the sensor modules with regular implants require a signal-to-threshold value of about 2.5 for an efficiency of 99 % while sensors with enlarged implants require approximately 2. There is only one deviation from this rule, the measurement in line 14 of the table. The sensor design with open p-stop inter-pixel isolation has even smaller implants and requires a signal-to-threshold value of 2.9 (line 16). It should be noted, that opposed to p-stop, the p-spray inter-pixel isolation allows for larger implant areas, but was excluded from further studies on recommendation of Hamamatsu Photonics K.K..

- The spatial resolution after proton irradiation to $\phi_{eq} = 2.3 \times 10^{15} \, \text{cm}^{-2}$ at the best track angle is found to degrade from 6 µm to 7 µm depending on the implant design. No significant changes of the best angle after irradiation are observed at these fluences, as the scan of the track angle in figure 7.26 shows.

- Additionally, it is found that the irradiated sensor with the smaller implants has the better resolution for track angles up to 10°, due to additional charge sharing as shown in figure 7.27.

In general presented results show that planar silicon sensors have an excellent performance, even in harsh irradiation environments. The findings were considered in a re-design of the sensor layout, to produce a new set of prototype sensors. These new prototypes are tested with the RD53A readout chip — similar to the final readout chip for the upgraded CMS detector — and are irradiated to even higher fluences ϕ_{eq}, to prove qualification of planar pixel sensors even in the innermost layer of the CMS detector.

8. Pixel Sensor Simulation

The simulation of the presented measurements mainly serves two purposes. First, a comparison between measurements and simulation, in terms of the previously defined observables, is used to validate the simulation procedure. Second, it shows that systematic effects are either understood, thus taken into account in the simulations, or negligible. A validated simulation program can be used to make predictions of the sensor performance in a wider range of conditions, like larger track angles and in magnetic fields. This is an important aspect since test-beam measurements are expensive in terms of costs and time so that in practice only a limited set of operation conditions can be investigated. So the presented simulation procedure improves our capabilities to make predictions of sensor performance in the future.

The simulation is performed in two steps. The program PIXELAV [144][33] is used for the simulation of the pixel sensors and introduced in the next section. Effects of the readout chip (digitization) and test-beam properties (track resolution) are taken into account in a second simulation step and discussed in the second section of this chapter. In section 8.3 simulation and measurements are compared for validation and in section 8.5 the simulation program is used to study make predictions on the resolutions in a 3.8 T magnetic field.

List of Own Contributions   The author's contributions to the results presented in this chapter include:

- Simulation [144] of the sensor response as a function of the track angle, for two different sensor designs, with and without magnetic field.

- Adding effects of the readout chip (digitization) and test-beam properties (track resolution) to the simulation framework.

- Reconstruction of the observables considered for the measurements from the simulation.

- Validation of the simulated results with measurements for non-irradiated sensors.

- Simulation of the sensor performance in the presence of a magnetic field.

This work has been performed under the supervision of Prof. Dr. Erika Garutti and Dr. Daniel Pitzl and in close collaboration with Dr. Jörn Schwandt.

8.1. Simulation of Pixel Sensors

The presented simulation of the pixel sensors is based on the program PIXELAV developed by Prof. M. Swartz, originally published in [144] and [33]. Since the original publication, the simulation program was refined, partially discussed in [145]. In addition, the program used in this work contains a few adjustments and fixes by Dr. Jörn Schwandt, thus a brief summary of the simulation program is given.

8.1.1. Charge Deposition

The detection of a charged particle in a silicon detector starts with its passage through the silicon sensor and the associated energy loss, resulting in the generation of electron-hole pairs, referred to as charge deposition. So the charge deposition is a natural starting point for the simulation. The energy loss of charged particles in matter is dominated by ionization, as discussed in section 2.2. The simulation of charge deposition in PIXELAV is based on the fundamental work of H. Bichsel [25], where ionization spectra in silicon are calculated.

The total differential cross-section for a single-collision energy loss E of $45\,\text{GeV/c}$ pions in silicon, presented in figure 8.1 is integrated to calculate the mean free path of such pions in silicon. With this mean free path, an exponential distribution is generated to sample random numbers as distances between single interactions. For each of these single interactions, the energy loss in return is sampled according to the total differential collision cross-section in figure 8.1. Each occurrence of energy loss results in a secondary electron. These secondaries propagate in randomly chosen directions, constrained with two-body kinematics, taking into account deflections in presence of a magnetic field. They generate a number of electron-hole pairs, sampled from a Poisson distribution with a mean of $\frac{E}{3.645\,\text{eV}}$. The energy-dependent range of electrons is taken from tables [146] and used to calculate the range of the secondaries and the distribution of electron-hole pairs along their path. This is a change with respect to the original publication of PIXELAV, where the ranges were taken from [147].

It should be noted that $\approx 5\,\text{GeV/c}$ electrons are used for the presented test-beam measurement, in contrast to the $45\,\text{GeV/c}$ pions considered in the simulation. As discussed in 2.2 this difference is negligible and good agreement between the ionization spectra in measurement and simulation is expected.

The position of the incident pion is chosen randomly within the central pixel of an array of 51×51 pixels. Its angle with respect to the sensor normal can be chosen for a set of simulated events (run).
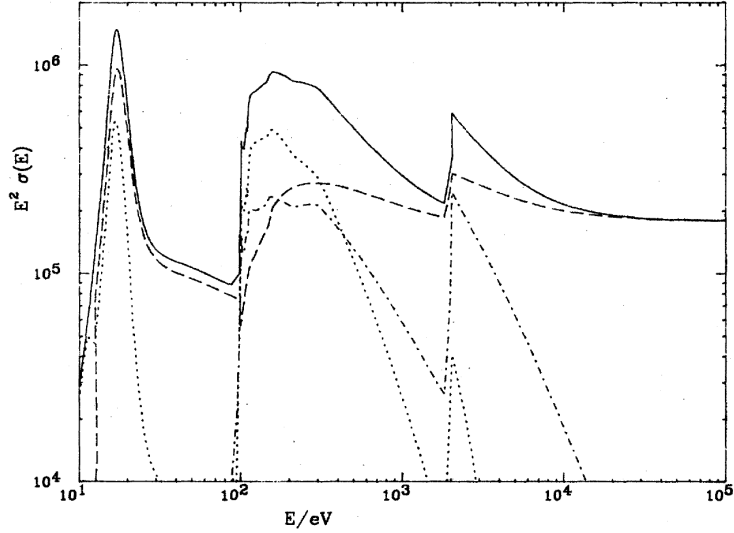
Figure 8.1.: Total differential cross section $\sigma(E) \cdot E^2$ for single-collision energy loss E of 45 GeV/c pions in silicon (solid line). The maxima are due to the M, L and K shells of silicon. Taken from [25].

8.1.2. Charge Transport

The drift of the generated electrons and holes pairs in the electric field of the silicon sensor and an external magnetic field is simulated in terms of a step-wise integration of

$$\frac{d\vec{r}}{dt} = \frac{\mu \left[qe\vec{E} + \mu r_H \vec{E} \times \vec{B} + qe\mu^2 r_H^2 (\vec{E} \cdot \vec{B})\vec{B} \right]}{1 + \mu^2 r_H^2 \vec{B}^2}. \tag{8.1}$$

This is derived from the equations of motion 2.7 by setting $\frac{d\vec{v}}{dt} = 0$, referred to as 'fully-saturated drift velocity' in [145]. In [144] and [33] this approximation is not made and the equations of motion were step-wise integrated, requiring a smaller step size to obtain numerically stable results.

The Hall factors r_H for electrons and holes are assumed to be 1.12 and 0.9, respectively. The electric fields $\vec{E} = \vec{E}(\vec{r})$, where $\vec{r}$ denotes a position, are provided by Dr. Jörn Schwandt and derived using Synopsys TCAD. An example is shown in figure 8.2, for one pixel cell. For the electron and hole mobilities, the parametrization introduced in section 2.3 is used.

For the numerical integration, a Cash-Karp 5th-order Runge-Kutta method with adaptive step size between 0.1 ps and 250 ps is used. To limit the computational costs, only one in ten generated charge carriers is propagated, which goes without major trade-offs in accuracy. In order to include diffusion in the simulation, an offset is added to the coordinates of a given charge carrier after each integration step. This offset is sampled from a Gaussian distribution. The width of this Gaussian distribution is derived from the drift time corresponding to the integration step and the diffusion constant, as introduced in section 2.3.
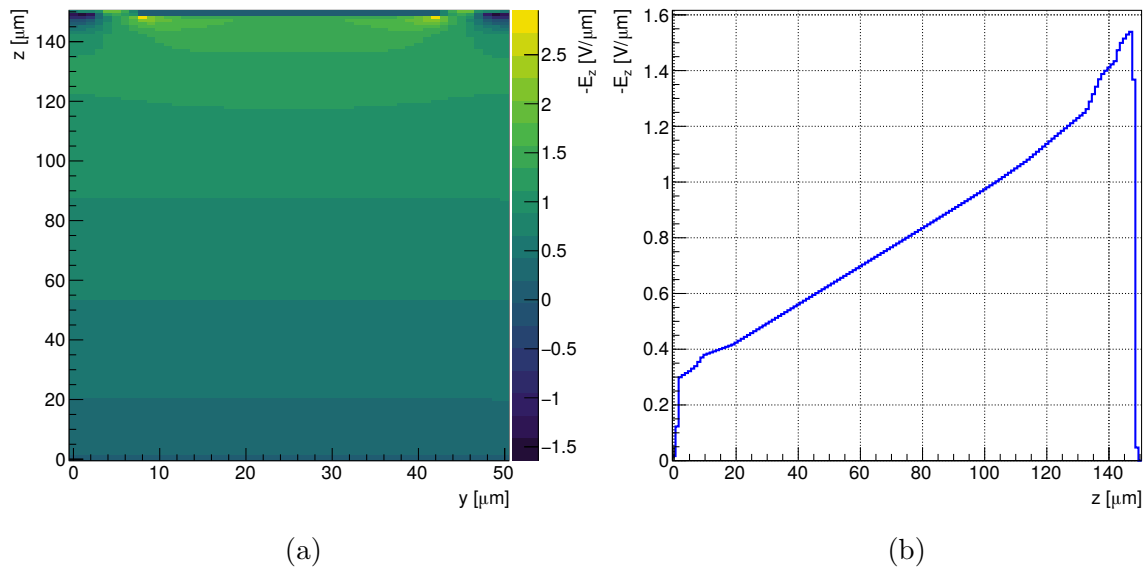
Figure 8.2.: z-Component E_z of the electric field for one pixel cell. In (a) it is shown in the yz-plane cutting through the center of the n$^+$ implant at $x = 25\,\mu\text{m}$. In (b) it is shown as a function of the z-coordinate for $x = y = 25\,\mu\text{m}$.
The electric fields are derived by Dr. Jörn Schwandt with Synopsys TCAD, for sensors with a pixel size of $50 \times 50\,\mu\text{m}^2$ and the design with enlarged implants and p-stop inter-pixel isolation. The assumed temperature is $20\,^{\circ}\text{C}$ and the bias voltage is $120\,\text{V}$. The n$^+$ implants are at $z \approx 150\,\mu\text{m}$ and centered around $x = y = 25\,\mu\text{m}$. The non-depleted region has a thickness of about $2\,\mu\text{m}$ at the n$^+$ implants and about $1\,\mu\text{m}$ at the backside, yielding an active thickness of about $147\,\mu\text{m}$ in agreement with measurements of the doping profile [96].

8.1.3. Charge Collection

The motion of the electrons and holes induces a current on the electrodes of the silicon sensor. Since the drift times in the silicon sensor, typically few ns, are small with respect to the integration time of the pre-amplifiers in the readout chip, $\approx 250\,\text{ns}$, the pulse shape of the induced transients does not need to be calculated. For non-irradiated silicon sensors trapping effects can be neglected and thus the induced current corresponds to the number of charge carriers reaching the readout electrode.

For irradiated sensors trapping needs to be taken into account. It should be mentioned that the local trapping probability depends on the trap occupation, which depends on the local current densities of electrons and holes. For simplicity effective trapping times are used in the PIXELAV simulation, which are derived assuming a constant trapping time for electrons and holes over the entire sensor volume. Measurements of the effective trapping times after irradiation with protons, pions and neutrons as a function of the $1\,\text{MeV}$ neutron equivalent fluence, temperature and annealing time are presented in [60] and parametrizations are given.

In the simulation, trapping is implemented in the following way. The trapping times

τ_e and τ_h are derived for the given fluence and temperature and used to derive a lifetime for the transported charge carriers. For each step of the numerical integration, the total drift time is computed and constrained to the lifetime of the corresponding charge carrier. Once the drift time reaches the lifetime a charge carrier is considered trapped if it has not reached an electrode yet. Electron hole pairs are simply counted if neither of the two is trapped. Else, the induced charge is calculated with the method of image charges.

8.2. Simulation Readout Chip and Setup Properties

For each simulated event the output file of the PIXELAV simulation includes the true position and direction of the incident pion, the number of generated electron-hole pairs and the number of pixels the charge was collected in. It follows the pixel index and induced charge for all pixels with an induced charge corresponding to more than one collected electron.

In a second step of the simulation procedure, these data are read event by event and structured in a way that permits analysis with the same code used for the analysis of data. This does obviously not hold for all analysis steps, e.g. track finding, but for most aspects related to the analysis of DUT data. In order to compare these results to measured data, properties of the used readout chip and the test beam setup need to be taken into account, which is also implemented in this second step of the simulation procedure. The considered properties are:

- **Electronic noise:** The charge measurements in each pixel are subject to electronic noise, which needs to be taken into account in the simulation. This is realized by adding a random number drawn from a Gaussian distribution with appropriate width σ_{el} and a mean of zero to the simulated pixel charge.

- **Noise variations:** The noise amplitude varies from pixel to pixel, so the width σ_{el} is not fixed but calculated from two components $\sigma_{el} = \frac{\sigma_{el,col}}{\sqrt{2}} + \sigma_{el,pix}$. The first component $\sigma_{el,col}$ is the same for one event and one column and is drawn from the measured distribution of $\mathrm{RMS}(\Delta PH)$, shown in figure 8.3. It is divided by $\sqrt{2}$ to calculate the single pixel noise. The second component $\sigma_{el,pix}$ takes into account pixel to pixel variations and follows a Gaussian distribution with an RMS of about 0.12 ADC.

- **Baseline oscillations:** The baseline oscillations, presented in figure 5.15, are modeled by adding a sinusoidal contribution

$$A_{osc} \times \sin\left(j \times \frac{2\pi}{p_{osc}} + \phi_{osc}\right) \tag{8.2}$$

to the simulated pulse height PH, where j is the row index. The amplitude A_{osc}

is set to 3 ADC and the period is set to 210. The phase ϕ_{osc} follows a uniform distribution between 0 and 2π and is sampled once for each event and column i. It is found that adding the baseline oscillation has a negligible effect on the results of the simulation after the correction introduced in equation 6.7.
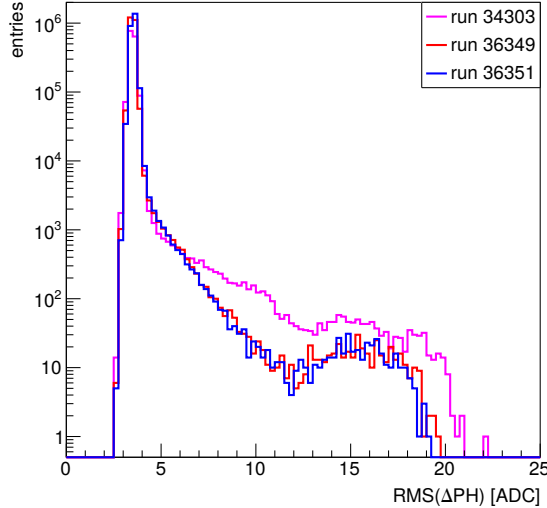
Figure 8.3.: Measured distributions of the noise RMS(ΔPH), used to accurately model noise variations in the ROC4SENS readout chip.

- **Charge to ADC conversion:** Since many steps of the analysis presented in section 5.3 and 6 are performed in terms of ADC counts. A conversion factor f_q between the charge in ke and ADC is needed.

- **Gain variations:** The gain — thus the conversion between ADC and ke — varies from pixel to pixel. To take this into account the conversion factor is multiplied with a value drawn from a Gaussian distribution of width σ_q and mean 1.

- **Crosstalk:** Due to the capacitive coupling between neighboring pixels crosstalk may occur. In this case, a small fraction f_x of the charge collected in one pixel is transferred to its neighbors, conserving the total collected charge.

- **Threshold:** In the analysis presented in section 6 a threshold cut th_{pix} is applied and needs to be applied also in the simulation to obtain comparable results.

- **Telescope track resolution:** In order to compare the shape of residual distributions, as defined in section 6.3 the telescope track resolution needs to be taken into account. Due to the non-Gaussian tails, Student's t-distributed shifts are added to the true track positions provided by PIXELAV. The Student's t-distribution [137]

$$f_\nu(x) = \frac{\Gamma((\nu + 1)/2)}{\sqrt{\nu\pi} \cdot \Gamma(\nu/2)} \left(1 + \frac{x^2}{\nu}\right)^{-(\nu+1)/2}, \tag{8.3}$$

where Γ is the Gamma function, is characterized by the number of degrees of freedom ν. It approaches a Gaussian distribution for $\nu \to \infty$. For $\nu = 1$ it produces a Lorentz distribution. The shift is stretched with an additional factor σ_{res}, to take into account the Gaussian core of the resolution function.

The explicit numbers differ, depending mostly on the configuration of the readout chip and the distance between the beam telescope planes and the DUT for a given set of measurements. For three runs they are given in table 8.1.

Table 8.1.: Parameters to model properties of the readout chip and the test beam setup.

variable	unit	run 34303	run 36349	run 36351
mean σ_{el}	[ADC]	2.49	2.48	2.51
f_q	[ADC/ke]	26.25	23.80	23.60
σ_q	[%]	7	7	7
f_x	[%]	1	1	1
th_{pix}	[ADC]	12	12	12
ν		14.6	12.0	10.0
σ_{res}	[mm]	3.44	3.4	3.9

8.3. Validation with Test-Beam Data

In order to validate the results from the simulation, a set of distributions is compared to data. Since the measurements on a non-irradiated sensor presented in 7.2.4 are taken with three (slightly) different configurations of the beam telescope and two readout chip configurations, three runs were chosen for the validation. The run numbers and the parameters to model properties of the readout chip and the test beam setup are given in table 8.1. The track angles are $\theta_y = 0°$ and $\theta_x = 2.2°$, $11.4°$, $18.4°$, increasing with the run number. The PIXELAV simulations are performed for a temperature of $20\,°\mathrm{C}$ and the electric field is calculated for a bias voltage of $120\,\mathrm{V}$ and the design with enlarged implants p-stop inter-pixel isolation and a pixel size of $50 \times 50\,\mathrm{\mu m}^2$ as presented in figure 8.2.

For the validation runs, the simulated telescope residual and DUT pedestal distributions are compared in figure 8.4 to 8.6. For the residual distributions the agreement between data and simulation is within the statistical uncertainties. For the measured pedestal distributions the mean is slightly displaced from zero, causing a negligible slope in the ratio between the measured and simulated distribution.

(a)   (b)
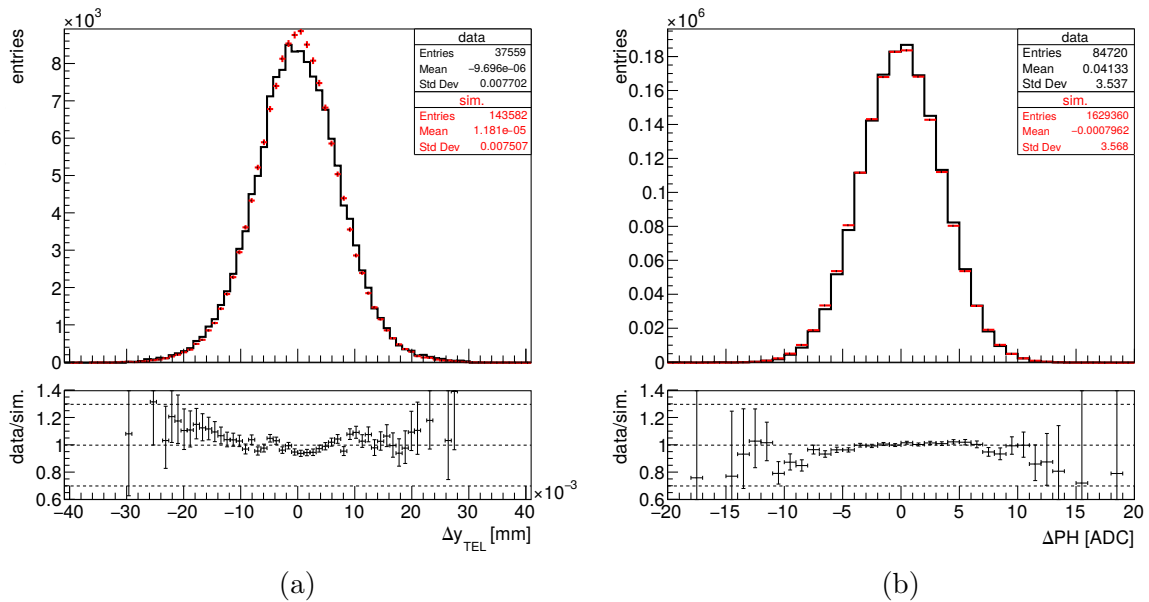
Figure 8.4.: Telescope residual (a) and DUT pedestal (b) distributions. For the residual distribution, the selection criteria are the same as for the results discussed in section 7. For the pedestal distributions, pixels without signal are selected by requesting them to be in the outer ring of a ROI. The track angle $\theta_x = 2.2°$. The simulated distributions are normalized to the number of entries in the measured ones.
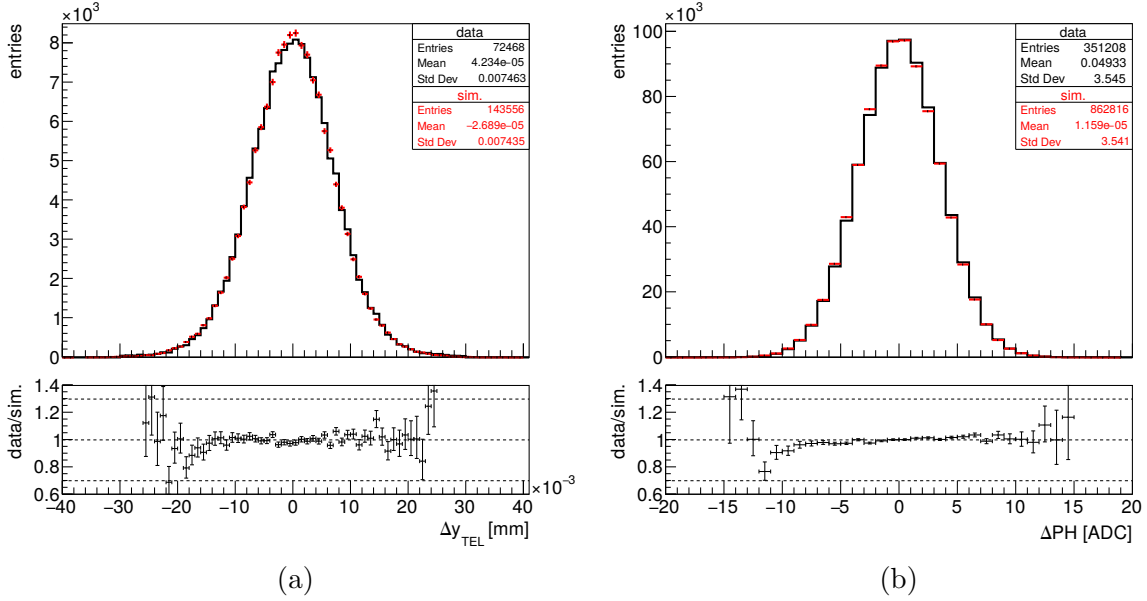
Figure 8.5.: Telescope residual (a) and DUT pedestal (b) distributions. For the residual distribution, the selection criteria are the same as for the results discussed in section 7. For the pedestal distributions, pixels without signal are selected by requesting them to be in the outer ring of a ROI. The track angle $\theta_x = 11.4°$. The simulated distributions are normalized to the number of entries in the measured ones.
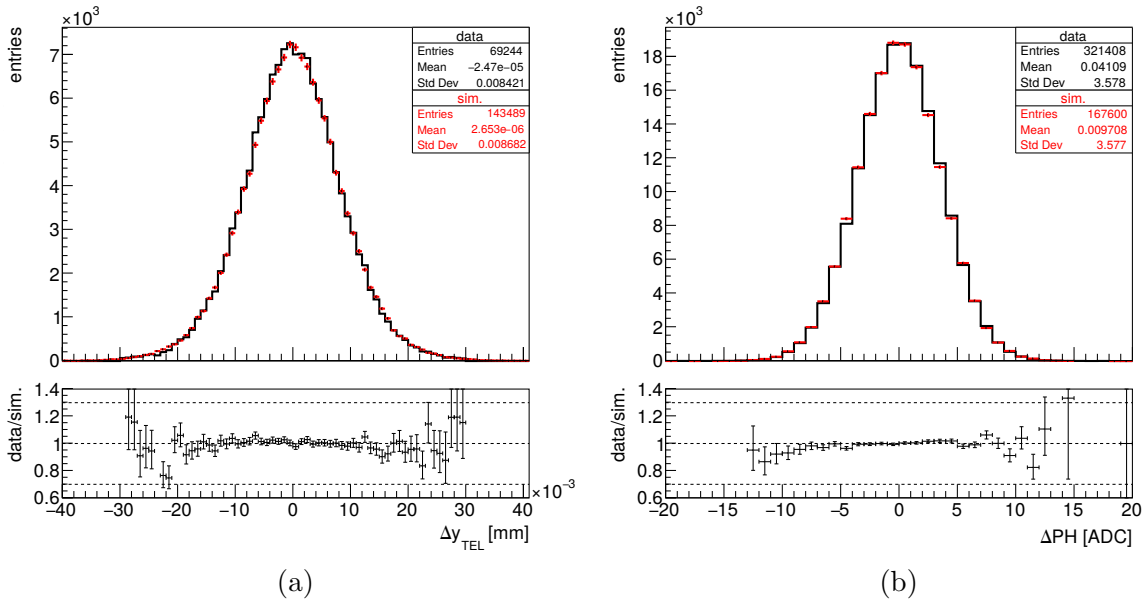
Figure 8.6.: Telescope residual (a) and DUT pedestal (b) distributions. For the residual distribution, the selection criteria are the same as for the results discussed in section 7. For the pedestal distributions, pixels without signal are selected by requesting them to be in the outer ring of a ROI. The track angle $\theta_x = 18.4°$. The simulated distributions are normalized to the number of entries in the measured ones.

8. Pixel Sensor Simulation

In figure 8.7 to 8.9, the distributions of the signal and the DUT residual are compared. The tails of the signal distribution are overestimated in the simulation, possibly because effects of amplifier saturation are not included in the simulation. The effect on the spatial resolution is negligible, since the cut on the signal, introduced in section 6.4.7, excludes the affected signal range. At the smallest track angle $\theta_x = 2.2°$ the core of the signal distribution is well modeled. For the larger track angles, the width of the distribution is underestimated. The shape of the residual distributions is well reproduced for all three validation runs. Still, two observations are made. First, the ratio between the measured and simulated distributions indicates a small over-/ underestimation of the measured width at $\theta_x = -2.2°$ and $\theta_x = 11.4°$, respectively. Second, the tails of the distribution are underestimated, becoming apparent from the ratio of the measured to the simulated distribution, as well as the different standard deviations in figure 8.9.

(a)   (b)
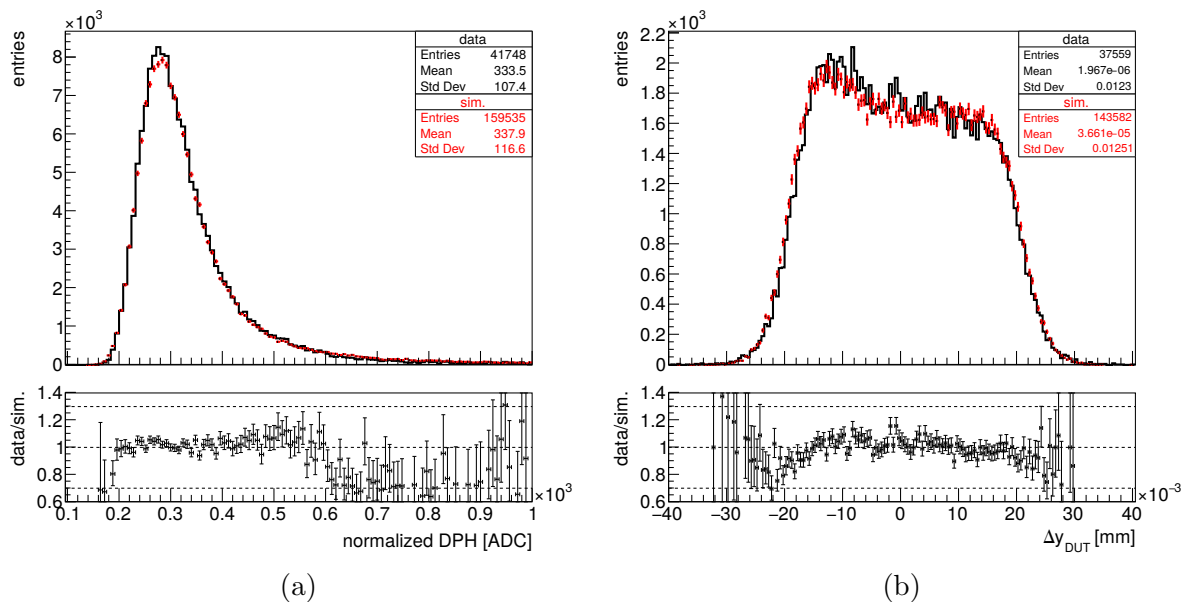
Figure 8.7.: Distributions of the pulse height for selected clusters, normalized by $\frac{1}{\cos(\theta_x)}$, (a) and the DUT residual (b). For both quantities the selection criteria are the same as for the results discussed in section 7. The simulated distributions are normalized to the number of entries in the measured ones.
It should be noted that the measurement is taken at a track angle $\theta_x = -2.2°$, while the other measurements were taken for positive angles. Hence the sign of the slope in the plateau region is different with respect to figure 8.8b.

The distributions of the projected cluster size n_{row} and its mean as a function of the in-pixel position are shown in figure 8.10 to 8.12. For the smallest angle, the number of one-row clusters is overestimated by 5 %. Figure 8.10b shows that this is the case for the entire range of in-pixel positions, although a small modulation of the ratio between measurement and simulation is observed. For the larger two angles, the numbers of two-row clusters is underestimated by 3 % to 4 %. Regarding figure 8.12b this can be associated with an underestimation of the cluster size around the centers of the pixels, e.g. at $y_{mod} = 25\,\mu m$.
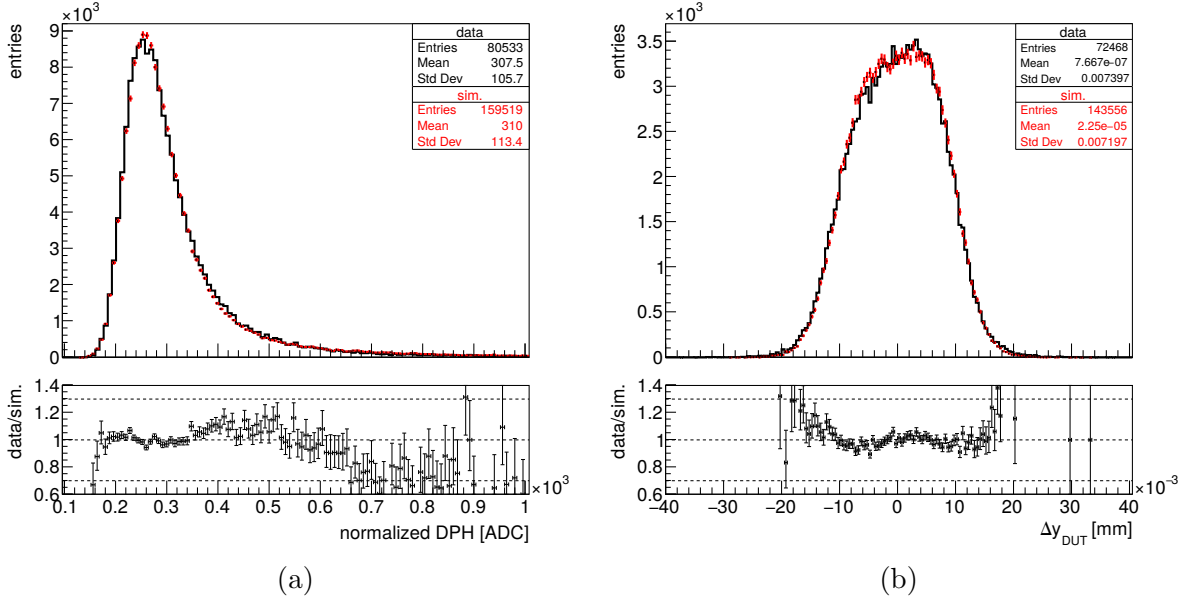
Figure 8.8.: Distributions of the pulse height for selected clusters, normalized by $\frac{1}{\cos(\theta_x)}$, (a) and the DUT residual (b). For both quantities the selection criteria are the same as for the results discussed in section 7. The track angle $\theta_x = 11.4°$. The simulated distributions are normalized to the number of entries in the measured ones.

Figure 8.9.: Distributions of the pulse height for selected clusters, normalized by $\frac{1}{\cos(\theta_x)}$, (a) and the DUT residual (b). For both quantities the selection criteria are the same as for the results discussed in section 7. The track angle $\theta_x = 18.4°$. The simulated distributions are normalized to the number of entries in the measured ones.
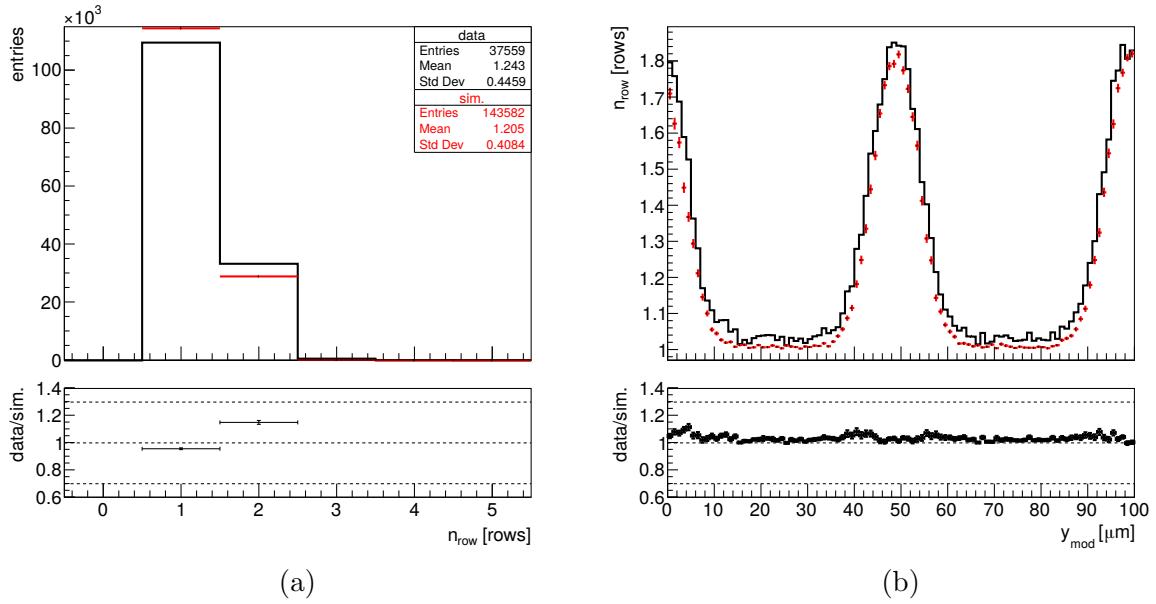
Figure 8.10.: The distributions of the projected cluster size n_{row} (a) and its mean as a function of the in-pixel position (b). The selection criteria are the same as for the results discussed in section 7. The track angle $\theta_x = 2.2°$. The simulated distributions are normalized to the number of entries in the measured ones.

Figure 8.11.: The distributions of the projected cluster size n_{row} (a) and its mean as a function of the in-pixel position (b). The selection criteria are the same as for the results discussed in section 7. The track angle $\theta_x = 11.4°$. The simulated distributions are normalized to the number of entries in the measured ones.
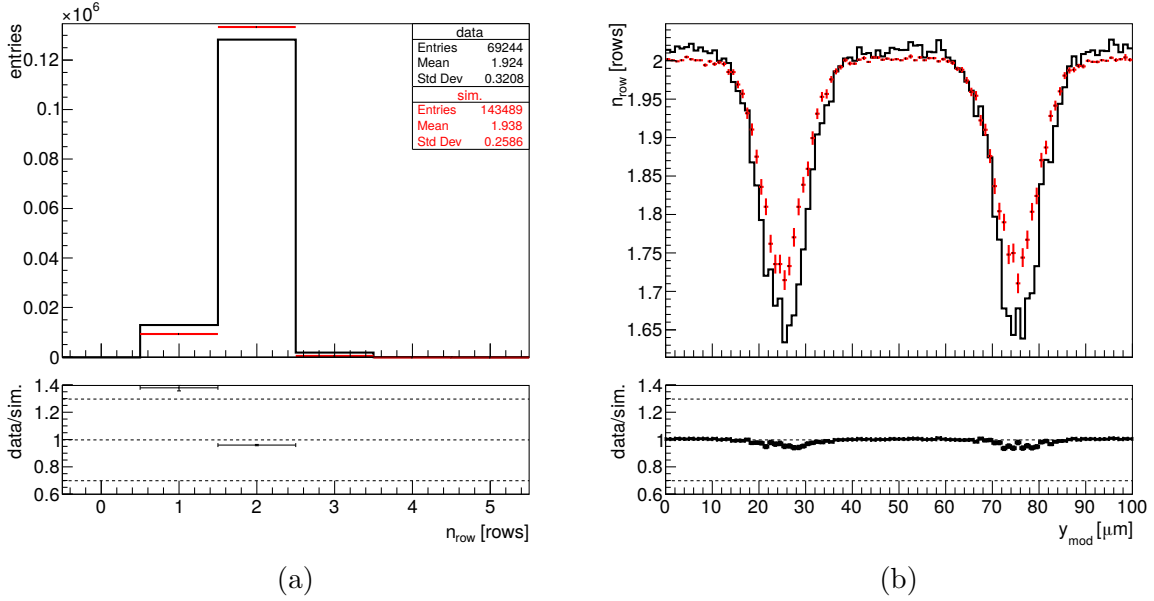
Figure 8.12.: The distributions of the projected cluster size n_{row} (a) and its mean as a function of the in-pixel position (b). The selection criteria are the same as for the results discussed in section 7. The track angle $\theta_x = 18.4°$. The simulated distributions are normalized to the number of entries in the measured ones.

In figure 8.13 the angular dependence of the projected cluster size and spatial resolution are compared between data and simulation. The projected cluster size is calculated as the mean of the corresponding distributions, shown and discussed above. The method to reconstruct the spatial resolution is discussed in section 6.3.4 and applied to both, data and simulation. The parameters to model the properties of the readout chip and the test beam setup are presented in table 8.1. They have been used for an overlapping range of angles and the results agree within the statistical uncertainties. The configuration of the PIXELAV simulation is identical in all cases, the track angle θ_x being the only exception. A second set of simulated results is included in the figures, obtained using the electric fields derived for the regular sensor design instead of the design with enlarged implants, as discussed in section 8.1.2.

For the projected cluster size data and simulation agree within less than 1 % except for the smallest angle where the cluster size is underestimated by less than 5 % in the simulation. The simulated spatial resolution is slightly overestimated at the smallest track angle θ_x and underestimated for all angles above. Around the optimal angle, the difference is 0.4 µm, it exceeds 0.6 µm for track angles above 22° and reaches 1 µm at the largest angle. In general, the differences between the two implant designs are negligible over the entire range of track angles. The biggest difference occurs at $\theta_x = 0°$, where the spatial resolution for the regular implant design is better by about 0.2 µm.
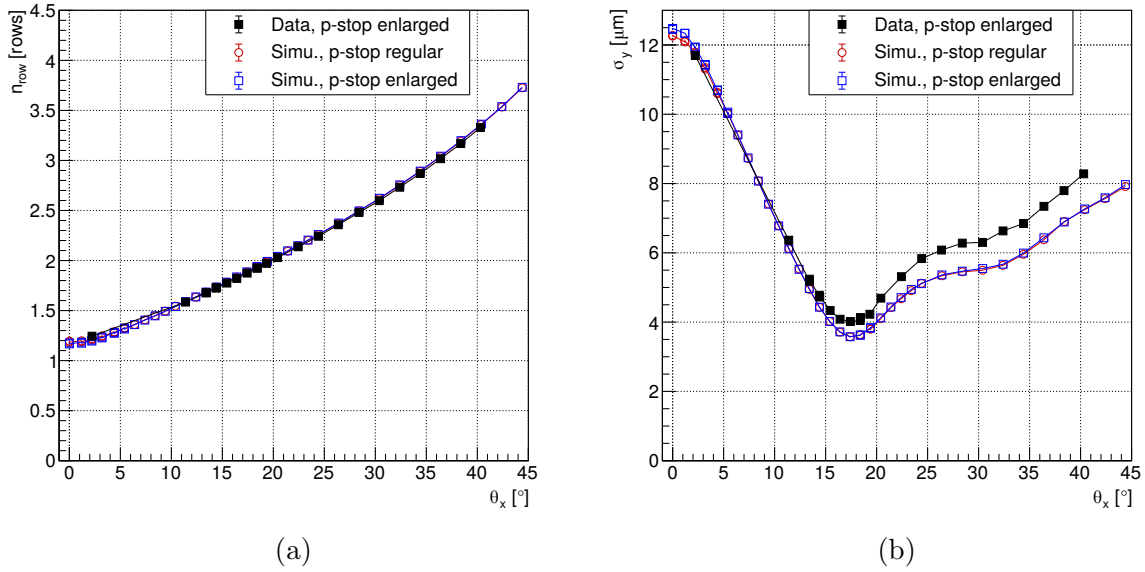
Figure 8.13.: Projected cluster size n_{row} (a) and spatial resolution σ_y (b) as a function of the track angle θ_x. The spatial resolution is reconstructed as discussed in section 6.3.4.

In section 6.3.4 the width of the residual distributions is estimated using a truncated RMS, denoted as RMS_{trc}. This truncated RMS is sensitive to outliers. Instead the width σ_g of the distributions can be estimated by fitting a generalization of the Gaussian distribution [148]

$$g_{gen}(\Delta y) = \frac{A_g \cdot s_g}{\sqrt{8} \cdot \sigma_g \cdot \Gamma(1/s_g)} \cdot \exp\left(-\left|\frac{\Delta y - \mu_g}{\sqrt{2} \cdot \sigma_g}\right|^{s_g}\right) \tag{8.4}$$

to the measured distribution, where Γ denotes the Gamma function and all variables with a subscript g are parameters of the fit. This approach is similar to the approach in [128]. The obtained estimate of the width is more robust with respect to outliers and the derived spatial resolution is shown in figure 8.14 as a function of the track angle. The differences between the simulated and measured resolutions are reduced to about 0.1 μm at the best and 0.6 μm at the largest angle, but still larger than in [128] and [149].

Another set of distributions for $\theta_x \approx 30°$ and $\theta_x \approx 40°$ is compared in figure 8.16. It turns out that the shape of the distributions is well modeled even for these large track angles. Quantitatively the width of both the distributions of the residuals and the signal are underestimated in the simulation. For the mean projected cluster size as a function of the in-pixel position, shown in 8.15 quantitative deviations are smaller than 5 % for all positions. Averaging over all positions the deviations are about 1 % as discussed above.
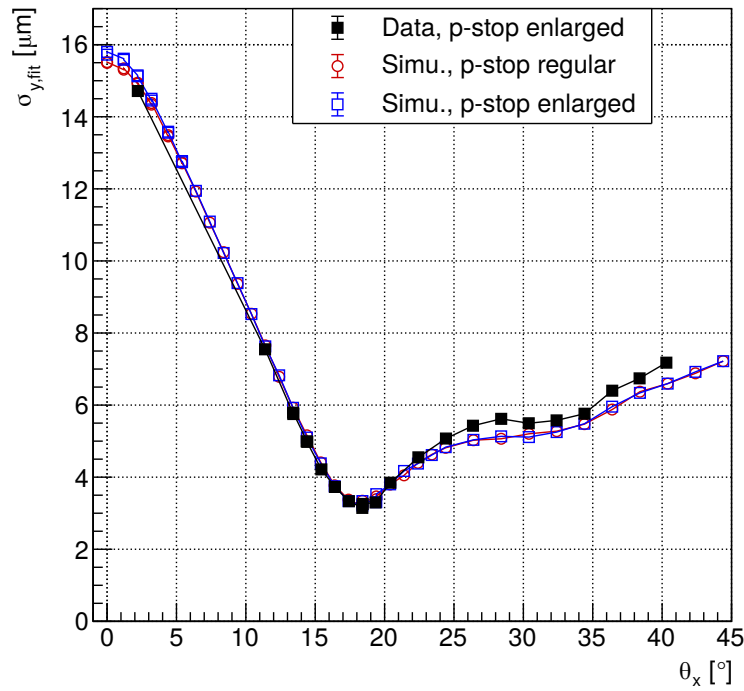
Figure 8.14.: Spatial resolution σ_y (b) as a function of the track angle θ_x. The width of the residual distributions Δy_{TEL} and Δy_{DUT} is estimated by fitting a generalization of the Gaussian distribution introduced in equation 8.4. Apart from that, the spatial resolution is reconstructed as discussed in section 6.3.4.

(a)

(b)
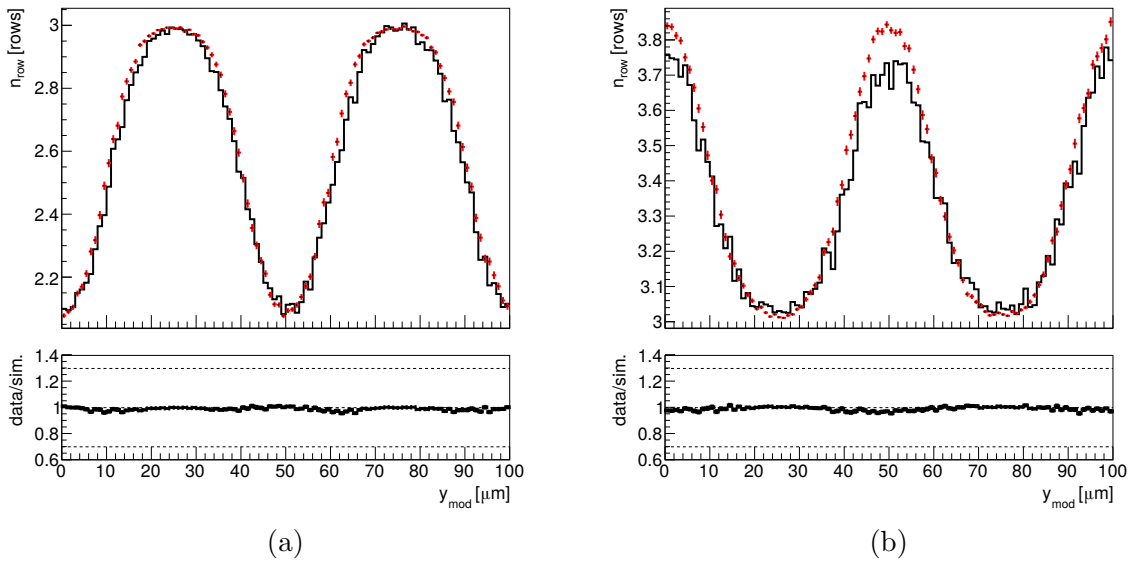
Figure 8.15.: Comparing measured and simulated mean of the projected cluster size for $\theta_x \approx 30°$ (a) and $\theta_x \approx 40°$ (b).

(a)

(b)

(c)

(d)
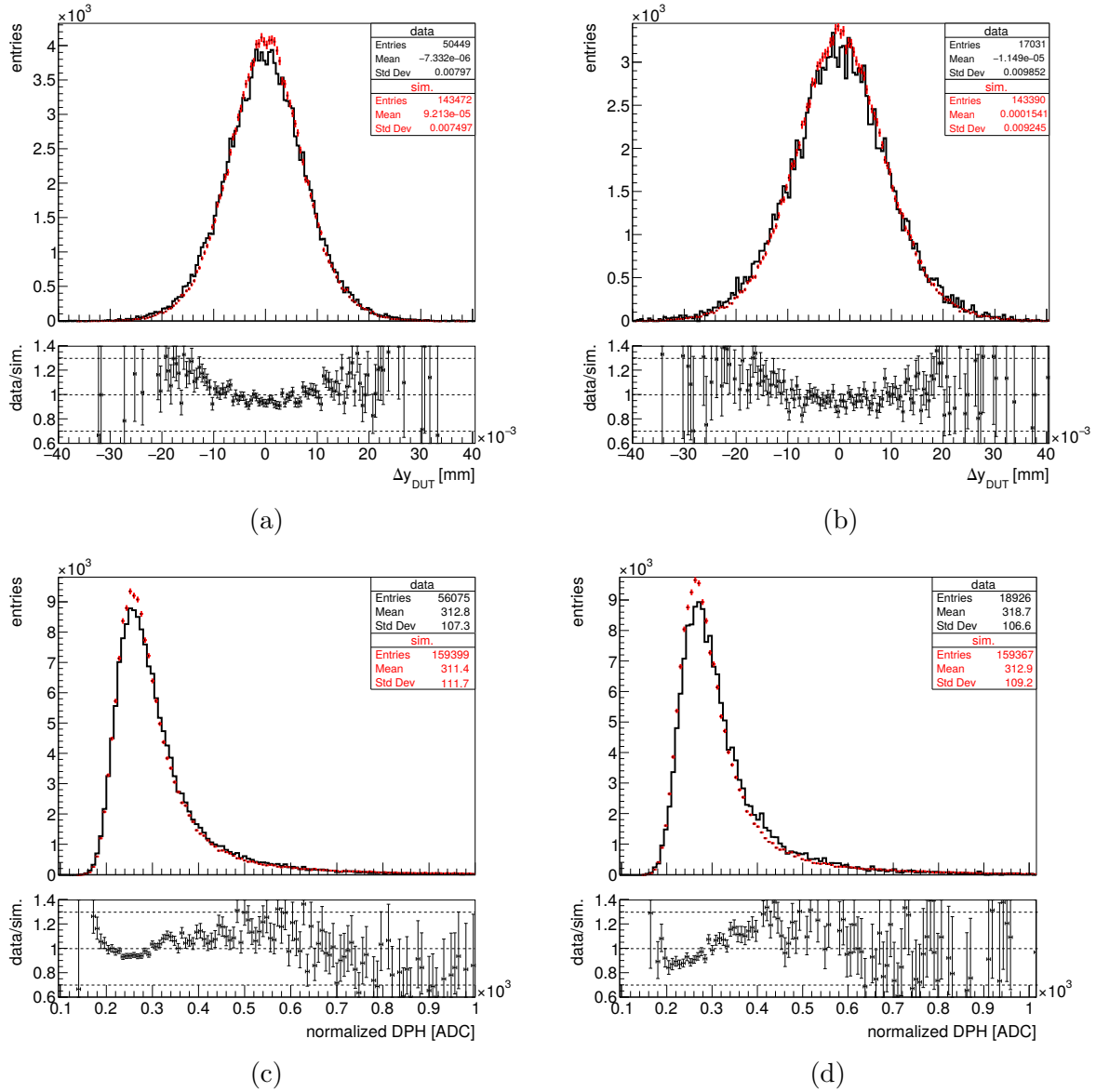
Figure 8.16.: Additional distributions of the DUT residuals and pulse height for selected clusters, normalized by $\frac{1}{\cos(\theta_x)}$, comparing data and simulation for $\theta_x \approx 30°$ (left) and $\theta_x \approx 40°$ (right). The simulated distributions are normalized to the number of entries in the measured ones.

8.4. Sensor Performance Predictions

The silicon tracker of the CMS experiment is operated inside a 3.8 T magnetic field, as discussed in chapter 3. The sensor characterization studies presented in chapter 7 were performed without magnetic field. So it is interesting to ask how the sensor performance changes in the presence of a magnetic field. To answer that question, PIXELAV simulations are made for a 3.8 T magnetic field, oriented parallel to the y-axis in the reference frame of the DUT. The track angles for these simulations range from $\theta_x = 0°$ to $\theta_x = 44.4°$, as in the previous section. Also the electric fields, calculated for p-stop sensors with the regular and enlarged implants at a bias voltage of 120 V, are reused. Further settings of PIXELAV are kept as discussed in section 8.1. These conditions correspond to operation in the barrel of the CMS pixel detector for Phase-2, where charge sharing in the z-direction is due to the track angle and charge sharing in the ϕ-direction is due to the Lorentz drift of electrons and holes in the magnetic field. The range of track angles in the Phase-2 CMS detector will exceed 80°. Given the systematic differences between data and simulation at large angles, see section 8.3, a smaller range of track angles is used for the presented studies.

To simplify the interpretation of the results, only a limited set of readout-chip effects is included in this simulation study. For the conversion between charge and ADC counts a factor $f_q = 26.25$ ADC/ke is used. The pixel threshold and the electronics noise are set to $th_{pix} = 12$ ADC and $\sigma_{el} = 2.5$ ADC. Noise variations, baseline oscillations, gain variations and crosstalk are not taken into account and the track resolution of the beam telescope is set to zero. Despite these changes the reconstruction procedure and selection criteria remain unchanged.

In figure 8.17 the mean projected cluster size and the spatial resolution are shown for both sensor designs (electric fields) and directions (n_{col}, n_{row} and σ_x, σ_y, respectively). In addition, results of simulations without magnetic field are included. The projected cluster sizes and resolution are calculated as the mean and truncated RMS of the corresponding distributions. The mean projected cluster sizes n_{row} are the same for all investigated angles. The same holds for the spatial resolutions σ_y apart from the differences between the two sensor designs around $\theta_x = 0°$ discussed in the previous section. The mean projected cluster sizes n_{col} depend on the magnetic field. At 0 T values of about 1.15 and at 3.8 T values between 1.95 and 2.00 are found. The spatial resolution σ_x improves from about 12.6 µm to about 4 µm between 0 T and 3.8 T. In addition, an improvement of the spatial resolution with θ_x is observed at 3.8 T. This improvement amounts to about 0.3 µm at the largest angle.

Neglecting the effects of the track resolution in the second step of the simulation procedure gives the opportunity to study residual distributions and the projected cluster size as a function of the in-pixel position in an unperturbed way. For a selection of angles the corresponding diagrams are shown in figure 8.18. The residual distributions in figure 8.18a

are displaced from zero, due to the Lorentz drift of the charge carriers in the magnetic field. In addition, the distributions are negatively skewed because of diffusion effects. For similar reasons, small peaks occur in figure 8.18c, at the edge of the plateau region for the residuals at σ_x between 0° and 12.4°.
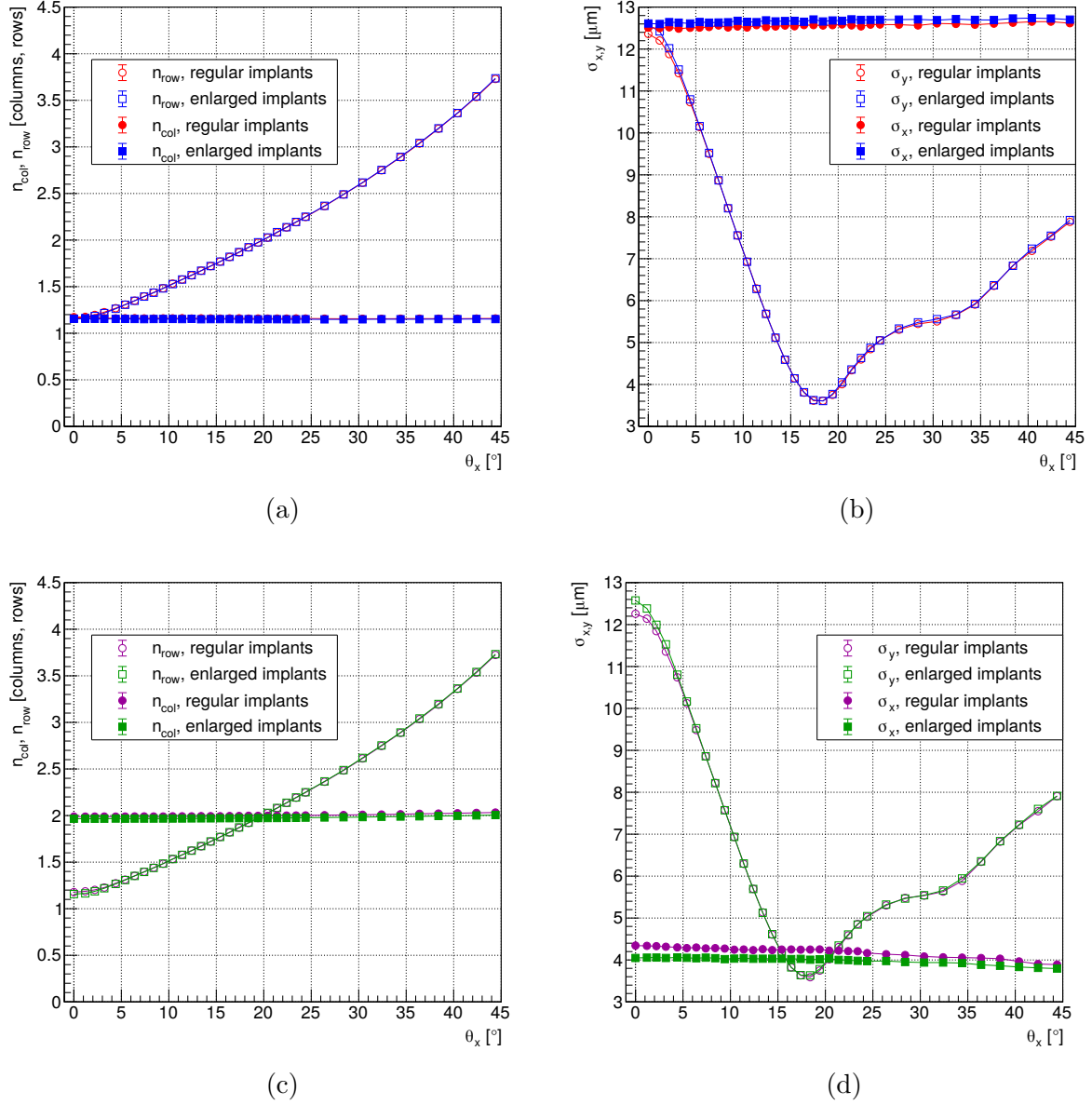
Figure 8.17.: Simulated projected cluster sizes n_{col}, n_{row} (a), (b), and spatial resolutions σ_x, σ_y (b), (d) as a function of the track angle θ_x. In (a), (b) the magnetic field is off, (c), (d) are for a magnetic field of 3.8 T.
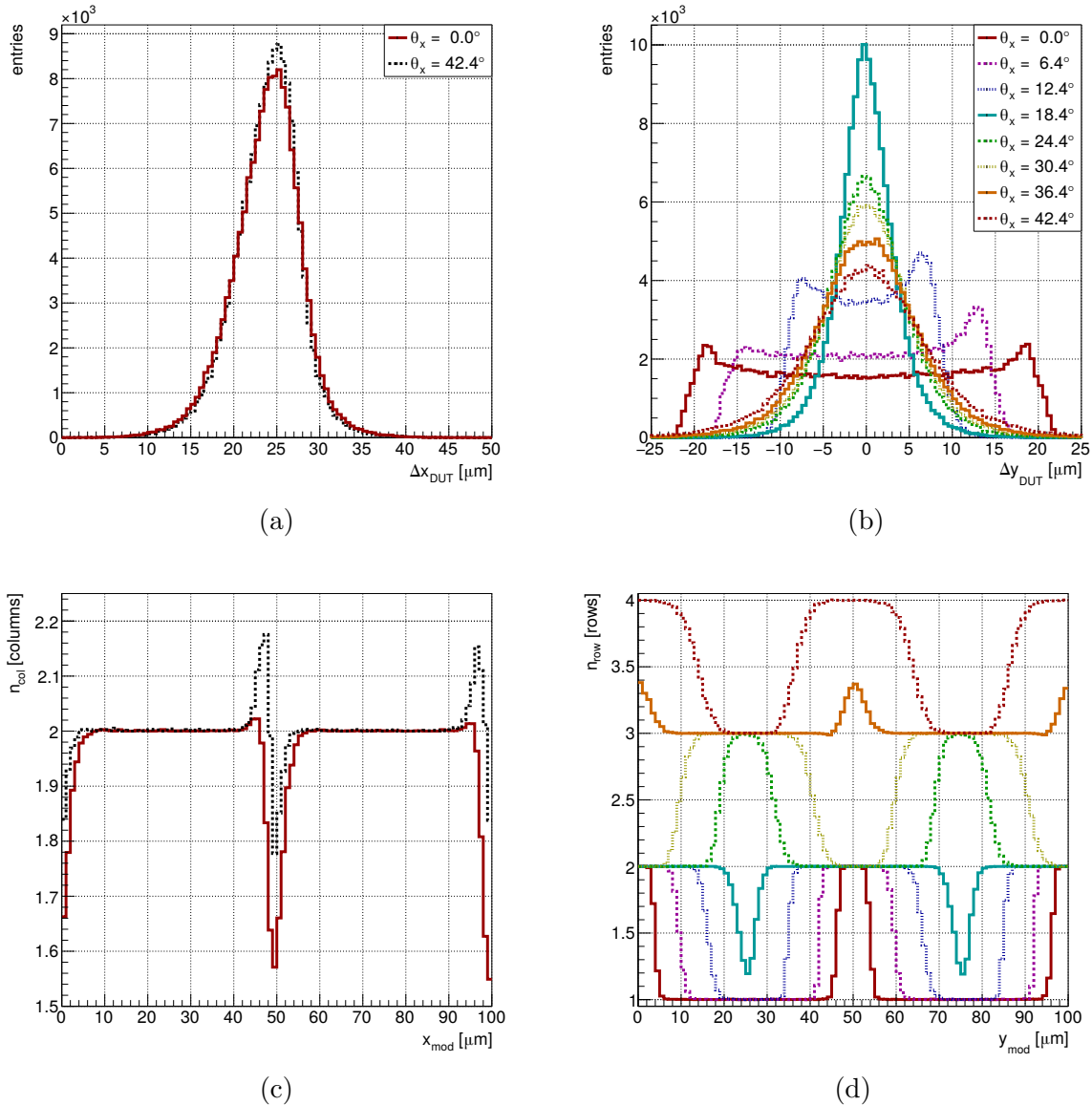
Figure 8.18.: Simulated distributions of the residuals Δx_{DUT}, Δy_{DUT} (a), (b) and the mean projected cluster size n_{col}, n_{row} (c), (d) for various track angles θ_x. The colors and line styles in the lower figures correspond to the legends in the upper figures. The PIXELAV simulation is performed for a magnetic field of 3.8 T, and the sensor design with enlarged implants.

8.5. Conclusion

The simulation program PIXELAV [144][33] is a powerful tool to study silicon pixel sensors. Within this work, it is used to simulate charge deposition and collection in non-irradiated pixel-sensor prototypes for the CMS Phase-2 Upgrade. The output of the simulation program is the simulated truth. Effects of the readout chip (digitization), the data acquisition and the track resolutions of the beam telescope are added in a second step of the simulation procedure. This is explicitly tailored to the ROC4SENS readout chip and the analysis procedure presented in this work. This enabled a direct compari-

son between the measurements and simulation, presented in section 7.2, in terms of the reconstructed observables, focusing on spatial resolution and cluster size.

Qualitatively the measurements are well described by the presented simulations. Quantitatively significant differences between measurements and simulation are observed. Especially comparing the spatial resolutions as a function of the track angle, see figure 8.13b, differences above 0.6 μm are found for track angles above 22°. This is partially explained by the sensitivity of the reconstruction method — using a truncated RMS — to outliers. Using a fit based method, which is less sensitive to outliers, the agreement between data and simulations is significantly improved, as shown in figure 8.14. Further investigations are needed to explain the remaining differences between data and simulations.

In the previous section, the simulation procedure is used to investigate the performance of the studied silicon sensors in presence of a magnetic field. The employed field strength and orientation corresponds to operation in the barrel of the CMS pixel detector for Phase-2. For the investigated range of track angles, 0° to 44.4°, the effect of the Lorentz drift on the resolution in the z-direction can be neglected. In the ϕ-direction the spatial resolution improves by more than a factor of 3, at a bias voltage of 120 V.

9. Summary

In chapter 4 measurements and model predictions of the full depletion voltage V_{depl} and the leakage current I_{leak} are compared for silicon sensors in the four barrel layers of the CMS pixel detector. The measurements are taken in the years 2017 and 2018, and the development of both observables is qualitatively described through the considered period. But quantitative deviations are apparent. Most evident is a systematic disagreement of the measured leakage current and model predictions by a factor of approximately 2 observed for layer 2, 3, and 4. Besides the revisions of the modeling framework, an attempt is made to quantify the systematic effects, but the disagreements are not fully explained. Especially the large systematic uncertainties on the temperature of the silicon sensor and the poor granularity of the leakage current measurements in the z-direction proved to be problematic. Further studies on the systematic effects in the measurements, but also improvements of the applied models are needed, especially in regard of the higher particle fluences expected in future operation scenarios.

The rest of this work is on the characterization of pixel sensor prototypes for the CMS Phase-2 Upgrade in beam tests. In chapter 7 cluster size, signal, noise, hit efficiency and spatial resolution are compared as a function of the bias voltage and beam incidence angle for non-irradiated and irradiated sensors. The irradiation was with neutrons or protons, reaching up to $\phi_{eq} = 14.4 \times 10^{15}\,\mathrm{cm}^{-2}$ and $\phi_{eq} = 5.4 \times 10^{15}\,\mathrm{cm}^{-2}$ respectively. The results are highly relevant for the choice of a final sensor for the CMS Phase-2 Upgrade and an extensive summary is given in section 7.6. Most importantly, they imply that planar sensors are qualified for at least the second layer of the upgraded detector, fulfilling the efficiency benchmark of $99\,\%$ for $\phi_{eq} > 5 \times 10^{15}\,\mathrm{cm}^{-2}$ after proton irradiation, requiring bias voltages of $380\,\mathrm{V}$ to $480\,\mathrm{V}$ at particle incidence parallel to the sensor normal. In the innermost layer a maximum fluence $\phi_{eq} = 11.5 \times 10^{15}\,\mathrm{cm}^{-2}$ will be reached in case of a replacement after half the operation time. For the neutron-irradiated samples, bias voltages of $500\,\mathrm{V}$ or below are sufficient to reach an efficiency of $99\,\%$, even for $\phi_{eq} = 14.4 \times 10^{15}\,\mathrm{cm}^{-2}$. This raises confidence, that planar sensors can tolerate these fluences also in the case of proton irradiation. It is found that wider n^+ implants reduce the efficiency losses at the pixel boundaries and yield better spatial resolution at the optimal track angle, after irradiation. This was considered in a re-design of the sensors for a new production of prototypes, realizing wider pixel implants.

The spatial resolutions of sensors with pixel sizes of $50 \times 50\,\mathrm{\mu m}^2$ are investigated up to track angles of $45°$. The measured spatial resolution is significantly better than the binary

resolution of 14.4 µm and reaches down to 4 µm at the optimal angle before irradiation. After proton irradiation to $\phi_{eq} = 2.3 \times 10^{15}\,\mathrm{cm}^{-2}$, the spatial resolution at the optimal angle is 6 µm for the design with enlarged implants. An explorative study on sensors with a bricked design and pixel sizes of $25 \times 100\,\mathrm{µm}^2$ shows that the spatial resolution in the direction of 100 µm improves by up to a factor of 2 compared to the regular design.

In chapter 8 the test-beam measurements are used to validate a simulation framework for non-irradiated sensors. This is used to predict the performance of these sensors in the presence of a magnetic field. Without a magnetic field, the spatial resolution at particle incidence parallel to the sensor normal is about 12.5 µm. It is found that the spatial resolution also improves due to charge sharing effects caused by the Lorentz drift and reaches values of about 4 µm.

List of Figures

List of Tables

Glossary

ADC Analog to Digital Converter. 60, 62, 64, 74, 81, 90, 144, 155

ALICE A Large Ion Collider Experiment. 23

ATLAS A Toroidal LHC ApparatuS. 23, 31

BPIX Barrel Pixel Detector. 28–30

BPM Beam Profile Monitor. 38

BRIL Beam Radiation Instrumentation and Luminosity. 43

CERN European Organization for Nuclear Research. 23, 38

CMS Compact Muon Solenoid. 1, 2, 23, 24, 27, 28, 30, 32, 33, 39, 40, 42–46, 48–53, 55, 56, 58, 69, 73, 80, 84, 105, 108, 113–115, 125, 126, 135–137, 155, 157–159

DESY Deutsches Elektronen-SYnchrotron. 64

DESY II DESY II synchrotron. 64, 65, 69

DLTS Deep-level Transient Spectroscopy. 19

DTB Digital Test Board. 58–60, 70, 71, 73, 74, 81, 100, 106

DUT Device Under Test. 66–72, 87–89, 92–97, 99–103, 106, 107, 115, 133, 143, 145–149, 154, 155, 189

FDB Flotzone Direct Bonded, see section 3.3. 106

FDD Flotzone Deep Diffused, see section 3.3. 106, 108, 110, 111

FPGA Field Programmable Gate Array. 59

FPIX Forward Pixel Detector. 28, 29

FTH Flotzone THinned, see section 3.3. 106, 110

HERA Hadron Elektron Ring Anlage. 1

Glossary

HL-LHC High-Luminosity LHC. 23, 30, 32, 33

HPK Hamamatsu Photonics K.K.. 33

HPTM Hamburg Penta Trap Model. 20

LGAD Low Gain Avalanche Diodes. 19

LHC Large Hadron Collider. 1, 23, 28, 30, 41, 42, 44, 52

LHCb Large Hadron Collider beauty. 23

LS2 Long Shutdown 2. 44

MIP Minimum-Ionizing Particle. 61, 76, 80

mip's Minimum-Ionizing Particles. 9

MPV Most-Probable Value. 9, 61, 89, 92, 108, 110, 111, 113, 114, 120, 122, 125, 126, 131

NIEL Non-Ionizing Energy Loss. 17, 20, 51

PCB Printed Circuit Board. 59, 60, 72, 88

PETRA III Positron-Elektron-Tandem-Ring-Anlage. 64

PFET Positive channel Field Effect Transistor. 58

PIXELAV Program for the simulation of pixel sensors. 139, 140, 142–144, 146, 151, 155, 157

PMT PhotoMultiplier Tube. 68, 71

PS PS-IRRAD Proton Facility. 38, 124

PSI Paul Scherrer Institute. 56, 74

R&D Research and development. 33, 35

RMS Root Mean Square. 10, 81, 82, 96, 97, 102, 103, 133, 134, 152, 155, 158, 185, 188, 189

ROC4SENS ROC4SENS readout chip. 33, 35–37, 56–61, 73, 74, 76, 78–82, 98, 99, 104–106, 126, 144, 157, 191

ROI Region Of Interest. 78–80, 82, 84, 90, 93, 146, 147

SM Standard Model of particle physics. 1

Synopsys TCAD Technology Computer-Aided Design software for simulation of semiconductor processes and devices. 19, 141, 142

TB21 Beam line 21. 64, 66, 69, 71, 98

TB22 Beam line 22. 64

TB24 Beam line 24. 64

TLU Trigger Logic Unit. 68, 70, 71, 100, 106

TRIGA TRIGA Mark II reactor. 37, 117

TSCs Thermally Stimulated Current's. 19

Bibliography

[1] J. Tolkien, *The Fellowship of the Ring.* Harper Collins, 1991, 2007.

[2] M. Własenko, "Measurement of the Structure of the Proton at HERA," *Nuclear Physics A*, vol. 827, no. 1, pp. 276c–278c, 2009.

[3] M. Thomson, *Modern Particle Physics.* Cambridge University Press, 2013.

[4] The CMS Collaboration, "Summaries of CMS cross section measurements." https://twiki.cern.ch/twiki/bin/view/CMSPublic/PhysicsResultsCombined. Accessed July 2021.

[5] B. Abi *et al.*, "Measurement of the Positive Muon Anomalous Magnetic Moment to 0.46 ppm," *Phys. Rev. Lett.*, vol. 126, p. 141801, 2021.

[6] S. P. Martin, *A Supersummetry primer.* 1998. arXiv:hep-ph/9709356.

[7] H. Georgi and S. L. Glashow, "Unity of All Elementary-Particle Forces," *Phys. Rev. Lett.*, vol. 32, pp. 438–441, 1974.

[8] L. Rossi, P. Fischer, T. Rohe, and N. Wermes, *Pixel Detectors From Fundamentals to Applications.* Springer-Verlag Berlin Heidelberg, 1st ed., 2006.

[9] R. Turchetta *et al.*, "A monolithic active pixel sensor for charged particle tracking and imaging using standard VLSI CMOS technology," *Nucl. Instr. and Meth. A*, vol. 458, no. 3, pp. 677–689, 2001.

[10] W. S. Boyle and G. E. Smith, "Charge Coupled Semiconductor Devices," *Bell System Technical Journal*, vol. 49, no. 4, pp. 587–593, 1970.

[11] P. Buzhan *et al.*, "An Advanced study of silicon photomultiplier," *ICFA Instrum. Bull.*, vol. 23, p. 28, 1970.

[12] H. Kolanoski and N. Wermes, *Particle Detectors: Fundamentals and Applications.* Oxford University Press, 2020.

[13] A. M. Sirunyan *et al.*, "Particle-flow reconstruction and global event description with the CMS detector," *Journal of Instrumentation*, vol. 12, no. 10, pp. P10003, 2017.

Bibliography

[14] The CMS Collaboration, "A MIP Timing Detector for the CMS Phase-2 Upgrade," Tech. Rep. CERN-LHCC-2019-003, CMS-TDR-020, CERN, Geneva, 2019.

[15] A. Harb, A. Mussgiller, and J. Hauk, "Test beam results of the first CMS double-sided strip module prototypes using the CBC2 read-out chip," *Nucl. Instr. and Meth. A*, vol. 845, pp. 93–96, 2017.

[16] G. Charpak, R. Bouclier, T. Bressani, J. Favier, and Č. Zupančič, "The use of multiwire proportional counters to select and localize charged particles," *Nuclear Instruments and Methods*, vol. 62, no. 3, pp. 262–268, 1968.

[17] The CMS Collaboration, "The Phase-2 Upgrade of the CMS Tracker," Tech. Rep. CERN-LHCC-2017-009, CMS-TDR-014, CERN, Geneva, 2017.

[18] S. M. Sze and M. K. Lee, *Semiconductor Devices Physics and Technology.* John Wiley & Sons, Ltd, 3rd ed., 2012.

[19] S. M. Sze and K. K. Ng, *Physics of Semiconductor Devices.* John Wiley & Sons, Ltd, 3rd ed., 2006.

[20] A. S. Grove, *Physics and Technology of Semiconductor Devices.* John Wiley & Sons, Ltd, 1967.

[21] M. Moll, "Displacement Damage in Silicon Detectors for High Energy Physics," *IEEE Transactions on Nuclear Science*, vol. 65, no. 8, pp. 1561–1582, 2018.

[22] C. Leroy and P.-G. Rancoita, *Principles of Radiation Interaction in Matter and Detection.* WORLD SCIENTIFIC, 4th ed., 2016.

[23] P. Zyla *et al.*, "Review of Particle Physics," *Prog. Theor. Exp. Phys.*, vol. 2020, no. 8, p. 083C01, 2020.

[24] J. Deasy, "ICRU Report 49, Stopping Powers and Ranges for Protons and Alph Particles," *Medical Physics*, vol. 21, no. 5, pp. 709–710, 1994.

[25] H. Bichsel, "Straggling in thin silicon detectors," *Rev. Mod. Phys.*, vol. 60, pp. 663–699, 1988.

[26] A. Owens and A. Peacock, "Compound semiconductor radiation detectors," *Nucl. Instr. and Meth. A*, vol. 531, no. 1, pp. 18–37, 2004.

[27] F. Scholze *et al.*, "Determination of the electron–hole pair creation energy for semiconductors from the spectral responsivity of photodiodes," *Nucl. Instr. and Meth. A*, vol. 439, no. 2, pp. 208–215, 2000.

[28] D. Groom, "Temperature Dependence of Mean Number of e-h Pairs per eV of X-ray Energy Deposit," 2004. https://www-ccd.lbl.gov/w_Si.pdf.

[29] G. R. Lynch and O. I. Dahl, "Approximations to multiple coulomb scattering," *Nucl. Instr. and Meth. B*, vol. 58, no. 1, pp. 6–10, 1991.

[30] G. Molière, "Theorie der Streuung schneller geladener Teilchen II Mehrfach- und Vielfachstreuung," *Zeitschrift für Naturforschung A*, vol. 3a, pp. 78–97, 1947.

[31] Y.-S. Tsai, "Pair production and bremsstrahlung of charged leptons," *Rev. Mod. Phys.*, vol. 46, pp. 815–851, 1974.

[32] S. Cihangir and S. Kwan, "Characterization of indium and solder bump bonding for pixel detectors," *Nucl. Instr. and Meth. A*, vol. 476, no. 3, pp. 670–675, 2002.

[33] M. Swartz, "CMS pixel simulations," *Nucl. Instr. and Meth. A*, vol. 511, no. 1, pp. 88–91, 2003.

[34] C. Jacoboni, C. Canali, G. Ottaviani, and A. Alberigi Quaranta, "A review of some charge transport properties of silicon," *Solid-State Electronics*, vol. 20, no. 2, pp. 77–89, 1977.

[35] C. Scharf and R. Klanner, "Precision measurement of the carrier drift velocities in $\langle 100 \rangle$ silicon," *Journal of Instrumentation*, vol. 10, no. 11, pp. C11008, 2015.

[36] S. Spannagel *et al.*, "Allpix^2: A modular simulation framework for silicon detectors," *Nucl. Instr. and Meth. A*, vol. 901, pp. 164–172, 2018.

[37] P. Schütze, *Silicon Pixel Detectors - Performance after Irradiation and Application in Three-dimensional Imaging.* Dissertation, Universität Hamburg, 2019. DESY-THESIS-2019-030.

[38] F. Cenna *et al.*, "Weightfield2: A fast simulator for silicon and diamond solid state detector," *Nucl. Instr. and Meth. A*, vol. 796, pp. 149–153, 2015. Proceedings of the 10th International Conference on Radiation Effects on Semiconductor Materials Detectors and Devices.

[39] W. Shockley, "Currents to Conductors Induced by a Moving Point Charge," *Journal of Applied Physics*, vol. 9, no. 10, pp. 635–636, 1938.

[40] S. Ramo, "Currents Induced by Electron Motion," *Proceedings of the IRE*, vol. 27, no. 9, pp. 584–585, 1939.

[41] H. Spieler, *Semiconductor Detector Systems.* Series on Semiconductor Science and Technology, OUP Oxford, 2005.

[42] J. Becker, *Signal development in silicon sensors used for radiation detection.* Dissertation, Universität Hamburg, 2010. DESY-THESIS-10-033.

Bibliography

[43] E. Belau *et al.*, "Charge collection in silicon strip detectors," *Nuclear Instruments and Methods in Physics Research*, vol. 214, no. 2, pp. 253–260, 1983.

[44] R. Turchetta, "Spatial resolution of silicon microstrip detectors," *Nucl. Instr. and Meth. A*, vol. 335, no. 1, pp. 44–58, 1993.

[45] M. Boronat, C. Marinas, A. Frey, I. Garcia, B. Schwenker, M. Vos, and F. Wilk, "Physical limitations to the spatial resolution of solid-state detectors," *IEEE Transactions on Nuclear Science*, vol. 62, no. 1, pp. 381–386, 2015.

[46] H. J. Barnaby, "Total-Ionizing-Dose Effects in Modern CMOS Technologies," *IEEE Transactions on Nuclear Science*, vol. 53, no. 6, pp. 3103–3121, 2006.

[47] T. Oldham and F. McLean, "Total ionizing dose effects in MOS oxides and devices," *IEEE Transactions on Nuclear Science*, vol. 50, no. 3, pp. 483–499, 2003.

[48] J. Schwandt, E. Fretwurst, R. Klanner, I. Pintilie, and J. Zhang, "Optimization of the radiation hardness of silicon pixel sensors for high x-ray doses using TCAD simulations," *Journal of Instrumentation*, vol. 7, no. 01, pp. C01006, 2012.

[49] T. Poehlsen *et al.*, "Charge losses in segmented silicon sensors at the Si–SiO2 interface," *Nucl. Instr. and Meth. A*, vol. 700, pp. 22–39, 2013.

[50] J. Schwandt, *Design of a Radiation Hard Silicon Pixel Sensor for X-ray Science*. Dissertation, Universität Hamburg, 2014. DESY-THESIS-14-029.

[51] Z. Jiaguo, *X-ray Radiation Damage Studies and Design of a Silicon Pixel Sensor for Science at the XFEL*. Dissertation, Universität Hamburg, 2013. DESY-THESIS-13-018.

[52] J. H. Crawford, "Radiation Effects in Diamond Lattice Semiconductors," *IEEE Transactions on Nuclear Science*, vol. 10, no. 5, pp. 1–10, 1963.

[53] M. Moll, *Radiation damage in silicon particle detectors: Microscopic defects and macroscopic properties*. Dissertation, Universität Hamburg, 1999. DESY-THESIS-1999-040.

[54] M. Huhtinen, "Simulation of non-ionising energy loss and defect formation in silicon," *Nucl. Instr. and Meth. A*, vol. 491, no. 1, pp. 194–215, 2002.

[55] L. R. Weisberg and H. Schade, "A Technique for Trap Determinations in Low-Resistivity Semiconductors," *Journal of Applied Physics*, vol. 39, no. 11, pp. 5149–5151, 1968.

[56] D. V. Lang, "Deep-level transient spectroscopy: A new method to characterize traps in semiconductors," *Journal of Applied Physics*, vol. 45, no. 7, pp. 3023–3032, 1974.

[57] G. Pellegrini *et al.*, "Technology developments and first measurements of Low Gain Avalanche Detectors (LGAD) for high energy physics applications," *Nucl. Instr. and Meth. A*, vol. 765, pp. 12–16, 2014.

[58] M. Ferrero *et al.*, "Radiation resistant LGAD design," *Nucl. Instr. and Meth. A*, vol. 919, pp. 16–26, 2019.

[59] V. Eremin, E. Verbitskaya, and Z. Li, "The origin of double peak electric field distribution in heavily irradiated silicon detectors," *Nucl. Instr. and Meth. A*, vol. 476, no. 3, pp. 556–564, 2002.

[60] G. Kramberger, V. Cindro, I. Mandić, M. Mikuž, and M. Zavrtanik, "Effective trapping time of electrons and holes in different silicon materials irradiated with neutrons, protons and pions," *Nucl. Instr. and Meth. A*, vol. 481, no. 1, pp. 297–305, 2002.

[61] "Synopsys TCAD." https://www.synopsys.com. Accessed July 2021.

[62] J. Schwandt *et al.*, "A new model for the TCAD simulation of the silicon damage by high fluence proton irradiation," in *2018 IEEE Nuclear Science Symposium and Medical Imaging Conference Proceedings (NSS/MIC)*, pp. 1–3, 2018.

[63] I. Pintilie, G. Lindstroem, A. Junkes, and E. Fretwurst, "Radiation Induced Point and Cluster-Related Defects with Strong Impact to Damage Properties of Silicon Detectors," *Nucl. Instr. and Meth. A*, vol. 611, pp. 52–68, 2009.

[64] C. Scharf, *Radiation damage of highly irradiated silicon sensors*. Dissertation, Universität Hamburg, 2018. https://ediss.sub.uni-hamburg.de/handle/ediss/7932.

[65] A. Chilingarov, "Temperature dependence of the current generated in Si bulk," *Journal of Instrumentation*, vol. 8, no. 10, pp. P10003, 2013.

[66] L. Evans and P. Bryant, "LHC machine," *Journal of Instrumentation*, vol. 3, no. 08, pp. S08001, 2008.

[67] O. S. Brüning *et al.*, *LHC Design Report*. CERN Yellow Reports: Monographs, Geneva: CERN, 2004.

[68] The ATLAS Collaboration, "LuminosityPublicResultsRun2." https://twiki.cern.ch. Accessed July 2021.

[69] The CMS Collaboration, "CMS Luminosity – Public Results." https://twiki.cern.ch. Accessed March 2021.

[70] O. Brüning and L. Rossi, "The High-Luminosity Large Hadron Collider," *Nature Reviews Physics*, vol. 1, pp. 241–243, 2019.

Bibliography

[71] G. Apollinari *et al.*, *High-Luminosity Large Hadron Collider (HL-LHC): Technical Design Report V. 0.1.* CERN Yellow Reports: Monographs, Geneva: CERN, 2017.

[72] The CMS Collaboration, "CMS Physics: Technical Design Report Volume 2: Physics Performance," *Journal of Physics G: Nuclear and Particle Physics*, vol. 34, pp. 995–1579. 669 p, 2007.

[73] The CMS Collaboration, "Observation of a new boson at a mass of 125 GeV with the CMS experiment at the LHC," *Physics Letters B*, vol. 716, no. 1, pp. 30–61, 2012.

[74] The CMS Collaboration, "The CMS experiment at the CERN LHC," *Journal of Instrumentation*, vol. 3, no. 08, pp. S08004, 2008.

[75] The CMS Collaboration, *CMS Physics: Technical Design Report Volume 1: Detector Performance and Software.* Technical design report. CMS, Geneva: CERN, 2006.

[76] K. Deiters *et al.*, "Double screening tests of the CMS ECAL avalanche photodiodes," *Nucl. Instr. and Meth. A*, vol. 543, no. 2, pp. 549–558, 2005.

[77] K. Bell *et al.*, "Vacuum phototriodes for the CMS electromagnetic calorimeter endcap," *IEEE Transactions on Nuclear Science*, vol. 51, no. 5, pp. 2284–2287, 2004.

[78] V. D. Elvira, "Validation of Geant4 Physics Using the CMS HCAL Test Beam 2002 Experiment," Tech. Rep. CMS-NOTE-2004-021, CERN, Geneva, 2004.

[79] The CMS Collaboration, "The CMS trigger system. The CMS trigger system," *Journal of Instrumentation*, vol. 12, pp. P01020, 2016.

[80] A. Dominguez *et al.*, "CMS Technical Design Report for the Pixel Detector Upgrade," Tech. Rep. CERN-LHCC-2012-016, CMS-TDR-11, CERN, Geneva, 2012.

[81] W. Adam *et al.*, "The CMS phase-1 pixel detector upgrade," *Journal of Instrumentation*, vol. 16, no. 02, pp. P02027, 2021.

[82] H. Kästli, "Frontend electronics development for the cms pixel detector upgrade," *Nucl. Instr. and Meth. A*, vol. 731, pp. 2284–2287, 2013. PIXEL 2012.

[83] A. Starodumov, P. Berger, and M. Meinhard, "High rate capability and radiation tolerance of the PROC600 readout chip for the CMS pixel detector," *Journal of Instrumentation*, vol. 12, no. 01, pp. C01078, 2017.

[84] M. P. Rauch, "Thermal Characterization and Optimization of the Pixel Module Support Structure for the Phase-1 Upgrade of the CMS Pixel Detector," Master's thesis, RWTH Aachen, 2015. CERN-THESIS-2015-247.

[85] P. Tropea *et al.*, "Design, construction and commissioning of a 15 kW CO2 evaporative cooling system for particle physics detectors: lessons learnt and perspectives for further development," *Proceedings of Science*, vol. TIPP2014, p. 223, 2015.

[86] D. Contardo, M. Klute, J. Mans, L. Silvestris, and J. Butler, "Technical Proposal for the Phase-II Upgrade of the CMS Detector," Tech. Rep. CERN-LHCC-2015-010, LHCC-P-008, CMS-TDR-15-02, CERN, Geneva, 2015.

[87] M. Garcia-Sciveres, "The RD53A Integrated Circuit," Tech. Rep. CERN-RD53-PUB-17-001, CERN, Geneva, 2017.

[88] G. Steinbrück, "Development of planar pixel sensors for the CMS Inner Tracker at the High-Luminosity LHC," *Nucl. Instr. and Meth. A*, vol. 978, p. 164438, 2020.

[89] M. Centis Vignali, *Silicon Sensors for the Upgrades of the CMS Pixel Detector.* Dissertation, Universität Hamburg, 2015. 10.3204/DESY-THESIS-2015-052.

[90] "FLUKA." https://fluka.cern/. Accessed March 2021.

[91] E. Currás *et al.*, "Study of small-cell 3D silicon pixel detectors for the high luminosity LHC," *Nucl. Instr. and Meth. A*, vol. 931, pp. 127–134, 2019.

[92] J. Lange *et al.*, "Radiation hardness of small-pitch 3D pixel sensors up to a fluence of $3 \times 10^{16} \mathrm{n_{eq}}/\mathrm{cm}^2$," *Journal of Instrumentation*, vol. 13, no. 09, pp. P09009, 2018.

[93] "Hamamatsu Photonics K.K.." https://www.hamamatsu.com/. Accessed July 2021".

[94] J. Schwandt, "CMS Pixel detector development for the HL-LHC," *Nucl. Instr. and Meth. A*, vol. 924, pp. 59–63, 2019.

[95] J. Schwandt, "Information about Planar Pixel Sensor Prototypes for the Phase-2 Upgrade." Personal communication.

[96] The Tracker Group of the CMS Collaboration, "Evaluation of HPK n$^+$-p planar pixel sensors for the CMS Phase-2 upgrade," *Nucl. Instr. and Meth. A*, 2021. in preparation.

[97] E. Fretwurst *et al.*, "The influence of edge effects on the determination of the doping profile of silicon pad diodes," *Nucl. Instr. and Meth. A*, vol. 867, pp. 231–236, 2017.

[98] C. Niemeyer, *Edge-on Measurements on Planar Pixel Sensors for the CMS Phase 2 Upgrade.* Dissertation in preparation, Universität Hamburg, 2021.

[99] G. Pellegrini *et al.*, "Technology development of p-type microstrip detectors with radiation hard p-spray isolation," *Nucl. Instr. and Meth. A*, vol. 566, no. 2, pp. 360–365, 2006.

Bibliography

[100] Dow Chemical, "SYLGARD$^{\text{TM}}$ 184 Silicone Elastomer." https://www.dow.com/. Accessed July 2021".

[101] D. Žontar, "Študij sevalnih poškodb silicijevih detektorjev za eksperimente z visoko luminoznostjo na trkalniku LHC," 1998. http://cds.cern.ch/record/1390822.

[102] F. Ravotti *et al.*, "A New High-Intensity Proton Irradiation Facility at the CERN PS East Area," *Proceedings of Science*, vol. TIPP2014, p. 354, 2015.

[103] P. Allport *et al.*, "Experimental determination of proton hardness factors at several irradiation facilities," *Journal of Instrumentation*, vol. 14, no. 12, pp. P12004, 2019.

[104] A. Curioni *et al.*, "Single- and multi-foils ^{27}Al(p,3pn)^{24}Na activation technique for monitoring the intensity of high-energy beams," *Nucl. Instr. and Meth. A*, vol. 858, pp. 101–105, 2017.

[105] I. Dawson, *Radiation effects in the LHC experiments: Impact on detector performance and operation.* CERN Yellow Reports: Monographs, Geneva: CERN, 2021.

[106] C. Barth, *Physikalische Analyse der Ansprechverhaltens des CMS Siliziumdetektors beim Betrieb am LHC = Performance of the CMS Tracker under Irradiation.* Dissertation, Karlsruher Institut für Technologie, 2013. 10.5445/IR/1000032944 .

[107] J. Hunt, "Evolution of silicon sensor parameters of the CMS tracker due to continuous irradiation during operation," Master's thesis, Karlsruher Institut für Technologie, 2018. CERN-THESIS-2018-398.

[108] F. Zhang, "Fill Numbers for Short- or Small-Bunch LHC Fills." Personal communication.

[109] J. Renner, "Planning and validation of the thermal mock-up for the cms pixel detector," Master's thesis, Karlsruher Institut für Technologie, 2017. IEKP-KA/2017-13.

[110] The CMS Collaboration, "1-D plot covering CMS tracker, showing FLUKA simulated 1 MeV neutron equivalent in Silicon including contributions from various particle types.," Tech. Rep. CMS-DP-2015-022, 2015.

[111] D. Campbell, A. Chilingarov, and T. Sloan, "Frequency and temperature dependence of the depletion voltage from CV measurements for irradiated Si detectors," *Nucl. Instr. and Meth. A*, vol. 492, no. 3, pp. 402–410, 2002.

[112] B. Vormwald, "The CMS Phase-1 pixel detector - experience and lessons learned from two years of operation," *Journal of Instrumentation*, vol. 14, no. 07, pp. C07008, 2019.

[113] F. Feindt and T. Prousalidi, "CMS pixel radiation damage measurements." Talk at 'Radiation effects in the LHC experiments and impact on operation and performance'. 2019.

[114] S. Wiederkehr, *The effective lifetime of $B_s^0 \to \mu^+\mu^-$ and designing a readout chip for pixel sensor development.* Dissertation, ETH Zurich, 2018. 10.3929/ethz-b-000314130.

[115] I. Zoi *et al.*, "Position resolution with $25\,\mu$m pitch pixel sensors before and after irradiation," *preprint submitted to Nucl. Instr. and Meth. A*, 2021. arXiv:2107.04640.

[116] H. C. Kästli *et al.*, "Design and performance of the CMS pixel detector readout chip," *Nucl. Instr. and Meth. A*, vol. 565, no. 1, pp. 188–194, 2006.

[117] T. Rohe *et al.*, "Radiation hardness of CMS pixel barrel modules," *Nucl. Instr. and Meth. A*, vol. 624, no. 2, pp. 414–418, 2010.

[118] F. Meier, *PIXEL DTB Testboard for Readout Chips Manual.* Paul Scherrer Institut, Villigen, Switzerland, 0.0 ed., 2013. https://github.com/frmeier/psi46manuals.

[119] S. Spannagel, B. Meier, and H. C. Perrey, "The pxarCore Library - Technical Documentation, Reference Manual, and Sample Applications," Tech. Rep. CERN-CMS-NOTE-2016-001, CERN, Geneva, 2015.

[120] J. Dreyling-Eschweiler *et al.*, "The DESY II test beam facility," *Nucl. Instr. and Meth. A*, vol. 922, pp. 265–286, 2019.

[121] H. Jansen *et al.*, "Performance of the EUDET-type beam telescopes," *EPJ Techniques and Instrumentation*, vol. 3, no. 7, 2006.

[122] C. Hu-Guo *et al.*, "First reticule size MAPS with digital output and integrated zero suppression for the EUDET-JRA1 beam telescope," *Nucl. Instr. and Meth. A*, vol. 623, no. 1, pp. 480–482, 2010.

[123] D. Cussans, "Description of the JRA1 Trigger Logic Unit (TLU), v0.2c," Tech. Rep. EUDET-MEMO-2009-04, Univerity of Bristol, 2009.

[124] "Mimosa pixel telescopes." https://telescopes.desy.de. Accessed March 2020.

[125] EUDAQ Development Team, "EUDAQ a generic data acquisition framework." http://eudaq.github.io/. Accessed March 2020.

[126] D. Pitzl, "tele-scope – test beam pixel telescope analysis based on eudaq only." https://github.com/pitzl/tele-scope. Accessed July 2021".

[127] M. Paterno, "Calculating Efficiencies and Their Uncertainties," Tech. Rep. FERMILAB-TM-2286-CD, FNAL, 2004.

Bibliography

[128] S. Spannagel, *Test Beam Measurements for the Upgrade of the CMS Pixel Detector and Measurement of the Top Quark Mass from Differential Cross Sections.* Dissertation, Universität Hamburg, 2016. 10.3204/DESY-THESIS-2016-010.

[129] C. Leroy and P.-G. Rancoita, *Silicon Solid State Devices and Radiation Detection.* WORLD SCIENTIFIC, 2012.

[130] I. Zoi, *Search for diboson resonances in the all jets final state with CMS at $s\sqrt{s} = 13$ TeV and pixel sensors development for HL-LHC.* Dissertation in preparation, Universität Hamburg, 2021.

[131] F. Feindt, "Beam Test Measurements on Planar Pixel Sensors for the CMS Phase 2 Upgrade," in *2019 IEEE Nuclear Science Symposium and Medical Imaging Conference (NSS/MIC)*, pp. 1–7, 2019.

[132] P. Weigell *et al.*, "Characterization and performance of silicon n-in-p pixel detectors for the ATLAS upgrades," *Nucl. Instr. and Meth. A*, vol. 658, no. 1, pp. 36–40, 2011.

[133] A. Ebrahimi, "Characteristics and Performance of RD53A Readout Chip Equipped with Small-pixel Silicon Sensors," in *2019 IEEE Nuclear Science Symposium and Medical Imaging Conference (NSS/MIC)*, pp. 1–5, 2019.

[134] The Tracker Group of the CMS Collaboration, "Evaluation of Silicon Pixel Sensors with RD53A Readout for the Phase-2 Upgrade of the CMS Inner Tracker," *Nucl. Instr. and Meth. A*, 2021. in preparation.

[135] Y. Allkofer *et al.*, "Design and performance of the silicon sensors for the CMS barrel pixel detector," *Nucl. Instr. and Meth. A*, vol. 584, no. 1, pp. 25–41, 2008.

[136] A. Ebrahimi *et al.*, "Position reconstruction for segmented detectors," *preprint submitted to Elsevier*, 2021. arXiv:2107.06600.

[137] V. Blobel and L. Erich, *Statistische und numerische Methoden der Datenanalyse.* Teubner Verlag, 1998.

[138] I. Pintilie, G. Lindstroem, A. Junkes, and E. Fretwurst, "Radiation-induced point- and cluster-related defects with strong impact on damage properties of silicon detectors," *Nucl. Instr. and Meth. A*, vol. 611, no. 1, pp. 52–68, 2009.

[139] G. Kramberger *et al.*, "Modeling of electric field in silicon micro-strip detectors irradiated with neutrons and pions," *Journal of Instrumentation*, vol. 9, no. 10, pp. P10016, 2014.

[140] A. Affolder, P. Allport, and G. Casse, "Charge collection efficiencies of planar silicon detectors after reactor neutron and proton doses up to $1.6 \times 10^{16} \mathrm{n_{eq}/cm^2}$," *Nucl. Instr. and Meth. A*, vol. 612, no. 3, pp. 470–473, 2010.

[141] E. Buchanan, "The LHCb vertex locator (VELO) pixel detector upgrade," *Journal of Instrumentation*, vol. 12, no. 01, pp. C01013, 2017.

[142] W. Adam *et al.*, "P-type silicon strip sensors for the new CMS tracker at HL-LHC," *Journal of Instrumentation*, vol. 12, no. 06, pp. P06018, 2017.

[143] W. Adam *et al.*, "Experimental study of different silicon sensor options for the upgrade of the CMS outer tracker," *Journal of Instrumentation*, vol. 15, no. 04, pp. P04017, 2020.

[144] M. Swartz, "A Detailed Simulation of the CMS Pixel Sensor," Tech. Rep. CMS-NOTE-2002-027, CERN, Geneva, 2002.

[145] V. Chiochia, M. Swartz, D. Fehling, G. Giurgiu, and P. Maksimovic, "A new technique for the reconstruction, validation, and simulation of hits in the CMS Pixel Detector," *Proceedings of Science*, vol. Vertex 2007, p. 035, 2008.

[146] M. Berger, J. Coursey, M. Zucker, and J. Chang, "Stopping-Power & Range Tables for Electrons, Protons, and Helium Ions." NIST Standard Reference Database 124.

[147] C. Damarell, "Vertex detectors: The state of the art and future prospects," in *Proceedings of the 1995 SLAC Summer Institute on Particle Physics*, pp. 103.

[148] S. Nadarajah, "A generalized normal distribution," *Journal of Applied Statistics*, vol. 32, no. 7, pp. 685–694, 2005.

[149] M. Dragicevic *et al.*, "Test beam performance measurements for the Phase I upgrade of the CMS pixel detector," *Journal of Instrumentation*, vol. 12, no. 05, pp. P05022, 2017.

A. Monitoring Plots

Full sets off these monitoring plots, recorded at the test beam for a non-irradiated and an irradiated sensor module. Both modules have pixel sizes of $50 \times 50\,\mu\mathrm{m}^2$. The displayed quantities are introduced in section 5.3.3.

(a)

(b)

(c)

(d)
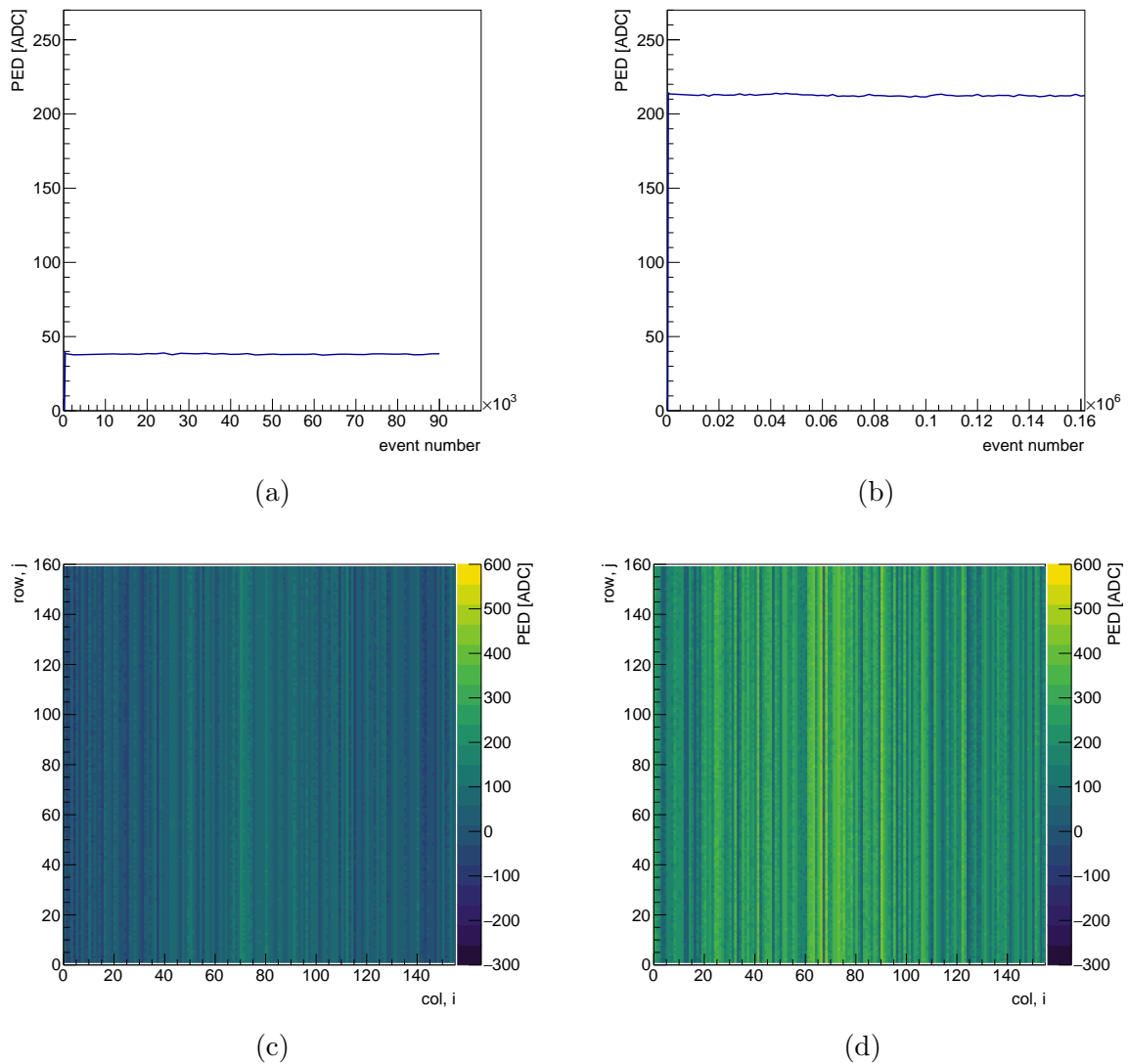
Figure A.1.: Average pedestal as a function of the event number (top) and map of each pixel's pedestal (bottom). The left figures are for a non-irradiated sample, the right figures are for a neutron irradiated sample with $\phi_{eq} = 7.2 \times 10^{15}\,\mathrm{cm}^{-2}$.
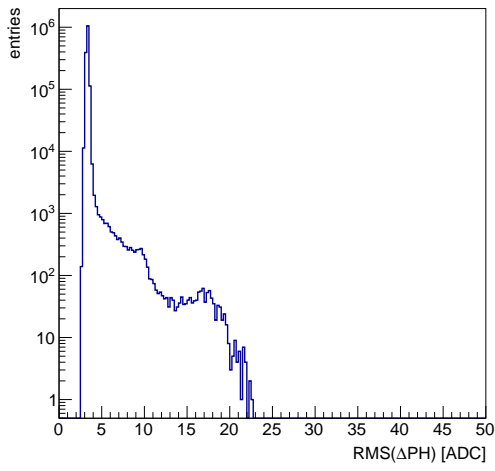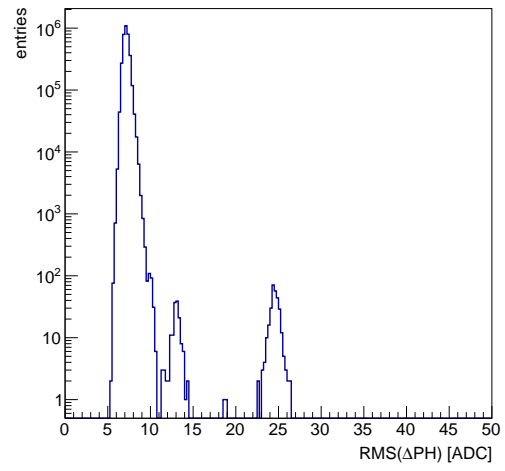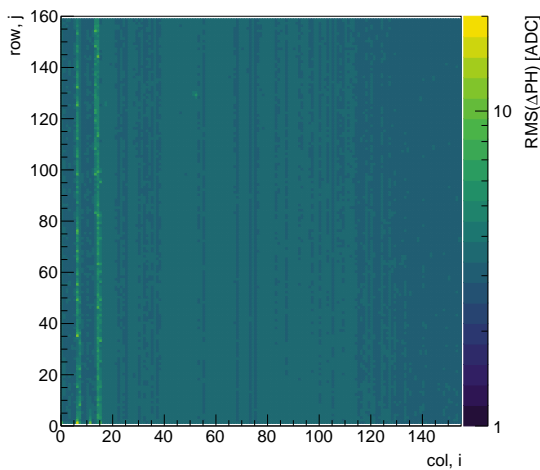
A. Monitoring Plots
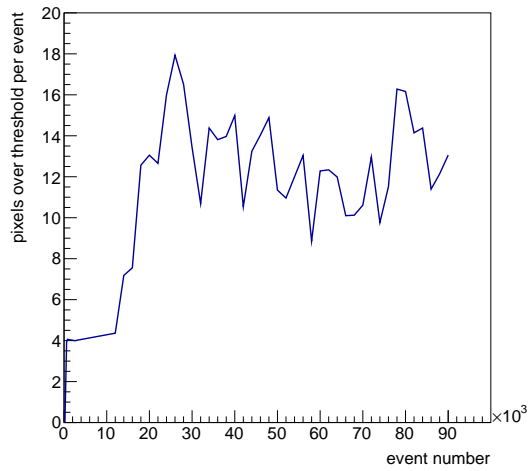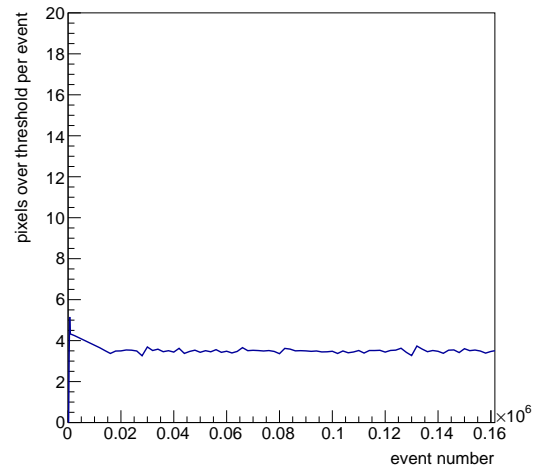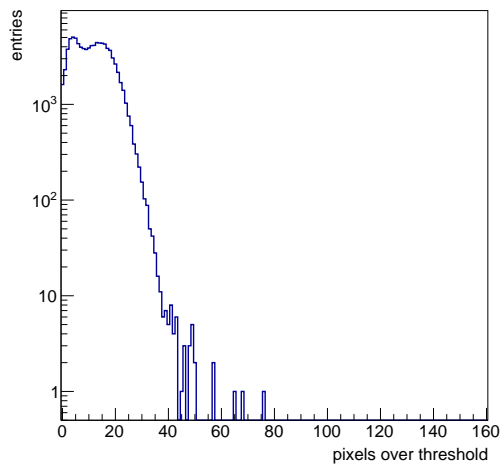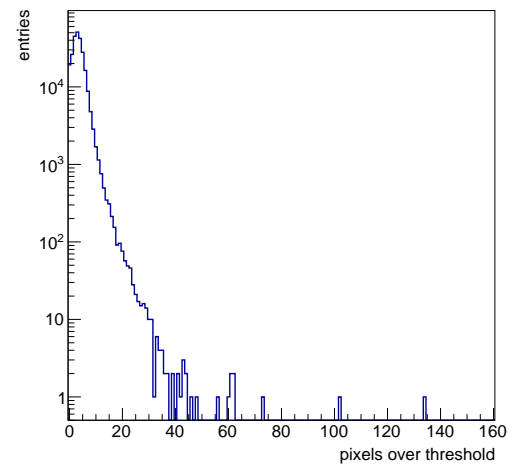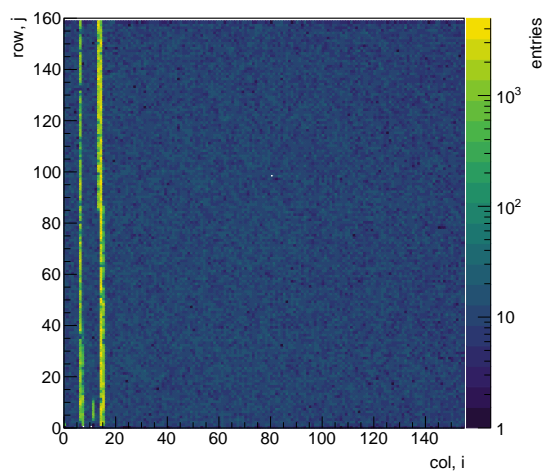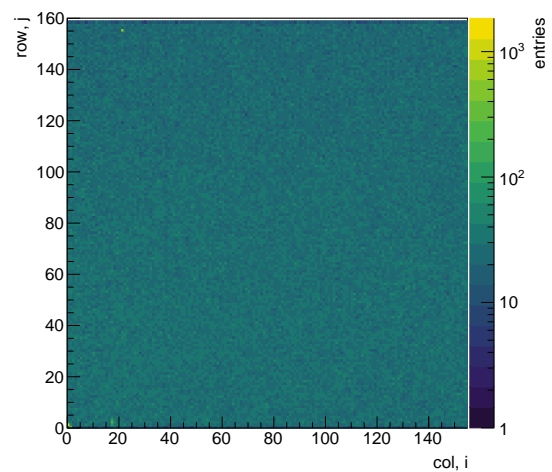
Figure A.2.: Number of pixels above threshold as average versus the event number (top), as distribution (mid) and as map for each pixel (bottom). The left figures are for a non-irradiated sample, the right figures are for a neutron irradiated sample with $\phi_{eq} = 7.2 \times 10^{15}\,\mathrm{cm}^{-2}$.
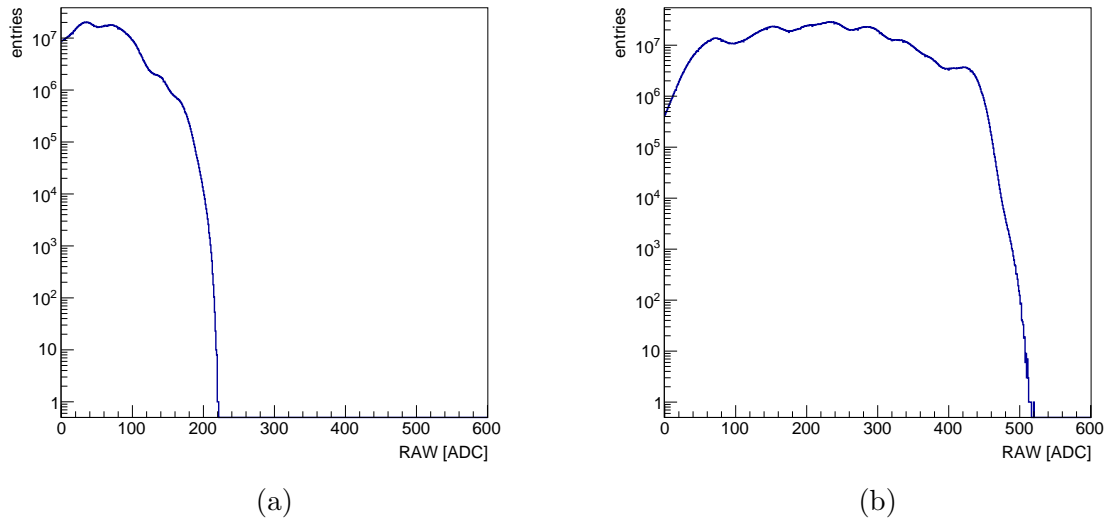
Figure A.3.: Distributions of the raw pixel response. The left figure is for a non-irradiated sample, the right figure is for a neutron irradiated sample with $\phi_{eq} = 7.2 \times 10^{15}\,\mathrm{cm}^{-2}$.
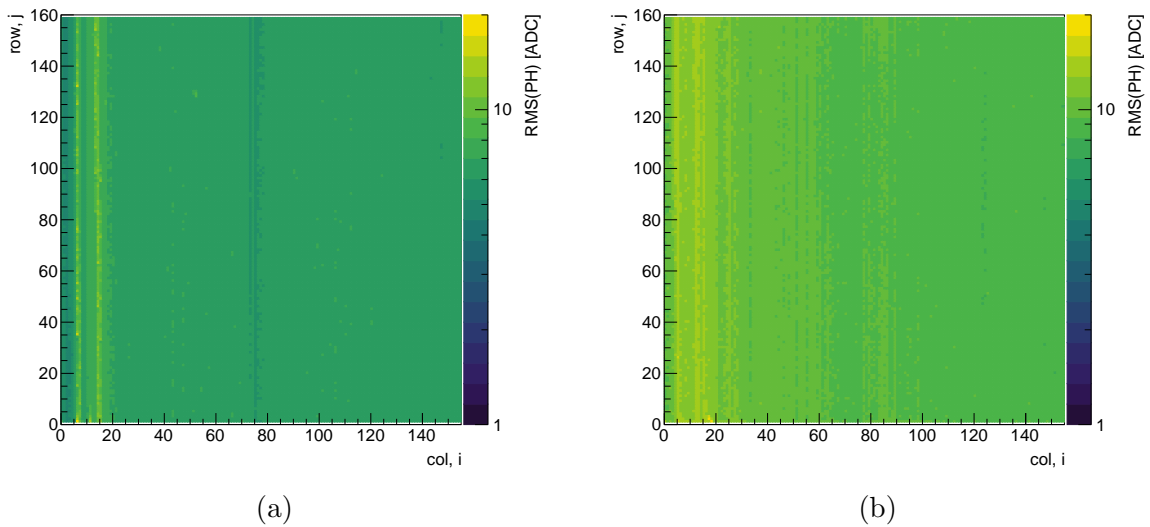
Figure A.4.: Maps of the RMS of the pulse height for each pixels. The left figure is for a non-irradiated sample, the right figure is for a neutron irradiated sample with $\phi_{eq} = 7.2 \times 10^{15}\,\mathrm{cm}^{-2}$.

(a)

(b)

(c)

(d)
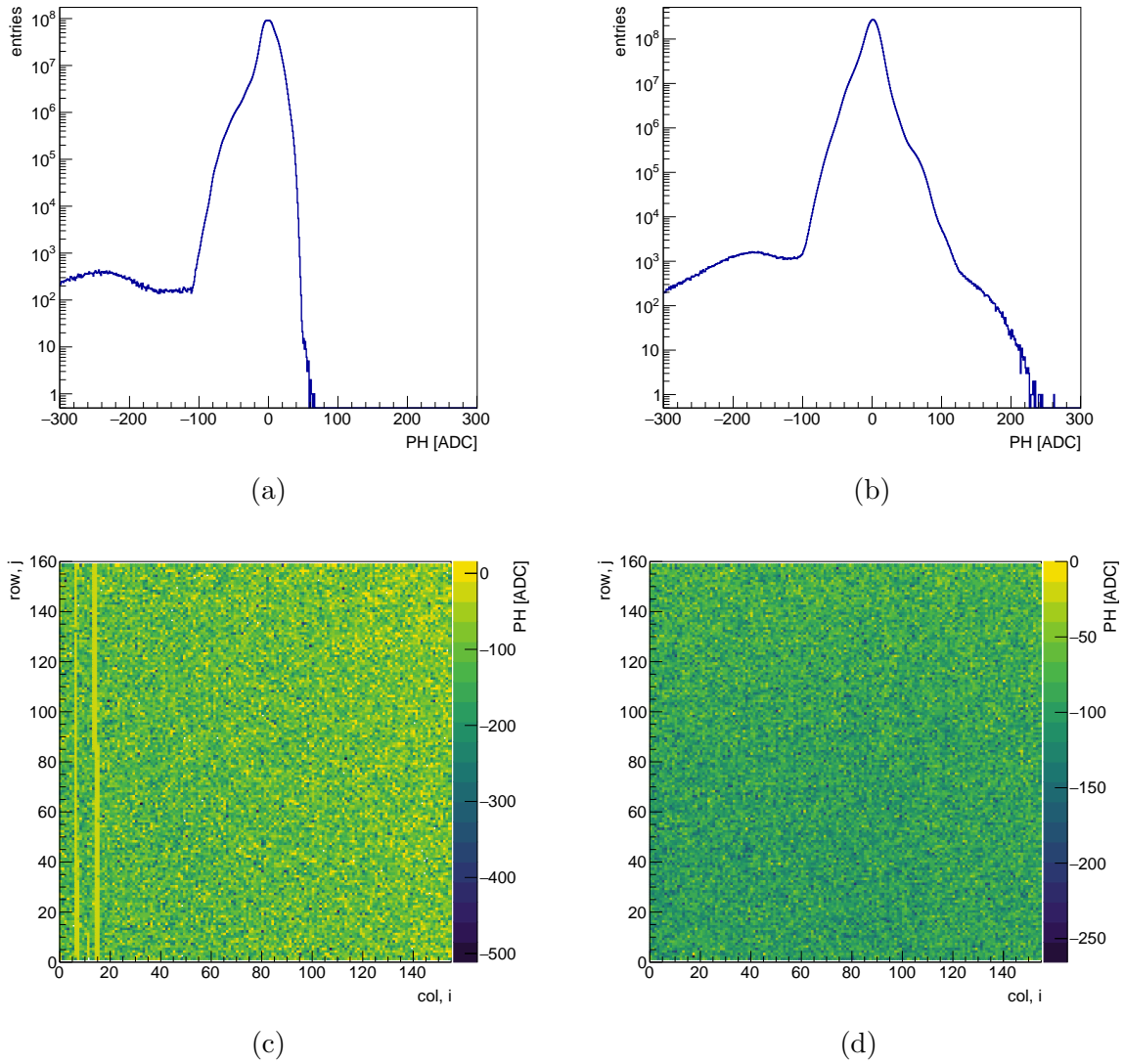
Figure A.5.: Distribution of the pulse height (top) and map of its average (bottom). The left figures are for a non-irradiated sample, the right figures are for a neutron irradiated sample with $\phi_{eq} = 7.2 \times 10^{15}\,\mathrm{cm}^{-2}$.
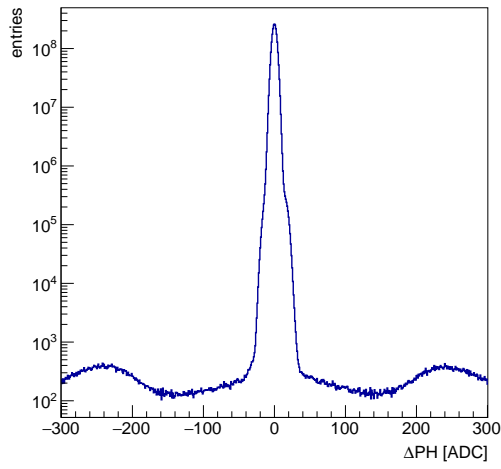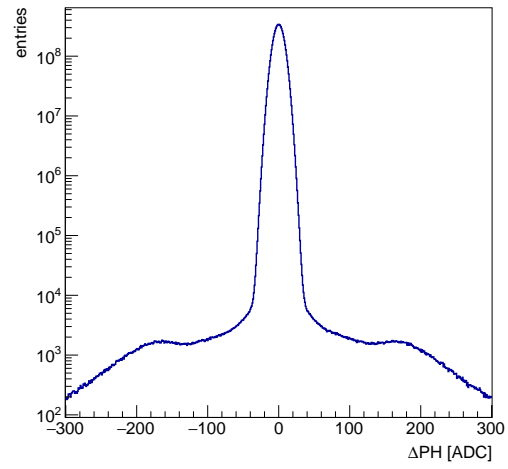
Figure A.6.: Distributions of the differential pulse height. The left figure is for a non-irradiated sample, the right figure is for a neutron irradiated sample with $\phi_{eq} = 7.2 \times 10^{15} \, \text{cm}^{-2}$.
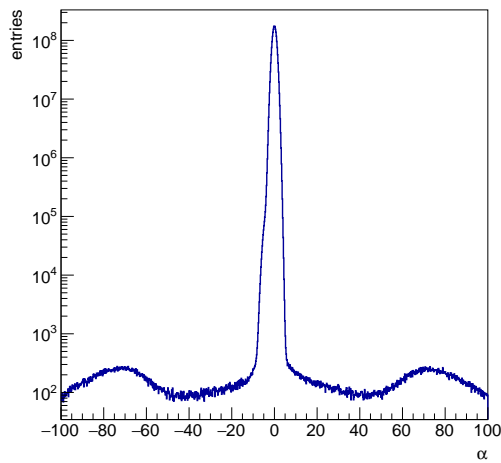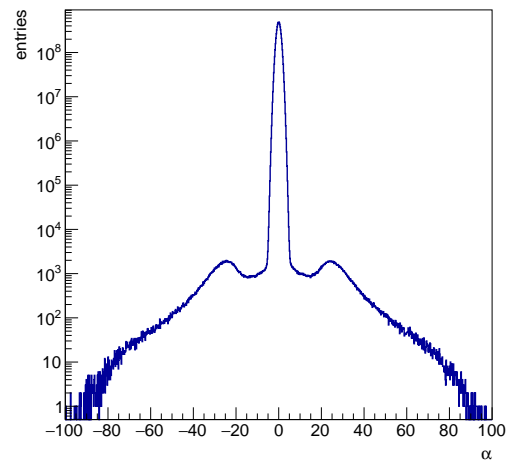
Figure A.7.: Distributions of the pulse height significance. The left figure is for a non-irradiated sample, the right figure is for a neutron irradiated sample with $\phi_{eq} = 7.2 \times 10^{15} \, \text{cm}^{-2}$.

A. Monitoring Plots
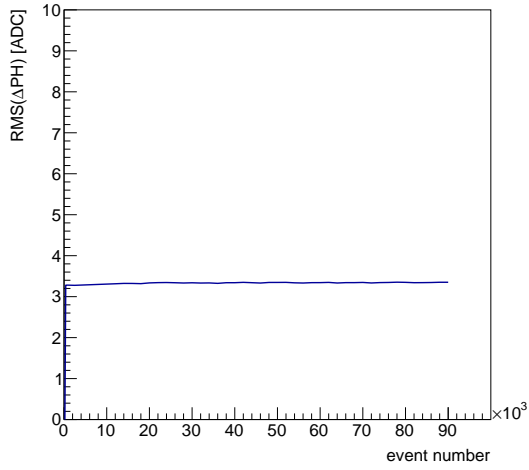
(a)
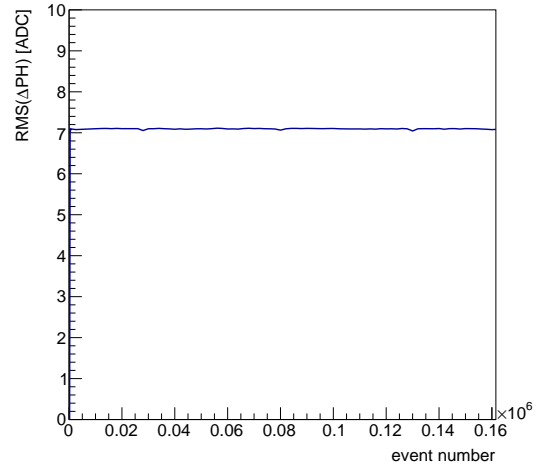
(b)

(c)

(d)

(e)
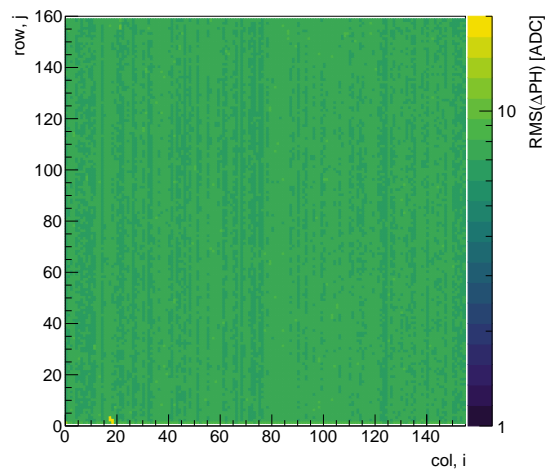
(f)

Figure A.8.: RMS of the differential pulse height as average versus the event number (top), as distribution (mid) and as map for each pixel (bottom) The left figures are for a non-irradiated sample, the right figures are for a neutron irradiated sample with $\phi_{eq} = 7.2 \times 10^{15}\,\mathrm{cm}^{-2}$.

B. Resolution Calculation

We start with

$$\Delta y_{DUT} = y_{DUT} - y_{TEL}. \tag{B.1}$$

This is the definition of the DUT residual. Both y_{DUT} and y_{TEL} are expressed in local coordinates of the DUT. From the distribution of Δy_{DUT} we determine

$$\text{RMS}_{trc}(\Delta y_{DUT})^2 = \sigma_{yDUT}^2 + \sigma_{yTEL}^2 \tag{B.2}$$

with two contributions, the DUT hit resolution σ_{yDUT} and the track resolution of the telescope σ_{yTEL} at the position of the DUT. We are interested in σ_{yDUT} so we need to calculate σ_{yTEL}. The position prediction from the the telescope track y_{TEL} consists of the extrapolation of the upstream and downstream triplet tracks (y_{utri} and y_{dtri})

$$y_{TEL} = \frac{y_{utri} + y_{dtri}}{2 \cdot cos(\theta_x)}. \tag{B.3}$$

We divide by 2 to take the average and by $cos(\theta_x)$ to take into account the inclination of the DUT with respect to the global (telescope) reference frame in which y_{utri} and y_{dtri} are calculated. We can define the residual

$$\Delta y_{TEL} = y_{utri} - y_{dtri} \tag{B.4}$$

and determine the truncated RMS of its distribution in data. Similar to equation B.2 there are two contributions to the width of the residual

$$\text{RMS}_{trc}(\Delta y_{TEL})^2 = \sigma_{y_{utri}}^2 + \sigma_{y_{dtri}}^2. \tag{B.5}$$

Now we do the error propagation of equation B.3

$$\sigma_{yTEL} = \sqrt{\left(\frac{dy_{TEL}}{dy_{utri}}\right)^2 \cdot \sigma_{y_{utri}}^2 + \left(\frac{dy_{TEL}}{dy_{dtri}}\right)^2 \cdot \sigma_{y_{dtri}}^2} = \sqrt{\left(\frac{1}{2 \cdot cos(\theta_x)}\right)^2 \cdot \left(\sigma_{y_{utri}}^2 + \sigma_{y_{dtri}}^2\right)}. \tag{B.6}$$

The hindmost parentheses can be replaced with equation B.5 and the expression simplifies to

$$\sigma_{yTEL} = \frac{\text{RMS}_{trc}(\Delta y_{g,TEL})}{2 \cdot cos(\theta_x)}. \tag{B.7}$$

B. Resolution Calculation

Thus the telescope contribution to equation B.2 can be estimated from data.

Acknowledgments

Eidesstattliche Versicherung / Declaration on oath

Hiermit versichere ich an Eides statt, die vorliegende Dissertationsschrift selbst verfasst und keine anderen als die angegebenen Hilfsmittel und Quellen benutzt zu haben.

Hamburg, den 31.07.2021

_____

Unterschrift der Doktorandin / des Doktoranden